

MASARYKOVA UNIVERZITA
PŘÍRODOVĚDECKÁ FAKULTA
ÚSTAV TEORETICKÉ FYZIKY A ASTROFYZIKY

Diplomová práce

BRNO 2021

TOMÁŠ PLŠEK

Vztah mezi Bondiho akrecí a energií jetů v obřích eliptických galaxiích

Diplomová práce

Tomáš Plšek

Bibliografický záznam

Autor:	Tomáš Plšek Přírodovědecká fakulta, Masarykova univerzita Ústav teoretické fyziky a astrofyziky
Název práce:	Vztah mezi Bondiho akrecí a energií jetů v obřích eliptických galaxiích
Studijní program:	Fyzika
Studijní obor:	Astrofyzika
Vedoucí práce:	doc. Mgr. Norbert Werner, PhD.
Akademický rok:	2020/21
Počet stran:	IX + 103
Klíčová slova:	obří eliptické galaxie; radiové galaxie; aktivní galaxie; zpětná vazba AGN; rentgenové dutiny; Bondiho akrece; CADET

Bibliographic Entry

Author:

Tomáš Plšek
Faculty of Science, Masaryk University
Department of Theoretical physics and Astrophysics

Title of Thesis:

The relation between the Bondi accretion rate and jet power in
giant elliptical galaxies

Degree Programme: Physics

Field of Study: Astrophysics

Supervisor: doc. Mgr. Norbert Werner, PhD.

Academic Year: 2020/21

Number of Pages: IX + 103

Keywords: giant ellipticals; radio galaxies; active galaxies; AGN feedback;
X-ray cavities; Bondi accretion; CADET

Abstrakt

Tato práce zkoumá rádiové laloky a rentgenové dutiny v atmosférách masivních galaxií a jejich závislost na zpětné vazbě aktivních galaktických jader poháněné akreujícími supermasivními černými děrami. Potvrdili jsme závislost mezi Bondiho akrečními výkony a mechanickými výkony relativistických výtrysků, kterou dříve pozoroval Allen a kol. (2006). Silná korelace je však pozorována pouze u galaxií s tepelně nestabilní atmosférou obsahující známky chladného plynu. Získaný vztah je velmi blízký lineární závislosti a za předpokladu, že akrece probíhá opravdu ve sférickém Bondiho režimu, výsledky ukazují, že asi 0,8 procent klidové hmotnosti akreované hmoty se přemění na energii pozorovaného jetu. Ukazuje se však, že tento vztah je důsledkem korelace mezi mechanickými výkony výtrysků a hmotnostmi centrálních supermasivních černých děr. Uvádíme také pozoruhodné souvislosti mezi řadou fyzikálních parametrů horkých galaktických atmosfér a centrálních aktivních galaktických jáder. Mimo to byl pozorován značný a nevysvětlený rozpor mezi jednotlivými metodami pro odhad výkonů relativistických výtrysků.

Ve druhé části této práce představujeme nástroj *CAvity DEtection Tool* (CADET), jež využívá metod strojového učení a který byl vyvinut pro vyhledávání a odhadování velikostí rentgenových dutin na zašuměných původních snímcích z rentgenové observatoře *Chandra*. Předpovědi této sítě jsme porovnali s vizuálně identifikovanými rentgenovými dutinami a představili jsme využití této sítě pro hledání nových dutin v méně prozkoumaných galaktických systémech. Budoucí vylepšení a zdokonalení této sítě, která již vedla k objevu 5 dříve neznámých dutin prezentovaných v této práci, může vést k dalekosáhlému pokroku v našem chápání radiomechanické zpětné vazby aktivních galaktických jader.

Abstract

The thesis explores radio lobes and X-ray cavities in hot atmospheres of massive galaxies and their connection to AGN feedback powered by accreting supermassive black holes. We have confirmed the correlation between Bondi accretion rate and mechanical jet power previously reported by [Allen et al. \(2006\)](#). However, a strong correlation is observed only for galaxies with thermally unstable atmospheres containing signs of cool gas tracers. The obtained relation is very close to linear, and assuming the accretion is really spherical and Bondi-like, the results indicate that about 0.8 percent of the rest mass of the accreted matter is converted to the observed jet energy. We show that the observed relation is a consequence of an underlying correlation between the mechanical jet power and the mass of the central supermassive black hole. We also report remarkable connections between a number of physical parameters of hot galactic atmospheres and of the central AGN engines. Besides that, a considerable and unexplained discrepancy between individual jet power estimating methods was observed.

In the second part of the thesis, we present the developed machine learning pipeline *CAvity DEtection Tool* (CADET) which was trained for finding and size-estimating arbitrary surface brightness depressions (X-ray cavities) on noisy *Chandra* images of galaxies. Predictions of the CADET network are compared with visually identified X-ray cavities and the utilization of the pipeline for finding new cavities in less explored galactic systems is presented. Future work on improving and refining the CADET pipeline, which already led to the discovery of 5 previously unknown cavities presented in this thesis, might lead to far-reaching advances in our understanding of radio-mechanical AGN feedback.

ZADÁNÍ DIPLOMOVÉ PRÁCE

Akademický rok: 2019/2020

Ústav: Ústav teoretické fyziky a astrofyziky

Student: Bc. Tomáš Plšek

Program: Fyzika

Specializace: Astrofyzika

Ředitel Ústavu teoretické fyziky a astrofyziky PřF MU Vám ve smyslu Studijního a zkušebního řádu MU určuje diplomovou práci s názvem:

Název práce: Vztah mezi Bondiho akrecí a energií jetů v obřích eliptických galaxiích

Název práce anglicky: The relation between the Bondi accretion rate and jet power in giant elliptical galaxies

Jazyk závěrečné práce: angličtina

Oficiální zadání:

In principle, the hot atmospheres of giant elliptical galaxies naturally provide a steady supply of fuel to the active galactic nuclei (AGN) in their centres. The accretion rates predicted by the simple Bondi model of a spherical accretion can be calculated from the atmospheric gas temperatures and density profiles in the vicinity of the central black hole. Most of the accretion power is likely converted into jets, the power of which can be inferred from the observed X-ray cavities. The student will determine the atmospheric gas temperatures and density profiles in the vicinity of the central AGN for a sample of giant elliptical galaxies to determine the Bondi accretion rates. For the same galaxies, the student will measure the jet powers from the pV work and time-scales required to inflate X-ray cavities in the surrounding hot atmospheres. The goal of the thesis is to confirm the previously reported correlation between the Bondi accretion and jet powers.

Vedoucí práce: doc. Mgr. Norbert Werner, Ph.D.

Datum zadání práce: 2. 12. 2019

V Brně dne: 4. 3. 2020

Souhlasím se zadáním (podpis, datum):

.....
Bc. Tomáš Plšek
student

.....
doc. Mgr. Norbert Werner, Ph.D.
vedoucí práce

.....
prof. Rikard von Unge, Ph.D.
ředitel Ústavu teoretické fyziky a
astrofyziky

Poděkování

Především bych chtěl poděkovat svému vedoucímu Norbertu Wernerovi za jeho vedení a laskavou pomoc při psaní této práce. Dále bych tímto chtěl poděkovat svému konzultantovi Martinu Topinkovi a doktorandům Romaně Grossové a Matěji Kosibovi za jejich cenné rady. A zvláštní poděkování patří mé přítelkyni, která vydržela všechny těžké chvíle, které jsem při psaní této práce prožíval.

Prohlášení

Prohlašuji, že jsem svou diplomovou práci vypracoval samostatně s využitím informačních zdrojů, které jsou v práci citovány.

Brno 7. června 2021

.....

Tomáš Plšek

Contents

Introduction	1
Chapter 1. Giant ellipticals	3
1.1 Hot atmospheres	4
1.2 X-ray cavities	6
1.2.1 Basic properties	6
1.2.2 Mechanical jet power	8
1.3 Supermassive black holes	9
1.3.1 Spherical Bondi accretion	10
Chapter 2. Data reduction	12
2.1 Sample selection	12
2.2 X-ray data analysis	12
2.2.1 Spectral analysis	14
2.2.2 X-ray cavities	15
2.3 VLA observations	16
2.3.1 Radio contours	17
2.4 VLBI observations	17
Chapter 3. CAvity DEtection Tool (CADET)	18
3.1 Network architecture	18
3.2 Dataset generation	20
3.2.1 Data analysis	22
3.2.2 Parameter distributions	24
3.2.3 Correlations between parameters	28
3.3 Training	33
3.4 Testing	35
3.5 Application	37
Chapter 4. Results	40
4.1 X-ray cavities	45
4.1.1 Questionable cavities	46
4.1.2 Multiple generations	47
4.1.3 Discovering new cavities	48
4.2 Correlated quantities	48

Chapter 5. Discussion	54
5.1 Bondi power to jet power correlation	54
5.2 Feeding from thermally unstable atmospheres	55
5.3 Mechanical jet power estimating methods	55
5.4 Evaluating the developed CADET pipeline	56
Conclusion	58
Appendix	60
A Radial profiles	60
B Correlated quantities	74
C Application of <i>CADET_search</i>	78
D Size-estimated X-ray cavities	90
E List of OBSIDs	101
Bibliography	104

Introduction

The study of massive galaxies, groups, and clusters of galaxies has undergone substantial progress at the turn of the millennium mainly due to the launch of two X-ray telescopes: the *Chandra X-ray Observatory* and the *XMM-Newton* satellite. Among many other key discoveries, their observations have enabled further examination of our knowledge about the hot atmospheres around these systems (further referred to as “hot galactic atmospheres”) and their connection to central engines represented by the accreting supermassive black holes (SMBHs). For the past two decades, the models describing these hot galactic atmospheres, the accretion processes and also the Active Galactic Nucleus (AGN) feedback itself have been put to a difficult test.

Hot galactic atmospheres are observed for all massive early-type galaxies, galaxy groups and clusters weighing more than 10^{12} solar masses and spanning hundreds and even thousands of kiloparsecs. Most of the baryonic matter in these systems is in the form of a dilute, hot, X-ray emitting plasma and is located in the galactic halo (atmosphere), the mass of which is of the order of tens of percent of the total galactic mass. However, something as small (up to hundreds of AU) and lightweight ($10^6 - 10^{10} M_\odot$), compared to the proportions of the whole galaxy, as the supermassive black hole in the centre, is capable of playing a substantial role in the energetics of the whole galactic atmosphere. As the supermassive black hole accretes the surrounding material, part of its rest mass may be turned into energy and expelled in the form of relativistic outflows (jets). The energy released by these outflows is transferred back into the galactic atmospheres and can compensate for radiative cooling of the X-ray emitting gas and thus prevent the subsequent star formation (Churazov et al., 2002).

A detailed description of such an accretion of supermassive black holes is nontrivial and demands a further understanding of individual processes taking place in the vicinity of these black holes. The rather simplified model of spherical Bondi accretion (Bondi, 1952) seemed to be ruled out by the fact that the observed luminosities of nearby AGNs are several orders of magnitude below the predicted Bondi values. Due to the nonzero momentum of the infalling material and also based on this radiative inefficiency, the accretion was believed to be rather disk or torus-like and dominated by advection (ADAF; Narayan & Yi, 1994). On the other hand, current estimates of jet powers inferred from volumes of radio lobes are within an order of magnitude comparable to powers predicted from the Bondi accretion (Allen et al., 2006). For galaxies whose AGNs are operating in this kinetic (radio) mode, the Bondi formula might therefore represent an acceptable rough estimate for the total power generated by the AGN.

The signs of previous AGN activity are observed either in the radio band as lobes of relativistic particles or in the X-ray band as void bubbles (so-called X-ray cavities) that were inflated into the hot galactic atmospheres. These cavities were first discovered as surface brightness depressions on X-ray images, initially captured by *ROSAT* and followed by *XMM-Newton* and *Chandra*. Subsequent multiwavelength observations of these galactic systems have shown that some of the cavities are filled with relativistic electrons

emitting via synchrotron radiation. A plausible explanation for this phenomenon is that the X-ray cavities are products of the interaction between the relativistic jets emanating from the AGNs and the hot intergalactic medium (McNamara et al., 2000b). For some of the cavities, the extended radio emission might be significantly misaligned (Gitti et al., 2006) or it can be completely missing (“ghost” cavities; McNamara et al., 2000a; Fabian et al., 2002), which is the case especially for older generations of X-ray cavities. In such cases, the X-ray cavities represent the only remnant leftover by previous AGN activity.

The process of the X-ray cavity inflation is expected to involve a significant amount of energy released by the accreting central supermassive black holes (SMBHs) and therefore play an important role in the energetics of the whole galactic atmosphere and the AGN feedback. The enormous amount of energy, represented by the work done to inflate the cavities and the energy deposited into the relativistic plasma is on timescales of $10^7 - 10^8$ years being dissipated back into the hot atmosphere via sound waves or turbulent flows (Churazov et al., 2002). A detailed description of such processes is therefore crucial for understanding the evolution and energetic balance of the whole galaxy. However, the identification of X-ray cavities and determination of their volume is not an easy task and so far it has been mainly done manually by humans and assuming only axially symmetric ellipsoidal geometry of cavities (e.g. Bîrzan et al., 2004; Allen et al., 2006). The reliability and real extent of thereby identified and size-estimated cavities are therefore rather contentious and might be significantly biased.

In the first Chapter, we outline the basic properties of giant elliptical galaxies, groups of galaxies and galaxy clusters focusing mainly on the interaction of relativistic outflows (jets) with hot galactic atmospheres and we also describe the basics of the spherical Bondi accretion. The data reduction methods utilized to process the *Chandra* X-ray observations and the subsequent image and spectral analyses are shown in Chapter 2. Chapter 3 focuses on the machine learning pipeline developed for finding and size-estimating of X-ray cavities, which we called the *CAvity DEtection Tool* (CADET). This Chapter also describes in detail the training dataset generation process. In Chapter 4, we present the resulting quantities determined from the spectral modelling of galaxies as well as jet powers inferred from sizes of radio lobes and X-ray cavities. The obtained results and their implications are discussed in Chapter 5 and we conclude the results in the last Chapter. In the Appendix the reader can find: the determined radial profiles of basic thermodynamic properties, X-ray images with identified cavities and overlaid by radio contours or predictions of the CADET network, and also the list of utilized observations.

Chapter 1

Giant ellipticals

Giant ellipticals together with S0 galaxies are historically referred to as massive *early-type* galaxies. These galaxies and their associations in the form of groups and clusters of galaxies are the largest, most massive and most luminous galactic systems and in their centres, they are harbouring the heaviest supermassive black holes in the Universe (Thomas et al., 2016; Mehrgan et al., 2019). In this thesis we focus on the most massive of these galactic systems with masses higher than $10^{12} M_{\odot}$ and sizes from hundreds of kiloparsecs up to a few megaparsecs, that are showing signs of hot atmospheres and active galactic nucleus (AGN) feedback.

The geometry of giant ellipticals is expected to be prolate, oblate or tri-axial (cigar-shaped) ellipsoids with favour to tri-axial shapes ($a_1 \neq a_2 \neq a_3$) (Binney, 1978). Although, their isophotes might deviate significantly from being ideally elliptical and their shapes can be much more boxy or disk-like (Schneider, 2006). Their optical luminosity profiles are often fitted with Sérsic's profile (Sérsic, 1963) (generalized de Vaucouleur's law). The deprojected distribution of baryonic gas significantly flattens in the galactic centre and is well described by the so-called beta model (Cavaliere & Fusco-Femiano, 1976) whereas the central distribution of the dark matter component is much steeper and is well fitted with an NFW-profile (Navarro et al., 1996).

Compared to spiral or irregular galaxies, giant ellipticals including those in the centres of groups and clusters contain only a very small amount of cold gas and dust, which would allow the formation of new stars. The observed star formation rates are typically lower than $1 M_{\odot} / \text{yr}$. These ellipticals are therefore composed mainly of old low-mass stars, which is the reason they are often called "red and dead". Most of the baryonic matter in these systems is in the form of diffuse, hot, X-ray emitting plasma heated to temperatures of tens of millions of kelvins. However, for some ellipticals, we observe also H α emission from a relatively small amount of warm gas (10^4 K) (up to $10^{10} M_{\odot}$; Rafferty et al., 2006) as well as HI (21 cm) or CO molecular emission from cold gas and dust ($\approx 100 \text{ K}$) (Schneider, 2006). The central regions of these massive haloes are therefore often multiphase. A typical example of a multiphase atmosphere is the one around the galaxy NGC 1275 in the centre of the Perseus cluster (Figure 1.1), where filamentary structures of warm gas are clearly visible.

A significant amount of warm and cold-phased gas is located in disk-like or filamentary structures that are extending out to $\approx 200 \text{ kpc}$ in diameter. Spatially resolved spectroscopic observations have shown that the UV excess indicating the formation of new stars is observed out to these diameters (even beyond the optical galactic emission) and that the star formation occurs also basically in the outskirts of galaxies. This phenomenon can be possibly explained by the fact that these new born stars are not being formed from the ambient material that is already trapped in the gravitational potential well of the galaxy, but instead from the infalling material that is being accreted from the intergalactic medium (Schneider, 2006).

1.1 Hot atmospheres

The existence of hot atmospheres embedding early-type galaxies, galactic groups and clusters was unknown for a long time. The extended X-ray emission coming from these hot atmospheres was discovered by early X-ray observations but was mistakenly believed to originate from the inverse Compton scattering of Cosmic Microwave Background (CMB) photons on free relativistic electrons. This idea was, however, ruled out by further observations by the *Ariel 5* observatory which showed emission lines of highly ionized iron in spectra of these galaxies ([Mitchell et al., 1976](#); [Serlemitsos et al., 1977](#)). It was established that these hot coronae are therefore consisting of almost entirely ionized X-ray emitting plasma heated to temperatures of 10^6 up to 10^8 K.

The hot atmospheric plasma is in the collisional ionization equilibrium (CIE), which implies that its state is destined only by the collisional ionization and recombination rates and it is not affected by the external radiation field. Due to the very low densities (much lower than 0.1 cm^{-3}), the plasma is optically thin and nearly all photons emitted from within this atmosphere will escape without interacting with its free electrons or ions. The observed surface brightness distribution therefore well reflects the projected distribution of atmospheric gas ([Werner & Mernier, 2020](#)).

Hot atmospheres are emitting X-ray radiation both by lowering the energy of free electrons during collisions with ions (*bremsstrahlung*), which contributes to the X-ray continuum and also by bound-bound transitions (line emission) of heavier elements (metals). The total amount of matter that cools from the hot phase by emitting the X-ray radiation is tied with the X-ray luminosity of the cooling region

$$\dot{m}_{\text{cool}} = \frac{2}{5} \frac{L_X \mu m_p}{kT} \quad (1.1)$$

where μm_p is the mean atomic weight, kT is the temperature of the hot gas and L_X is the cooling luminosity. For typical parameters of hot galactic atmospheres, this formula gives cooling rates of hundreds to thousands of solar masses per year. Such enormous cooling rates would fuel a precipitous formation of new stars and also the accretion onto the central supermassive black hole. However, observations of star formation rates in nearby galaxies mark much lower cooling rates, typically lower than $1 M_\odot / \text{yr}$.

The discrepancy indicates that there must be a certain mechanism responsible for heating the atmospheric gas and preventing it from cooling. The cooling rate in atmospheres of galaxies with lower masses ($\lesssim 10^{11} M_\odot$) is believed to be moderated by the star formation itself (supernova feedback), whereas for high mass elliptical galaxies and brightest cluster galaxies the feedback of radio mode AGNs is most probably responsible for the heating. Only less than 10 percent of nearby giant cluster galaxies are actually experiencing high star formation rates ($> 100 M_\odot / \text{yr}$), which may be a result of the inability of their active galactic nuclei to balance the radiative cooling.

The susceptibility of galactic atmospheres to thermal instabilities can be expressed by the ratio of the cooling time to the free-fall time of the X-ray emitting gas. The cooling time is defined as a timescale needed for gas of certain density, temperature and metallicity to thermally emit all of its energy via bremsstrahlung and line emission

$$t_{\text{cool}} = \frac{3}{2} \frac{n k T}{n_e n_i \Lambda(T, Z)}, \quad (1.2)$$

where n is the total particle density $n = n_e + n_i$ and $\Lambda(T, Z)$ is the temperature and abundance dependent cooling function, values of which were taken from [Schure et al. \(2009\)](#) assuming solar metallicities. Given this formula the cooling and star formation

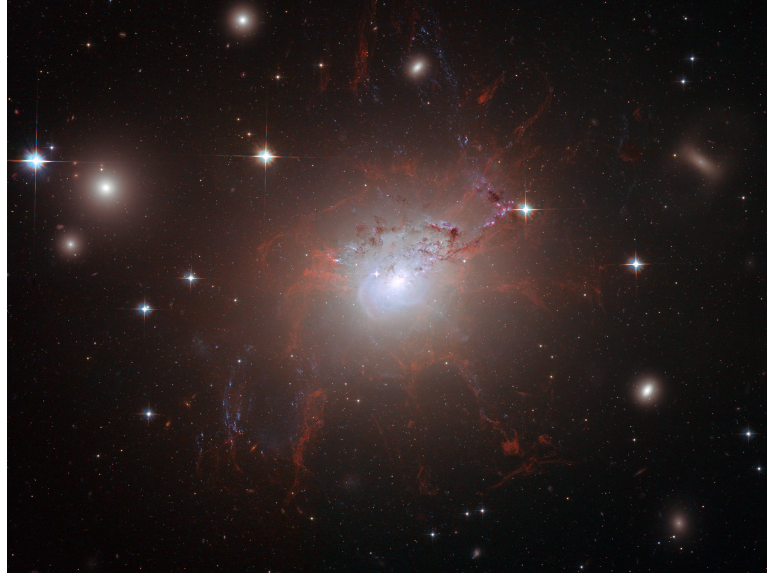


Figure 1.1: Image of the brightest galaxy (NGC 1275) in the centre of the Perseus cluster taken by the *Hubble Space Telescope* (ACS camera). The red structures represent the filamentary cold gas which was produced by thermal instabilities in the galactic atmosphere and trapped by the magnetic field of the galaxy. The image was taken from the ESA/Hubble image database¹.

rates should be the highest in the central regions where the particle density is greater ($\gtrsim 0.1 \text{ cm}^{-3}$) and the cooling time is therefore the lowest ($< 10^9$ years).

The timescale required for a condensed clump with zero momentum to fall into the centre of the galaxy (dynamical timescale) is expressed by its free-fall time. The free-fall time is given by $t_{\text{ff}} = \sqrt{2r/g}$, where the local gravitational acceleration $g = GM(<r)/r$ can be in general determined both by assuming an isothermal sphere with constant velocity dispersion (Binney & Tremaine, 1987)

$$M_{\text{ISO}}(< r) = 2\sigma^2 r/G, \quad (1.3)$$

where σ is the velocity dispersion and r is the distance from the galactic centre or it can be calculated directly from the measured thermodynamic properties and the assumption of hydrostatic equilibrium (HE)

$$M_{\text{HE}}(< r) = -\frac{rkT}{G\mu m_p} \left(\frac{d \ln \rho}{d \ln r} + \frac{d \ln T}{d \ln r} \right), \quad (1.4)$$

where μ is the mean atomic weight, m_p is the mass of a proton and ρ and T are the density and temperature of the atmospheric gas, respectively.

The atmospheres of galaxies are expected both from analytical (Nulsen, 1986) and also numerical computations (McCourt et al., 2012) to become thermally unstable when the cooling time t_{cool} falls below the free-fall time t_{ff} . However, the most up-to-date observations (reported by Voit & Donahue, 2015) and simulations (Gaspari et al., 2013) have shown that atmospheres of realistic galaxies may become thermally unstable even when the cooling time to free-fall time ratio falls below $t_{\text{cool}}/t_{\text{ff}} \lesssim 10$, which is often referred to as the *precipitation limit*. However, we note that it resembles an approximate division line rather than a strict limit. For many galaxies also other processes such as turbulences may play an important role in the formation of instabilities.

¹<https://esahubble.org/images/heic0817a/>

1.2 X-ray cavities

Elliptical surface brightness depressions on images of hot X-ray emitting galactic atmospheres (called X-ray cavities) were firstly discovered by *ROSAT*'s observations of the Perseus cluster (NGC 1275) (Boehringer et al., 1993). Subsequent low-frequency Very Large Array (VLA) radio observations have shown that they are filled with extended radio-emitting lobes of relativistic plasma emanating from the nucleus of the Perseus cluster. Further *ROSAT* observations proved the existence of similar brightness depressions in atmospheres of also other galactic systems (giant ellipticals, groups of galaxies and galaxy clusters) (Huang & Sarazin, 1998) and early models describing the formation and evolution of X-ray cavities were developed (Clarke et al., 1997; Heinz et al., 1998).

The low spatial resolution of *ROSAT* (5 arcsec), which limited the uncovering of new X-ray cavities, was surpassed at the turn of the millennium right after the launch of the *Chandra X-ray Observatory*. The spatial resolution of *Chandra*'s ACIS chip, which is below 0.5 arcseconds, has brought a substantial improvement in the detection of X-ray cavities and lead to the discovery of plenty of them in atmospheres of nearby elliptical galaxies (McNamara et al., 2000b; Fabian et al., 2000; Blanton et al., 2001). Soon after that also radio-faint later called “ghost” cavities with no significant VLA radio (1.4 GHz) counterpart were discovered (McNamara et al., 2001; Fabian et al., 2002; Bîrzan et al., 2004). However, for many of these systems, signs of extended radio counterparts were observed later on at lower radio frequencies (e.g. Giacintucci et al., 2011). The low-frequency radio emission is therefore capable of capturing the record of relativistic outflows for much longer time than the high-frequency radio emission and the concept of “ghost” cavities is thus indistinct and depends strongly on the examined radio frequency range. For the upcoming two decades, several comprehensive studies of X-ray cavities and radio lobes in atmospheres of near giant ellipticals (Dunn et al., 2010), distant galaxy clusters (Hlavacek-Larrondo et al., 2012, 2015) or both nearby and distant systems (Bîrzan et al., 2004; Diehl et al., 2008; Dong et al., 2010; Rafferty et al., 2006; McNamara et al., 2011; Panagoulia et al., 2014) were performed, tens of new cavities were discovered and their underlying attributes were inferred.

1.2.1 Basic properties

X-ray cavities, just like radio lobes, typically come in pairs and originate in a single relativistic outflow. Their observations show that the cavities are way more just separate “bubbles” rather than continuous funnel-like structures and for many galactic systems (e.g. NGC 5813; Figure 1.2) even multiple generations of cavities are observed. However, to this day it is not clear whether the discrete nature of X-ray cavities is a result of occasional episodic relativistic outbursts or whether they are caused by fragmentation of relatively still, permanent outflows – in analogy to a dripping tap, where the water increases steadily but individual droplets are separate.

Individual cavities may vary significantly in size and also in the amount of displaced gas from 1 kpc and $10^{10} M_{\odot}$ for M87 up to hundreds of kiloparsecs and more than $10^{12} M_{\odot}$ for Hydra A (McNamara & Nulsen, 2007). Typical mechanical powers of jets released into the ICM are of the order of $10^{41} - 10^{43}$ erg/s, however, for most powerful outflows (Hercules A; Nulsen et al., 2005) it can be up to 10^{46} erg/s, which is comparable to the energy output of a quasar. Although the cavities come in various shapes they are most commonly being approximated as prolate or oblate ellipsoids with rotational symmetry along the semi-axis closer to the direction towards the centre of the galaxy (see Bîrzan et al., 2004; Allen et al., 2006). We note that many real cavities are far from



Figure 1.2: Composite image of elliptical galaxy NGC 5813 composed from *Chandra* X-ray image (purple) and optical image from the *Sloan Digital Sky Survey* (SDSS) (yellow and blue) showing up to three generations of X-ray cavities. The field of view of the image is 8.6 arcmin and it was taken from the *Chandra* photo album database².

being ideally ellipsoidal and their structure is much more complex. Many cavities are actually more mushroom-like shaped (e.g. M87; Figure 1.3; Churazov et al., 2001), which is supported also by current simulations of cavities (Brüggen et al., 2009; Guo, 2015).

Typical features observed around cavities are their bright rims. These rims are either shell-like or arm-like structures of cooler gas pushed away by the cavities or regions of weakly shocked intergalactic medium. Although also strongly shocked regions caused by the highly supersonic inflation of cavities were expected, no significant temperature jumps were detected and some of the bright rims were observed to be paradoxically cooler than the surrounding gas (Fabian et al., 2000). There were only observed mildly supersonic weak shocks with Mach numbers between 1.2 and 1.7, that are close to being in pressure balance with the ambient medium (McNamara & Nulsen, 2007). These weak shocks can deposit a significant amount of the total energy released by the outflows (see Section 1.2.2). Such nearly isothermal nature of weak shocks may be a result of thermal conduction which is suppressing the temperature jumps (Fabian et al., 2006).

Comparison of basic cavity parameters and their approximate jet powers with other underlying properties of their host galaxies have shown interesting implications. Bîrzan et al. (2004) reported a correlation between the mechanical power of jets and radio luminosity at 1.4 GHz. Similarly, Rafferty et al. (2006) found a relation between mechanical jet powers estimated from sizes of X-ray cavities and the luminosity of the X-ray emitting gas from within a cooling radius (cooling luminosity), which is the radius where the cooling

²<https://chandra.harvard.edu/photo/2015/ngc5813/>

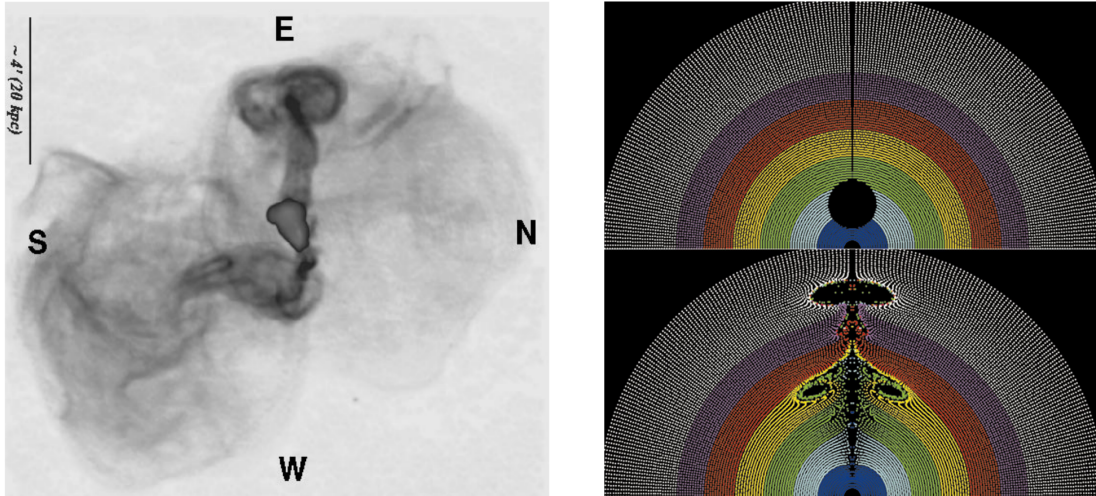


Figure 1.3: VLA radio image of galaxy M87 (NGC4486) (left) showing extended radio “cocoons” and a simulation of a void bubble being uplifted from the central parts of the galaxy (right). Both images were adapted from [Churazov et al. \(2001\)](#).

time (Equation 1.2) falls below some given threshold (e.g. Hubble time). Results of [Raferty et al. \(2006\)](#) have also shown that mechanical powers of jets and estimated molecular gas supply seem to be uncorrelated and that only a very small amount of molecular gas is actually reaching the black hole, which is supported also by [Emonts et al. \(2007\)](#), who reported an anti-correlation between the size of the extended radio source and estimated amount of neutral hydrogen. On the contrary, [Allen et al. \(2006\)](#) found a tight correlation between the mechanical jet powers determined from the combination of observations of radio lobes and X-ray cavities and approximate SMBH accretion powers estimated from the assumption of the spherical Bondi accretion (Equation 1.10). However, this strong relation was not observed by the subsequent study of [Russell et al. \(2013\)](#). On the other hand, [Russell et al. \(2013\)](#) reported a mild correlation between the cavity powers and nuclear X-ray luminosities and also between the approximate SMBH accretion rate (ADAF) and nuclear luminosity. A solid relation was observed also between mechanical powers inferred from sizes of X-ray cavities and cooling luminosities of their host atmospheres by [Panagoulia et al. \(2014\)](#).

1.2.2 Mechanical jet power

The total mechanical power of the relativistic outflow can be estimated from the volume of the radio lobe or X-ray cavity inflated by this outflow. The total kinetic energy needed to inflate a cavity of volume V into the interstellar medium with pressure p is equal to its total enthalpy H , which is the sum of the internal energy of the relativistic plasma and the work done on the ambient gas

$$H = \frac{1}{\gamma - 1} pV + pV, \quad (1.5)$$

where γ is the adiabatic index (ratio of specific heats) of the plasma filling the cavity. The value of the adiabatic index depends on whether the gas pressure support is caused by either nonrelativistic ($\gamma = 5/3$) or relativistic plasma ($\gamma = 4/3$). Modern observations of clusters of galaxies (Sunayev Zeldovich effect; [Abdulla et al., 2019](#)) have shown that the

X-ray cavities are filled mainly with relativistic gas ($\gamma = 4/3$) and the total enthalpy is therefore given by $H = 4pV$, which is also in a good agreement with magnetohydrodynamical simulations (Mendygral et al., 2011; McNamara & Nulsen, 2012).

Assuming that the inflation of X-ray cavities is still ongoing, the total mechanical power required to inflate a cavity with total enthalpy of $4pV$ is given by

$$P_{\text{jet}} = \frac{4pV}{t_{\text{age}}}, \quad (1.6)$$

where t_{age} is the age of the cavity. The cavity age can be calculated from its distance from the galactic centre R and the speed v at which it was inflated $t_{\text{age}} = R/v$. The velocity of the inflation is assumed to be equal to the average speed of sound in the hot intergalactic medium c_s along the path from the galactic centre into the centre of the cavity.

However, the duration of the cavity inflation calculated from the speed of sound represents rather a lower limit for the total age of the cavity and most cavities might be slightly older. Although this momentum-driven nature (speed of sound) of cavities is supported also by simulations (Omma et al., 2004). Following Bîrzan et al. (2004), the cavity ages can be calculated also under the assumption that they rise buoyantly, which should instead give an upper limit for their final age. Due to their lower densities, the cavities should rise with a buoyant velocity $v_b = \sqrt{2gV/SC}$, where g is the local gravitational acceleration, V is the volume of the cavity, $S \approx \pi r_w^2$ is its cross-sectional area and $C \approx 0.75$ is the drag coefficient of an ellipsoid. The local gravitational acceleration can be calculated from the velocity dispersion under the assumption of an isothermal sphere $g \approx 2\sigma^2/r$ (Binney & Tremaine, 1987).

During the process of cavity inflation, part of the released energy can be dissipated into heat, transferred into the energy of sound waves or radiated in the form of cosmic rays or radio synchrotron radiation. But the total amount of thereby released energy is only of the order of percents of the energy deposited into cavities and can be neglected (Churazov et al., 2002; Fabian et al., 2005; McNamara & Nulsen, 2012). However, if the cavity expansion velocities are slightly supersonic, important amount of energy can be deposited into the energy of shocks. Weak shocks are relatively inefficient in energy dissipation and therefore can deposit significant amount of the total mechanical energy (up to tens of percent) released by the jet (Churazov et al., 2002). Typical examples of galaxies with cavities enclosed by weak shocks are NGC 4636 (Jones et al., 2002) and NGC 5813 (Randall et al., 2011, 2015). The total energy stored in weak shocks is given by

$$E \approx p_1 V_s \frac{p_2}{p_1 - 1}, \quad (1.7)$$

where p_1 and p_2 are values of pressure before and at the position of the shock, respectively, and V_s is the total volume enclosed by the shocked gas.

1.3 Supermassive black holes

Observations of nearby galaxies have shown that every single massive elliptical galaxy harbours a supermassive black hole in its centre, the mass of which is typically of the order of $10^6 - 10^{10}$ solar masses. And as the supermassive black holes evolve jointly with their host galaxies, their masses correlate with the basic properties of bulges and atmospheres of these galaxies: stellar and gas velocity dispersions ($M_\bullet - \sigma$; Merritt & Ferrarese, 2001; Tremaine et al., 2002), numbers of globular clusters ($M_\bullet - N_{\text{GC}}$; Burkert & Tremaine, 2010), total stellar masses ($M_\bullet - M_*$), effective radii ($M_\bullet - R_e$; Mancini &

(Feoli, 2012), bulge luminosities ($M_\bullet - L_{\text{bulge}}$; Gltekin et al., 2009) and bulge masses ($M_\bullet - M_{\text{bulge}}$) (see also Kormendy & Ho, 2013). The narrowest scatter among these relations is observed for the $M_\bullet - \sigma$ relation for velocity dispersion derived from stellar dynamics, which is typically being used as a scaling relation for inferring the SMBH masses.

The radiative powers and mechanical jet powers emanating from AGNs in nearby giant ellipticals are several orders of magnitude below the Eddington luminosities

$$L_{\text{Edd}} = \frac{4\pi GMm_p c}{\sigma_T} \approx 1.26 \cdot 10^{38} \left(\frac{M}{M_\odot} \right) \text{erg / s}, \quad (1.8)$$

where M is the mass of the supermassive black hole, m_p is the mass of a proton and σ_T is the Thomson cross-section of an electron. The real accretion must therefore proceed at sub-Eddington rate. In general, two basic concepts of accretion of supermassive black holes are expected: continuous Bondi-like spherical accretion (Section 1.3.1; Bondi, 1952) of the *hot* gas phase and chaotic *cold* accretion of infalling gas clouds and blobs that are being stripped from the cooling flows (McNamara & Nulsen, 2007).

A tempting explanation for the radiative inefficiency of nearby AGNs is that the accretion proceeds in optically thin disks or toruses, in which the energy is transported into the black hole by advection (Narayan & Yi, 1994). However, recent observations of radio galaxies have shown that a significant amount of energy is expelled by these AGNs in the form of relativistic outflows and deposited into the internal energy of the relativistic plasma and the work done to displace the ambient gas (Section 1.2.2). For the lower luminosity giant ellipticals, the Bondi accretion seems to be energetically plausible for fueling the relativistic outflows but it is probably insufficient to provide enough energy for the most extreme outbursts inside of clusters of galaxies (Rafferty et al., 2006; McNamara & Nulsen, 2007).

Independently of the model used for describing the accretion process, the black hole accretion rate naturally scales with the main SMBH parameter which is its total mass. The precise measurement of supermassive black hole masses is therefore crucial for the proper estimation of their accretion rate. On the other hand, the spin of the black hole may also play an important role in the overall energy conversion efficiency (McNamara et al., 2011).

1.3.1 Spherical Bondi accretion

The total input power that supermassive black holes acquire by accreting the surrounding gas can be estimated from the Bondi accretion rate. This rather simplified model of Bondi spherical accretion (Bondi, 1952) seems to be not very plausible for the case of accretion of supermassive black holes mainly due to the presence of the angular momentum and magnetic field of the gas (Blandford & Znajek, 1977; Blandford & Payne, 1982; Pringle, 1981). However, the Bondi accretion model can be parametrized only using the mass of the supermassive black hole and thermodynamic properties of gas in its vicinity and for galaxies in the kinetic (radio) mode it resembles an acceptable rough estimate for the total power generated by the SMBH (Churazov et al., 2002; Allen et al., 2006).

The radius for which the gravitational influence of the SMBH is dominant over the thermal energy of the gas is called the Bondi radius

$$r_B = \frac{GM_\bullet}{c_s^2}, \quad (1.9)$$

where M_\bullet is mass of the SMBH and $c_s = \sqrt{\gamma kT/\mu m_p}$ is the speed of sound in the surrounding gas, where $\mu \approx 0.62$ is the mean atomic weight for fully ionized gas and $\gamma = 5/3$

is an adiabatic index of the X-ray emitting plasma. The accretion rate can be expressed as a flux of matter through a spherical shell

$$\dot{m}_B = 4\pi\lambda\rho(GM_\bullet)^2c_s^{-3} = \pi\lambda\rho c_s r_B^2, \quad (1.10)$$

with a numerical coefficient for adiabatic gas $\lambda \approx 0.25$. The equation can be rewritten in terms of specific entropy to express the direct dependence on a measurable thermodynamic quantity

$$\dot{m}_B \propto M_\bullet^2 K^{-3/2}, \quad (1.11)$$

where $K = kT/n_e^{2/3}$ is the specific entropy of the gas. The accreted matter is then with an efficiency η turned into the energy

$$P_B = \eta \dot{m}_B c^2, \quad (1.12)$$

which can be expelled in the form of relativistic jets. Regularly assumed is the efficiency of 10 percent.

Since the Bondi accretion depends only on the mass of the supermassive black hole and the entropy of the X-ray emitting gas, the accretion rate should in principle be able to self-regulate. The energy of an outflow dissipated into the galactic atmosphere heats the ambient gas and causes its expansion which lowers the accretion rate, and vice versa – if the atmosphere cools by radiating a significant amount of energy, it starts to contract and the accretion rate rises ([McNamara & Nulsen, 2007](#)).

Chapter 2

Data reduction

Parameters of the Bondi accretion were inferred from X-ray observations captured by the *Chandra* X-ray Observatory, whereas the mechanical power of relativistic jets emanating from the supermassive black holes (SMBHs) was estimated from both X-ray cavities on *Chandra* images and also from extended radio emission observed by the Very Large Array (VLA) telescope. The exact positions of SMBHs were either determined from the centre of hard X-ray emission (*Chandra*) and from small scale radio emission observed with Very-Long-Baseline Interferometry (VLBI) or taken from Atacama Large Millimeter Array (ALMA) measurements stated in the literature (Table 4.1).

2.1 Sample selection

The sample was chosen so that the galaxies are known to contain X-ray cavities and their Bondi radii are well resolved by *Chandra*'s ACIS observations (1 pixel $\approx 0.492''$). We subsequently added other galaxies that were used in previous studies (Allen et al., 2006; Russell et al., 2013) that investigated the relation between the Bondi accretion rate and mechanical jet power and compared the results. The galaxies in our sample are listed in Table 2.1. The masses of supermassive black holes (SMBHs) were taken either from direct measurements reported by Kormendy & Ho (2013) and Saglia et al. (2016) or derived from $M_\bullet - \sigma$ relation

$$\log \left(\frac{M_\bullet}{10^9 M_\odot} \right) = \alpha + \beta \log \left(\frac{\sigma}{200 \text{ km/s}} \right), \quad (2.1)$$

where $\alpha = 8.49 \pm 0.05$ and $\beta = 4.38 \pm 0.29$ (Kormendy & Ho, 2013) and velocity dispersions σ were taken from Lauer et al. (2007) and the HyperLeda database (Makarov et al., 2014). The distances were taken from the Nasa Extragalactic Database (NED) and except for NGC 6166 (FP method; Tully et al., 2013) they were derived from measurements of Surface Brightness Fluctuations (Tonry et al., 2000; Jensen et al., 2003).

2.2 X-ray data analysis

Throughout this analysis, we used archival *Chandra* observations of early-type galaxies, groups and clusters of galaxies. The *Chandra* data were reprocessed using classical CIAO 4.13 (Fruscione et al., 2006) procedures and current calibration files CALDB 4.9.4. The observations were obtained from *Chandra Data Archive* using `download_chandra_obsid` tool and reprocessed via `chandra_repro` script. For most objects, observations were obtained by the ACIS-S chip in the VFAINT mode, but for some galaxies (NGC 507, NGC 4636, NGC 5846 and NGC 6166) we included also ACIS-I observations. The light curves, extracted in the 0.5 – 7.0 keV band after exclusion of point sources, were deflared

Galaxy	Alternative name	D (Mpc)	r_B (pc)	r_B (")	Cavity references
IC 4296	Abell 3565	49.0	70.0	0.29	[1]
NGC 1399	Fornax c.	21.1	38.0	0.24	[3], [4]
NGC 1407		25.1	164.0	1.3	2, [4]*
NGC 1600		63.7	539.0	1.7	[1]
NGC 4261		32.4	81.0	0.52	[1], [4]*
NGC 4472	M49	16.5	106.0	1.3	[1], [3], [4]
NGC 4486	M87	16.5	208.0	2.6	[3], [4]
NGC 4636		14.7	35.0	0.49	[1], [4]
NGC 4649	M60	16.5	122.0	1.5	[3], [4]*
NGC 5813		32.2	40.0	0.26	[1], [4]
NGC 5846		24.9	48.0	0.35	[1], [2], [3], [4]
NGC 507		64.6	86.0	0.28	[1], [2]
NGC 708	Abell 262	62.8	17.0	0.056	[2], [4]
NGC 1316	Fornax A	22.7	8.0	0.077	[1], [4]
NGC 4374	M84	16.5	62.0	0.77	[1], [4]
NGC 4552	M89	16.5	14.0	0.18	[4]
NGC 4696	Centaurus c.	42.5	36.0	0.17	[3], [4]
NGC 4778	HCG 62	66.2	39.0	0.12	[2], [4]
NGC 5044		32.2	10.0	0.065	[1], [2], [3], [4]
NGC 6166	Abell 2199	125.0	63.0	0.1	[4]

* According to these sources, the galaxies are paradoxically supposed to have no cavities.

Cavity references: 1. [Cavagnolo et al. \(2010\)](#) 2. [Dunn et al. \(2010\)](#) 3. [Dong et al. \(2010\)](#) 4. [Shin et al. \(2016\)](#)

Table 2.1: The sample of elliptical galaxies with measured Bondi accretion rates and jet powers. The top eleven galaxies have fairly resolved Bondi radii by *Chandra*'s observations ($2r_B \gtrsim 1$ pixel $\approx 0.492''$), for the bottom nine galaxies the Bondi radii are unresolved and the density measurements had to be significantly extrapolated toward the centre.

using the `lc_clean` algorithm within the `defflare` routine and the good time intervals were obtained.

For targets with more observations, the individual OBSIDs were reprojected onto one of the observations via `reproject_obs` script. As a background, we used the `blanksky` background files, which were reprojected, scaled so that they match the particle background of observations in the 9 – 12 keV band and filtered for VFAINT events. The `blanksky` files were used both as a background for the spectral analysis and also for subtraction from the original images. The images were then divided by corresponding exposure maps and merged together.

Point sources as well as regions of strong non-thermal emission emanating from relativistic jets (e.g. NGC4261, NGC4486) that could have been resolved were found using `wavdetect` procedure, corrected visually and excluded from the spectral analysis. In the case of β -modeling and searching for cavities, the resolved point sources were filled using Poisson statistics via `dmfilth` procedure with a mean surface brightness of gas from their vicinity and regions of non-thermal jet emission were omitted during the fitting.

2.2.1 Spectral analysis

The spectral files were produced via the `specextract` script, which also creates the corresponding ARF and RMF files. The spectra were extracted in the 0.5–7.0 keV band in concentric annuli with increasing radius. The number of counts within individual annuli were chosen so that we still obtain a reasonable fit while maximizing the central spatial resolution. The spectra were extracted for each observation separately, summed by the `combine_spectra` command and deprojected assuming spherical symmetry using the DSDEPROJ code (Sanders & Fabian 2007; Russell et al. 2008), which also bins the spectra to contain at least 25 counts per spectral bin.

In the case of galaxy NGC 4486 (M87), the combination of bright central AGN and jet emission lead to very strong pile-up effects within the central few arcsec on *Chandra* ACIS-S observations in the classical full-array 3.2 s EXPTIME mode. Following the analysis of Russell et al. (2015, 2018), we therefore utilized also archival observations in the 1/8th subarray 0.4 s EXPTIME mode. The spectral files for the short frame-time observations were extracted in circular annuli up to 30 arcsec from the centre, whereas for observations in the full-frame mode the spectra were extracted for annuli in the 15–150 arcsec range. All possible spectral files for each annulus were combined and the spectra were deprojected similarly as in the case of other galaxies.

The deprojected spectra were fitted simultaneously using XSPEC spectral fitting package version (12.11.1) and ATOMDB database (version 3.0.9) (Arnaud, 1996). The optimization was performed using the Levenberg-Marquardt minimization method (Levenberg, 1944; Marquardt, 1963) and the Chi-square statistics. Uncertainties of individual parameters were determined from the Monte Carlo Markov Chain (MCMC) simulation. Unless stated otherwise, all uncertainties are expressed in the $1-\sigma$ confidence interval. During the fitting, we assumed the standard Lambda Cold Dark Matter (Λ CDM) cosmology with $H_0 = 70 \text{ km/s/Mpc}$, $\Lambda_0 = 0.73$ and $q_0 = 0$.

To account for the single-phase collisionally ionized diffuse gas, we used a single *apec* model component, which describes the state of the gas by its temperature kT , abundance Z , redshift z and normalization Y , which is directly proportional to the emission measure of the X-ray emitting gas

$$Y = \frac{10^{-14} \int n_e n_p dV}{4\pi D_A^2 (1+z)^2}, \quad (2.2)$$

where D_A is the angular diameter distance and n_e and n_p are electron and proton concentrations, respectively, where for fully ionized medium with solar abundance applies $n_e = 1.18 n_p$.

The redshift for all objects was taken from the NASA Extragalactic Database (NED) and fixed. Abundances were allowed to vary during the fitting, however, for most galaxies, we tied the abundances of 2 to 3 neighbouring shells together in order to make the abundance transition more smooth and to suppress accidental spurious surges. The abundances were measured relatively with respect to solar abundances reported by Lodders (2003). All other parameters were kept free during the fitting.

The Galactic absorption was modelled using the *phabs* photoelectric absorption model. The hydrogen column density n_H was fixed to the value obtained from the HEASARC database¹ which takes values reported by HI4PI Collaboration et al. (2016) and the *bcmc* cross-section was used (Balucinska-Church & McCammon, 1992). We also tried to fit the hydrogen column density parameter but it only introduced minor changes to the final fit statistics and to the parameter values.

¹<https://heasarc.gsfc.nasa.gov/cgi-bin/Tools/w3nh/w3nh.pl>

For the innermost annulus, we added an absorbed powerlaw component $zphabs(pow)$ to account for the non-thermal powerlaw emission of the active galactic nucleus. The absorbing hydrogen density column $n_{H,z}$ at the redshift z as well as the photon index Γ were freed during the fitting. However, for galaxies for which the fitted values of the density column and photon index were not significant (3σ above its uncertainty), we eventually fixed these parameters to $n_{H,z} = 0$ and $\Gamma = 1.9$ (following [Russell et al., 2013](#)), where $\Gamma = 1.9$ represents a mean value of the photon index for both obscured and unobscured nearby AGNs ([Gilli et al., 2007](#)). Unabsorbed fluxes and corresponding uncertainties of the powerlaw component were determined in the $0.5 - 7.0$ keV energy range using the $cflux$ multiplicative model component.

For the remaining outer annuli, we added the bremsstrahlung ([Karzas & Latter, 1961](#); [Kellogg et al., 1975](#)) component ($bremss$) with the temperature fixed to 7.3 keV, which should well describe the emission of point sources that could not have been resolved. These unresolved point sources are being mostly Low Mass X-ray Binaries (LMXBs), Cataclysmic Variables (CVs) and Coronally Active Binaries (CABs) ([Irwin et al., 2003](#)).

Besides the spatially resolved spectral analysis, we modeled also the spectra extracted from the cooling radius to obtain the total cooling luminosity. The cooling radius is defined as the radius at which the cooling time profile (Equation 1.2) reaches a certain value. Commonly used are the values of $7.7 \cdot 10^9$ yr ([Rafferty et al., 2006](#)) or the Hubble time ([Omma & Binney, 2004](#)), however, because most galaxies are relatively nearby, such radius would often be outside of ACIS chip's edges. Instead, we used the value of one gigayear (10^9 yr), which also resembles a much more comparable timescale to the ages of studied outflows and X-ray cavities. Central 2 arcseconds containing most of the non-thermal emission of the AGN were omitted. Thereby obtained spectra were modeled using either single or two-temperature *apec* model with a bremsstrahlung (*bremss*) component describing the emission of unresolved points sources. The cooling luminosity was determined as the combination of luminosities of both *apec* components. The fitting was performed similarly as in the case of the deprojected spatially resolved spectra, but instead of the Chi-square statistics we used the Cash statistics ([Cash, 1979](#)) and the spectral background was not subtracted but taken into account while modelling.

2.2.2 X-ray cavities

For detection of surface brightness depressions (X-ray cavities) on *Chandra* images and estimation of their sizes, we used two different methods: β -modeling and a convolutional neural network. We also tried the Gaussian Gradient Magnitude filter ([Sanders et al., 2016a,b](#)) and Unsharp Masking ([Malin, 1977](#)) methods, which should highlight details and structures on the original images. But since these methods tend to slightly change the sizes of studied features, they served rather as detection tools and were not used for size estimation.

Beta modeling

The β -modeling method is based on two-dimensional modelling of surface brightness distribution of the X-ray images, where the surface brightness distribution is simulated with a classical β -model ([Cavaliere & Fusco-Femiano, 1976](#)) projected onto 2D plane ([Et-
tori, 2000](#)). The fitting was performed in the SHERPA 4.13 package ([Freeman et al., 2001](#)) using the Cash statistics ([Cash, 1979](#)) and Monte Carlo optimization method ([Storn, 1995](#)). Most galaxies were fitted by a single β -model component with a constant background. However, for galaxies with more complex structure, we added also another β -component

and for galaxies with a very bright central point source, we included also a Gaussian component with a small FWHM. Central coordinates of all model components were tied together and freed, and in the case of multiple β -components, we tied their ellipticities and rotational angles. All other parameters were kept free during the fitting.

Thereby fitted two-dimensional models were subtracted from the original images producing the residual images, which were then slightly smoothed and individual cavities were searched for by eye. The reliability of detected cavities was then checked using count statistics – the number of counts inside of the cavity had to be at least 4σ under the surrounding background. The confirmed cavities were then manually size-estimated using SAOImageDS9 (Joye & Mandel, 2003) ellipse regions.

Neural network

For the purpose of an automatized detection of X-ray cavities and human-unbiased estimation of their sizes, we have trained a convolutional neural network which we called the *CAvity DEtection Tool* (CADET)². The creation of the network was inspired by the previous work of Jaroslava Secká (Secká, 2018) and the architecture of the network was taken from Fort (2017), although we did some major changes to the network architecture and also to the process of dataset generation. The network was trained on artificially generated images of galaxies with and also without cavities. The generated images were adjusted to resemble realistic *Chandra* images. The input of the network is a 128×128 *Chandra*-like image and on the output there is a pixel-wise prediction of the same shape as the input image, which is decomposed into individual cavities using a clustering algorithm DBSCAN (Ester et al., 1996). Detailed description of the CADET network and the process of generation of the training dataset can be found in Chapter 3.

2.3 VLA observations

The processed Very Large Array (VLA) radio images were either kindly provided by Romana Grossová or obtained from the NRAO VLA Archive Survey (NVAS)³. The VLA observations in A, B, C or D configurations centred at 1.4 GHz were reduced using NRAO pipeline Common Astronomy Software Applications (CASA, McMullin et al., 2007) version 4.7.2 and 5.6.1 (for data of NGC 4552, NGC 4636 and NGC 4649 calibrated by automated CASA pipeline).

Two categories of data were analyzed depending on the year of their observation. The “old” data which include observations before an important VLA upgrade, which happened in 2011 and “new” data after this upgrade. These “new” data were calibrated using the automatic pipeline version 1.3 and reduced by standard procedures as described in Grossová et al. (2019). On the other hand, ‘old’ observations were manually calibrated using the NRAO pre-upgrade calibration methods⁴.

For most targets, the model Perley & Butler (2013) for standard VLA calibrator 3C 286 was used to determine the flux scales, except for NGC 4552 and NGC 4649, both in A configuration, which were calibrated with 3C 48. In the end, for both new and old observations, the final total intensity images were created using the CASA clean algorithm in multi-frequency synthesis mode and Briggs weighting. The self-calibration, consisting of three cycles of phase and one cycle of amplitude and phase calibration, were performed,

²<https://github.com/tomasplsek/CADET>

³<https://archive.nrao.edu/nvas/>

⁴https://casaguides.nrao.edu/index.php/Jupiter:_continuum_polarization_calibration

if the signal-to-noise ratio of the image reached a value higher than 100, in order to improve and refine the standard calibration results for the targets.

2.3.1 Radio contours

Processed VLA images were used for size estimation of radio lobes and for the subsequent mechanical jet power calculation. The mechanical jet powers were thus determined independently of X-ray data. For observations showing an extended radio emission, we produced radio contours and similarly as in the case of X-ray cavities we estimated the sizes of radio lobes by manually overlaying the radio contours with ellipse regions using the SAOImageDS9. The minimum contour level was set to 5 times the root mean square error (RMSE) of the surrounding background.

In order to probe the most recent cavities, we mainly used images in the L band (1.4 GHz) and A array configuration. The A configuration has a similar angular resolution as *Chandra* ACIS data, so the spatial distinction of studied features is comparable. However, for some objects, there were no observations in the A configuration available or they did not show any signs of extended emission. For these objects, we therefore used other array configurations with the best possible spatial resolution. For galaxies for which it was possible, we utilized multiple array configurations to estimate sizes of also older generations of radio lobes. However, we only used array configurations capturing really distinct physical structures belonging to various generations of cavities and we tried to avoid estimating the size of the same features observed on different scales.

2.4 VLBI observations

Observations by the Very-Long-Baseline Interferometry (VLBI) were retrieved from the *Astrogeo VLBI FITS image database*⁵. All utilized observations were observed in the X-band (8 – 8.8 GHz). The observations were obtained under the *VLBI 2MASS Survey* (V2M) and *Wide-Field VLBA Calibration Survey* (WFCS) and analyzed by Leonid Petrov (Condon et al., 2013; Petrov, 2021; Petrov & Kovalev in prep.). The exact positions of SMBHs were determined simply from the peak of the small scale VLBI radio emission.

⁵http://astrogeo.org/vlbi_images/

Chapter 3

CAvity DEtection Tool (CADET)

The exact determination of the real extent of X-ray cavities, as mentioned in the Introduction, is crucial for an accurate estimation of the mechanical power of relativistic jets and also for understanding the energetics of the whole galactic atmosphere. The current detection and size estimation methods, widely used in the previous studies of X-ray cavities (e.g. Bîrzan et al., 2004; Dong et al., 2010; Shin et al., 2016; Hlavacek-Larrondo et al., 2015) and further described in Section 2.2.2, are all ultimately based mainly upon visual inspection and manual estimation of cavity sizes. Such an approach of cavity volume determination might therefore lead, also due to over-simplifying assumptions (ellipsoidal shape, rotational symmetry, etc.), to rather inaccurate or even incorrect results. We have decided to tackle this task of searching for and estimating sizes of X-ray cavities using the power of convolutional neural networks (CNN) and modern computer technology. We have therefore built and trained a detection pipeline which we have called the *CAvity DEtection Tool (CADET*¹).

The utilization of machine learning techniques has registered significant progress in the field of observational astronomy and astrophysics. It has a great potential in automation of tasks that would otherwise require human or even expert insight into the problematics and also for processing of enormously large datasets and the so-called data-driven astronomy. Neural networks and other machine learning techniques are already being widely used in various astronomical fields either for classification tasks: point source vs extended source classification (Alhassan et al., 2018), galaxy morphology classification (Dieleman et al., 2015; Hausen & Robertson, 2020), radio emission morphology classification (Wu et al., 2019), recognition of clusters of galaxies using multiwavelength observations (Kosiba et al., 2020), distinguishing between gamma-ray photons and cosmic rays from Cherenkov radiation (Shilon et al., 2019) or for distinguishing between single and multi-temperature plasma from X-ray spectra (Ichinohe & Yamada, 2019); for regression tasks: photometric redshift estimation (D’Isanto & Polsterer, 2018) and pre-fitting of X-ray spectral properties (Ichinohe et al., 2018); and also for more complex problems: predicting the cosmological structure formation (He et al., 2019) or producing hydrodynamical simulations by learning the basic physical laws (Dai & Seljak, 2021).

3.1 Network architecture

The *CAvity DEtection Tool (CADET)* pipeline is composed of a convolutional neural network (CNN) and a clustering algorithm. The convolutional neural network is trained for finding pairs of elliptical surface brightness depressions (cavities) on noisy *Chandra*-like images of elliptical galaxies and the clustering algorithm is used for the decomposition of thereby obtained predictions into individual cavities. The creation of the network was inspired by the previous work of Jaroslava Secká (Secká, 2018) and the architecture of the

¹<https://github.com/tomasplsek/CADET>

convolutional network and the idea of generating the dataset artificially comes from [Fort \(2017\)](#), although we did some major changes to the network and also to the process of dataset generation.

The convolutional network was implemented using the high-level Python deep learning API *Keras* ([Chollet et al., 2015](#)) with the *Tensorflow* backend ([Abadi et al., 2015](#)). For the clustering task, we used the density-based spatial clustering algorithm *DBSCAN* ([Ester et al., 1996](#)) incorporated into the *Scikit-Learn* library ([Pedregosa et al., 2011](#)). The architecture of the convolutional network is similar to that developed by [Fort \(2017\)](#) and consists of a series of 5 convolutional blocks (Figure 3.1). Each block resembles an Inception-like layer ([Szegedy et al., 2015](#)) as it concatenates the outputs of multiple parallel 2D convolutions with various kernel sizes (Figure 3.2). The inception layers within the first 4 blocks consist of convolutional layers with 32 of 1×1 filters, 32 of 3×3 filters, 16 of 5×5 filters, 8 of 7×7 filters, 4 of 9×9 filters, 2 of 11×11 filters and one 13×13 filter. Individual 2D convolutions within the inception layer are not ended by an activation function, so they serve rather as linear convolutional filters. Each of the inception layers is then followed by a 2D convolutional layer with 32 or 64 of 1×1 filters, which was introduced mainly due to dimensionality reduction. The output of the convolutional block is normalized by batch normalization and activated using the Rectified Linear Unit (ReLU) activation function. The ReLU activation function is meant to bring a nonlinear element into the network to actually enable the learning process. The whole network is ended by a final block, which is also composed as an inception layer, but it differs from the previous blocks mainly in the number and sizes of individual 2D convolutional filters (8 of 8×8 filters, 4 of 16×16 filters and 2 of 32×32 filters) and also in the activation function. The output of the network is intended to be a pixel-wise prediction of whether a corresponding pixel belongs to a cavity or not. The activation function of the final layer was, therefore, set to be the *sigmoid* function, which is typically used for ordinary binary classification tasks.

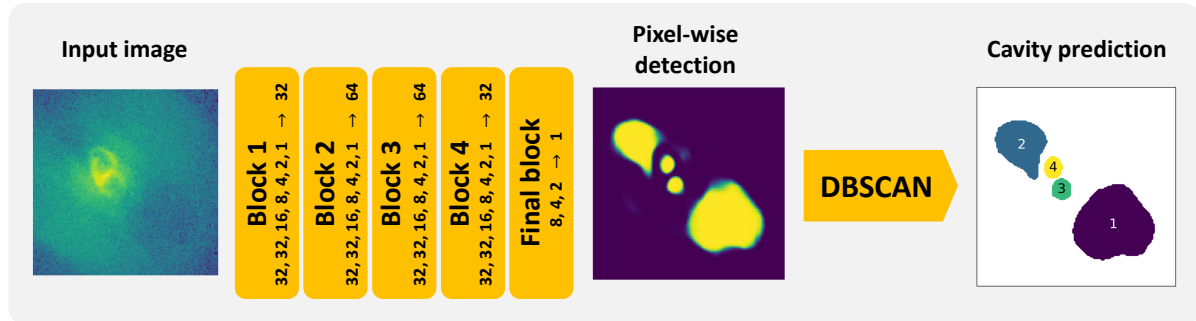


Figure 3.1: The architecture of the CADET pipeline consisting of five convolutional blocks producing a pixel-wise cavity prediction and a clustering algorithm *DBSCAN* used for the decomposition of the prediction into individual cavities. The numbers of individual filters within the inception layer and also the number of filters of the subsequent dimensionality reducing 1×1 layer are stated alongside individual blocks.

The input of the convolutional network is a set of noisy 128×128 images of galaxies with either zero or one pair of cavities. Since the profile of the beta model is rather exponential, we normalized the images by a logarithm (the value of each pixel was raised by one to avoid calculating the logarithm of zero) and then scaled them by the highest pixel value so the values of all images are between 0 and 1. We tried also different ways of normalizing the input images including widely used techniques incorporated into *Scik-*

itLearn or *Keras* libraries (unit normalization, zero mean–unit variance, etc.), however, the best results were obtained for the above-stated approach. On the output of the network, there is again a 128×128 image representing the pixel-wise prediction of whether there are cavities on the image and where they are located. As corresponding labels (ground truth), we took the 3D cavity masks summed into 128×128 images and binned to contain either ones (inside of the cavity) and zeros (outside of it). For galaxies with no inserted cavities, the ground truth is represented by a zero matrix. This binary binning was used in order to express the probability that a certain pixel is inside of a cavity or not. We also tried not binning the label masks and only normalizing them by the maximal value to fit the depth of the cavity. However, this only worsened the performance of the network.

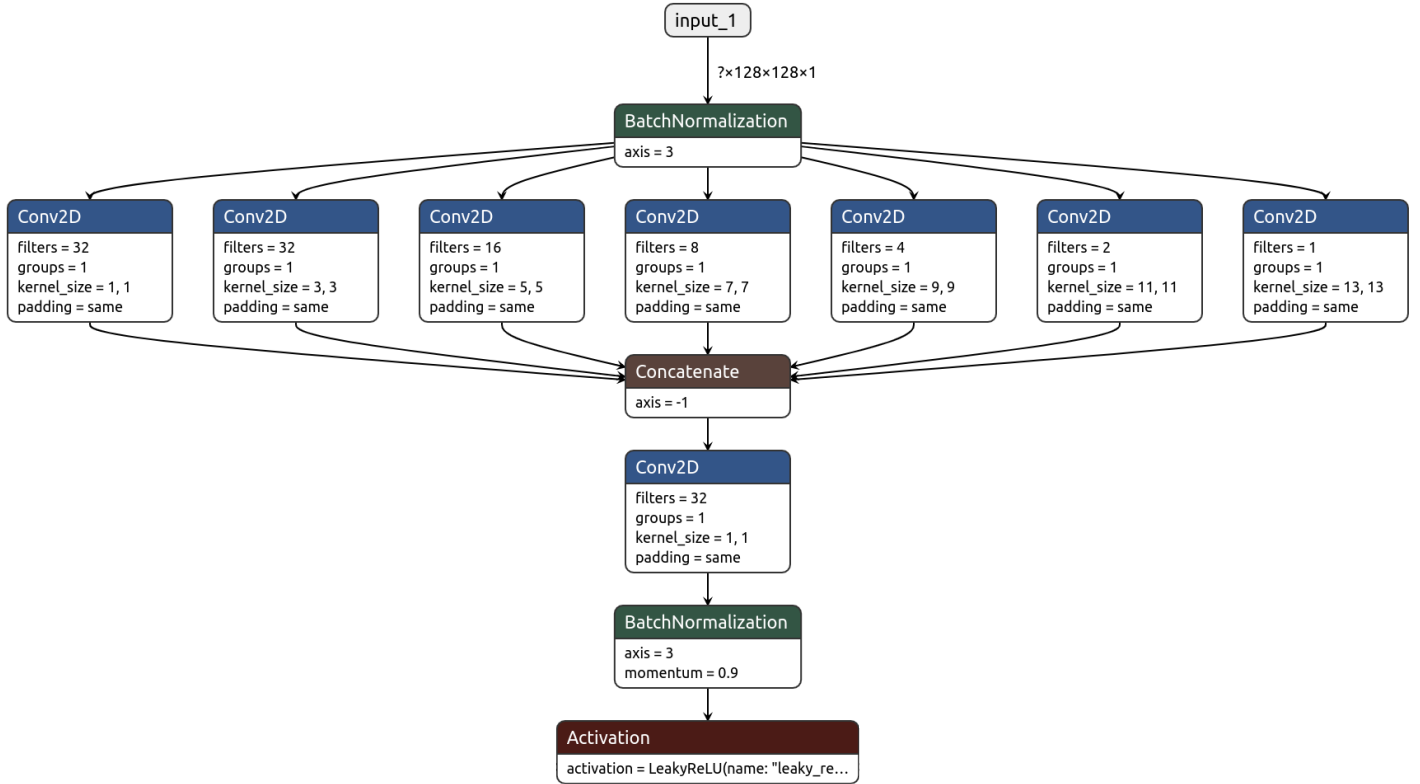


Figure 3.2: The scheme of the first block of the convolutional network consisting of a series of different numbers of linear convolutional filters followed by a convolutional layer with 32 of 1×1 filters, normalized by a batch normalization and ended by a ReLU activation function. The schematic image was created using [Netron](#) visualization tool.

3.2 Dataset generation

The network was not trained on real images of galaxies with known X-ray cavities. Instead, we used artificially generated images that were processed to resemble low count X-ray images of elliptical galaxies. We did not use the real data for two main reasons: we simply do not have a big enough dataset of images of galaxies with classified cavities and even if we would, we would have to search for and size estimate all of these cavities manually, which would bring a human bias into the training process.

We therefore produced arbitrary 3D models of elliptical galaxies and randomly inserted cavities into them. The models were then reprojected onto the 2D plane by simply summing the values across one axis – we could use this approximation under the assumption that the atmospheres of elliptical galaxies are optically thin and due to their distance there is also no need to account for projection effects. Thereby obtained images were noised using Poisson statistics to resemble low count X-ray images of galaxies as observed by the *Chandra X-ray Observatory*. The point spread function (PSF) of the *Chandra* telescope was neglected.

The distribution of gas in real galaxies is often not ideally smooth but is disrupted by sloshing effects (Sanders et al., 2016a), past mergers, ram pressure stripping (NGC4552; Kraft et al., 2017), by the AGN feedback and also by the cavities itself (see also Werner & Mernier, 2020). However, simulating such an inner structure is beyond the scope of this work. For generating the particle distribution in galaxies, we instead used either a single or a double beta model (Cavaliere & Fusco-Femiano, 1976)

$$n(r) = n_0 \left[1 + \left(\frac{r}{r_c} \right)^2 \right]^{-3\beta/2}, \quad (3.1)$$

where r_c is the core radius, n_0 is the central particle concentration and β is the beta parameter, which describes the logarithmic slope of the distribution at large radii. While the double beta model combines two simple beta models (Equation 3.1) with various core radii, amplitudes (central particle concentrations) and beta parameters.

To imitate real cavities, we randomly generated ellipsoidal masks and cut off the corresponding areas from the 3D model of the galaxy, assuming that the cavities are filled with relativistic plasma and therefore emit nearly no X-rays (McNamara & Nulsen, 2012). We either entirely removed the gas from corresponding regions or displaced it to the edges of cavities to resemble bright rims, that are actually observed around some cavities (e.g. NGC 4636, NGC 5813; Jones et al., 2002; Randall et al., 2011, 2015). The bright rims are regions of weakly shocked gas caused by the slightly supersonic inflation of the cavities (Churazov et al., 2002). As mentioned in the Section 1.2, the shapes of real cavities are not ideally rotationally symmetric. The cavities can also partially intersect or even be overlaid by more complex structures (cold fronts, shocks, jets). However, for simplicity, we approximated the cavities to be prolate or oblate ellipsoids with rotational symmetry along the axis closer to the direction towards the galactic centre.

The nonspherical perturbation of gas distribution brought on by gas sloshing triggered by a merging event was also simulated. To reproduce such an effect, we generated a two-dimensional meshgrid with an axially antisymmetric spiral-like pattern (Figure 3.9) representing an “overdensity / underdensity” field and multiplied the model with this grid. The sloshing spiral was approximated by an arithmetic (Archimedean) spiral:

$$r = \sqrt{x^2 + y^2}, \quad \theta = \text{atan} \left(\frac{y}{x} \right), \quad r = b \cdot \theta, \quad (3.2)$$

where x and y are coordinates of the 2D cartesian grid and parameter b determines the distance between loops. The main parameters of the spiral pattern (periodicity, depth) were generated based on the basic assumptions further discussed in Section 3.2.2.

Real galaxies often contain also bright point sources, which are being mostly the Low Mass X-ray Binaries (LMXB), Coronally Active Binaries (CAB), or Cataclysmic Variables (CV) (Irwin et al., 2003). Many galaxies also have a bright active galactic nucleus (AGN) represented by a strong point-like nonthermal emission in the centre and some of them might even contain prominent jets (e.g. NGC315, NGC4261, NGC4486). Except for the

central point source, which was simulated using a low-FWHM Gaussian model, we did not take these point sources into account while generating our dataset. However, when testing the network on real *Chandra* images of galaxies, we detected these regions and replaced them with the mean surface brightness of gas in their vicinity (see Section 3.2.1).

3.2.1 Data analysis

The distributions of β -model parameters are based on real *Chandra* observations of elliptical galaxies with and also without detected cavities. The observations were processed using classical CIAO 4.12 (Fruscione et al., 2006) procedures and current calibration files (CALDB 4.9.1). For galaxies observed multiple times, the individual observations were reprojected and merged. Most galaxies were observed in the VFAINT mode using the ACIS-S chip, however, for a couple of galaxies we combined ACIS-S and ACIS-I observations and for some of them, there were only ACIS-I observations available.

The observations were deflared using the `lc_clean` algorithm within the `defflare` routine. The images were generated from the merged observations using the `fluximage` procedure with a binsize of 1 pixel (0.492 arcsec). The images were background-subtracted using `blanksky` background files, which were scaled to match the observations in the 9 – 12 keV band, and exposure corrected by corresponding exposure maps. The point sources were found using the `wavdetect` tool and filled with mean surface brightness from the elliptical annulus around the source using the `dmfilth` procedure (CIAO 4.12). Before the utilization of the `dmfilth` procedure, the background and exposure corrected images were multiplied by an arbitrary constant (mostly by the lowest pixel value) to enable the use of Poisson statistics.

The β -model parameters were determined from 2D modelling of the surface brightness distribution of the source-filled images. The surface brightness distribution was modelled using the projection of the classical beta model (Eq. 3.1) onto a 2D plane under the assumption of isothermality (Ettori, 2000)

$$S(r) = n_0^2 \Lambda(T) r_c B(3\beta - 0.5, 0.5) \left[1 + \left(\frac{r}{r_c} \right)^2 \right]^{0.5-3\beta}, \quad (3.3)$$

where $\Lambda(T)$ is the cooling function and B is the beta function. The temperature and thus also the cooling function were assumed to be constant for all analyzed and generated galaxies and the cooling function was therefore omitted from further calculations. Instead, we accounted a scatter of 0.3 dex in the distribution of the central particle concentration, which corresponds to the difference of cooling functions at temperatures of 0.3 and 2.5 keV (limit values of central temperature for the sample of galaxies; see Figure A.2) and solar abundances.

The fitting of the two-dimensional β -model was performed in the SHERPA 4.13 package (Freeman et al., 2001) using the Cash statistics (Cash, 1979) and Monte Carlo optimization method (Storn, 1995). The galaxies were firstly fitted using a single beta model with a constant background. For galaxies for which it improved the fit statistics (mainly galaxies with more complex structure), we included another beta component and for galaxies with a bright central point source, we added also a low-FWHM Gaussian component. Central coordinates of all model components were tied together and freed, and in the case of multiple beta components we tied also their ellipticities and rotational angles. All other parameters were kept free during the fitting. The fitted parameters are listed in Table 3.2 and the distributions and correlations between the parameters can be found in Figures 3.5, 3.6 and 3.7.

Galaxy	r_c [pixels]	β	e	$r_{c,2}$ [pixels]	β_2
3C 449	$0.44^{+0.05}_{-0.05}$	$0.3^{+0.8}_{-0.6}$	$0.12^{+0.07}_{-0.07}$	140.0^{+21}_{-18}	$0.488^{+0.09}_{-0.08}$
IC 310 †	$1.32^{+0.05}_{-0.06}$	$0.7^{+0.1}_{-0.1}$	$0.2^{+0.1}_{-0.1}$		
IC 1459 †	$0.43^{+0.1}_{-0.08}$	$0.5^{+0.06}_{-0.06}$	$0.09^{+0.28}_{-0.1}$		
IC 1860 †	$5.7^{+0.3}_{-0.5}$	$0.38^{+0.05}_{-0.06}$	$0.1^{+0.2}_{-0.2}$		
IC 4296 †	$0.96^{+0.05}_{-0.04}$	$0.54^{+0.06}_{-0.06}$	$0.05^{+0.03}_{-0.03}$		
NGC 57 †	$6.2^{+0.7}_{-0.7}$	$0.6^{+0.3}_{-0.2}$	$0.1^{+0.2}_{-0.2}$		
NGC 315 †	$0.78^{+0.04}_{-0.04}$	$0.49^{+0.03}_{-0.03}$	$0.05^{+0.08}_{-0.08}$		
NGC 410 †	$3.2^{+0.7}_{-0.6}$	$0.5^{+0.2}_{-0.2}$	$0.1^{+0.3}_{-0.3}$		
NGC 499	$15.5^{+0.4}_{-0.7}$	$0.38^{+0.02}_{-0.03}$	$0.5^{+0.1}_{-0.2}$	129.0^{+26}_{-24}	$1.1^{+0.3}_{-0.2}$
NGC 507	$0.98^{+0.1}_{-0.1}$	$0.38^{+0.04}_{-0.04}$	$0.04^{+0.04}_{-0.04}$	72.0^{+2}_{-2}	$0.60^{+0.7}_{-0.06}$
NGC 533 †	$15.4^{+0.6}_{-0.6}$	$0.53^{+0.08}_{-0.08}$	$0.21^{+0.05}_{-0.05}$		
NGC 708	$19.2^{+0.4}_{-0.4}$	$0.38^{+0.03}_{-0.03}$	$0.21^{+0.02}_{-0.02}$		
NGC 741	$2.4^{+0.4}_{-0.3}$	$0.44^{+0.09}_{-0.08}$	$0.1^{+0.2}_{-0.2}$	19.0^{+7}_{-6}	$0.9^{+3.0}_{-0.1}$
NGC 777 †	$4.4^{+0.6}_{-0.5}$	$0.44^{+0.09}_{-0.08}$	$0.1^{+0.1}_{-0.1}$		
NGC 1132 †	$1.44^{+0.09}_{-0.08}$	$0.35^{+0.02}_{-0.02}$	$0.15^{+0.04}_{-0.04}$		
NGC 1316 †	$7.4^{+0.2}_{-0.2}$	$0.52^{+0.05}_{-0.05}$	$0.31^{+0.04}_{-0.04}$		
NGC 1399	$4.7^{+0.1}_{-0.1}$	$0.46^{+0.02}_{-0.02}$	$0.07^{+0.04}_{-0.04}$		
NGC 1404 †	$5.53^{+0.05}_{-0.05}$	$0.48^{+0.01}_{-0.01}$	$0.04^{+0.02}_{-0.02}$		
NGC 1407 †	$14.7^{+0.6}_{-0.6}$	$0.48^{+0.06}_{-0.06}$	$0.11^{+0.05}_{-0.05}$		
NGC 1550 †	$14.3^{+0.4}_{-0.4}$	$0.38^{+0.01}_{-0.01}$	$0.23^{+0.02}_{-0.02}$		
NGC 1600	$7.0^{+0.4}_{-0.4}$	$0.48^{+0.08}_{-0.08}$	$0.1^{+0.1}_{-0.1}$		
NGC 2300	$9.8^{+0.5}_{-0.5}$	$0.48^{+0.07}_{-0.07}$	$0.04^{+0.09}_{-0.1}$		
NGC 2305 †	$4.0^{+1.0}_{-1.0}$	$0.4^{+0.1}_{-0.1}$	$0.1^{+0.1}_{-0.2}$		
NGC 3091 †	$3.0^{+4.0}_{-2.0}$	$0.4^{+0.4}_{-0.4}$	$0.4^{+0.5}_{-0.3}$	149.0^{+10}_{-6}	$1.1^{+0.2}_{-0.1}$
NGC 3923	$6.4^{+0.2}_{-0.1}$	$0.53^{+0.04}_{-0.04}$	$0.16^{+0.05}_{-0.05}$		
NGC 4073	$11.7^{+0.4}_{-0.4}$	$0.43^{+0.04}_{-0.04}$	$0.17^{+0.04}_{-0.04}$		
NGC 4125 †	$8.8^{+0.9}_{-0.9}$	$0.41^{+0.1}_{-0.1}$	$0.25^{+0.08}_{-0.08}$		
NGC 4203	$0.68^{+0.02}_{-0.02}$	$0.72^{+0.07}_{-0.07}$	$0.11^{+0.06}_{-0.06}$		
NGC 4261	$1.3^{+0.03}_{-0.03}$	$0.52^{+0.02}_{-0.02}$	$0.13^{+0.04}_{-0.04}$		
NGC 4374 †	$9.9^{+0.2}_{-0.2}$	$0.46^{+0.03}_{-0.03}$	$0.15^{+0.03}_{-0.03}$		
NGC 4406 †	$0.9^{+0.8}_{-0.3}$	$0.28^{+0.06}_{-0.06}$	$0.34^{+0.06}_{-0.06}$		

Table 3.1: To be continued.

Galaxy	r_c [pixels]	β	e	$r_{c,2}$ [pixels]	β_2
NGC 4472	$5.08^{+0.06}_{-0.06}$	$0.404^{+0.009}_{-0.009}$	$0.09^{+0.01}_{-0.01}$		
NGC 4486	$27.18^{+0.07}_{-0.07}$	$0.363^{+0.001}_{-0.001}$	$0.05^{+0.003}_{-0.003}$		
NGC 4552 †	$1.8^{+0.9}_{-0.7}$	$0.4^{+5.0}_{-1.0}$	$0.3^{+0.2}_{-0.2}$	27^{+9}_{-7}	$0.7^{+0.1}_{-0.1}$
NGC 4636	$27.0^{+5.0}_{-3.0}$	$0.71^{+0.07}_{-0.07}$	$0.25^{+0.03}_{-0.03}$	811^{+100}_{-47}	$1.3^{+0.4}_{-0.2}$
NGC 4649	$9.41^{+0.07}_{-0.07}$	$0.51^{+0.01}_{-0.01}$	$0.04^{+0.02}_{-0.02}$		
NGC 4696	$7.01^{+0.08}_{-0.08}$	$0.34^{+0.006}_{-0.006}$	$0.228^{+0.007}_{-0.008}$	$77.5^{+0.7}_{-0.7}$	$0.55^{+0.04}_{-0.04}$
NGC 4778 †	$27.3^{+0.5}_{-0.4}$	$0.51^{+0.04}_{-0.04}$	$0.03^{+0.02}_{-0.02}$		
NGC 4782 †	$37.0^{+16.0}_{-24.0}$	$0.42^{+0.13}_{-0.12}$	$0.10^{+0.04}_{-0.04}$		
NGC 4936	$0.5^{+0.2}_{-0.1}$	$0.37^{+0.08}_{-0.07}$	$0.1^{+0.2}_{-0.2}$		
NGC 5044 †	$12.0^{+4.0}_{-4.0}$	$0.4^{+4.0}_{-0.5}$	$0.1^{+0.01}_{-0.01}$	226^{+32}_{-15}	$1.1^{+0.2}_{-0.1}$
NGC 5129 †	$2.0^{+0.3}_{-0.3}$	$0.43^{+0.06}_{-0.06}$	$0.2^{+0.1}_{-0.1}$		
NGC 5419 †	$3.0^{+1.0}_{-2.0}$	$0.5^{+0.2}_{-0.3}$	$0.1^{+0.4}_{-0.4}$		
NGC 5813 †	$16.0^{+3.0}_{-1.0}$	$0.4^{+7.0}_{-0.7}$	$0.2^{+1.5}_{-0.7}$	187^{+19}_{-7}	$1.0^{+0.3}_{-0.2}$
NGC 5846	$22.0^{+1.0}_{-1.0}$	$0.5^{+0.2}_{-0.2}$	$0.2^{+0.1}_{-0.1}$	336^{+44}_{-23}	$1.3^{+1.1}_{-0.1}$
NGC 6166 †	$22.0^{+2.0}_{-2.0}$	$0.6^{+0.7}_{-0.6}$	$0.2^{+0.1}_{-0.1}$	327^{+3}_{-1}	$1.3^{+0.2}_{-0.2}$
NGC 7619	$2.8^{+0.2}_{-0.2}$	$0.43^{+0.04}_{-0.04}$	$0.09^{+0.08}_{-0.08}$		

† For these galaxies, we included a low-FWHM Gaussian model to account for the bright central source.

Table 3.1: Parameters obtained from β -modeling of our sample of galaxies: beta parameter β and core radius r_c of the first component, common ellipticity e and beta parameter β_2 and core radius $r_{c,2}$ of the second component.

3.2.2 Parameter distributions

The models of artificial galaxies were generated using both single and double beta models. Their relative frequency was estimated from the results of beta modelling stated in Table 3.2 to be nearly 75 % and 25 % for the single and double beta model, respectively. Each beta model can be in general described by 7 parameters: central coordinates x_0 and y_0 , core radius r_c , beta parameter β , amplitude A , ellipticity e and rotational angle φ .

The central coordinates were chosen to be equal to the centre of the image with random Gaussian variation in both axes with a 3-pixel standard deviation truncated at 10 pixels. For the double beta model, the central coordinates of individual components were linked together. Distribution of core radii r_c and beta parameters β were obtained by concatenating results (Figure 3.4) from Diehl et al. (2008), Dong et al. (2010) and this work (Table 3.2). The amplitude A of the beta model was, according to results obtained from beta modelling (see Figure 3.5), set to be inversely proportional to the core radius r_c with a defined scatter (Table 3.3).

The exact values of the central amplitude (central electron density) could be in principle also derived from the measured surface brightness, but since the images were multiplied by an arbitrary constant to permit the functioning of Poisson statistics while filling the point sources, we decided to scale the absolute value of the amplitude manually in a

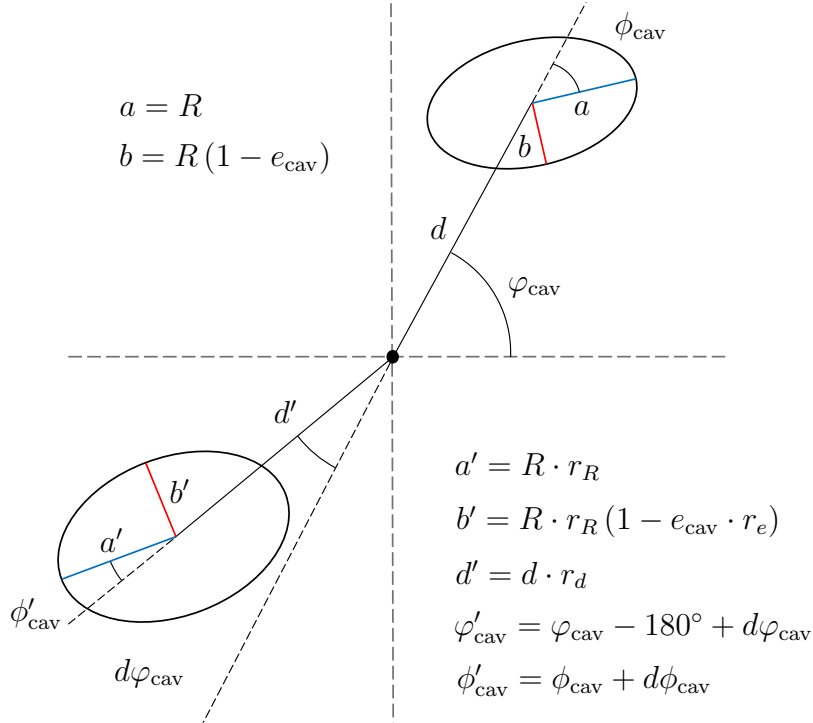


Figure 3.3: Schematic description of parameters used for generating the pairs of cavities. Each cavity is described by its distance from the galactic center d , positional angle φ_{cav} , radius (semi-axis) R , ellipticity e and rotational angle ϕ_{cav} . Since the parameters of pair cavities are closely related, the parameters of the second cavity $\{d', \varphi'_{\text{cav}}, R', e', \phi_{\text{cav}}\}$ were generated with respect to the first one.

way to obtain a reasonable total number of counts (minimally 10000 counts for 128×128 image). The distribution of ellipticities e was also determined from the beta modelling (Table 3.2, Figure 3.5) and in the case of the double beta model, we linked the ellipticities between the two components. For the rotational angle φ , as it should be naturally random, we assumed uniform distribution from 0° to 360° . For the double beta model, the rotational angles were tied between individual beta components.

In order for the network to really distinguish between the galaxies that do and do not contain cavities, the ellipsoidal cavity masks were inserted only into one half of the generated galaxies and the other half was kept intact. However, for comparison of the precision of the cavity size estimation, we trained also another network of the same architecture purely on images of galaxies that do contain cavities.

Single pair of inserted cavities can be described by 10 parameters – parameters describing the first cavity: distance from the galactic centre d , positional angle ϕ_{cav} , semi-major axis R , ellipticity e_{cav} , rotational angle φ_{cav} , and parameters describing the second cavity with respect to the first one: relative change in distance r_d , difference in positional angle $d\phi_{\text{cav}}$, relative change in semi-major axis r_R , relative change in ellipticity r_e and difference in rotational angle $d\varphi_{\text{cav}}$. We note that we took into account only positional or rotational angles around the axis along the line of sight and omitted any other possible rotations because otherwise, it would bring a degeneracy into the training dataset.

Parameter	Distribution	Range
single beta model		
dx_0	truncated gaussian	± 5 pixels
dy_0	truncated gaussian	± 5 pixels
r_c	from data	$0.5 - 30$ pixels
β	from data	$0.35 - 0.65$
$A \cdot r_c$	from data	$0.5 - 2.5$
e	from data	$0 - 0.4$
φ	uniform	$0^\circ - 360^\circ$
double beta model (25 %)		
$r_{c,2} / r_c$	from data	$10 - 100$
A_2 / A	from data	$0.05 - 0.3$
β_2 / β	from data	$1.5 - 3.0$
primary cavities		
d	from data	$3 - 78$ pixels
R/d	from data	$0.32 - 1.00$
e_{cav}	from data	$0 - 0.6$
φ_{cav}	uniform	$0^\circ - 360^\circ$
ϕ_{cav}	from data	$\pm 90^\circ$
secondary cavities		
r_d	from data	$0.5 - 1.0$
r_R	from data	$0.5 - 1.0$
$r_{e_{\text{cav}}}$	from data	$0.0 - 1.35$
$d\varphi_{\text{cav}}$	from data	$\pm 76^\circ$
$d\phi_{\text{cav}}$	from data	$\pm 58^\circ$
cavity rims (33 %)		
width	uniform	$0.5 - 1.5$
height	uniform	$0.5 - 1.5$
type	binary	I / II
gas sloshing (33 %)		
periodicity	uniform	$0.5 - 2.0$
depth	uniform	$1.05 - 1.3$
central point sources (50 %)		
amplitude	uniform	$50 - 300$
FWHM	uniform	$0.1 - 2.0$

Table 3.2: Parameter ranges and distributions used for generating the training dataset. Distributions of parameters which could have been estimated from observed properties of real cavities (**from data**) were determined from the sample of manually inspected galaxies (see also Figures 3.6, 3.7). The rest of the parameters and their distributions are either naturally uniformly random or they were estimated based on basic assumptions discussed in Section 3.2.2.

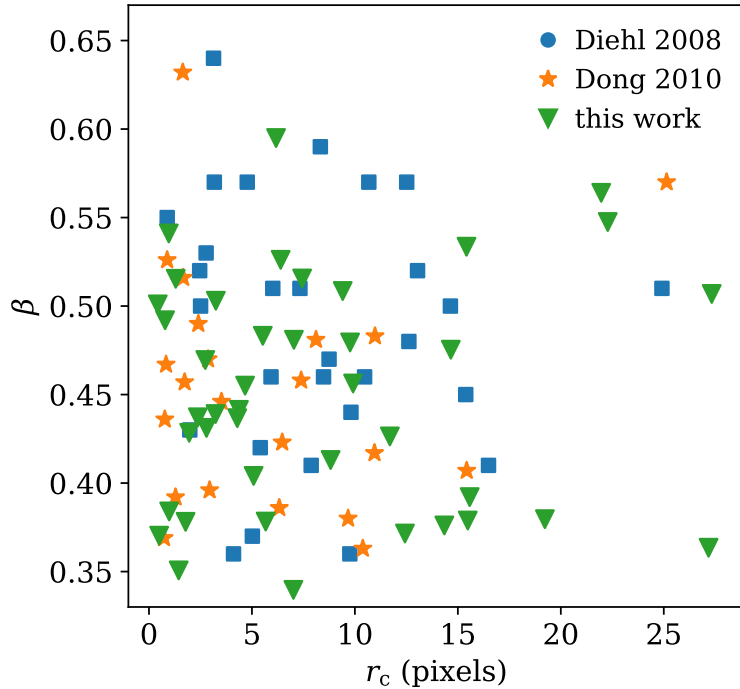


Figure 3.4: Comparison of the relation between the beta parameter β and core radius r_c obtained from beta modelling analyses of *Chandra* images of galaxies by Diehl et al. (2008), Dong et al. (2010) and this work.

The distributions of primary and secondary cavity parameters were determined from the analysed sample of elliptical galaxies containing X-ray cavities (Table D.1) and they can be found in the Figures 3.6 and 3.7. The distributions were binned, smoothed, and used for generating the training dataset. The correlations of individual parameters were also taken into account in the sense that one from the strongly correlated parameters was generated with respect to the second one (see Section 3.2.3). The positional angle of the cavity was, similarly as in the case of the beta model, expected to be uniformly random in the range of 0° to 360° . All other cavity parameters were generated based on their measured distributions. Note that the cavities tend to have their rotational angles φ grouped at 0° (prolate) and 90° (oblate) and therefore have their semi-major axis either aligned with the direction towards the centre of the galaxy or perpendicular to that direction.

The bright rims around the cavities representing the shocked regions were produced for approximately one half of the generated cavities. The rims were generated as ellipsoidal shells of the same ellipticity as the corresponding cavities and they can be in general described by many various parameters. For simplicity, we linked the parameters of individual rims within a cavity pair together and assumed only 3 basic parameters: *width*, *height* and *type* of the rim. The values of the *width* of the rim were drawn from a uniform distribution ranging from 0.5 to 1.5 times the original size of the cavity. For the *height* of the rim, we assumed a uniform distribution from 0.5 to 1.5 of the local surface brightness at the position of the rim. The value of the *height* factor was set to be linearly decreasing from its maximal value at the inner side of the rim to zero at its outer side, so the sharp boundary of the rim is produced only at its inner edge. The bright rims were produced in two different realizations (Figure 3.9) – type I: simple shell-like rims without

any angular dependence, and type II: rims, for which the height decreases with decreasing angular distance from the axis between the galaxy and cavity centres. The relative frequency of each rim type is 50 %.

The effects of gas sloshing were simulated for approximately one half of the galaxies by multiplying the original model with a grid of a spiral-like pattern. The values of the grid are axially antisymmetric and the whole pattern can be described by two parameters: the *periodicity* describing the number of angular periods and the *depth* which represents a maximal / minimal value of the whole pattern. The possible values of the *periodicity* were taken from a uniform distribution from 0.5 to 2.0 and the *depth* of the “overdensity / underdensity” field (with a mean value of 1) was drawn from a uniform distribution between 1.05 and 1.3. The rotational angle, as well as the direction of the spiral pattern, were generated randomly.

The central point sources, representing mainly the nonthermal emission of the AGN or the thermal emission of the hot gas due to the influence of the SMBH, were simulated using a low-FWHM Gaussian model component for approximately one half of generated galaxies. The amplitude of the Gaussian model was generated uniformly in the range from 50 to 300 and the values of the FWHM were drawn from a uniform distribution between 0.1 and 2.0. The ratio of galaxies containing the bright central emission as well as the parameter ranges of the Gaussian component were determined using the beta modelling analysis (Table 3.2).

3.2.3 Correlations between parameters

Although most of the parameters were uncorrelated and therefore could have been generated purely from their measured distributions, some of them seem to be strongly correlated with others. We tried to uncover these relations and take them into account while generating the data. The correlations were identified using the Pearson correlation coefficient and the corresponding coefficients are stated above individual plots of these quantities in Figures 3.5, 3.6 and 3.7.

The correlations between individual cavities within the pair were expected from the beginning and each parameter of the second cavity was generated with respect to the first one. We found further correlations between the parameters of individual beta components and also between single cavity parameters. The parameters of the second beta component tend to be related to the first component (Figure 3.5). The correlation coefficients of core radii and beta parameters of individual beta components are 0.94 and 0.82, respectively. For artificial galaxies generated using the double beta model, the parameters of the second component were therefore calculated with respect to parameters of the first component with a measured scatter. We note that the detected relation between the individual beta components might be a result of the fitting process itself, however, we believe that for the purpose of generating the training dataset this resembles an acceptable assumption.

We also found a strong correlation ($r = 0.86$) between the cavity distance and its radius. We have, therefore, decided to generate the ratio of radius and distance and calculate the radius from this ratio and the distance instead of generating the radius based on its measured distribution. For the ratio of cavity radius to distance R/d , we also truncated the observed distribution to be maximally equal to unity to avoid producing cavities that would intersect the centre of the galaxy or each other.

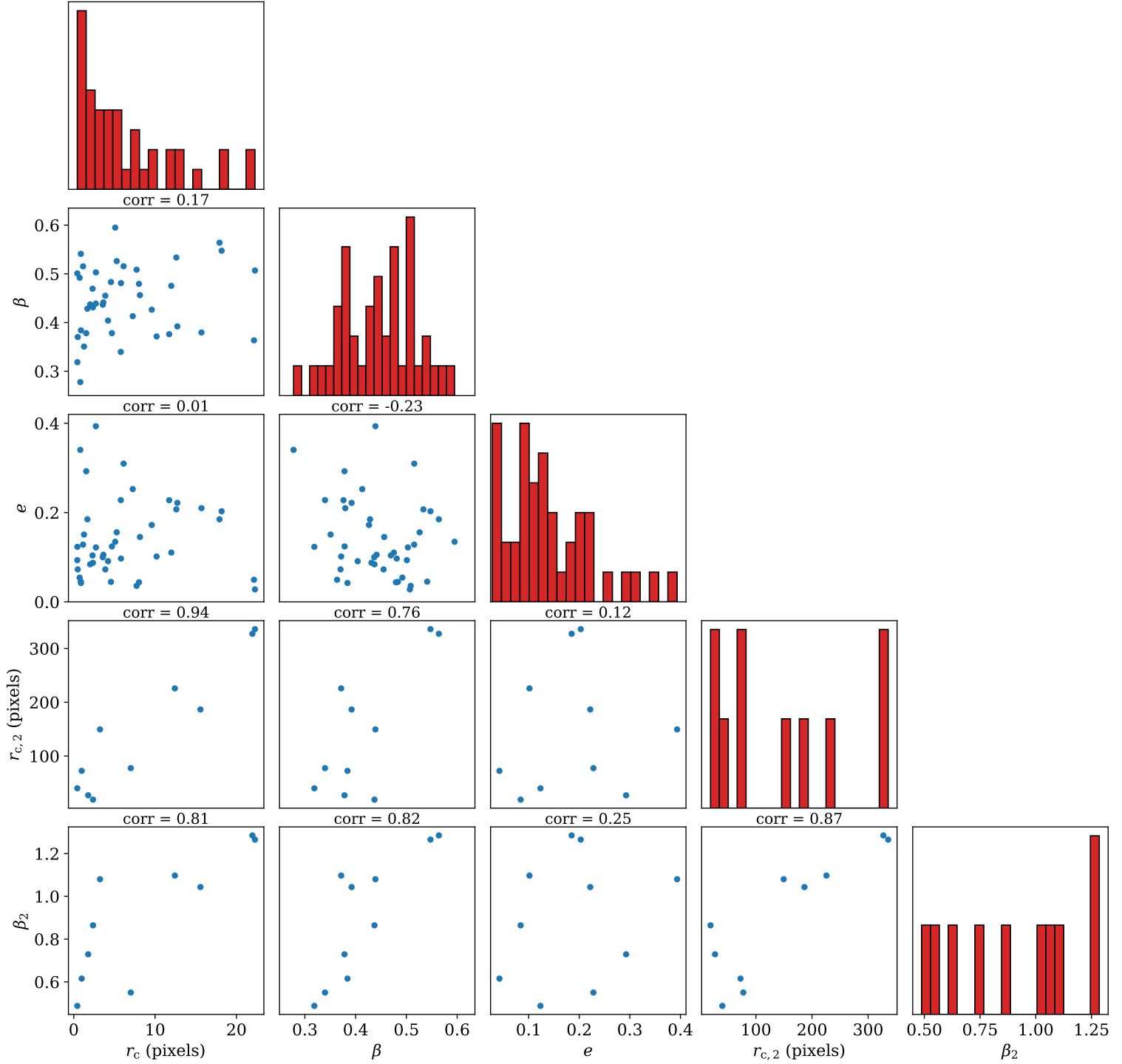


Figure 3.5: Corner plot showing distributions and correlations between β -modeling parameters: core radius r_c , beta parameter β of the first component, common ellipticity e and core radius $r_{c,2}$, beta parameter β_2 of the second component. Pearson correlation coefficients are stated above individual correlation plots.

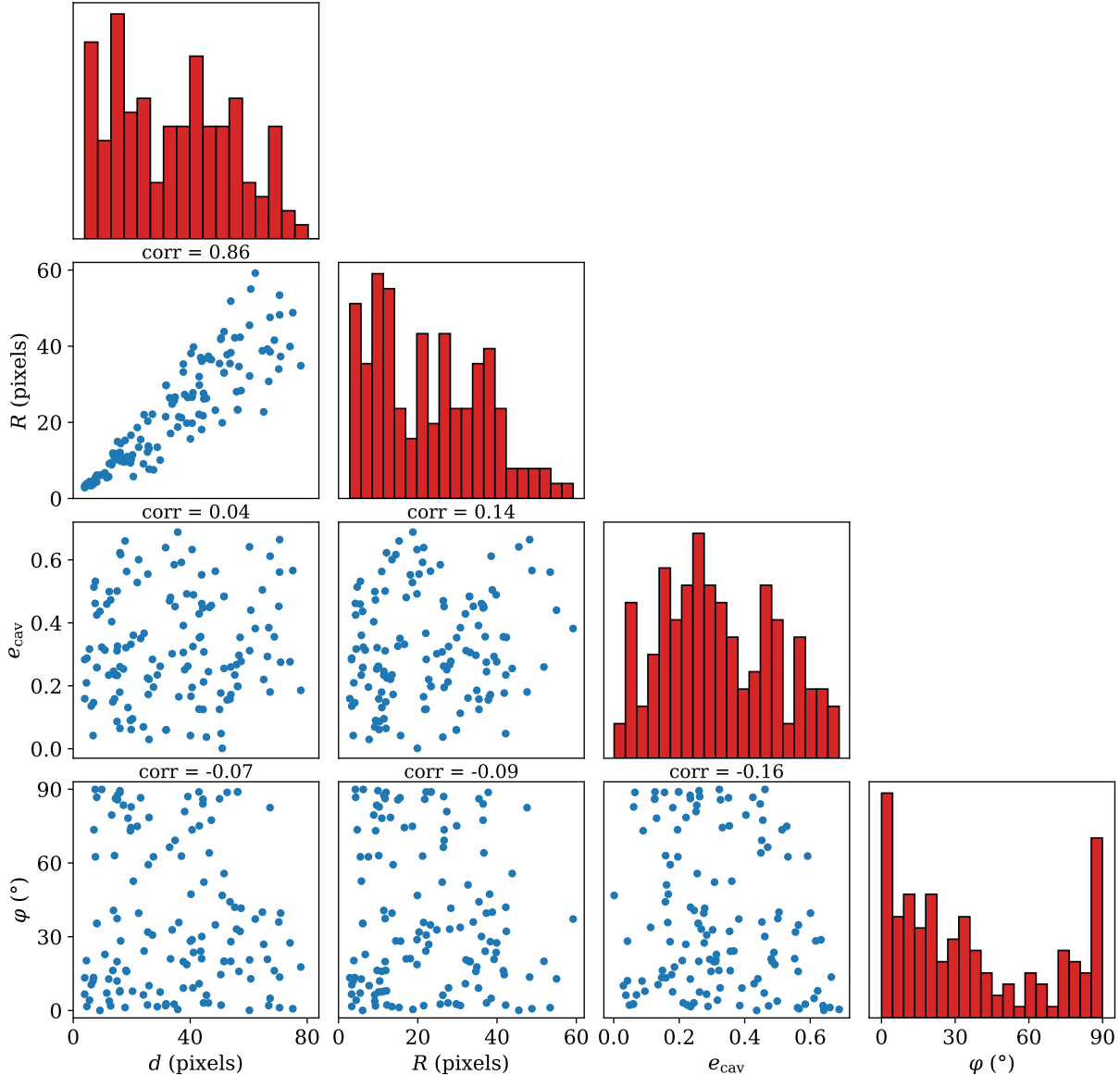


Figure 3.6: Corner plot showing distributions and correlations between primary cavity parameters: distance from the centre of the galaxy d , semi-major axis R , ellipticity e_{cav} and rotational angle φ (angle between the semi-major axis and the direction towards the centre of the galaxy). Pearson correlation coefficients are stated above individual correlation plots. Among all the parameters, only the cavity distances d and radii R are strongly correlated (correlation coefficient ≈ 0.86). The distance-radius parameter space was therefore sampled based on the measured correlation (similarly as in the case of multiple β components). All other parameters were generated based on their measured distributions.

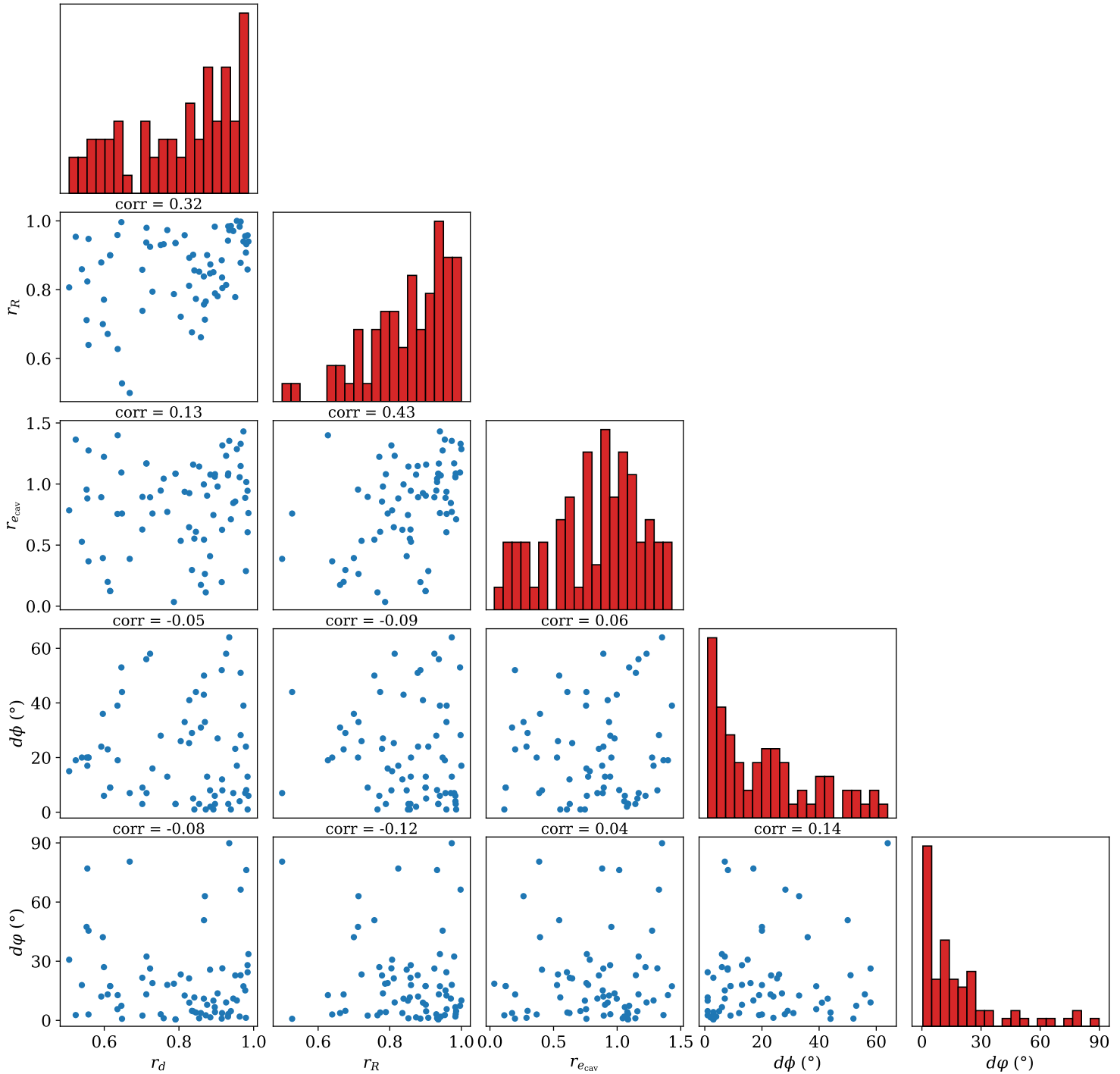


Figure 3.7: Corner plot showing distributions and correlations between secondary cavity parameters (ratios and differences between individual cavity parameters within a cavity pair): relative distance r_d , relative semi-major axis r_R , relative ellipticity $r_{e\text{cav}}$, difference between positional angles $d\phi$ and difference between rotational angles $d\varphi$. Pearson correlation coefficients are stated above individual correlation plots. None of the secondary parameters, however, seems to be strongly correlated. All the secondary cavity parameters were therefore generated directly from their measured distributions and no correlations were assumed.

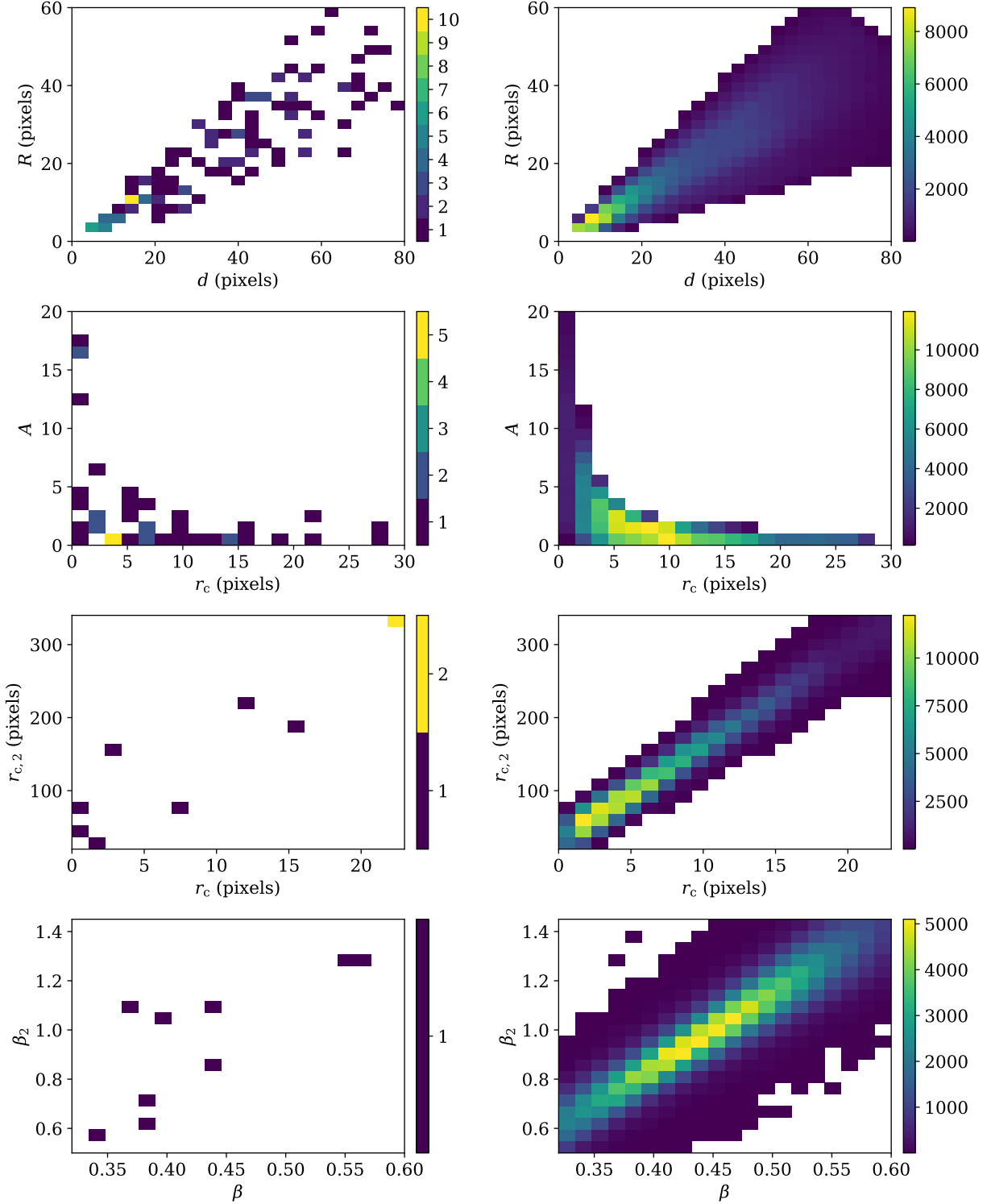


Figure 3.8: Comparison of measured (left) and simulated (right) dependence of correlated parameters: cavity distance from the centre and its radius $R - d$, single beta model's amplitude and core radius $A - r_c$, double beta model core radii $r_c - r_{c,2}$, and double beta model beta parameters $\beta - \beta_2$.

3.3 Training

A total number of 300000 artificial images and corresponding cavity masks were generated for the training of the network, 10000 images were used for validation purposes, and another 10000 for the evaluation of the network. Examples of artificially generated images with a comparison of various simulated features (bright rims, gas sloshing) can be found in Figure 3.9. Individual features were generated based on their probabilities stated in Table 3.3 and randomly combined. The elliptical beta model and also the ellipsoidal cavities and their rims were generated with the use of the *Numpy* library (version 1.20.0; Harris et al., 2020) and a modified version of the *pyellipsoid*² library. The source code used for the dataset generation can be found on the Github page of the CADET³ network. The process of generation of the training dataset was parallelized and took over 18 hours using 64 cores on Intel Xeon Silver 4216 CPU. The simulated 3D models of artificial galaxies and corresponding cavity masks were summed into 2D images, converted into the .npy format (*Numpy*) and stored.

The loss function of the convolutional neural network was calculated as the binary cross-entropy of the pixel-wise prediction with respect to the ground truth, which is represented by the binary version of the cavity mask

$$\mathcal{L} = -\frac{1}{N} \sum_i^N y_{\text{true},i} \cdot \log y_i + (1 - y_{\text{true},i}) \cdot \log(1 - y_i), \quad (3.4)$$

where $y_{\text{true},i}$ is the ground truth (binary cavity mask), y_i is the pixel-wise prediction and N is the total number of pixels in each image. The minimization of the loss function was realized using the *Adaptive Moment Estimation* (ADAM) optimizer (Kingma & Ba, 2014) with a learning rate of $5 \cdot 10^{-4}$ and decay of the learning rate of 10^{-4} . For controlling the learning rate, in order for the network to prevent overfitting, we utilized also the *ReduceLROnPLateau Tensorflow* callback, which reduces the learning rate when the validation loss (loss function calculated on the validation dataset) started flattening. The prediction accuracy of the network was evaluated using the binary accuracy metrics. Various sets of hyper-parameters and slightly different architectures of the convolutional network were tried and for the subsequent evaluation and application of the network, we chose the combination of hyper-parameters and the architecture with the best possible test score (highest value of binary accuracy on the test set).

Two separate versions of the CADET network were trained in order to create both a pipeline for searching for unknown X-ray cavities in less explored galactic systems (*CADET_search*) and also a tool for exact localization and size-estimation (*CADET_size*) of known X-ray cavities, that were analyzed also manually (Section 2.2.2, Figure D.1). For this reason, we trained the second network purely on images of galaxies that do contain cavities, whereas for the searching pipeline we used also images without any cavities. Both networks were trained for 5 epochs, while at each epoch we used all training images, and after every epoch, the sequence of the training data was randomly shuffled. The batch size was set to 8 images and each batch was normalized separately. The training of the network was performed using the commercial NVIDIA GPU type GeForce RTX 2080 SUPER (8 GiB) and lasted approximately 6 hours for both pipelines. The network architectures together with trained weights for both pipelines were stored in the Hierarchical Data Format (HDF5) and they are available together with scripts for subsequent analysis on the CADET Github page.

²<https://pypi.org/project/pyellipsoid/>

³<https://github.com/tomasplsek/CADET>

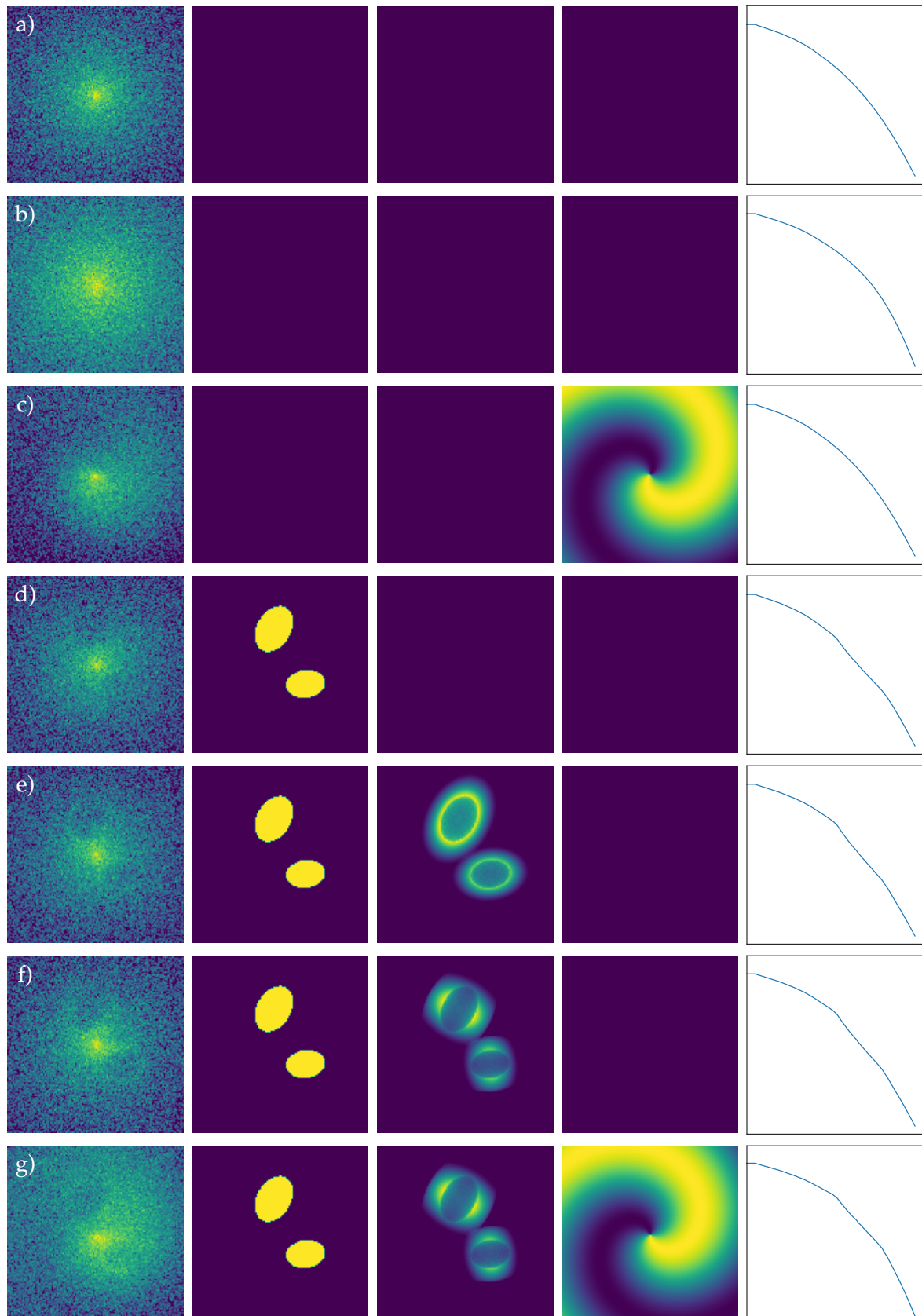


Figure 3.9: Examples of artificially generated images with corresponding features - from left to right: resulting noisy image, binary cavity mask, bright rims around cavities, sloshing pattern and the brightness profile of the resulting image. The utilization of individual features is compared in rows: **a)** single beta model without any features, **b)** double beta model, **c)** single beta model with gas sloshing, **d)** single beta model containing cavities, **e)** single beta model containing cavities with bright rims of type I, **f)** single beta model containing cavities with bright rims of type II and **g)** double beta model with all features included (rims of type II).

3.4 Testing

Both versions of the CADET network (*CADET_search*, *CADET_size*) were tested using the test set of artificial images as well as using real images of galaxies and the reliability of individual predictions was checked both quantitatively and also qualitatively. As already mentioned in section 3.3, the precision of the network’s predictions was tested using the binary accuracy metrics. However, we note that such validation metrics is rather abstract and can be also slightly misleading. The fact, that the majority of pixels both in the ground truth images and also predictions are equal to zero and therefore are accounted as “correct”, leads to an artificial increase in the accuracy metrics. On the other hand, this binary accuracy metrics is still valid for evaluating the predictions of individual network architectures trained with various hyper-parameters.

Note that while testing the networks on real images, the predictions could have been tested purely on a qualitative basis and compared only with the naturally expected cavity extent. We therefore selected images of galaxies with the most prominent and apparent cavities (NGC 4696, NGC 4778, NGC 5813) and compared the predictions with the original images by eye. For comparison and visualizing purposes while testing the network, we utilized the *Tensorboard* visualization toolkit.

CADET_search

The searching pipeline *CADET_search* was tested and tuned for proper finding and localization of cavities. The accuracy of the network’s predictions was checked using traditional classification accuracy metrics – total numbers of True Negative (TN), False Negative (FN), True Positive (TP) and False Positive (FP) cavity predictions. The division of predictions into individual statistical measures (TN, FN, TP and FP) depends strongly on two free parameters – first one is the minimal pixel value threshold (the so-called discrimination threshold), for which the prediction is still classified as a valid cavity, and the second one is the minimal recovered cavity area required for the cavity prediction to be classified as True Positive (TP).

The optimal operating mode can be found by comparing rates of true positives (TPR) and false positives (FPR) given by

$$\text{TPR} = \frac{\text{TP}}{\text{TP} + \text{FN}}, \quad \text{FPR} = \frac{\text{FP}}{\text{FP} + \text{TN}} \quad (3.5)$$

for different values of the discrimination threshold. Thereby obtained dependence is called the Receiver Operating Characteristic (ROC) curve and it enables to select the adequate threshold with an acceptable trade-off between the rates of true and false positives. For a completely non-trained (random) classifier, the ROC curve is a linear curve with zero intercept and unit slope, whereas for a perfect classifier the ROC curve is represented by a single point with $\text{TPR} = 1$ and $\text{FPR} = 0$, for any value of the discrimination threshold. The performance of the network across all possible discrimination thresholds can be measured using the Area Under the (ROC) Curve (AUC). The possible interpretation of the AUC metrics is the overall probability of the network for producing a True Positive prediction rather than a False Positive one (see Machine Learning Crash Course by Google⁴). The comparison of different ROC curves with the corresponding AUCs for various values of the minimal recovered cavity area threshold can be found in Figure 3.10. The utilization of the detection CADET pipeline on real images of galaxies is displayed in Figure 3.11.

⁴<https://developers.google.com/machine-learning/crash-course/classification/roc-and-auc>

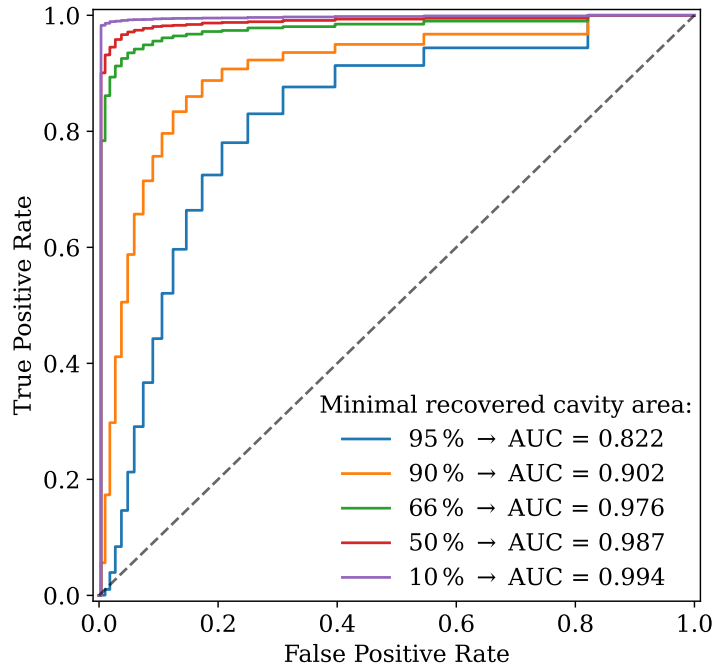


Figure 3.10: The Receiver Operating Characteristic (ROC) curves for various values of the minimal recovered cavity area. The gray dashed line represents a non-trained random classifier.

CADET_size

To test the size-estimating network we introduced also another way of measuring the accuracy of the network's predictions, which is based on comparing the inferred cavity areas and volumes with their real values known from the simulations. The prediction 128×128 matrices were decomposed into individual cavities using the DBSCAN clustering algorithm – the minimal number of expected clusters was set to two, however, we did not put any constraints on the maximal number of clusters, mainly because real galaxies are expected to contain multiple generations of cavities. If the clustering algorithm finds more than two cavities while being tested on artificial images, only the two cavities with the highest area are selected – we note that this oversimplification was required only for less than 5 percent of cavity predictions when used on the test set. The area of the cavity prediction was calculated by simply summing the pixels classified as belonging to that specific cavity. For the volume computations, we utilized the exact predicted cavity shapes and only assumed symmetry around the direction from the centre of the galaxy to the cavity centre (see Section 4.1).

Similarly, as in the case of the *CADET_search* network, we defined the minimal pixel value required for each pixel to be accounted as a valid prediction (discrimination threshold) and we cut off pixels of individual prediction matrices at this value. The discrimination threshold was applied before decomposing the prediction into individual cavities. The optimal value of this minimal threshold was derived from the dependence of relative error of cavity total areas and volumes on this threshold obtained by varying its value in the range from 0.05 to 0.95.

Based on the dependency shown in Figure 3.12, we selected the discrimination threshold to be approximately 0.55, for which we obtain the best possible absolute relative error while centring the distribution of the relative error around zero. The median values

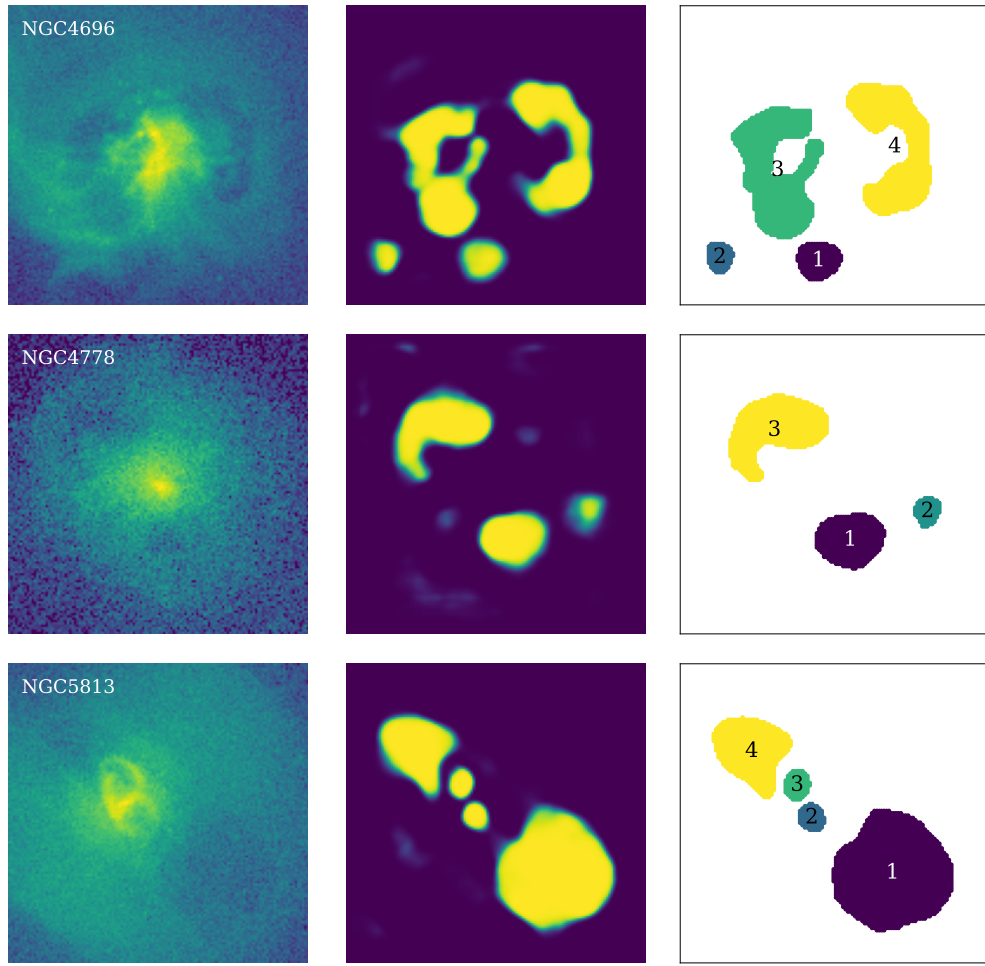


Figure 3.11: Testing of the *CADET_search* network on real *Chandra* images of galaxies, that were selected for the visual testing of the network. **Left:** Processed and cropped *Chandra* image, **center:** pixel-wise prediction of the CNN and **right:** prediction decomposed into individual cavities using the DBSCAN algorithm.

of absolute relative errors of the cavity area and volume estimations for the discrimination threshold of 0.55 are $4.7^{+5.0}_{-2.6}\%$ and $11.9^{+10.4}_{-6.2}\%$, respectively, where the corresponding stated uncertainties are the 25 % and 75 % quartiles. For this value of the discrimination threshold, we examined the overall distribution of predicted volumes versus the true volumes when applied on the testing set of artificial images (see Figure 3.13). The performance of the network was tested also using real images of galaxies with confirmed and apparent cavities (Figure 3.14).

3.5 Application

After both CADET networks (*CADET_search*, *CADET_size*) were tested and their thresholds were optimized using the testing set of artificial images, we applied the networks also onto the set of real images of previously analyzed galaxies (Table 3.2). The predictions can be found in the Appendix (Section C) – firstly the detection tool *CADET_search* was utilized on all the analyzed galaxies (Figure C.1) and then we used the *CADET_size* pipeline to estimate the sizes of confirmed cavities analyzed also in Section 2.2.2 (Figure D.1). Further description of thereby obtained results can be found in Section 4.1.3.

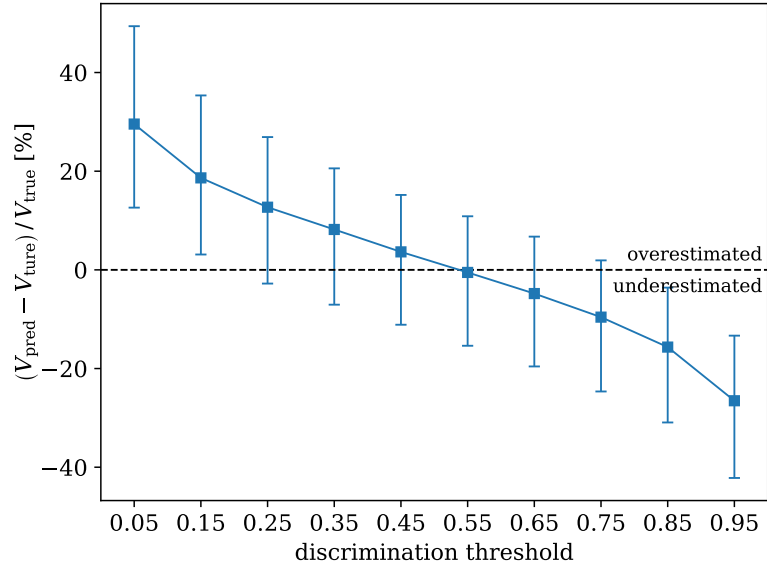


Figure 3.12: Dependence of the relative cavity volume error on different values of the discrimination threshold while tested on the testing dataset. For the discrimination threshold of 0.55 the error distribution is centered around zero.

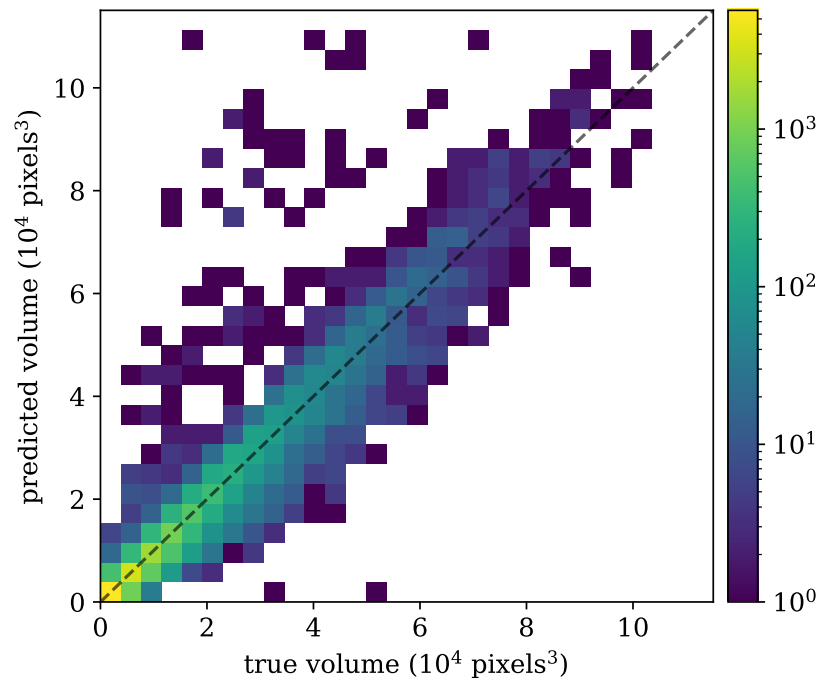


Figure 3.13: Predicted vs true cavity volumes of the testing dataset obtained for the discrimination threshold of 0.55. The black dashed line represents the perfect recovery. The colour indicates the total number of points inside the corresponding bin.

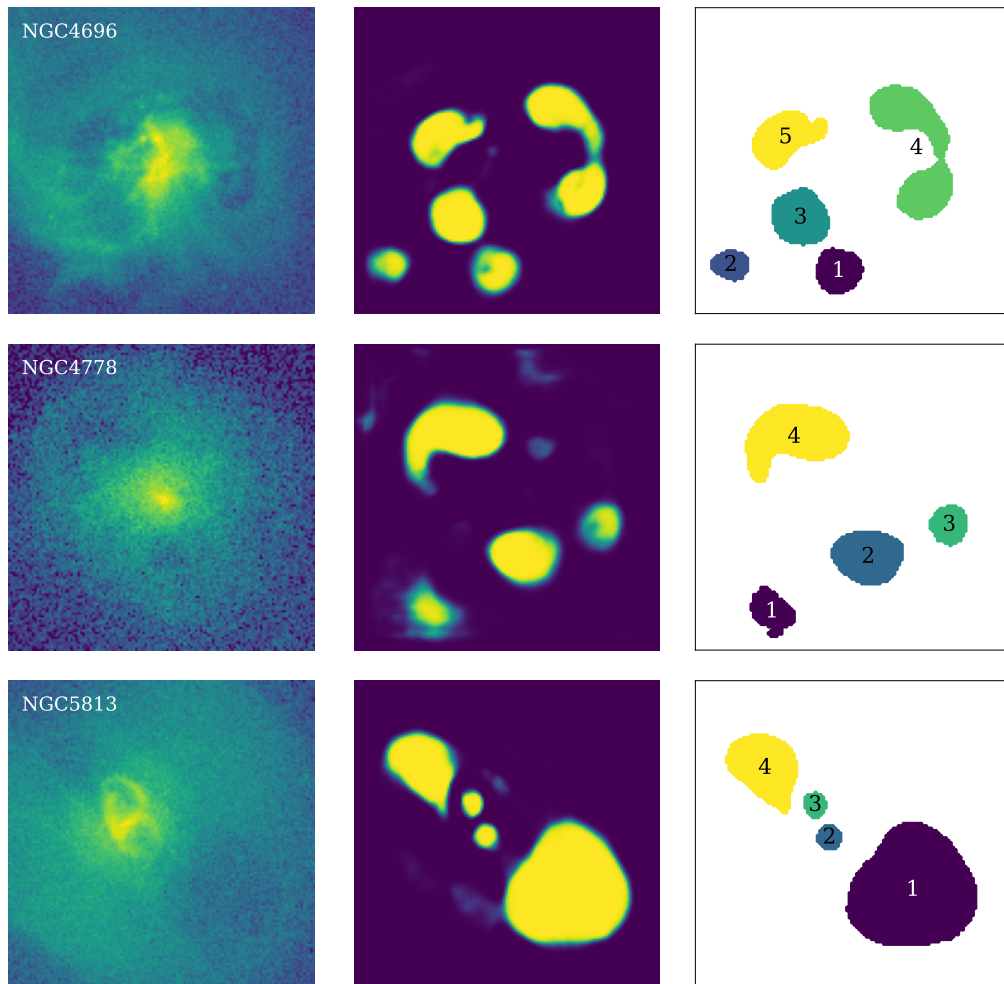


Figure 3.14: Testing of the *CADET_size* network on real *Chandra* images of galaxies that were selected for the visual testing of the network. **Left:** processed and cropped *Chandra* image, **center:** pixel-wise prediction of the CNN and **right:** prediction decomposed into individual cavities using the DBSCAN algorithm.

Chapter 4

Results

The deprojected radial profiles of temperature kT , abundance Z and electron density n_e were determined from spatially resolved spectral analysis which was performed for all the selected galaxies. Radial profiles of these quantities were used to calculate additional thermodynamic quantities such as thermal gas pressure $p = nkT$, specific entropy $K = kT/n_e^{2/3}$ and cooling time of the X-ray emitting gas (Equation 1.2). For most galaxies, the spatial resolution of *Chandra* ACIS chip was not sufficient to constrain the thermodynamic properties at the Bondi radius and extrapolations were necessary. The central temperature and metallicity were assumed to be constant within the innermost bin. The electron density, however, had to be extrapolated (using the below-described methods). Central values of all thermodynamic quantities are listed in Tables 4.2 and 4.3 and corresponding radial profiles can be found in the Appendix (Figures A.1-A.6).

In order to probe how susceptible to thermal instabilities are the atmospheres of individual galaxies, we calculated the ratio of the cooling time to the free-fall time. The free-fall time was calculated both assuming an isothermal sphere or hydrostatic equilibrium (Equations 1.3, 1.4) and these two approaches are compared in the Appendix (Figure A.7). The free-fall time calculated under the assumption of hydrostatic equilibrium is for many galaxies slightly underestimated with respect to the isothermal sphere. This discrepancy is probably the result of non-thermal pressure support caused by micro-turbulences or cosmic rays and which can contribute up to 30 % of total thermal gas pressure (Churazov et al., 2010; Lakhchaura et al., 2019).

Parameters of the Bondi accretion were determined from spectral properties (Table 4.2) of the X-ray emitting gas in the vicinity of the supermassive black hole and the results are listed in Tables 4.3 and 4.4. For extrapolating the electron density into the Bondi radius, we used, similarly as Russell et al. (2013), 3 different profiles: powerlaw model, β -model (Cavaliere & Fusco-Femiano, 1976) and sersic profile (Sérsic, 1963). The mean of these three profiles was then taken as the final value of the electron density and the scatter was accounted in the final uncertainty. To account for uncertainties in both axes, the profile fitting was carried out using the Orthogonal Distance Regression (Scipy 1.4.1; Boggs & Rogers, 1990). In the case of the powerlaw model, we only used inner 2 to 3 radial bins in order to properly fit the innermost substructure. When fitting the β -model and the sersic profile, we included more radial bins up to the point where the profile changes significantly or starts flattening again.

As mentioned in Chapter 2, for the spectra in the innermost radial bin, we included an absorbed powerlaw model component to describe the non-thermal emission of the AGN. The unabsorbed flux of this component was determined in the 0.5 – 7.0 keV energy range using the *cflux* multiplicative component and their final values are stated in Table 4.2. Assuming that the nuclear emission is isotropic, total luminosities were calculated using the measured fluxes and known distances stated in Table 2.1. For galaxies NGC 507 and NGC 1600, the spectra could have been well fitted only using a simple *apec* component and the central powerlaw component was therefore not significant.

Galaxy	Alternative name	RA ^a (hh:mm:ss.s)	DEC ^a (dd:mm:ss.s)	ACIS chips	Exptime (ks)	VLA conf. ^b	H α +[N II] morphology	σ_v^c (km/s)	M_\bullet^d (M_\odot)	Ref
IC 4926	Abell 3565	13:36:39.0325	-33:57:57.072	S3	28.5	D	E	327 ± 5	$1.30^{+0.24}_{-0.20}$	[4]
NGC 507		01:23:39.9409 *	33:15:21.858 *	S3, I3	62.2	C	N	292 ± 6	$2.14^{+0.58 \ddagger}_{-0.46}$	[1]
NGC 708	Abell 262	01:52:46.458	36:09:06.494	S3	139.4	A [†] , C	E	222 ± 8	$0.49^{+0.07 \ddagger}_{-0.07}$	[3]
NGC 1316	Fornax A	03:22:41.7052 *	-37:12:28.557 *	S3	228.4	A	E	223 ± 3	$0.17^{+0.03}_{-0.03}$	[2]
NGC 1399	Fornax c.	03:38:29.0170	-35:27:01.507	S3	204.5	A, C [†]	N	332 ± 5	$0.88^{+0.90}_{-0.45}$	[2]
NGC 1407		03:40:11.79 *	-18:34:48.9 *	S3	44.5	A, B	N	266 ± 5	$4.65^{+0.73}_{-0.41}$	[2]
NGC 1600		4:31:39.8510 *	-5:05:10.476 *	S3	243.6	A	N	331 ± 7	$17.0^{+1.5}_{-1.5}$	[7]
NGC 4261		12:19:23.2357	05:49:29.650	S3	135.3	A, C	NE	297 ± 4	$1.67^{+0.39}_{-0.24}$	[5]
NGC 4374	M84	12:25:3.743	12:53:13.139	S3	882.4	B	NE	278 ± 2	$0.93^{+0.10}_{-0.09}$	[2]
NGC 4472	M49	12:29:46.7619	08:00:01.713	S3	367.0	A, C	N	282 ± 3	$2.54^{+0.58}_{-0.20}$	[2], [8]
NGC 4486	M87	12:30:49.4234	12:23:28.044	S3	370.7 / 136.4 ^e	B, C	E	323 ± 4	$6.15^{+0.38}_{-0.37}$	[2]
NGC 4552	M89	12:35:39.8141	12:33:22.732	S3	201.4	C	N	250 ± 3	$0.50^{+0.06}_{-0.06}$	[4]
NGC 4636		12:42:49.827	02:41:15.99	S3, I3	197.4	A	NE	200 ± 3	$0.33^{+0.04 \ddagger}_{-0.04}$	[1], [9]
NGC 4649	M60	12:43:39.986 *	11:33:09.86 *	S3	293.8	B	N	330 ± 5	$4.72^{+1.04}_{-1.05}$	[2]
NGC 4696	Centaurus c.	12:48:49.2762 *	-41:18:39.532 *	S3	711.1	A	E	243 ± 6	$0.89^{+0.18 \ddagger}_{-0.15}$	[1]
NGC 4778	HCG 62	12:53:05.7003 *	-09:12:14.676 *	S3	167.0	B/A	NE	251 ± 21	$0.84^{+0.17 \ddagger}_{-0.14}$	[3]
NGC 5044		13:15:23.9727 *	-16:23:07.779 *	S3	563.7	A, B	E	225 ± 9	$0.22^{+0.12}_{-0.07}$	[6]
NGC 5813		15:01:11.2345 *	01:42:07.244 *	S3	638.2	B	E	236 ± 3	$0.71^{+0.10}_{-0.09}$	[4]
NGC 5846		15:06:29.253 *	01:36:20.29	S3, I3	113.4	A, D/C	E	237 ± 4	$1.10^{+0.16}_{-0.14}$	[4], [9]
NGC 6166	Abell 2199	16:28:38.245	39:33:04.234	S3, I3	158.3	A [†] , B [†]	E	301 ± 6	$2.11^{+0.57 \ddagger}_{-0.45}$	[1]

References: [1] Lauer et al. (2007) [2] Kormendy & Ho (2013) [3] Makarov et al. (2014) [4] Saglia et al. (2016) [5] Boizelle et al. (2021) [6] Schellenberger et al. (2021) [7] Thomas et al. (2016) [8] Nagar et al. (2002) [9] Temi et al. (2018)

^a Coordinates marked with * represent SMBH positions derived from the hard X-ray (3 – 7 keV) central peak, for the rest of the galaxies the positions are based on radio observations and they were either derived from our analysis of VLBI observations or taken from ALMA measurements stated in the Reference column.

^b VLA array configurations marked with [†] were taken from the NRAO VLA Archive Survey (NVAS).

^c Velocity dispersions were taken from the HyperLeda database (Makarov et al., 2014).

^d SMBH masses marked with [‡] were derived from $M_\bullet - \sigma$ scaling relations, whereas masses for all other galaxies were taken from direct measurements of gas or star kinematics from within the sphere of influence of the SMBH.

^e The first number represents the total exposure time for 1/8th subarray observations (OBSIDs 18232-21458) and the second number is the total exposure time for full-array observations which are strongly affected by pile-up effects (OBSIDs 352, 2707).

Table 4.1: Basic parameters for the sample of galaxies: alternative galaxy names, right ascension and declination coordinates of the SMBH position, *Chandra*'s ACIS chips used for the analysis, total cleaned exposure time in kiloseconds, VLA configurations used for estimation of cavity sizes, morphology of cool gas tracer H α +[N II] emission, velocity dispersions, masses of the supermassive black holes and references. The H α +[N II] morphology was adopted from Lakhchaura et al. (2018) and is as follows: N - no cool gas emission, NE - nuclear emission and E - emission extended beyond 2 kpc from the centre.

Galaxy	n_{H}^a (10^{20} cm^{-2})	z	$n_{\text{H},z}$ (10^{20} cm^{-2})	Γ	F_{pow} , 0.5–7.0 keV ($\text{erg s}^{-1} \text{ cm}^{-2}$)	F_{cool} , 0.5–7.0 keV ($\text{erg s}^{-1} \text{ cm}^{-2}$)	kT (keV)	$n_e(r_{\text{B}})$ (cm^{-3})	Z (Z_{\odot})
IC 4296	3.96	0.0125	238 ± 25	1.9	$6.79^{+0.59}_{-0.57} \cdot 10^{-13}$	$2.43^{+0.09}_{-0.09} \cdot 10^{-13}$	$0.62^{+0.03}_{-0.03}$	$1.12^{+0.17}_{-0.18}$	$1.03^{+0.45}_{-0.26}$
NGC 507	5.24	0.0165	-	-	-	$2.73^{+0.09}_{-0.09} \cdot 10^{-13}$	$0.81^{+0.03}_{-0.03}$	$0.76^{+0.07}_{-0.07}$	$0.53^{+0.14}_{-0.10}$
NGC 708	6.87	0.0162	0	1.9	$6.58^{+4.06}_{-4.22} \cdot 10^{-15}$	$2.22^{+0.14}_{-0.14} \cdot 10^{-12}$	$0.96^{+0.07}_{-0.07}$	$0.17^{+0.02}_{-0.02}$	$0.35^{+0.10}_{-0.07}$
NGC 1316	2.11	0.0059	0	1.57 ± 0.11	$6.87^{+0.32}_{-0.34} \cdot 10^{-14}$	$7.73^{+0.47}_{-0.46} \cdot 10^{-13}$	$0.67^{+0.09}_{-0.11}$	$0.42^{+0.06}_{-0.06}$	$0.56^{+0.16}_{-0.11}$
NGC 1399	1.39	0.0048	0	1.9	$1.01^{+0.41}_{-0.42} \cdot 10^{-14}$	$2.34^{+0.98}_{-0.68} \cdot 10^{-12}$	$1.11^{+0.03}_{-0.03}$	$0.52^{+0.03}_{-0.03}$	$1.05^{+0.13}_{-0.11}$
NGC 1407	4.94	0.0059	0	1.9	$5.08^{+0.62}_{-0.64} \cdot 10^{-14}$	$4.83^{+6.3}_{-2.13} \cdot 10^{-13}$	$0.95^{+0.03}_{-0.03}$	$0.15^{+0.02}_{-0.02}$	$0.84^{+0.31}_{-0.18}$
NGC 1600	3.19	0.0156	-	-	-	$1.99^{+0.83}_{-0.52} \cdot 10^{-13}$	$1.05^{+0.07}_{-0.08}$	$0.11^{+0.01}_{-0.01}$	$0.42^{+0.09}_{-0.06}$
NGC 4261	1.65	0.0074	866 ± 37	1.9	$1.21^{+0.05}_{-0.04} \cdot 10^{-12}$	$3.09^{+0.04}_{-0.04} \cdot 10^{-13}$	$0.69^{+0.01}_{-0.01}$	$1.09^{+0.04}_{-0.04}$	$0.53^{+0.05}_{-0.04}$
NGC 4374	2.85	0.0034	16 ± 8	2.08 ± 0.07	$9.51^{+0.36}_{-0.34} \cdot 10^{-14}$	$1.17^{+0.05}_{-0.05} \cdot 10^{-12}$	$0.50^{+0.18}_{-0.10}$	$0.31^{+0.09}_{-0.08}$	$0.55^{+0.29}_{-0.16}$
NGC 4472	1.56	0.0033	0	1.9	$6.35^{+1.36}_{-1.35} \cdot 10^{-15}$	$2.50^{+0.49}_{-0.42} \cdot 10^{-12}$	$0.80^{+0.02}_{-0.02}$	$0.37^{+0.01}_{-0.01}$	$0.71^{+0.06}_{-0.05}$
NGC 4486	1.23	0.0043	11 ± 1	2.24 ± 0.03	$1.16^{+0.02}_{-0.02} \cdot 10^{-12}$	$6.18^{+0.26}_{-0.26} \cdot 10^{-11}$	$0.78^{+0.03}_{-0.03}$	$0.23^{+0.01}_{-0.01}$	$0.63^{+0.12}_{-0.16}$
NGC 4552	2.72	0.0011	7 ± 2	1.9	$9.86^{+0.46}_{-0.51} \cdot 10^{-14}$	$6.52^{+0.48}_{-0.47} \cdot 10^{-13}$	$1.18^{+0.07}_{-0.06}$	$1.95^{+0.39}_{-0.42}$	$0.68^{+0.44}_{-0.21}$
NGC 4636	1.82	0.0031	0	1.9	$7.52^{+1.33}_{-1.80} \cdot 10^{-15}$	$5.83^{+0.41}_{-0.38} \cdot 10^{-12}$	$0.32^{+0.48}_{-0.09}$	$0.17^{+0.05}_{-0.09}$	$0.51^{+0.05}_{-0.04}$
NGC 4649	2.02	0.0037	0	1.9	$6.07^{+2.29}_{-2.37} \cdot 10^{-15}$	$2.14^{+0.01}_{-0.01} \cdot 10^{-12}$	$1.29^{+0.04}_{-0.04}$	$0.36^{+0.02}_{-0.02}$	$1.23^{+0.09}_{-0.08}$
NGC 4696	7.78	0.0099	0	1.9	$3.96^{+2.05}_{-2.05} \cdot 10^{-15}$	$1.28^{+0.01}_{-0.02} \cdot 10^{-11}$	$0.83^{+0.12}_{-0.12}$	$0.26^{+0.11}_{-0.10}$	$0.43^{+0.10}_{-0.07}$
NGC 4778	3.86	0.0147	0	1.9	$5.06^{+2.17}_{-2.19} \cdot 10^{-15}$	$1.48^{+0.32}_{-0.34} \cdot 10^{-12}$	$0.71^{+0.04}_{-0.04}$	$0.26^{+0.03}_{-0.03}$	$0.60^{+0.20}_{-0.13}$
NGC 5044	4.92	0.0093	69 ± 20	1.9	$3.22^{+0.22}_{-0.21} \cdot 10^{-14}$	$2.10^{+0.16}_{-0.12} \cdot 10^{-11}$	$0.73^{+0.05}_{-0.05}$	$0.42^{+0.07}_{-0.08}$	$0.46^{+0.07}_{-0.06}$
NGC 5813	4.29	0.0065	0	2.13 ± 0.17	$1.17^{+0.12}_{-0.12} \cdot 10^{-14}$	$4.66^{+0.14}_{-0.16} \cdot 10^{-12}$	$0.59^{+0.10}_{-0.10}$	$0.20^{+0.03}_{-0.03}$	$0.53^{+0.12}_{-0.09}$
NGC 5846	4.31	0.0057	0	1.9	$2.28^{+0.37}_{-0.37} \cdot 10^{-14}$	$2.71^{+0.01}_{-0.01} \cdot 10^{-12}$	$0.77^{+0.04}_{-0.04}$	$0.18^{+0.01}_{-0.01}$	$0.46^{+0.06}_{-0.05}$
NGC 6166	0.79	0.0304	0	1.9	$2.68^{+0.40}_{-0.42} \cdot 10^{-14}$	$3.46^{+1.18}_{-1.05} \cdot 10^{-12}$	$1.12^{+0.09}_{-0.08}$	$0.13^{+0.03}_{-0.02}$	$0.99^{+0.31}_{-0.24}$

^a The galactic hydrogen density columns n_{H} were fixed to the values obtained from the HEASARC database (H4PI Collaboration et al., 2016).

Table 4.2: Central thermodynamic properties obtained from spectral fitting: hydrogen density column n_{H} , redshift z , redshifted hydrogen density column $n_{\text{H},z}$, powerlaw index of the central point source Γ , X-ray flux (0.5 – 7.0 keV) of the central powerlaw component, X-ray flux (0.5 – 7.0 keV) of the thermal component within the cooling radius, temperature of the innermost radial bin kT , electron density at the Bondi radius $n_e(r_{\text{B}})$, abundance of the innermost radial bin Z . All uncertainties are stated at the 68.3% confidence level (1- σ).

Galaxy	$p(r_B)$ (keV cm $^{-3}$)	$K(r_B)$ (keV cm 2)	α_K	α_{n_e}	t_{cool} $/ t_{\text{ff, ISO}}$	min	t_{cool} $/ t_{\text{ff, HE}}$	min	r_{cool} (kpc)	c_s (km s $^{-1}$)	r_B (pc)	\dot{M}_B (M_\odot / yr)
IC 4296	$0.70^{+0.11}_{-0.12}$	$0.57^{+0.08}_{-0.08}$	1.07	0.81	$9.8^{+1.5}_{-1.5}$	$7.2^{+1.1}_{-1.1}$	3.9 ± 1.5	401^{+10}_{-11}	70^{+18}_{-14}	$5.1^{+3.9}_{-2.3} \cdot 10^{-2}$		
NGC 507	$0.62^{+0.06}_{-0.06}$	$0.97^{+0.08}_{-0.08}$	0.60	1.03	$13.6^{+1.2}_{-1.2}$	$11.5^{+0.2}_{-0.2}$	5.0 ± 1.9	458^{+8}_{-8}	88^{+28}_{-21}	$6.3^{+5.4}_{-2.9} \cdot 10^{-2}$		
NGC 708	$0.16^{+0.02}_{-0.02}$	$3.14^{+0.38}_{-0.39}$	0.93	0.34	$7.5^{+0.3}_{-0.3}$	$7.8^{+0.3}_{-0.3}$	8.7 ± 1.9	497^{+19}_{-19}	17^{+4}_{-3}	$5.7^{+3.9}_{-2.3} \cdot 10^{-4}$		
NGC 1316	$0.28^{+0.05}_{-0.06}$	$1.19^{+0.20}_{-0.23}$	0.78	0.37	$10.7^{+1.1}_{-1.1}$	$8.9^{+1.1}_{-1.1}$	8.2 ± 1.2	417^{+27}_{-34}	8^{+3}_{-2}	$2.9^{+2.9}_{-1.5} \cdot 10^{-4}$		
NGC 1399	$0.58^{+0.04}_{-0.04}$	$1.71^{+0.10}_{-0.10}$	0.81	0.32	$17.0^{+0.8}_{-0.8}$	$12.4^{+0.6}_{-0.6}$	4.1 ± 0.8	534^{+8}_{-7}	38^{+17}_{-20}	$9.4^{+11.4}_{-7.3} \cdot 10^{-3}$		
NGC 1407	$0.14^{+0.02}_{-0.02}$	$3.37^{+0.40}_{-0.36}$	1.05	0.92	$26.2^{+3.4}_{-3.4}$	$25.1^{+3.2}_{-3.2}$	4.0 ± 1.7	494^{+7}_{-7}	164^{+31}_{-19}	$4.7^{+2.7}_{-1.5} \cdot 10^{-2}$		
NGC 1600	$0.12^{+0.01}_{-0.01}$	$4.47^{+0.54}_{-0.43}$	1.26	0.54	$20.6^{+1.3}_{-1.3}$	$15.4^{+0.9}_{-0.9}$	5.0 ± 1.5	521^{+18}_{-19}	539^{+94}_{-80}	$4.1^{+1.7}_{-1.4} \cdot 10^{-1}$		
NGC 4261	$0.75^{+0.03}_{-0.03}$	$0.65^{+0.02}_{-0.02}$	1.19	1.09	$9.5^{+0.4}_{-0.4}$	$10.0^{+0.4}_{-0.4}$	4.0 ± 1.7	421^{+4}_{-4}	81^{+21}_{-13}	$7.1^{+4.4}_{-2.2} \cdot 10^{-2}$		
NGC 4374	$0.15^{+0.07}_{-0.05}$	$1.10^{+0.46}_{-0.35}$	1.11	0.30	$14.6^{+3.0}_{-3.0}$	$8.1^{+2.6}_{-2.6}$	4.5 ± 0.9	358^{+60}_{-38}	62^{+24}_{-21}	$9.9^{+12.0}_{-6.2} \cdot 10^{-3}$		
NGC 4472	$0.30^{+0.01}_{-0.01}$	$1.55^{+0.06}_{-0.06}$	1.02	0.42	$16.1^{+0.5}_{-0.5}$	$11.7^{+0.2}_{-0.2}$	4.5 ± 0.7	454^{+7}_{-7}	106^{+28}_{-11}	$4.4^{+2.9}_{-1.0} \cdot 10^{-2}$		
NGC 4486	$0.18^{+0.01}_{-0.01}$	$2.05^{+0.11}_{-0.11}$	0.65	0.20	$15.0^{+0.9}_{-0.9}$	$9.3^{+0.1}_{-0.1}$	9.4 ± 0.9	448^{+9}_{-10}	208^{+88}_{-92}	$1.1^{+1.1}_{-0.7} \cdot 10^{-1}$		
NGC 4552	$2.30^{+0.48}_{-0.51}$	$0.76^{+0.14}_{-0.13}$	1.29	1.06	$13.0^{+1.5}_{-1.5}$	$12.2^{+1.4}_{-1.4}$	5.5 ± 0.9	550^{+14}_{-14}	14^{+3}_{-2}	$5.1^{+3.2}_{-2.2} \cdot 10^{-3}$		
NGC 4636	$0.05^{+0.08}_{-0.03}$	$1.06^{+1.64}_{-0.40}$	0.85	0.16	$6.8^{+0.2}_{-0.2}$	$6.8^{+0.1}_{-0.1}$	8.7 ± 0.9	286^{+168}_{-45}	35^{+20}_{-23}	$1.4^{+2.4}_{-1.2} \cdot 10^{-3}$		
NGC 4649	$0.46^{+0.03}_{-0.03}$	$2.56^{+0.13}_{-0.13}$	0.98	0.48	$22.1^{+0.7}_{-0.7}$	$19.4^{+0.6}_{-0.6}$	4.1 ± 0.5	577^{+10}_{-9}	122^{+32}_{-30}	$7.2^{+4.6}_{-3.3} \cdot 10^{-2}$		
NGC 4696	$0.21^{+0.10}_{-0.09}$	$2.05^{+0.73}_{-0.79}$	1.14	0.18	$6.8^{+0.2}_{-0.2}$	$5.2^{+0.5}_{-0.5}$	8.9 ± 1.8	464^{+32}_{-35}	36^{+14}_{-10}	$3.5^{+5.8}_{-2.3} \cdot 10^{-3}$		
NGC 4778	$0.19^{+0.03}_{-0.03}$	$1.73^{+0.21}_{-0.20}$	0.94	0.55	$10.3^{+0.7}_{-0.7}$	$8.8^{+1.0}_{-1.0}$	13.4 ± 2.5	428^{+11}_{-12}	39^{+11}_{-8}	$4.1^{+3.2}_{-1.8} \cdot 10^{-3}$		
NGC 5044	$0.30^{+0.05}_{-0.06}$	$1.31^{+0.23}_{-0.20}$	0.48	0.51	$5.2^{+0.3}_{-0.2}$	$1.6^{+0.1}_{-0.1}$	33.9 ± 4.9	433^{+14}_{-15}	10^{+7}_{-4}	$4.3^{+9.0}_{-2.9} \cdot 10^{-4}$		
NGC 5813	$0.12^{+0.03}_{-0.03}$	$1.74^{+0.36}_{-0.36}$	0.72	0.42	$8.1^{+0.4}_{-0.4}$	$7.5^{+0.6}_{-0.6}$	13.8 ± 4.9	389^{+30}_{-34}	40^{+15}_{-10}	$2.9^{+2.9}_{-1.4} \cdot 10^{-3}$		
NGC 5846	$0.14^{+0.01}_{-0.01}$	$2.42^{+0.18}_{-0.18}$	0.73	0.42	$11.0^{+0.5}_{-0.5}$	$9.5^{+0.4}_{-0.4}$	10.7 ± 2.5	446^{+12}_{-13}	48^{+10}_{-8}	$4.2^{+2.2}_{-1.4} \cdot 10^{-3}$		
NGC 6166	$0.15^{+0.03}_{-0.03}$	$4.28^{+0.67}_{-0.72}$	0.67	0.24	$12.5^{+0.1}_{-0.1}$	$10.3^{+0.4}_{-0.4}$	10.8 ± 3.0	537^{+22}_{-20}	63^{+23}_{-17}	$6.7^{+7.7}_{-3.6} \cdot 10^{-3}$		

Table 4.3: Properties derived from profiles of thermodynamical quantities (Figure A.1, A.4) and basic parameters of the Bondi accretion: central pressure $p(r_B)$, central specific entropy slope α_K at the distance of 1 kpc and higher, central electron density slope α_{n_e} , minimal value of cooling time over free fall time $t_{\text{cool}}/t_{\text{ff}}$ assuming the isothermal sphere, minimal value of cooling time over free fall time $t_{\text{cool}}/t_{\text{ff}}$ assuming the hydrostatic equilibrium, cooling radius r_{cool} , speed of sound in the hot diffuse gas c_s , Bondi radius r_{Bondi} , Bondi accretion rate \dot{M}_{Bondi} .

Galaxy	P_{Bondi} (erg / s)	$P_{\text{jet, radio}}$ (erg / s)	$P_{\text{jet, X-ray, visual}}$ (erg / s)	$P_{\text{jet, X-ray, CADET}}$ (erg / s)	$L_{\text{nuclear, 0.5–7.0 keV}}$ (erg / s)	$L_{\text{cool, 0.5–7.0 keV}}$ (erg / s)	L_{Edd} (erg / s)
IC 4296	$2.9^{+2.2}_{-1.3} \cdot 10^{44}$	$4.3^{+3.6}_{-1.8} \cdot 10^{43}$	$4.6^{+3.5}_{-1.6} \cdot 10^{41}$	$1.5^{+1.1}_{-0.6} \cdot 10^{42}$	$2.0^{+0.2}_{-0.2} \cdot 10^{41}$	$7.0^{+0.3}_{-0.3} \cdot 10^{40}$	$1.6^{+0.3}_{-0.3} \cdot 10^{47}$
NGC 507	$3.6^{+3.1}_{-1.7} \cdot 10^{44}$	$8.0^{+5.8}_{-2.8} \cdot 10^{43}$	$1.5^{+1.2}_{-0.6} \cdot 10^{43}$	$9.5^{+7.5}_{-3.8} \cdot 10^{42}$	-	$1.4^{+0.1}_{-0.1} \cdot 10^{41}$	$2.7^{+0.7}_{-0.6} \cdot 10^{47}$
NGC 708	$3.2^{+2.2}_{-1.3} \cdot 10^{42}$	$8.9^{+6.5}_{-3.1} \cdot 10^{41}$	$9.1^{+6.6}_{-3.2} \cdot 10^{42}$	$1.8^{+1.5}_{-0.8} \cdot 10^{43}$	$3.1^{+1.9}_{-2.0} \cdot 10^{39}$	$1.0^{+0.1}_{-0.1} \cdot 10^{42}$	$6.1^{+0.9}_{-0.8} \cdot 10^{46}$
NGC 1316	$1.6^{+1.6}_{-0.8} \cdot 10^{42}$	$1.7^{+1.3}_{-0.5} \cdot 10^{41}$	$6.8^{+5.1}_{-2.4} \cdot 10^{41}$	$9.4^{+7.3}_{-3.6} \cdot 10^{41}$	$4.2^{+0.2}_{-0.2} \cdot 10^{39}$	$4.8^{+0.3}_{-0.3} \cdot 10^{40}$	$2.1^{+0.4}_{-0.4} \cdot 10^{46}$
NGC 1399	$5.3^{+6.5}_{-4.1} \cdot 10^{43}$	$3.4^{+2.4}_{-1.2} \cdot 10^{41}$	$2.8^{+2.0}_{-1.0} \cdot 10^{41}$	$7.6^{+5.5}_{-2.7} \cdot 10^{41}$	$5.4^{+2.2}_{-2.2} \cdot 10^{38}$	$1.2^{+0.5}_{-0.4} \cdot 10^{41}$	$1.6^{+0.7}_{-0.8} \cdot 10^{47}$
NGC 1407	$2.6^{+1.5}_{-0.8} \cdot 10^{44}$	$1.3^{+1.0}_{-0.5} \cdot 10^{42}$	$1.7^{+1.4}_{-0.7} \cdot 10^{42}$	$1.1^{+0.9}_{-0.5} \cdot 10^{42}$	$3.8^{+0.5}_{-0.5} \cdot 10^{39}$	$3.6^{+4.8}_{-1.6} \cdot 10^{40}$	$5.9^{+0.9}_{-0.5} \cdot 10^{47}$
NGC 1600	$2.3^{+1.0}_{-0.8} \cdot 10^{45}$	$4.4^{+4.0}_{-2.1} \cdot 10^{42}$	$2.9^{+2.6}_{-1.4} \cdot 10^{42}$	$1.6^{+1.3}_{-0.6} \cdot 10^{42}$	-	$9.7^{+4.0}_{-2.5} \cdot 10^{40}$	$2.1^{+0.2}_{-0.2} \cdot 10^{48}$
NGC 4261	$4.0^{+2.5}_{-1.3} \cdot 10^{44}$	$2.0^{+1.5}_{-0.7} \cdot 10^{43}$	$3.0^{+2.2}_{-1.0} \cdot 10^{41}$	$7.4^{+5.6}_{-2.5} \cdot 10^{42}$	$1.5^{+0.1}_{-0.1} \cdot 10^{41}$	$3.9^{+0.1}_{-0.1} \cdot 10^{40}$	$2.1^{+0.5}_{-0.3} \cdot 10^{47}$
NGC 4374	$5.6^{+6.8}_{-3.5} \cdot 10^{43}$	$2.7^{+2.1}_{-1.1} \cdot 10^{42}$	$8.2^{+6.4}_{-3.2} \cdot 10^{41}$	$1.0^{+0.8}_{-0.4} \cdot 10^{42}$	$3.1^{+0.1}_{-0.1} \cdot 10^{39}$	$3.8^{+0.2}_{-0.2} \cdot 10^{40}$	$1.2^{+0.1}_{-0.1} \cdot 10^{47}$
NGC 4472	$2.5^{+1.6}_{-0.6} \cdot 10^{44}$	$5.0^{+3.5}_{-1.8} \cdot 10^{41}$	$3.3^{+2.7}_{-1.4} \cdot 10^{41}$	$2.2^{+1.6}_{-0.8} \cdot 10^{41}$	$2.1^{+0.4}_{-0.4} \cdot 10^{38}$	$8.1^{+1.6}_{-1.4} \cdot 10^{40}$	$3.2^{+0.7}_{-0.3} \cdot 10^{47}$
NGC 4486	$6.0^{+6.4}_{-4.2} \cdot 10^{44}$	$1.9^{+1.5}_{-0.8} \cdot 10^{43}$	$5.7^{+5.1}_{-2.9} \cdot 10^{42}$	$2.6^{+2.7}_{-1.6} \cdot 10^{42}$	$3.8^{+0.1}_{-0.1} \cdot 10^{40}$	$2.0^{+0.1}_{-0.1} \cdot 10^{42}$	$6.1^{+2.2}_{-2.6} \cdot 10^{47}$
NGC 4552	$2.9^{+1.8}_{-1.2} \cdot 10^{43}$	$9.6^{+7.3}_{-3.2} \cdot 10^{41}$	$9.3^{+7.4}_{-3.7} \cdot 10^{41}$	$1.1^{+0.9}_{-0.4} \cdot 10^{42}$	$3.2^{+0.2}_{-0.2} \cdot 10^{39}$	$2.1^{+0.2}_{-0.2} \cdot 10^{40}$	$6.3^{+0.8}_{-0.7} \cdot 10^{46}$
NGC 4636	$7.6^{+13.5}_{-6.9} \cdot 10^{42}$	$2.8^{+2.3}_{-1.1} \cdot 10^{41}$	$2.2^{+1.6}_{-0.7} \cdot 10^{41}$	$1.6^{+1.2}_{-0.6} \cdot 10^{41}$	$1.9^{+0.3}_{-0.5} \cdot 10^{38}$	$1.5^{+0.1}_{-0.1} \cdot 10^{41}$	$4.2^{+0.5}_{-0.5} \cdot 10^{46}$
NGC 4649	$4.1^{+2.6}_{-1.8} \cdot 10^{44}$	$2.2^{+1.9}_{-1.0} \cdot 10^{41}$	$2.1^{+1.5}_{-0.7} \cdot 10^{41}$	$1.5^{+1.0}_{-0.5} \cdot 10^{41}$	$2.0^{+0.7}_{-0.8} \cdot 10^{38}$	$7.0^{+0.1}_{-0.1} \cdot 10^{40}$	$5.9^{+1.3}_{-1.3} \cdot 10^{47}$
NGC 4696	$2.0^{+3.3}_{-1.3} \cdot 10^{43}$	$4.6^{+3.4}_{-1.6} \cdot 10^{42}$	$1.4^{+1.0}_{-0.5} \cdot 10^{43}$	$1.3^{+1.0}_{-0.5} \cdot 10^{43}$	$8.6^{+4.4}_{-4.4} \cdot 10^{38}$	$2.8^{+0.1}_{-0.1} \cdot 10^{42}$	$1.1^{+0.2}_{-0.2} \cdot 10^{47}$
NGC 4778	$2.3^{+1.8}_{-1.0} \cdot 10^{43}$	$8.3^{+6.2}_{-3.1} \cdot 10^{41}$	$6.9^{+6.0}_{-3.1} \cdot 10^{41}$	$3.9^{+3.1}_{-1.6} \cdot 10^{41}$	$2.7^{+1.1}_{-1.1} \cdot 10^{39}$	$7.7^{+1.7}_{-1.8} \cdot 10^{41}$	$1.1^{+0.2}_{-0.2} \cdot 10^{47}$
NGC 5044	$2.4^{+5.1}_{-1.6} \cdot 10^{42}$	$1.5^{+1.1}_{-0.5} \cdot 10^{41}$	$2.2^{+1.7}_{-0.7} \cdot 10^{41}$	$3.7^{+3.0}_{-1.3} \cdot 10^{41}$	$4.0^{+0.3}_{-0.3} \cdot 10^{39}$	$2.6^{+0.2}_{-0.1} \cdot 10^{42}$	$2.8^{+1.5}_{-0.9} \cdot 10^{46}$
NGC 5813	$1.7^{+1.6}_{-0.8} \cdot 10^{43}$	$7.2^{+5.5}_{-2.7} \cdot 10^{41}$	$8.5^{+6.4}_{-3.2} \cdot 10^{41}$	$1.7^{+1.3}_{-0.6} \cdot 10^{42}$	$1.4^{+0.1}_{-0.1} \cdot 10^{39}$	$5.8^{+0.2}_{-0.2} \cdot 10^{41}$	$8.9^{+1.3}_{-1.1} \cdot 10^{46}$
NGC 5846	$2.4^{+1.3}_{-0.8} \cdot 10^{43}$	$1.5^{+1.2}_{-0.6} \cdot 10^{42}$	$8.1^{+7.5}_{-4.0} \cdot 10^{41}$	$1.2^{+1.3}_{-0.8} \cdot 10^{42}$	$1.7^{+0.3}_{-0.3} \cdot 10^{39}$	$2.0^{+0.1}_{-0.1} \cdot 10^{41}$	$1.4^{+0.2}_{-0.2} \cdot 10^{47}$
NGC 6166	$3.8^{+4.4}_{-2.0} \cdot 10^{43}$	$9.5^{+7.2}_{-3.5} \cdot 10^{42}$	$1.4^{+1.0}_{-0.5} \cdot 10^{43}$	$1.9^{+1.4}_{-0.7} \cdot 10^{43}$	$5.0^{+0.7}_{-0.8} \cdot 10^{40}$	$6.5^{+2.2}_{-2.0} \cdot 10^{42}$	$2.7^{+0.7}_{-0.6} \cdot 10^{47}$

Table 4: Resulting power estimates; Bondi accretion power P_{Bondi} , mechanical jet power determined from radio lobes $P_{\text{jet, radio}}$, mechanical jet power determined manually from X-ray cavities $P_{\text{jet, X-ray, visual}}$, mechanical jet power determined from X-ray cavities using CADET $P_{\text{jet, X-ray, CADET}}$, nuclear (powerlaw) luminosity L_{nuclear} and Eddington luminosity L_{Edd} .

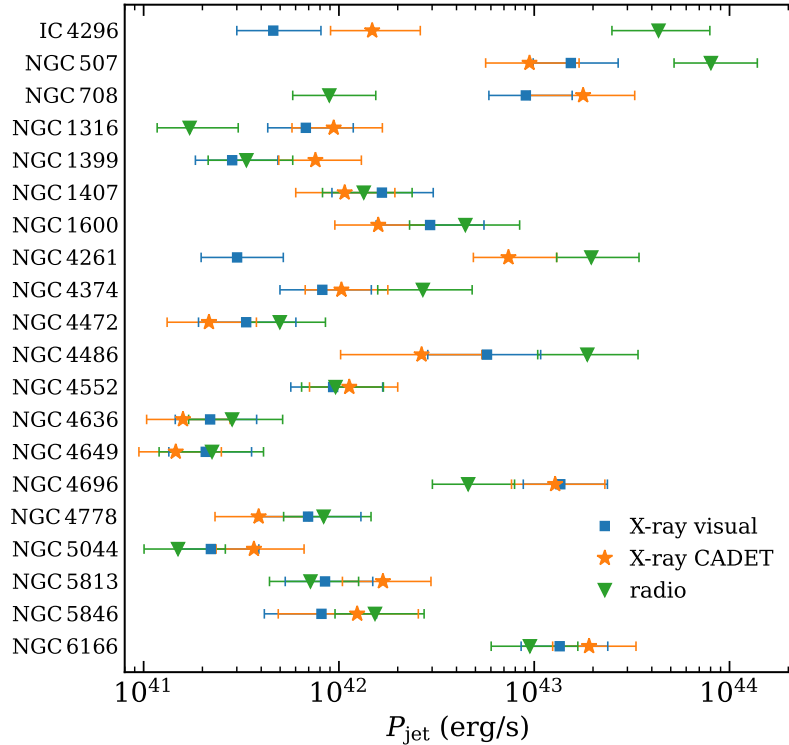


Figure 4.1: Comparison of mechanical jet powers calculated from visually estimated sizes of radio lobes and X-ray cavities or from *CADET* cavity predictions.

The total power output of hot galactic atmospheres was estimated from their cooling luminosity, which was calculated from the flux of the *apec* component when fitted to the thermal emission of the atmosphere from within the cooling radius. The cooling radii of individual galaxies were determined as radii where the cooling time profiles (Figure A.6) reached the value of 1 gigayear (10^9 yr). Values of individual cooling radii and cooling fluxes are stated in Tables 4.3 and 4.2, respectively. The cooling luminosities were calculated similarly as in the case of nuclear luminosities under the assumption of isotropy, the resulting values can be found in Table 4.4 and their connections to other essential parameters were examined in Section 4.2.

4.1 X-ray cavities

The X-ray cavities and radio lobes were size-estimated either visually using the SAOImageDS9 ellipse regions or predicted by the *CADET_size* pipeline and corresponding jet powers were calculated. For all visually estimated cavities, we assumed prolate or oblate ellipsoidal geometry with rotational symmetry along the semi-axis which is closer to the direction towards the centre of the galaxy. The volume of the ellipsoid is given by $V = 4\pi/3 r_l r_w^2$, where r_w (width) is the semi-axis of the ellipsoid which is perpendicular to the direction of the jet, whereas r_l (length) is the semi-axis along that direction. Due to the assumption of the rotational symmetry, we accounted the volume uncertainty of a factor of ~ 2 in the final systematic error of the mechanical power. In the case of cavity predictions obtained using the *CADET* pipeline, the exact cavity shape was utilized for a more accurate determination of the total cavity volume. We only assumed symmetry along the direction from the galactic centre to the centre of the cavity (determined as the centre of mass of the 2D cavity prediction). In other words, the depth of the cavity in every point along that direction was assumed to be equal to its width at that point.

The total enthalpy was numerically integrated on a linearly scaled cartesian grid of pressure, which was interpolated from the pressure profile (Figure A.4) using linear interpolation in log-log space. This approach is more accurate compared to the previously used method which is based on estimating the gas enthalpy $4pV$ only using the exact value of pressure in the centre of the cavity and its total volume. For most prolate cavities and galaxies with a non-smooth pressure profile, it introduced relative changes up to 25 percent, however, for most of the cavities, it was only around 5 percent. For some of the galaxies (NGC 507, NGC 4261), the outer edge of either one or both cavities was outside the measured radial range, for these galaxies the pressure profiles were extrapolated similarly as in the case of interpolation. In the case of IC 4296, the value of gas pressure at the position of the radio lobes was taken from [Grossová et al. \(2019\)](#), which is based on XMM-Newton measurements.

During the pressure integration and also in the case of the cavity age estimation, the distance of the cavity from the galactic centre was calculated purely based on its angular distance and we did not account for any possible projection effects. This might have led to an overestimation of pressure inside cavities and therefore also of the corresponding jet power, however, we did not include any uncertainty factor related to this simplification.

The cavity ages and corresponding jet powers were calculated using both the speed of sound and buoyant velocity and the comparison of these two approaches can be found in the Appendix (Table D.1).

4.1.1 Questionable cavities

The relevance of individual X-ray cavities was checked using photon statistics so that they are really significant surface brightness depressions rather than spurious brightness drops due to low count statistics. However, the real physical nature or extent of individual cavities might be contentious. For many of the innermost X-ray cavities, their reliability is supported also by the corresponding extended radio emission. On the other hand, for some of the cavities the extended radio counterpart is slightly misaligned (e.g. NGC 5044). And for many of the older cavity generations, we observed no radio counterpart in the 1.4 GHz band at all. These radio-faint cavities may probably be the so-called ghost cavities ([McNamara et al., 2001](#)). However, for many of these systems (e.g. NGC 4636, NGC 4778, NGC 5813), signs of extended radio counterparts were observed by the *Giant Metrewave Radio Telescope* (GMRT) at lower radio frequencies (235 – 610 MHz) even for these older generations of X-ray cavities ([Giacintucci et al., 2011](#)).

In the case of IC 4296 and NGC 4261 the first generations of visually found X-ray cavity-like regions are more likely just channels excavated by the jet during the ongoing inflation of the radio lobes and not real cavities. This idea is supported also by the fact that the jet powers calculated from the volumes of X-ray cavities for these two galaxies differ by almost 2 orders of magnitude from the jet powers determined from the volumes of radio lobes (Figure 4.1). For this reason, these two galaxies were not accounted while estimating the correlations between the X-ray cavity jet power and other parameters. We note that the X-ray cavities in these two galaxies detected using the CADET pipeline are also rather contentious and the estimated cavity regions may not reflect the real physical extent of these cavities (see Figure D.1).

For NGC 507 the size of generation 1 northern cavity is also uncertain because on the residual image there is apparent only a concave shape at the inner side of the cavity, the outer edge of the cavity was therefore estimated from the unsharp-masked image. The cavity prediction for NGC 507 produced by the CADET network was also significantly misaligned from the radio emission.

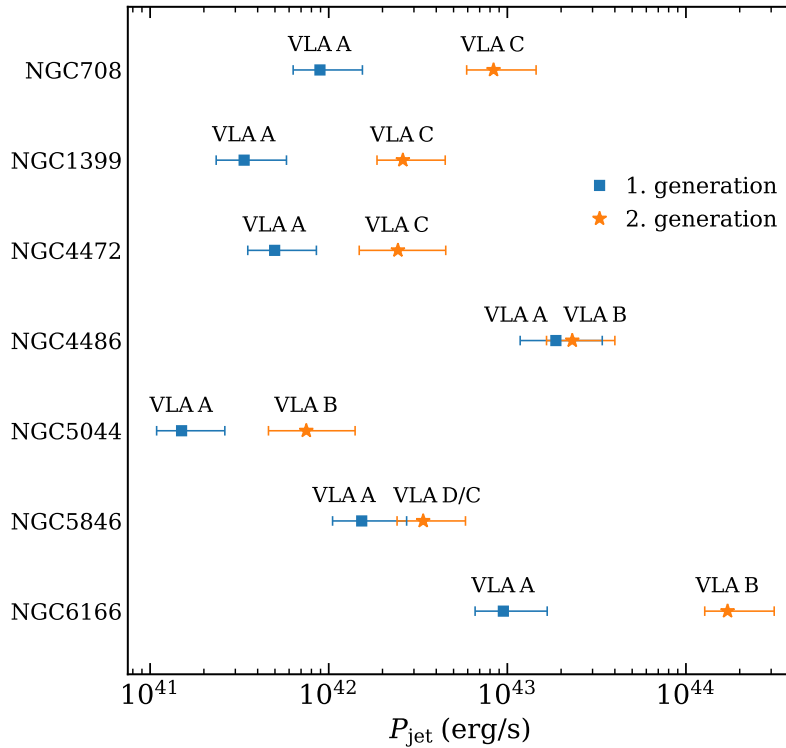


Figure 4.2: Mechanical jet powers of individual generations of radio lobes determined by visual inspection of radio contours. Multiple generations of radio lobes were identified using various VLA array configurations and corresponding configurations are stated above individual data points.

4.1.2 Multiple generations

For some of the systems, we detected multiple generations of X-ray cavities on *Chandra* images (e.g. NGC 5813) and also multiple generations of radio lobes using different VLA configurations (e.g. NGC 4486, NGC 6166). In some cases (NGC 4636, NGC 5044), we even found up to 4 different X-ray cavity generations. The ages of the youngest cavity pairs (denoted as generation 1), for which the inflation is believed to be still ongoing, were calculated from the average speed of sound along the path from the galactic centre into the centre of the cavity. Whereas the ages of all other older generations that have already detached from the AGN were determined under the assumption that they rose buoyantly. The comparison of mechanical jet powers calculated from individual generations of cavities for visually estimated radio lobes and X-ray cavities or X-ray cavities predicted using the *CADET* network is shown in Figure B.12.

Note that for most of the jet powers estimated from the sizes of radio lobes, there is roughly an order of magnitude discrepancy between the individual generations and all of the second generation radio lobes tend to be more powerful (see Figure 4.2). On the other hand, such a strong systematic discrepancy is not observed for X-ray cavities estimated either visually or using the *CADET* network (Figure B.12). The mechanical powers of second-generation cavities are higher than that of the first generation by a factor of 13.9 ± 4.9 for radio lobes, by a factor of 3.7 ± 1.0 for visually estimated X-ray cavities and by a factor of 6.8 ± 2.1 for X-ray cavities estimated using the *CADET* pipeline.

4.1.3 Discovering new cavities

The *CADET_search* pipeline was applied to the whole dataset of elliptical galaxies, which has been used for β -modelling when determining the parameter distributions of beta models (Section 3.2.1). In approximately one half of these systems, the existence of cavities was previously confirmed (most of them were analyzed also manually as described in Section 2.2.2) and for the rest of the galaxies, the eventual existence of X-ray cavities in their atmospheres was unknown.

The original *Chandra* images of all galaxies were analyzed as described in Section 3.2.1. Thereby obtained background-subtracted, exposure-corrected and source-filled images were cropped around the galactic centre in five different realizations: 512×512 pixels with binsize of 4 pixels, 384×384 pixels with binsize of 3 pixels, 256×256 pixels with binsize of 2 pixels, 128×128 pixels with binsize of 1 pixel and 64×64 pixels with binsize of 0.5 pixels. For galaxies with bigger angular sizes (nearby galaxies or large brightest cluster galaxies), we included also realizations with higher down-scaling factors (up to 5 and 6 pixels). The *CADET_search* pipeline was afterwards applied to all of these cropped images and the results are shown in the Appendix (Figure C.1).

Although the discrimination threshold of the *CADET_search* pipeline was set to 90 %, in order to suppress the rate of false-positive detections, the network still tends to produce a significant amount of false-positive cavities, especially when applied to images of galaxies with more complex structures (further discussed in Section 5.4). The network also has considerable difficulties particularly with up-scaled images with a binsize of 0.5 pixels, where it tends to predict many, most probably false positive, cavities.

In order to inhibit the false positive predictions of new cavities in less explored systems, we took as valid only cavity predictions detected on minimally two or more scales (binsizes) and the scale with a binsize of 0.5 pixels was treated very cautiously. The possible inability of the network to resolve more complex structures (mergers, gas sloshing, etc.) was also taken into account while reviewing individual predictions. All thereby obtained more serious cavity candidates were inspected visually (also using residual and unsharp-masked images) and eventually their reliability was checked using photon count statistics (4σ under the surrounding background).

Based on the above-stated approach, we claim the discovery of several new X-ray cavities in the following systems: NGC 499, NGC 3091, NGC 3923, NGC 4125 and NGC 5129, and for the following galaxies the reliability of predicted cavities is rather contentious and further confirmation is needed: NGC 533, NGC 1132, NGC 1860, NGC 2300, NGC 2305, NGC 4406, NGC 4936, NGC 7619. Original images and corresponding predictions for all these galaxies can be found in the Appendix (Figure C.1).

4.2 Correlated quantities

In order to examine the energetics of galactic atmospheres, we searched for correlations between individual input and output power estimates (P_{jet} , P_{Bondi} , L_{Edd} , L_{nuclear} and L_{cool}) and also other underlying parameters (M_{BH} , $\min t_{\text{cool}}/t_{\text{ff}}$, K and α_K). The fitting was performed using a Bayesian approach to linear regression incorporated into the LINMIX package¹ (Kelly, 2007). All fitted quantities were therefore linearized and their uncertainties were recomputed based on laws of error propagation. The correlations were probed both using the LINMIX correlation coefficient between the latent variables (r) and also by the Pearson correlation coefficient (ρ) (Student, 1908). The LINMIX correlation co-

¹<https://github.com/jmeyers314/linmix>

Parameters	Points	LINMIX			Pearson		
		α	β	r	ρ	p-value	
P_{Bondi} vs P_{jet}	all	1.50 ± 0.18	0.67 ± 0.16	0.73	0.58	0.0068	
	H α	1.10 ± 0.22	0.99 ± 0.20	0.87	0.91	$1.5 \cdot 10^{-5}$	
P_{jet} vs M_{\bullet}	all	35.0 ± 4.3	0.79 ± 0.48	0.60	0.45	0.045	
	H α	21.4 ± 8.7	2.36 ± 0.98	0.92	0.87	$9.0 \cdot 10^{-5}$	
$\min t_{\text{cool}}/t_{\text{ff}} - M_{\bullet}$	all	-1.92 ± 0.63	0.33 ± 0.07	0.88	0.76	$9.1 \cdot 10^{-5}$	
	H α	-1.98 ± 1.69	0.33 ± 0.19	0.77	0.64	0.0191	
$P_{\text{jet}} - L_{\text{X-ray, nuclear}}$	all	15.7 ± 7.9	0.67 ± 0.20	0.91	0.80	$7.9 \cdot 10^{-5}$	
	H α	13.3 ± 10.6	0.73 ± 0.27	0.87	0.76	0.0025	

Table 4.5: Fitting parameters for strongly correlated quantities: fitted quantities, fitted points, intercept α , slope β , LINMIX correlation coefficient r , Pearson correlation coefficient ρ and corresponding p-value. The mechanical jet power for all stated correlations were estimated from sizes of radio lobes. For other size-estimating methods (X-ray visual and X-ray CADET) no strong correlations were found.

efficients for individual pairs of quantities are stated inside of each plot, while the fitted parameters (α, β) together with corresponding uncertainties can be found in Table 4.5.

Similarly as [Allen et al. \(2006\)](#), we report a correlation between the Bondi accretion power and mechanical jet power (Figure 4.3). We observed only a mild correlation for mechanical powers of jets estimated from sizes of radio lobes when fitted for all the data points ($r = 0.59$). However, when we examined only galaxies with some signs of cool gas tracers (either nuclear or extended H α emission) we found a strong correlation ($r = 0.91$) between the two quantities.

In order to compare the resulting relation with [Allen et al. \(2006\)](#), we expressed the Bondi powers and jet powers in units of 10^{43} erg/s. This dependency can be described by a linearized powerlaw relation

$$\log \left(\frac{P_{\text{Bondi}}}{10^{43} \text{ erg/s}} \right) = \alpha + \beta \log \left(\frac{P_{\text{jet}}}{10^{43} \text{ erg/s}} \right), \quad (4.1)$$

where $\alpha = 1.10 \pm 0.22$ and $\beta = 0.99 \pm 0.20$. Nevertheless, for mechanical jet power calculated from sizes of X-ray cavities (estimated either visually or using CADET), paradoxically no strong correlations were observed (Figure B.1). Therefore, a considerable discrepancy between the mechanical jet power estimates recovered from sizes of radio lobes and X-ray cavities exists.

Among many other interesting relations, we also found strong correlations between mechanical jet powers and supermassive black hole masses (Figure 4.4), and also between mechanical jet powers and nuclear powerlaw luminosities (Figure 4.7). Their relationships are well described by the powerlaw relations

$$\log \left(\frac{P_{\text{jet}}}{\text{erg/s}} \right) = \alpha + \beta \log \left(\frac{M_{\bullet}}{M_{\odot}} \right), \quad (4.2)$$

and

$$\log \left(\frac{P_{\text{jet}}}{\text{erg/s}} \right) = \alpha + \beta \log \left(\frac{L_{\text{X-ray, nuclear}}}{\text{erg/s}} \right), \quad (4.3)$$

where the α and β parameters together with corresponding correlation coefficients are stated in Table 4.5. The fitting was similarly as in the case of Bondi power – jet power relation performed using the LINMIX package.

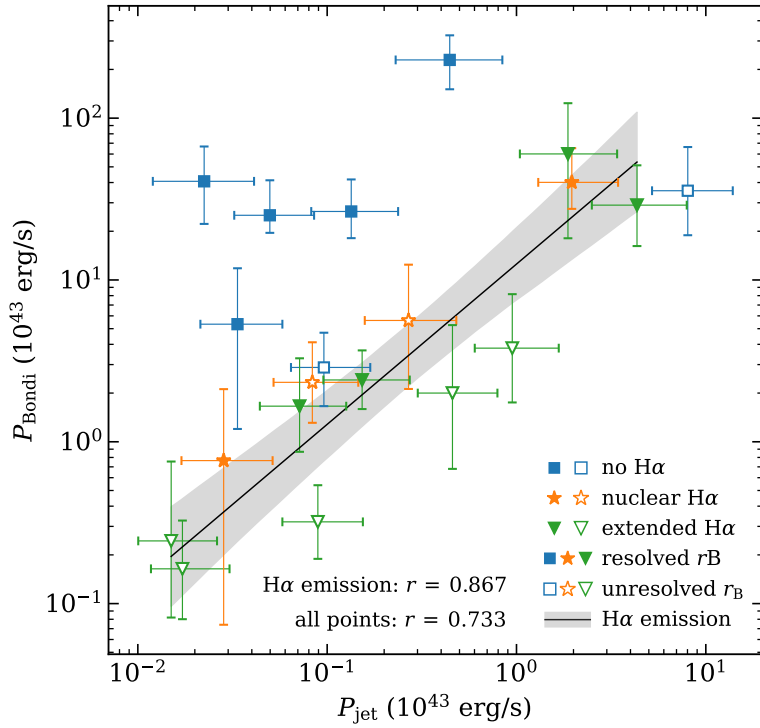


Figure 4.3: Relation between the Bondi accretion power and mechanical jet power estimated from sizes of radio lobes. The black line is the powerlaw fit for galaxies containing cold gas (either extended or nuclear H α emission), while the grey area represents its 1- σ confidence interval sampled from the posterior distribution. Correlation coefficients for individual subsets are stated next to the legend.

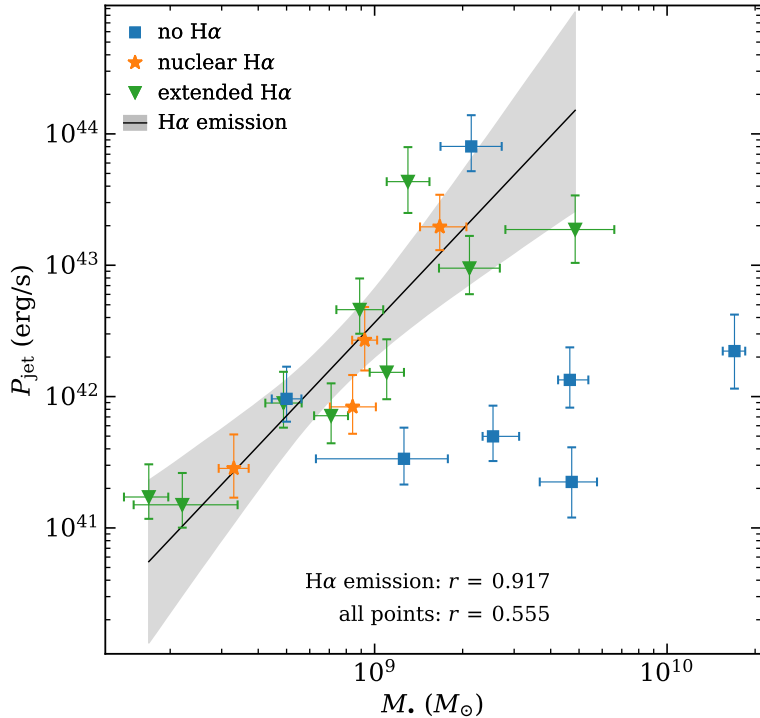


Figure 4.4: Relation between the mechanical jet power determined from the size of radio lobes in VLA observations and the mass of the SMBH. The black line is the powerlaw fit for galaxies containing cold gas (either extended or nuclear H α emission), while the grey area represents its 1- σ confidence interval sampled from the posterior distribution.

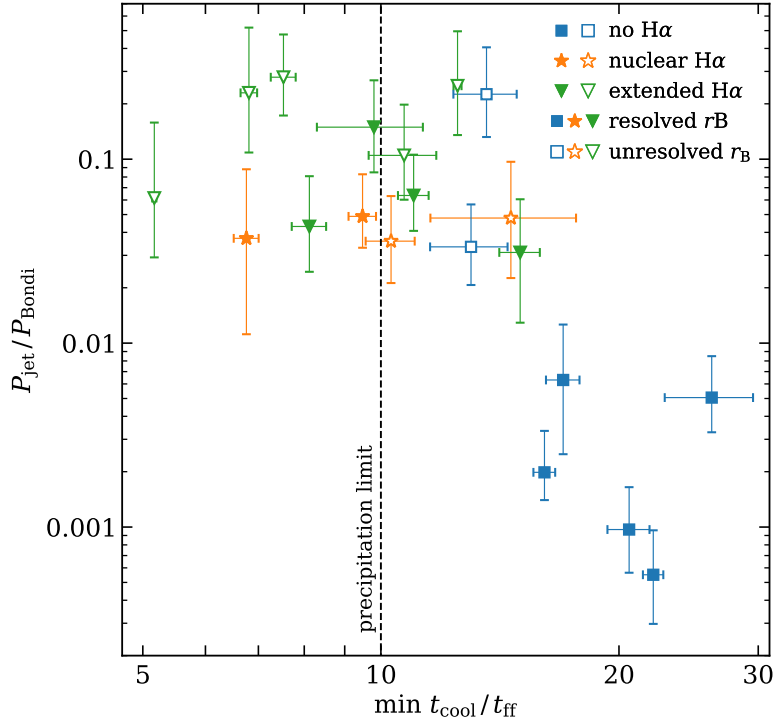


Figure 4.5: Ratio of the jet power of radio lobes to Bondi power versus the minimal value of cooling time over free fall time ratio calculated from the assumption of isothermal sphere. The dashed line represents the precipitation limit of $t_{\text{cool}}/t_{\text{ff}} \approx 10$.

We also probed whether the jet power to Bondi power efficiency is a function of other underlying parameters like those of the central AGN or of the hot galactic atmosphere itself. For galaxies containing signs of H α emission, the jet to Bondi power ratio is constant ($8.3 \pm 7.9\%$ on average) with the increasing mass of the SMBH (Figure B.4), while for the whole sample of galaxies (including galaxies with no H α emission) the ratio decreases approximately as $\propto M_{\bullet}^{-1.18 \pm 0.09}$. Similarly, with the increasing susceptibility of galactic atmospheres to thermal instabilities expressed by the minimal value of the cooling time to free-fall time ratio the jet to Bondi power ratio of H α galaxies is constant, while for the whole sample of galaxies this dependency is decreasing as $\propto \min t_{\text{cool}}/t_{\text{ff}}^{-0.13 \pm 0.04}$ (Figure 4.5). Very similar results were obtained also in the case of jet powers expressed in units of Eddington luminosities (Figure B.6). These consequences show that a positive correlation between the SMBH mass and minimum of the cooling time to free-fall time ratio must exist (Figure 4.6) and can be described by the formula

$$\log(\min t_{\text{cool}}/t_{\text{ff}}) = \alpha + \beta \log \left(\frac{M_{\bullet}}{M_{\odot}} \right). \quad (4.4)$$

In addition, we examined also the relationships of X-ray band luminosities with other relevant quantities. The radiative energy output of the central AGN was approximated by the luminosity of the non-thermal powerlaw component, while the radiative output of the whole atmosphere was estimated from its cooling luminosity (X-ray luminosity of the thermal component within the cooling radius). A strong correlation was found between the mechanical jet power and nuclear luminosity (Figure 4.7). However, paradoxically, no significant relation was observed between nuclear (powerlaw) and cooling luminosities and between mechanical jet powers and cooling luminosities (Figures 4.8 and 4.9).

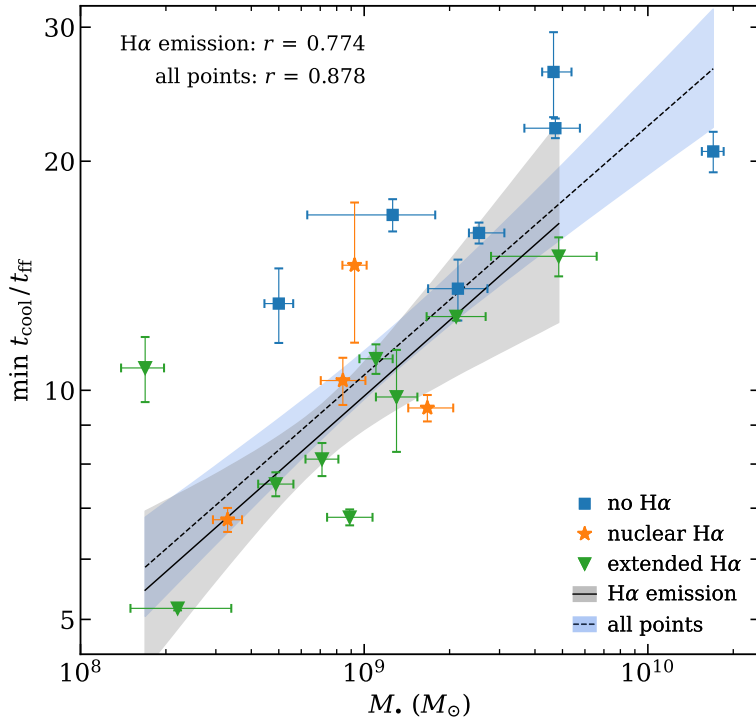


Figure 4.6: Minimal value of the cooling time over free fall time (isothermal sphere) ratio versus the mass of the supermassive black hole. The black (dashed or solid) line are the powerlaw fits, while the gray area represents their 1- σ confidence interval sampled from the posterior distribution.

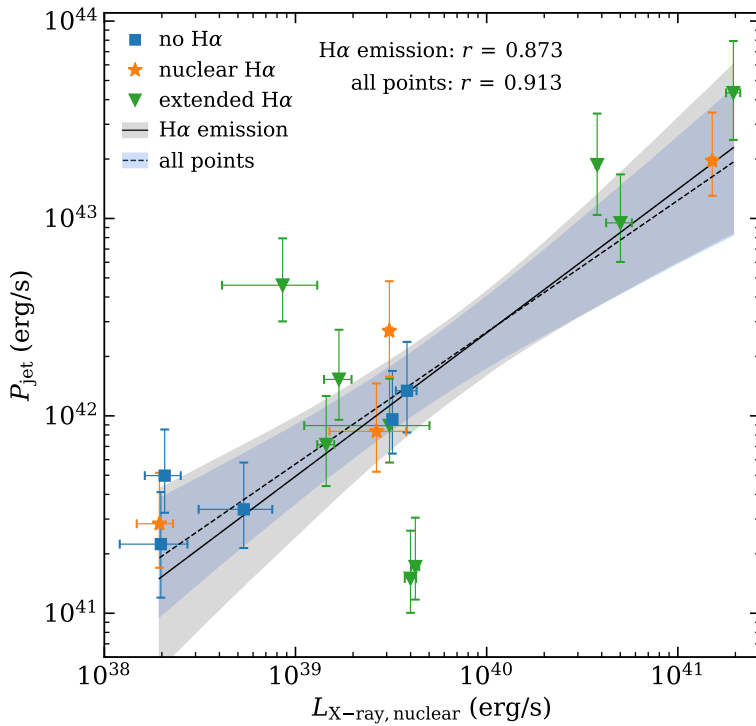


Figure 4.7: Mechanical jet power estimated from sizes of radio lobes versus nuclear luminosity of the non-thermal (powerlaw) component in the 0.5 – 7.0 keV range. The black (dashed or solid) line are the powerlaw fits, while the gray area represents their 1- σ confidence interval sampled from the posterior distribution.

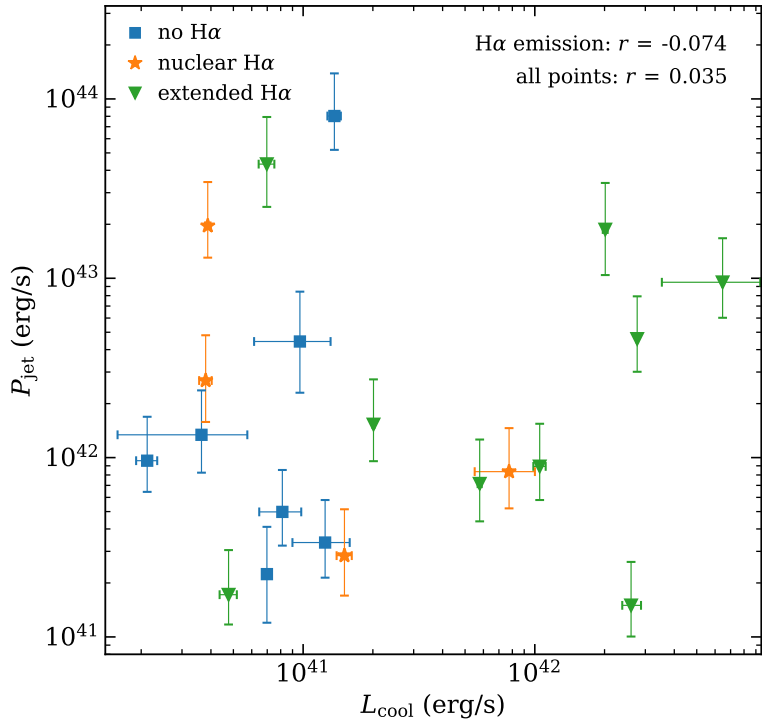


Figure 4.8: Mechanical jet power estimated from sizes of radio lobes versus the cooling luminosity (X-ray luminosity from within the cooling radius) in the 0.5 – 7.0 keV range.

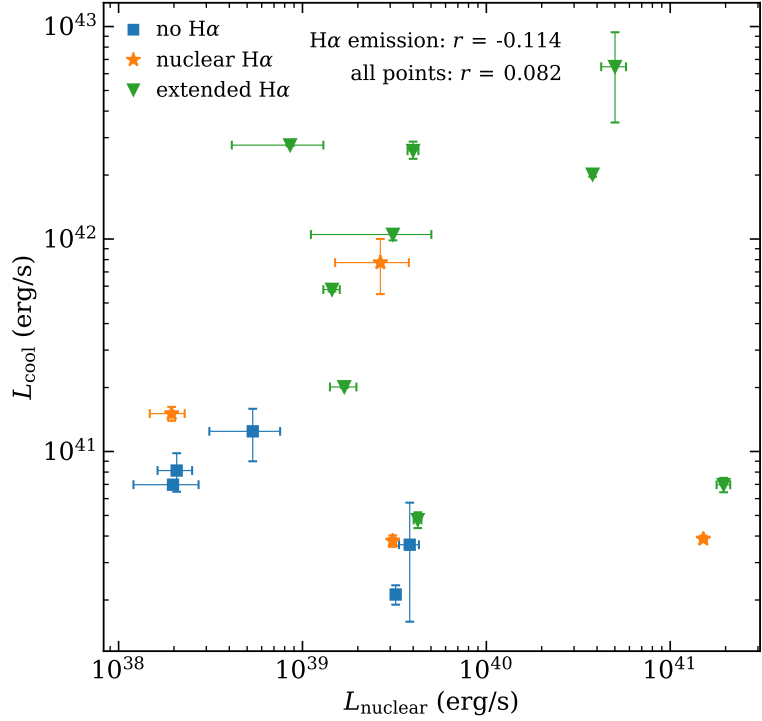


Figure 4.9: Nuclear luminosity of the non-thermal (powerlaw) component range versus cooling luminosity (X-ray luminosity from within the cooling radius) both in the 0.5 – 7.0 keV energy range.

Chapter 5

Discussion

Throughout this Chapter we discuss the most important results obtained from the spectral and imaging analyses of atmospheres of nearby early-type galaxies, groups and clusters. We show the true nature of the observed $P_{\text{Bondi}} - P_{\text{jet}}$ correlation and discuss its implications. In addition, we compare individual mechanical jet power estimating methods and we tackle the possible causes of the observed discrepancies. Besides that, we discuss the most probable sources of errors of the *CAvity DEtection Tool* (CADET) and its possible improvements.

5.1 Bondi power to jet power correlation

We have confirmed the correlation between the Bondi accretion rates and mechanical jet powers, which was previously reported by (Allen et al., 2006). However, we show that the correlation holds only for galactic systems with some signs of cool gas tracers ($\text{H}\alpha + \text{[N II]}$) and for jet powers inferred from sizes of radio lobes. In the case of X-ray cavities estimated either visually or using the CADET pipeline, paradoxically no strong correlations are observed.

As already discussed by Allen et al. (2006), the positive correlation of $P_{\text{Bondi}} - P_{\text{jet}}$ is not a result of the Bondi accretion rates and mechanical jet powers being a function of distances of these galaxies. First of all, the measured distances of these galaxies (except for NGC 6166) are all within an order of magnitude similar. And more importantly, while the Bondi accretion rates depend on the distance approximately as $\propto d^{-0.5}$ (without accounting for the distance dependency of SMBH masses), the mechanical jet powers are proportional to $\propto d^{1.5}$. The observed positive correlation therefore cannot be caused by the dependency on the distance.

Instead, we note that the observed correlation between Bondi and mechanical jet powers is most probably, according to Equation 1.11, a consequence of the observed positive correlation between mechanical jet powers and SMBH masses (Figure 4.4). This is supported by the fact that the Bondi accretion rate is proportional to the mass of the supermassive black hole as $\propto M_{\bullet}^2$, while based on the measured dependence the mechanical jet power is a function of SMBH mass as $P_{\text{jet}} \propto M_{\bullet}^{2.36}$. The Bondi accretion rate depends also on the thermodynamic properties ($K^{-3/2}$) of the gas inside of the Bondi radius, but since the central specific entropy and mechanical jet powers are rather uncorrelated, the dependence of the Bondi accretion power on the central specific entropy does not contribute to the Bondi power – jet power correlation. The observed $P_{\text{Bondi}} - P_{\text{jet}}$ relation is therefore mainly a result of the $P_{\text{jet}} - M_{\bullet}$ correlation.

The ratio of mechanical jet power to Bondi accretion power for nearby galaxies with thermally unstable atmospheres ($\text{H}\alpha$ emission) is approximately constant, whereas for galaxies with no signs of cool gas tracers the efficiency decreases with increasing SMBH mass or cooling time over the free-fall time ratio (Figures 4.5 and B.4). Together with

the previously assumed ten percent efficiency (Equation 1.12) and assuming that the accretion is Bondi-like, the efficiency of converting the rest mass of the accreted material into the energy of relativistic outflows is for H α galaxies slightly less than one percent ($0.83 \pm 0.79\%$).

5.2 Feeding from thermally unstable atmospheres

The fact that we only see a correlation for thermally unstable atmospheres with lower $\min(t_{\text{cool}}/t_{\text{ff}})$ indicates that the black holes producing the jets and lobes are fed by thermally unstable gas from the galactic atmospheres. The ratios of jet powers and the Eddington luminosities inferred for the given black hole masses are within an order of magnitude similar for all these systems (of the order of 10^{-5} of the Eddington luminosity). The scatter in the inferred ratio is remarkably small.

It appears that once the atmosphere becomes thermally unstable, the cooling gas feeds the black hole in the centers of all galaxies at a similar Eddington ratio, possibly indicating a key universal property of black hole accretion in early-type galaxies. The fact that all 13 thermally unstable atmospheres have similar jet powers relative to the inferred Eddington luminosity, indicates that the accretion in early-type galaxies is stable and the accreted cooling gas is relatively uniform and not particularly clumpy.

Interestingly, for 6/7 galaxies with no detected H α emission and thus most likely hosting thermally stable atmospheres, the jet power is of the order $10^{41} - 10^{42}$ erg/s and does not appear to trace the black hole mass. All these galaxies have within the order of magnitude similar stellar populations, and similar stellar masses. We speculate that in these thermally stable atmospheres the stellar mass loss material provides a similar amount of fuel in all these massive galaxies regardless of their central black hole mass, resulting in a similar “floor” jet power of $10^{41} - 10^{42}$ erg/s. Once the atmospheres become thermally unstable, the amount of additional fuel that reaches the black hole and results in jet production will scale with the black hole mass.

[Lakhchaura et al. \(2019\)](#) showed that the average atmospheric gas temperature in giant ellipticals correlates with the mass of the central black hole (see also [Gaspari et al., 2019](#)). By comparing observations and state-of-the-art numerical simulations (Illustris TNG), [Truong et al. \(2021\)](#) shows that this is primarily due to an underlying correlation between the halo mass and the mass of the central supermassive black hole and jet heating will have a secondary effect. Our result shows that more massive black holes will provide more heat to galactic atmospheres (see also [Martín-Navarro et al., 2020](#)), which should also contribute to the correlation between black hole mass and the atmospheric gas temperature.

5.3 Mechanical jet power estimating methods

The energetic output of relativistic outflows of radio mode AGNs was estimated both from sizes of radio lobes filled with relativistic particles and also from volumes of void bubbles (cavities) inflated into the ambient gas by these outflows. In Figure 4.1 we compare the individual visual-based approaches used for radio lobes and X-ray cavities with the CADET pipeline developed for predicting the extent of cavities on original *Chandra* images. Mechanical jet powers of radio lobes are on average by 40 percent higher than powers of visually identified X-ray cavities and by 80 percent higher than the CADET cavity predictions, while their mean absolute differences are 80 percent and 130 percent for visual and CADET estimates, respectively. This systematic discrepancy together with

the observed scatter are the most probable source of the inconsistency between the correlations for the jet powers inferred from radio lobes and X-ray cavities (Figures B.1, B.2 and B.8).

A possible explanation to this phenomenon is that some of the relativistic plasma escapes the cavities, as has been seen e.g. in M84 ([Finoguenov et al., 2008](#)) and thus the radio structure appears larger than the corresponding X-ray cavity. The other possibility is that for some reason we systematically underestimate the cavity sizes in *Chandra* images. In the future, we will investigate this possibility using the *CAvity DEtection Tool* and simulated cavities.

A discrepancy in jet power is observed also for galactic systems with multiple radio lobe or X-ray cavity generations. The older generations of lobes and cavities are on average by almost an order of magnitude more powerful than that of the younger generations. However, we note that the real mechanical powers of older generations of lobes and cavities might be even higher because since there is already a new generation of outflows being formed, the ages calculated from buoyancy velocities do not represent the proper timescale on which the older generation was formed. This effect is even amplified by the fact that as the detached cavities rise adiabatically due to buoyancy forces, a significant amount of their energy is dissipated. The total energy inferred from the $4pV$ formula should therefore decrease with the increasing distance from the galactic centre d and decreasing surrounding pressure as

$$E(d) = E_0 \left[\frac{p(d)}{p_0} \right]^{1-1/\gamma}, \quad (5.1)$$

where E_0 and p_0 are the initial values of energy and pressure, respectively, and γ is the adiabatic coefficient of the ambient gas. For typical parameters of cavities and nearby galaxies, half of the energy is lost when the cavity reaches the distance of ~ 20 kpc from the galactic centre ([Churazov et al., 2002](#)). This indicates that either the jet powers of younger outflows are underestimated because their inflation is still ongoing or that the formula for calculating the jet power is possibly incorrect for the already detached lobes and cavities.

In the case of radio contours, where the difference between the generations is the biggest, the discrepancy may be also partially caused by the fact that the sizes of older generation radio lobes were inferred using VLA configurations with higher beam sizes and therefore with lower spatial resolution, which might have led to an underestimation of their sizes.

5.4 Evaluating the developed CADET pipeline

We report that the utilization of machine learning techniques for detection and size-estimation of X-ray cavities on noisy *Chandra* images provides at least satisfactory results. Although both pipelines were trained purely using elliptical cavity masks (ellipsoidal cavities), they were able to produce arbitrarily shaped cavity predictions, which was utilized in a more accurate determination of the total mechanical jet power ($4pV$). Moreover, while producing the artificial image dataset, we only generated either zero or one pair of X-ray cavities, however, the network is capable of predicting any number (also non-even numbers) of X-ray cavities.

For all the galactic systems with known X-ray cavities that were analyzed manually (Figure D.1), the *CADET_size* network detected correctly most of the cavities. Except for NGC 4261 for which the *CADET_size* cavity prediction differs by almost two orders in jet

power, the average difference between mechanical jet powers inferred from CADET predictions and our manual estimation is approximately 60 %. Based on the visual comparison of *CADET_size* cavity predictions we state that for some of the galaxies the CADET network hardly recognizes the inner parts of cavities (closer to the galactic centre). This is supported also by the resulting mechanical powers of jets, which are in the case of the CADET predictions being slightly underestimated with respect to visually size-estimated X-ray cavities (by approximately 30 %). The possible solution to this problem might be to use beta model or profile-subtracted residual images (or potentially unsharp masked images) instead of the original *Chandra* or *Chandra*-like images for training and inference of the CADET network. Such an approach would, however, require substantial pre-processing procedures and in the case of the β -modelling, it would also be less automatic.

Based on the combination of *CADET_search* predictions, visual inspection of analyzed images and photon count statistics, we claim the discovery of several new X-ray cavities in the following systems: NGC 499, NGC 3091, NGC 3923, NGC 4125 and NGC 5129. For the following galaxies, the reliability of predicted cavities is rather contentious and further confirmation is needed: NGC 533, NGC 1860, NGC 2300, NGC 2305, NGC 4406, NGC 4936, NGC 7619. And for all other galaxies with positive *CADET_search* predictions, the detected “cavities” are believed to be rather spurious false positive detections – mainly for the below discussed reasons.

We note that X-ray cavities in galaxies with more complex central structure (NGC 1600, NGC 4552) are still only poorly discovered by the network and it is therefore unable to properly predict their sizes. The network has also difficulties with finding cavities on images of galaxies with a very steep central surface brightness profile – it tends to predict the cavities to be located around the whole bright central core (e.g. 3C 449, IC 310, IC 4296, NGC 4203 and NGC 5419). The network is unable to resolve jets and similar elongated structures and predicts the cavities to be located on either one or both sides of such structures (e.g. NGC 315, NGC 4696). Another type of hardly analyzable images of galaxies are, as expected, the very distant or faint galaxies with a very low number of counts (e.g. NGC 57, NGC 410, NGC 777, NGC 2305) and galaxies observed only using the ACIS-I chips (also due to spaces between the chips). The proper detection and estimation of the real cavity extent is nearly impossible also for galaxies that are noticeably currently undergoing a merging event (e.g. NGC 741, NGC 1132, NGC 4782, NGC 5419).

Although the outflows and associated radio lobes and X-ray cavities are expected to emerge at random orientations with respect to the observer, throughout this analysis we assumed the lobes and cavities to be located in the plane of the sky. We note that this simplification might have led for many systems to underestimation of cavity distances and therefore to overestimation of their internal pressure and corresponding jet powers. However, we did not include any uncertainties caused by possible projection effects. On the other hand, for X-ray cavities launched at higher angles with respect to the plane of the sky their contrast decreases rapidly with increasing distance from the galactic centre. For a spherical cavity launched at the angle of 45 degrees with respect to the plane of the sky, the detectability declines with distance as d^{-1} , whereas at the angle of 90 degrees as $d^{-2.5}$ ([Enßlin & Heinz, 2002](#)). For the detected cavities, there is therefore a higher chance that they are located very close to the plane of the sky. This idea is supported also by the observed correlation and scatter between cavity sizes and their distances from the galactic centre (Figure 3.6).

Conclusion

We have presented spectral and imaging analysis of *Chandra* X-ray observations accompanied with a visual inspection of VLA radio images of 20 nearby massive early-type galaxies, groups and clusters of galaxies. The profiles of basic thermodynamic properties such as temperature, abundance, electron density, specific entropy and cooling time were obtained and the basic parameters of the Bondi accretion were determined. By comparing individual input and output power estimates with other basic parameters of galactic atmospheres and central AGNs, we detected several important correlations that are having substantial implications for the energetics of galactic atmospheres and the AGN feedback.

In addition, we introduced the developed machine learning pipeline called *CAvity DEtection Tool* (CADET), which was trained for finding and size-estimating the cavities on noisy X-ray images of galaxies. From the combination of visual imaging analyses of *Chandra* or VLA data and the application of the CADET network, we size-estimated 39 pairs of X-ray cavities and 27 pairs of radio lobes. Besides that, the CADET network led to the discovery of 5 pairs of new X-ray cavities in less explored galactic systems, that were further confirmed visually and using photon count statistics.

Mechanical jet power to Bondi power correlation

We have confirmed the correlation between Bondi accretion rate and mechanical jet power that was previously reported by [Allen et al. \(2006\)](#). A strong correlation ($\rho = 0.91$) is detected only for galaxies with thermally unstable atmospheres containing signs of cool gas tracers ($H\alpha + [N\text{ II}]$), while for the whole sample of galaxies (including systems without $H\alpha$ emission) the observed correlation is only mild ($\rho = 0.58$). The obtained relation is well described by the powerlaw model

$$\log \frac{P_{\text{Bondi}}}{10^{43} \text{ erg s}^{-1}} = (1.10 \pm 0.22) + (0.99 \pm 0.20) \log \frac{P_{\text{jet}}}{10^{43} \text{ erg s}^{-1}}, \quad (6.1)$$

where P_{Bondi} and P_{jet} are expressed in units of 10^{43} erg/s. We note that the obtained relation is very close to linear, which indicates that if the accretion really proceeds in the spherical Bondi-like regime, about 0.8 percent of the rest mass of the accreted matter is converted to the observed jet energy.

Figure 4.4 shows that the observed $P_{\text{Bondi}} - P_{\text{jet}}$ relation is a consequence of an underlying correlation between the mechanical jet power and mass of the central supermassive black hole ($P_{\text{jet}} - M_{\bullet}$), while being independent of thermodynamic properties of the ambient gas (specific entropy; Figure B.3). Mechanical jet powers in galaxies with signs of cold gas scale with the supermassive black holes mass as $\propto M_{\bullet}^{2.36}$, while for 6 out of 7 galaxies with no $H\alpha$ emission the jet power is approximately constant ($\sim 10^{42}$ erg/s), and Bondi accretion power scales with the SMBH mass as $\propto M_{\bullet}^2$. The correlation is therefore driven mainly by the supermassive black hole mass.

Utilization of the CADET pipeline

We have shown that the brute force of modern computer technology combined with the state-of-the-art algorithms represented by convolutional neural networks is capable of automation of more complex astronomical tasks such as detecting and estimating the extent of surface brightness depressions (X-ray cavities) on noisy *Chandra* images. The presented machine learning technique has therefore great potential in replacing the manpower for solving this task.

We have built two convolutional pipelines: one for cautious detection of X-ray cavities that can be utilized for finding new X-ray cavities in less explored galactic systems (*CADET_search*) and second for the proper estimation of the real extent of detected cavities (*CADET_size*). Both pipelines are available on the *CADET* GitHub page¹, however, we note that the utilization of the *CADET* network for proper cavity volume estimation is rather experimental – the released pipelines are in the “alpha” version and several below stated upgrades are being planned.

The possible speed-up of the training dataset generation process could be brought up by the utilization of the *Tensorflow* library and Graphical Processing Units (GPUs) for generating the 3D meshgrids, for their rotations and other basic mathematical operations. The training dataset could then possibly be in principle generated “on-the-fly”. Another important planned feature is the ability of inputting nearly arbitrarily sized square-shaped images, that would be automatically rescaled to 128×128 pixels while properly conserving their fluxes – because so far we only used images with proper shapes and sizes, which were at most scaled by various powers of two or integers (0.5, 1, 2, 3 and 4), so that they were compatible with the network’s input shape. Possible improvement in the overall performance and accuracy of the *CADET* network could be brought up by including also various other features while generating the training dataset, especially when superimposed over the cavities. The planned features that are typical for real X-ray images are the point sources, jet-like structures and cold fronts. This could also potentially enable the network to be used on much more non-processed, practically raw *Chandra* images.

¹<https://github.com/tomasplsek/CADET>

Appendix

Appendix A: Radial profiles

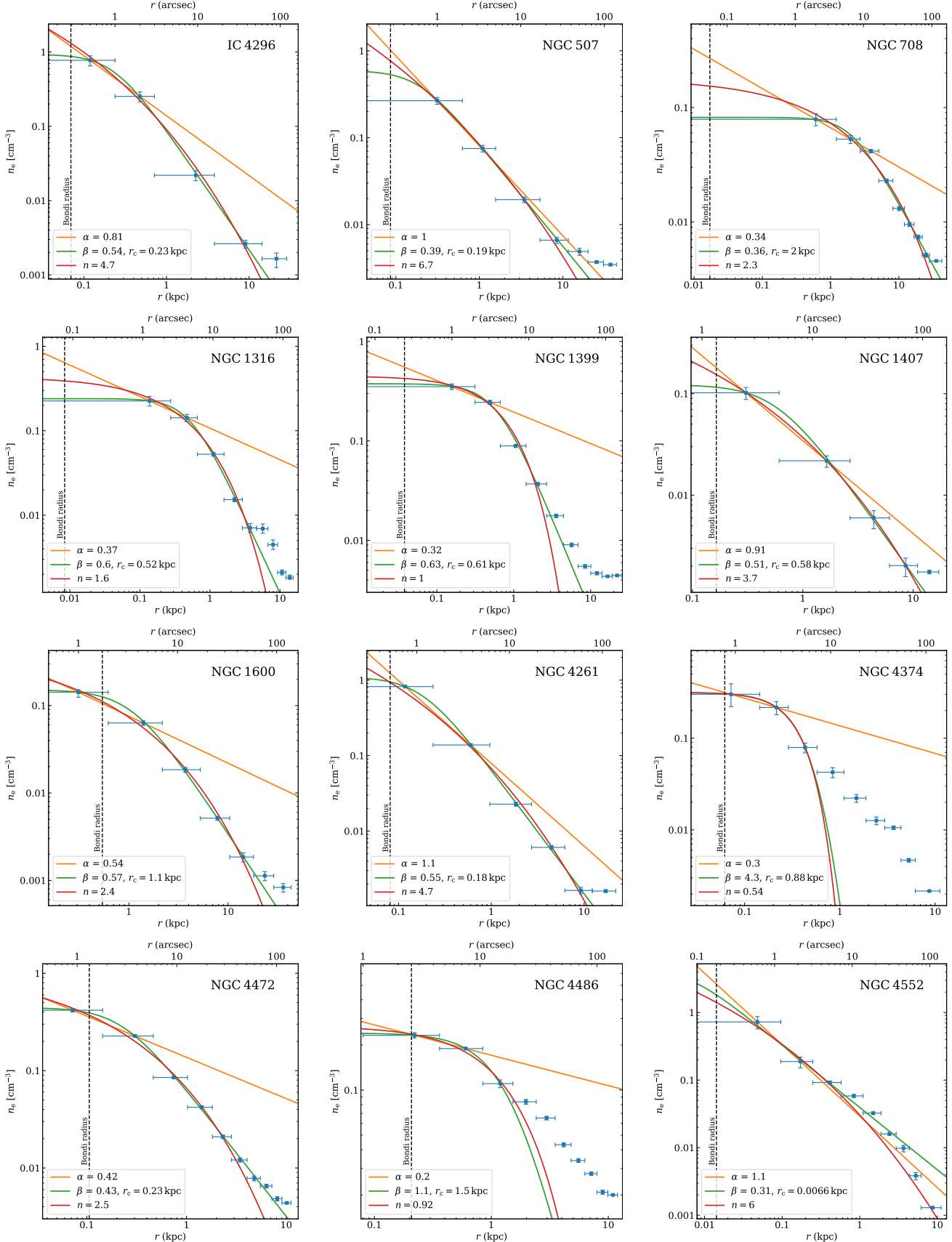


Figure A1: To be continued.

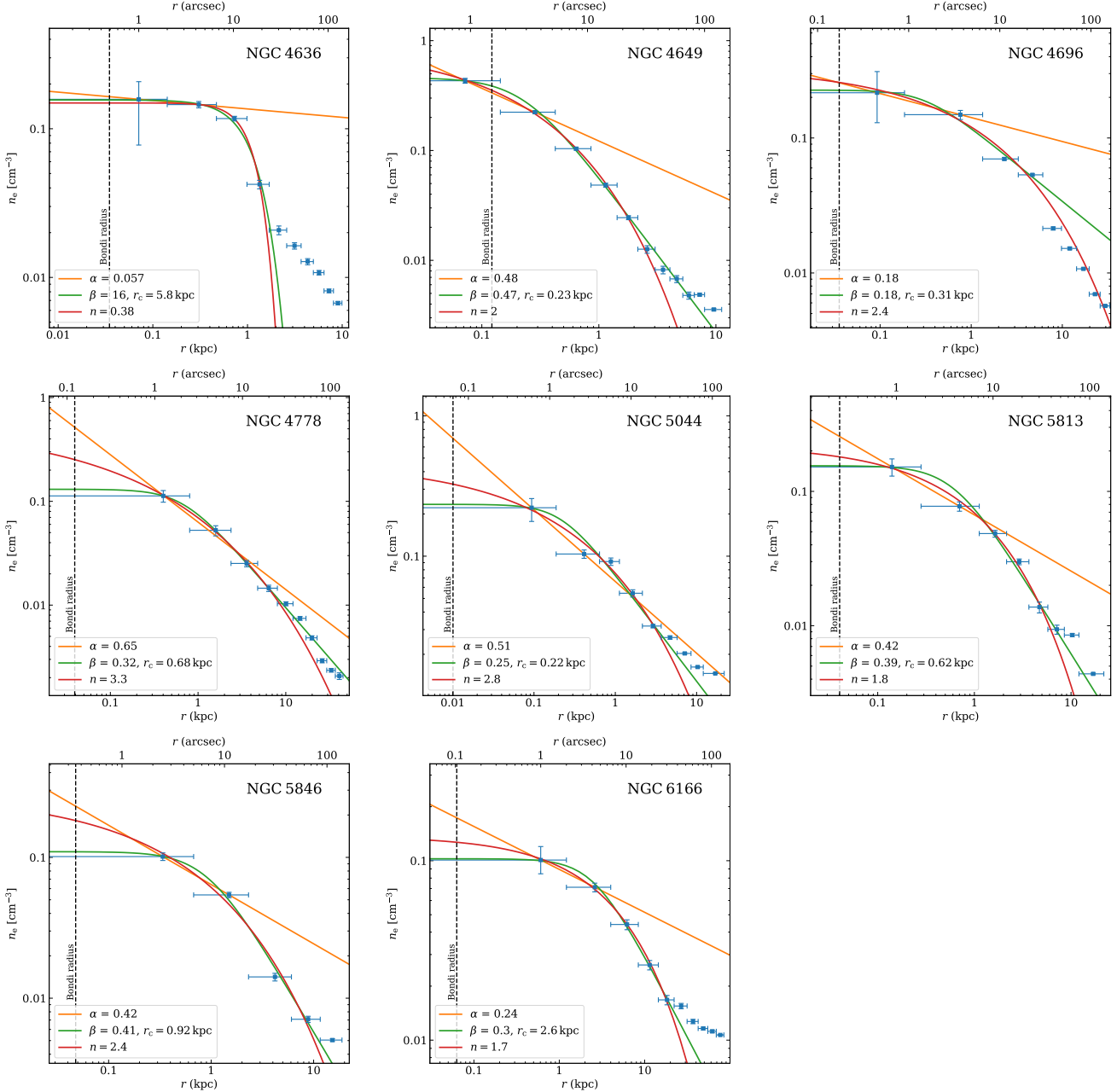


Figure A1: Azimuthally averaged electron density radial profiles for all the analysed galaxies. The vertical dashed lines represents the Bondi radius r_B , to which the electron densities were extrapolated. For the extrapolation, we used three different profiles: powerlaw model (orange lines), beta model (green lines) and sersic profile with freed parameter n (red lines). The final value of electron density at the Bondi radius was calculated as a mean from these three profiles and the scatter was accounted in the uncertainties.

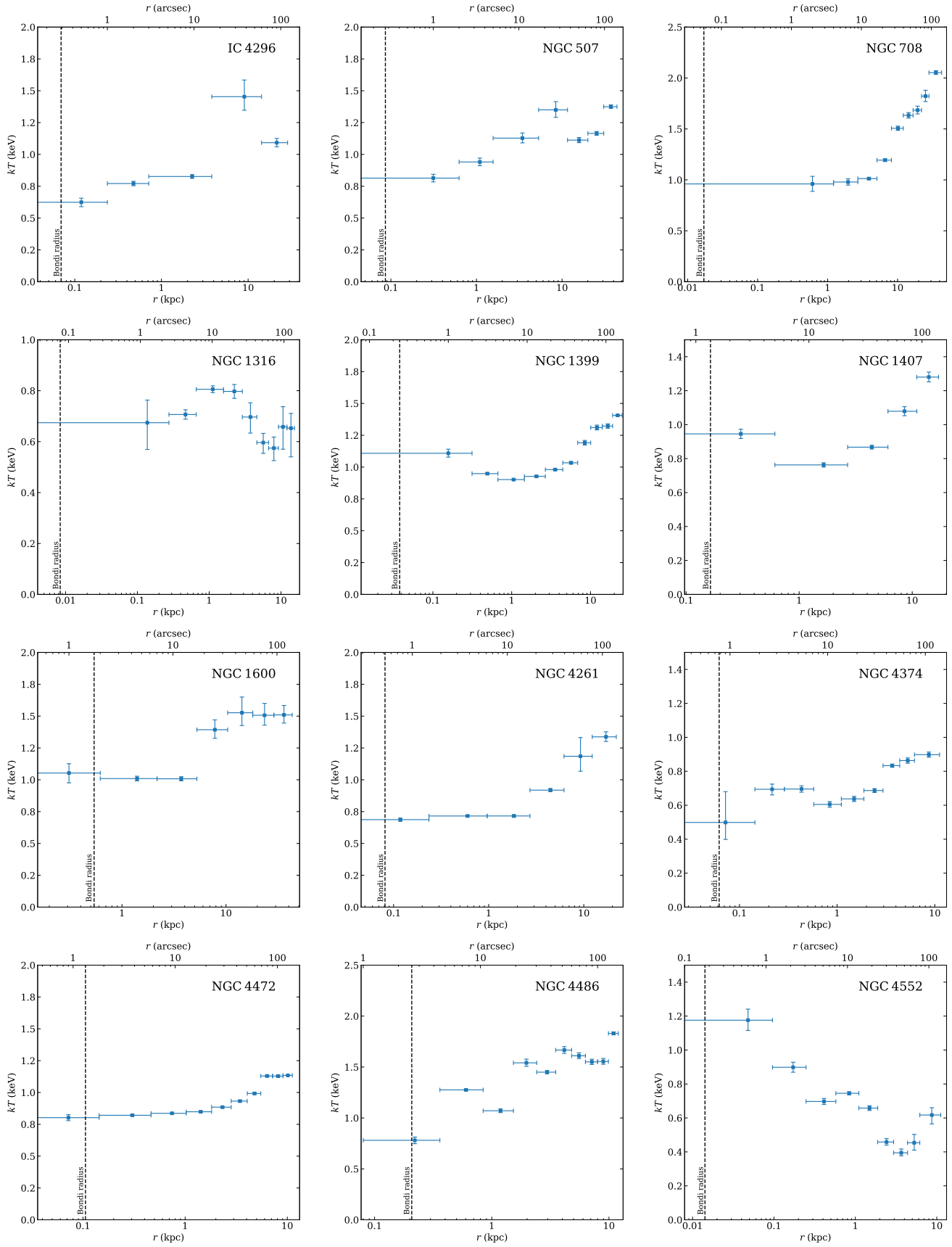


Figure A2: To be continued.

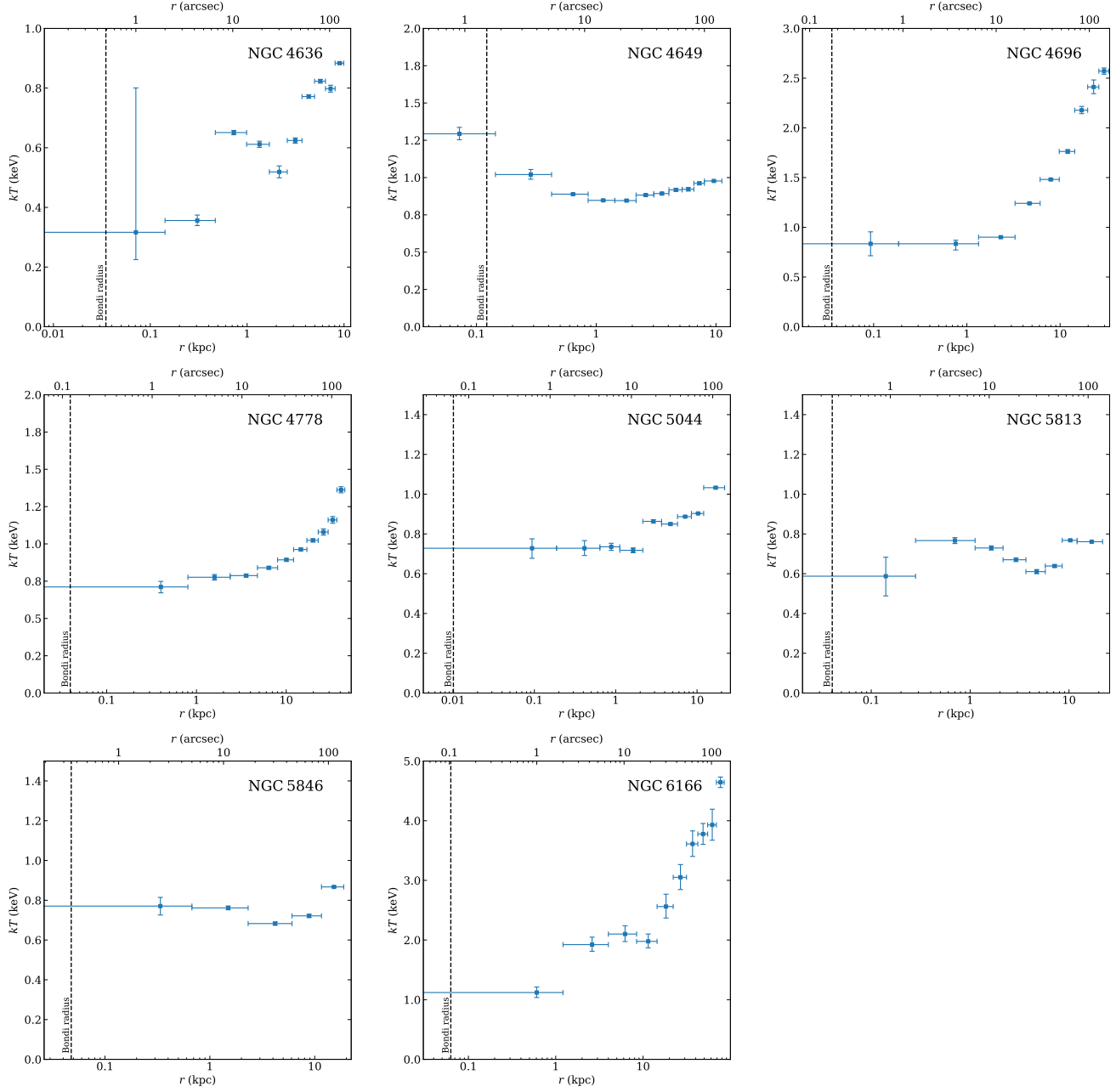


Figure A2: Azimuthally averaged temperature radial profiles for all the analysed galaxies. The vertical dashed lines represents the Bondi radius r_B . The temperature of the gas inside the Bondi radius was assumed to be the same as the temperature of the innermost bin.

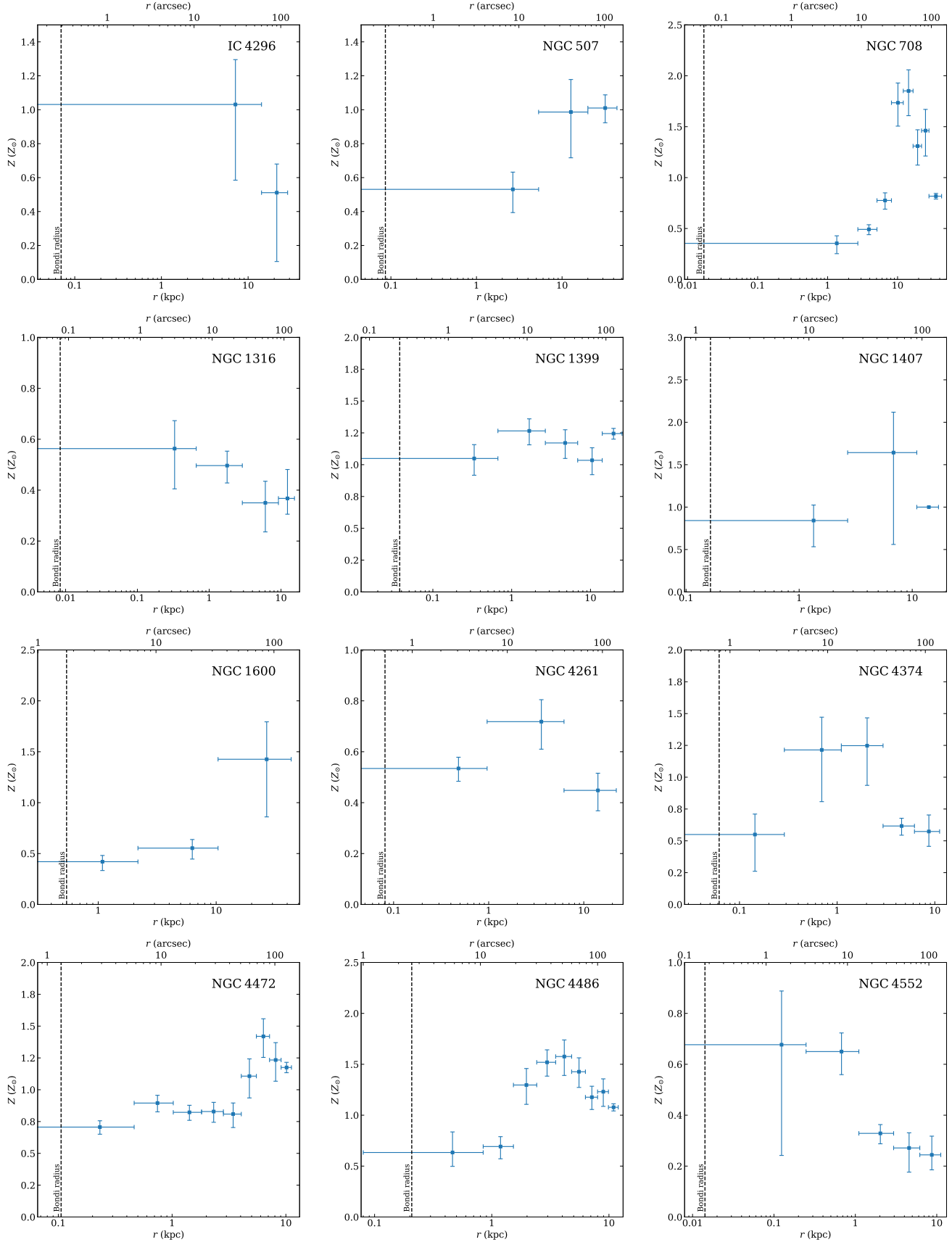


Figure A3: To be continued.

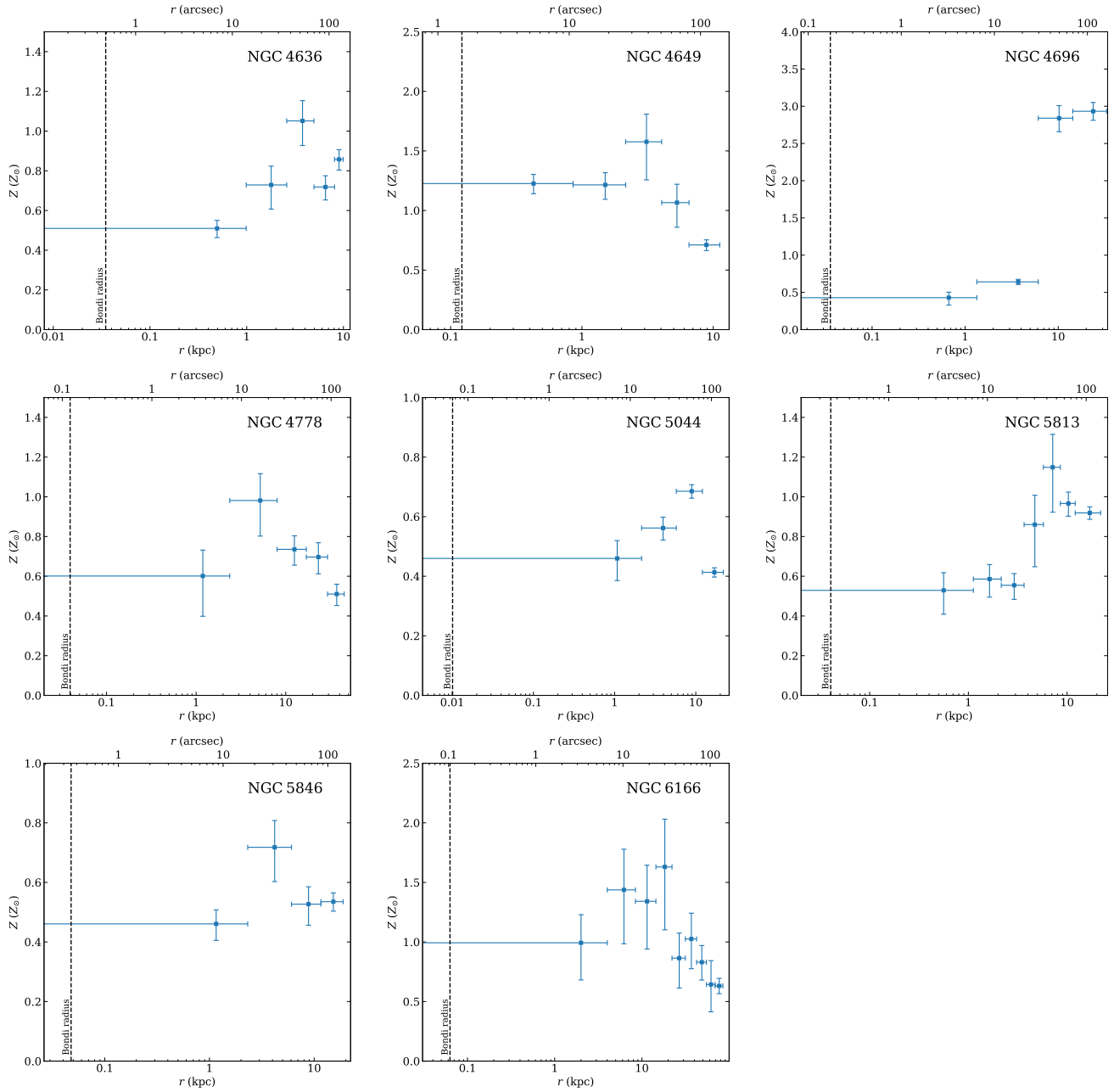


Figure A3: Azimuthally averaged abundance radial profiles for all the analysed galaxies. The vertical dashed line represents the Bondi radius r_B . The abundances are expressed relatively with respect to solar abundance measurements reported by [Lodders \(2003\)](#). For most galaxies, the abundances were tied between 2 or more neighbouring radial bins.

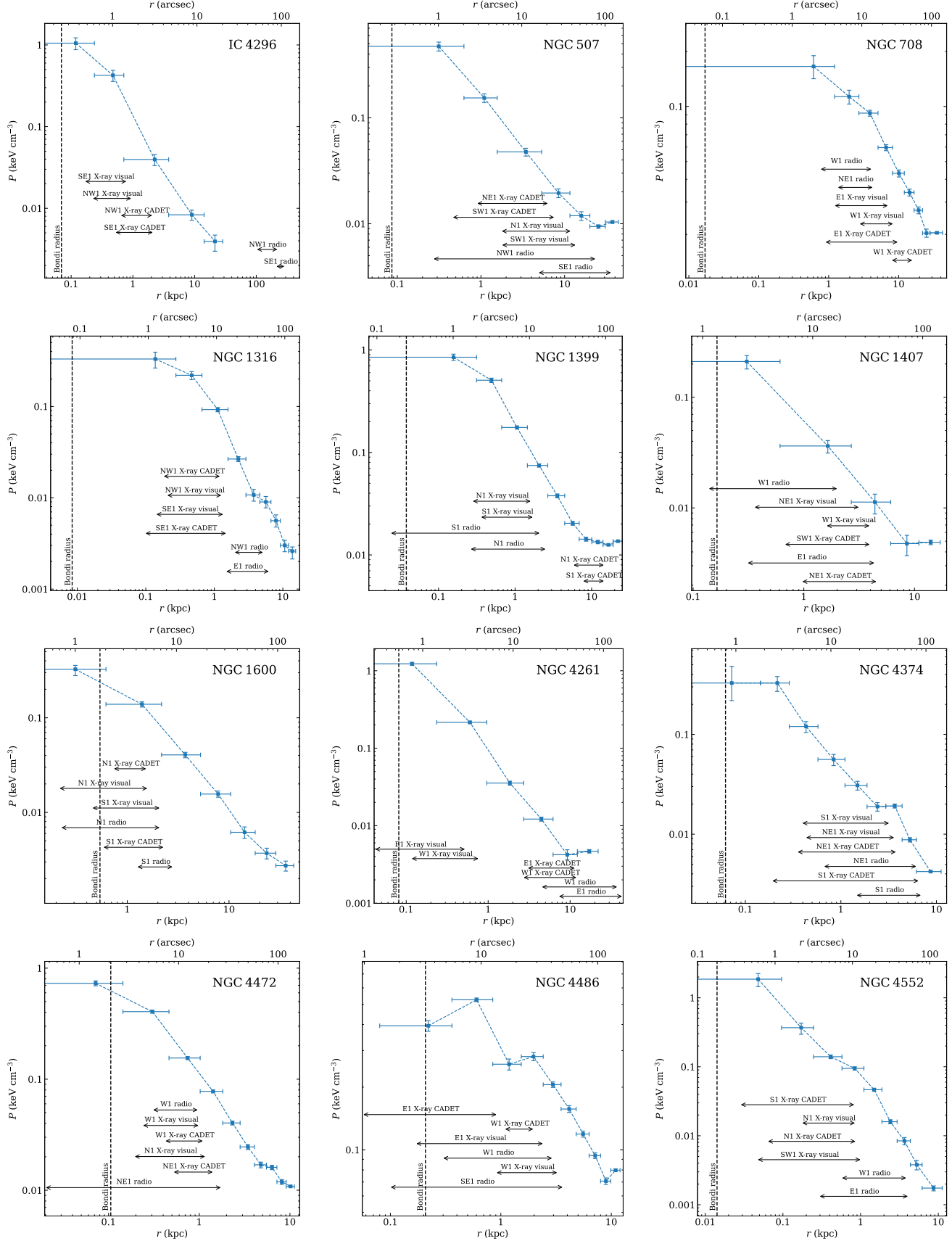


Figure A4: To be continued.

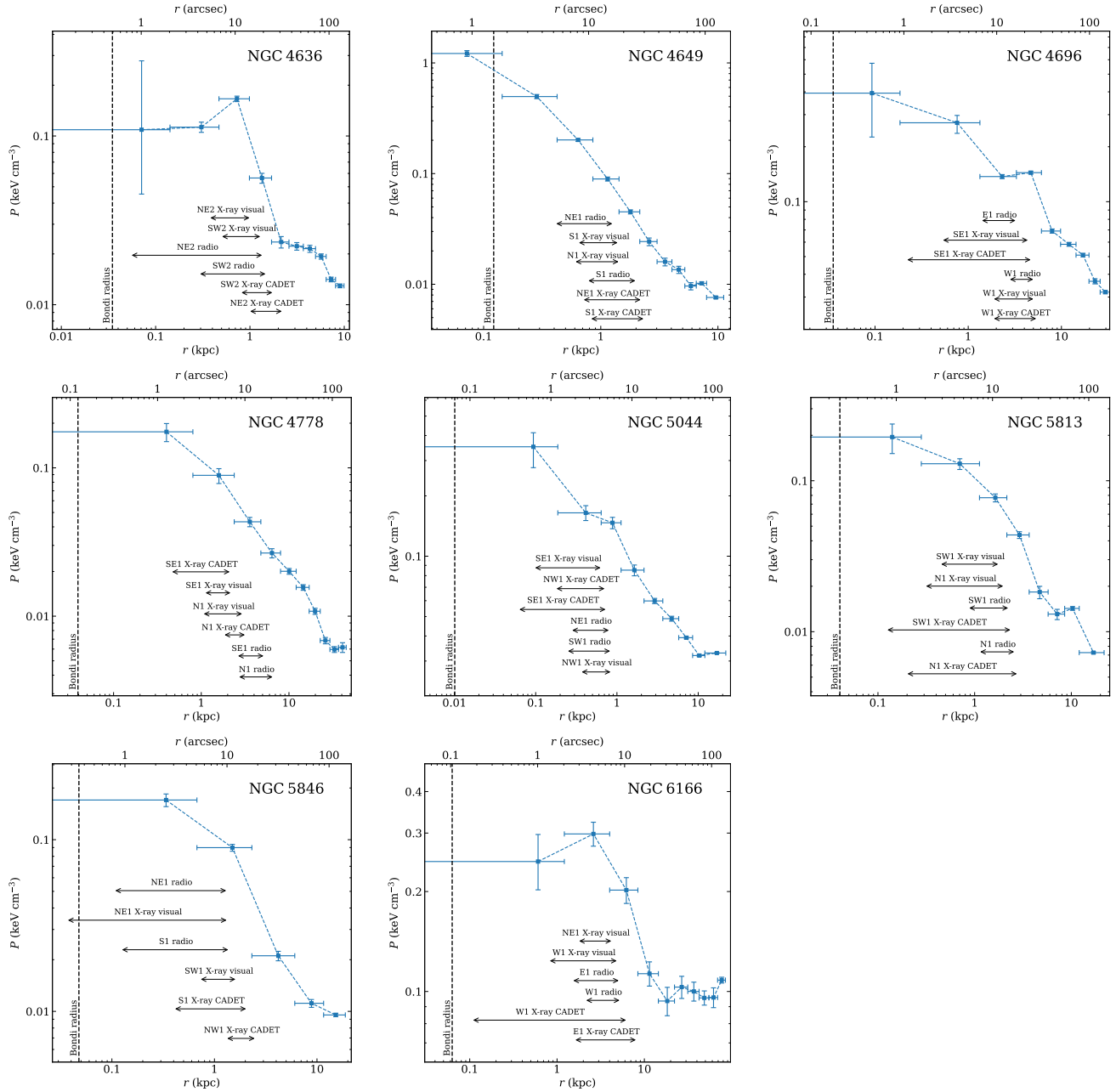


Figure A4: Azimuthally averaged pressure radial profiles for all the analysed galaxies. The vertical dashed line represents the Bondi radius r_B . The double-sided arrows represent radial ranges of individual first-generation cavities for all cavity detection methods.

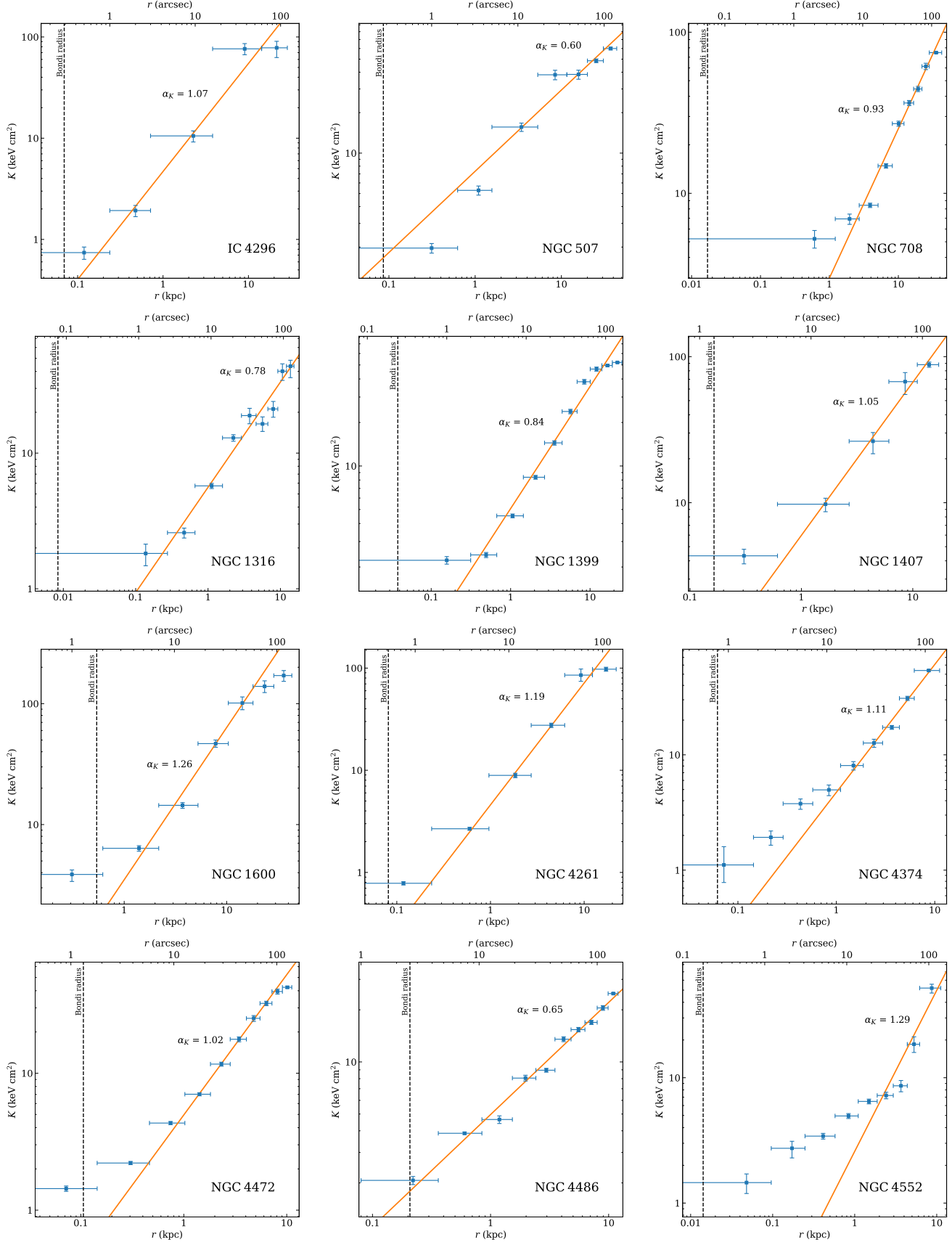


Figure A5: To be continued.

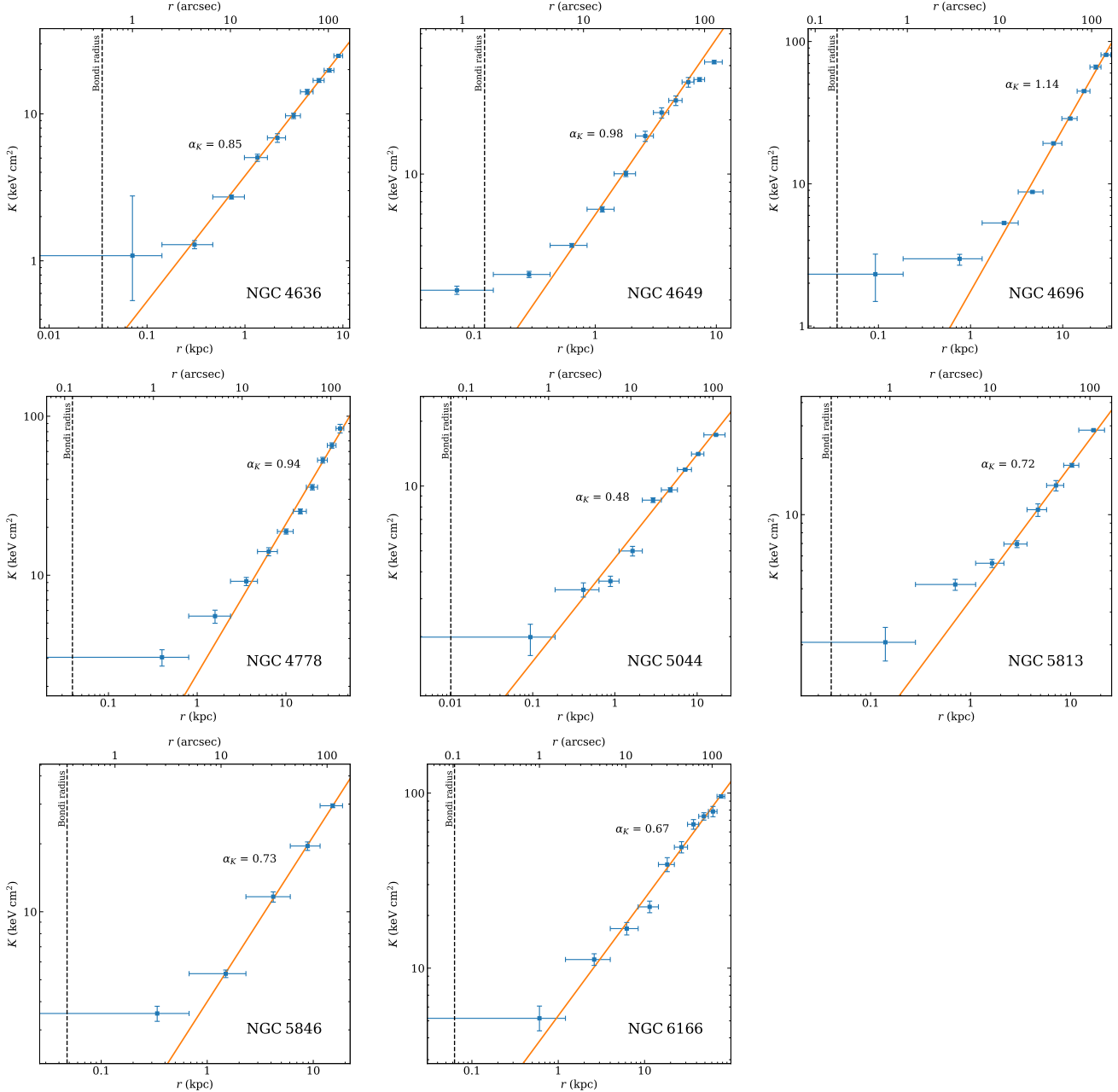


Figure A5: Azimuthally averaged specific entropy radial profiles for all the analysed galaxies. The vertical dashed line represents the Bondi radius r_B . The powerlaw fit was performed for radii higher than 1 kpc in order the probe how susceptible are the galactic atmospheres to thermal instabilities.

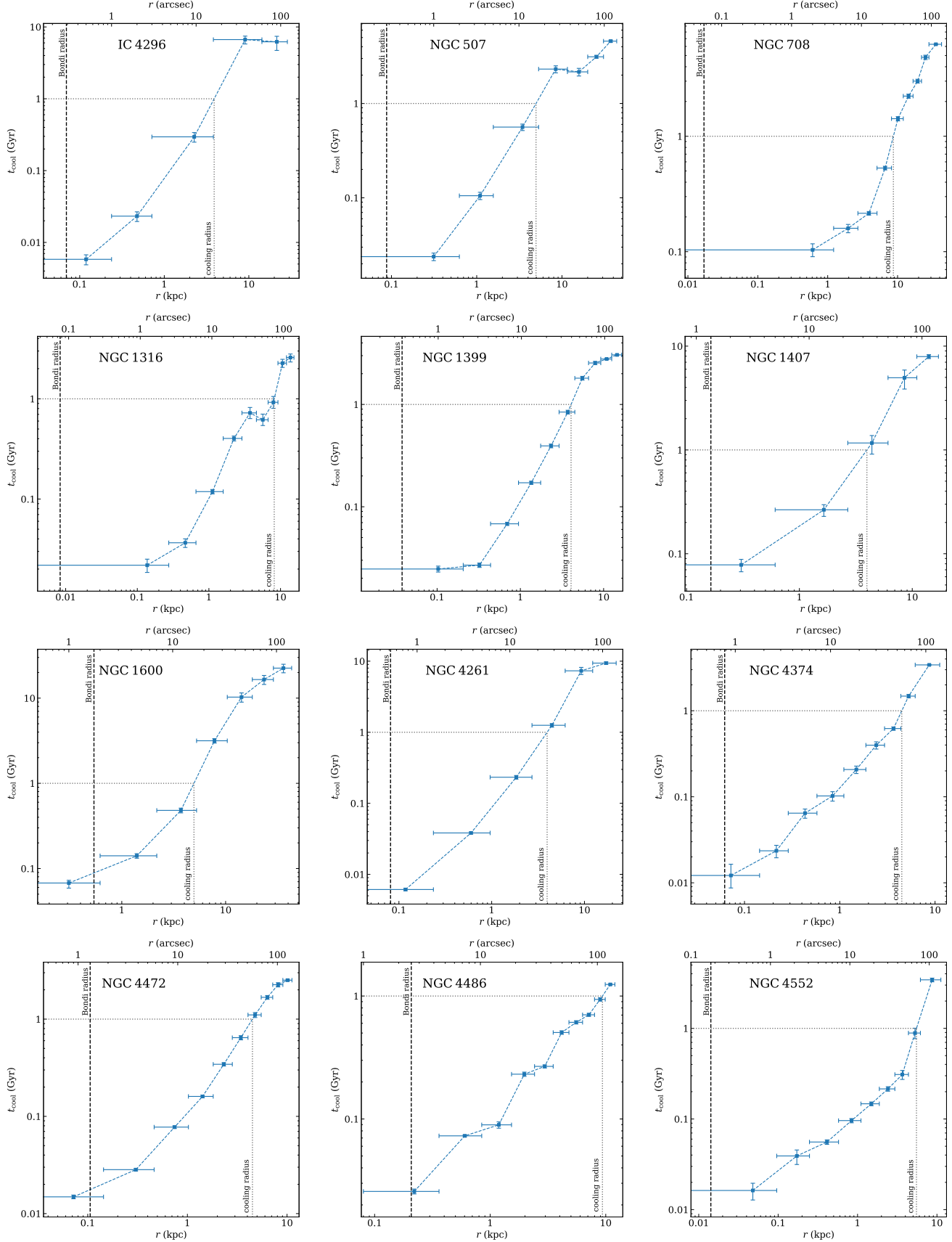


Figure A6: To be continued.

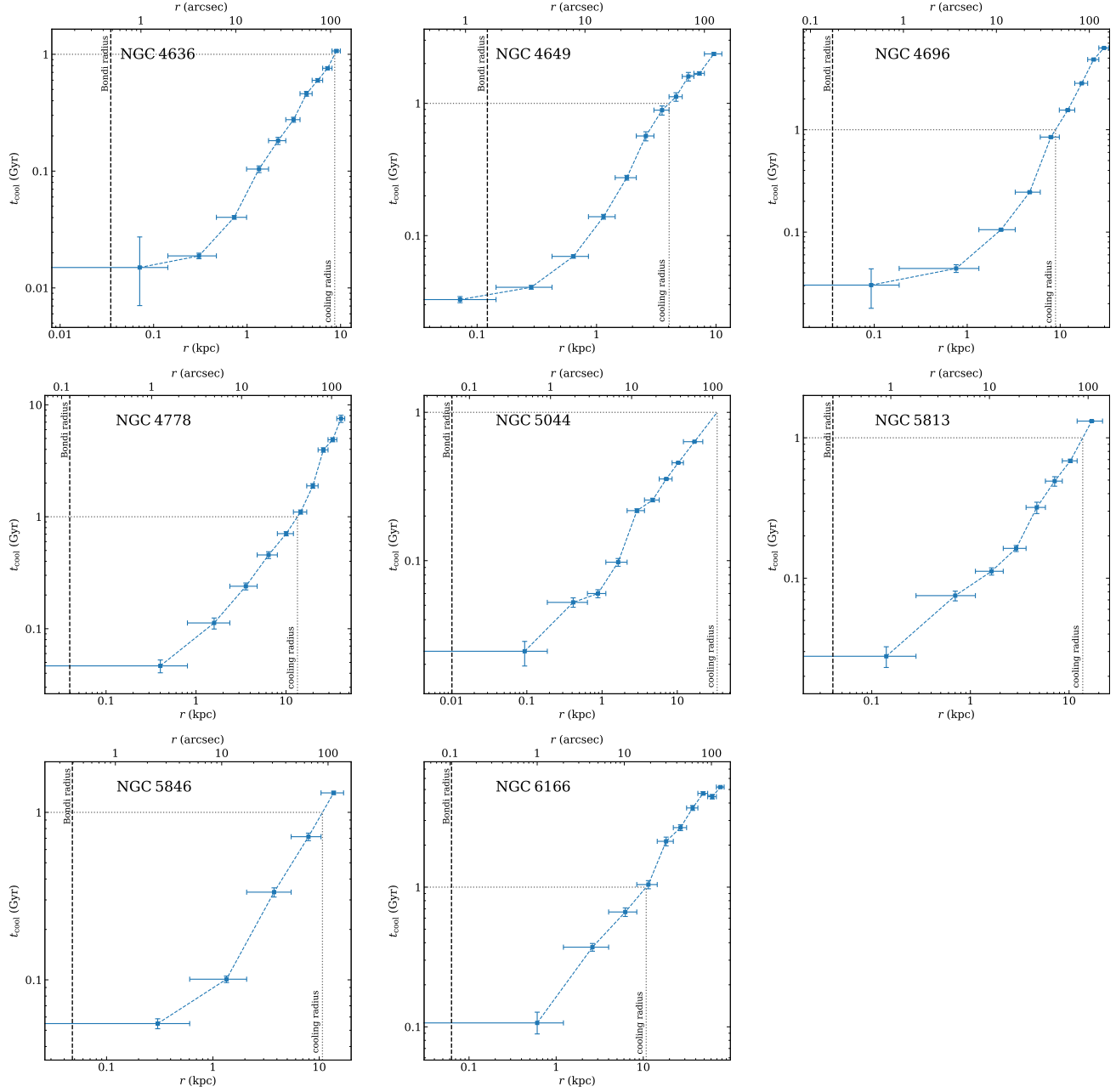


Figure A6: Azimuthally averaged cooling time profiles for all the analysed galaxies. The vertical dashed line represents the Bondi radius, while the dotted lines show the 1 Gyr limit and the cooling radius.

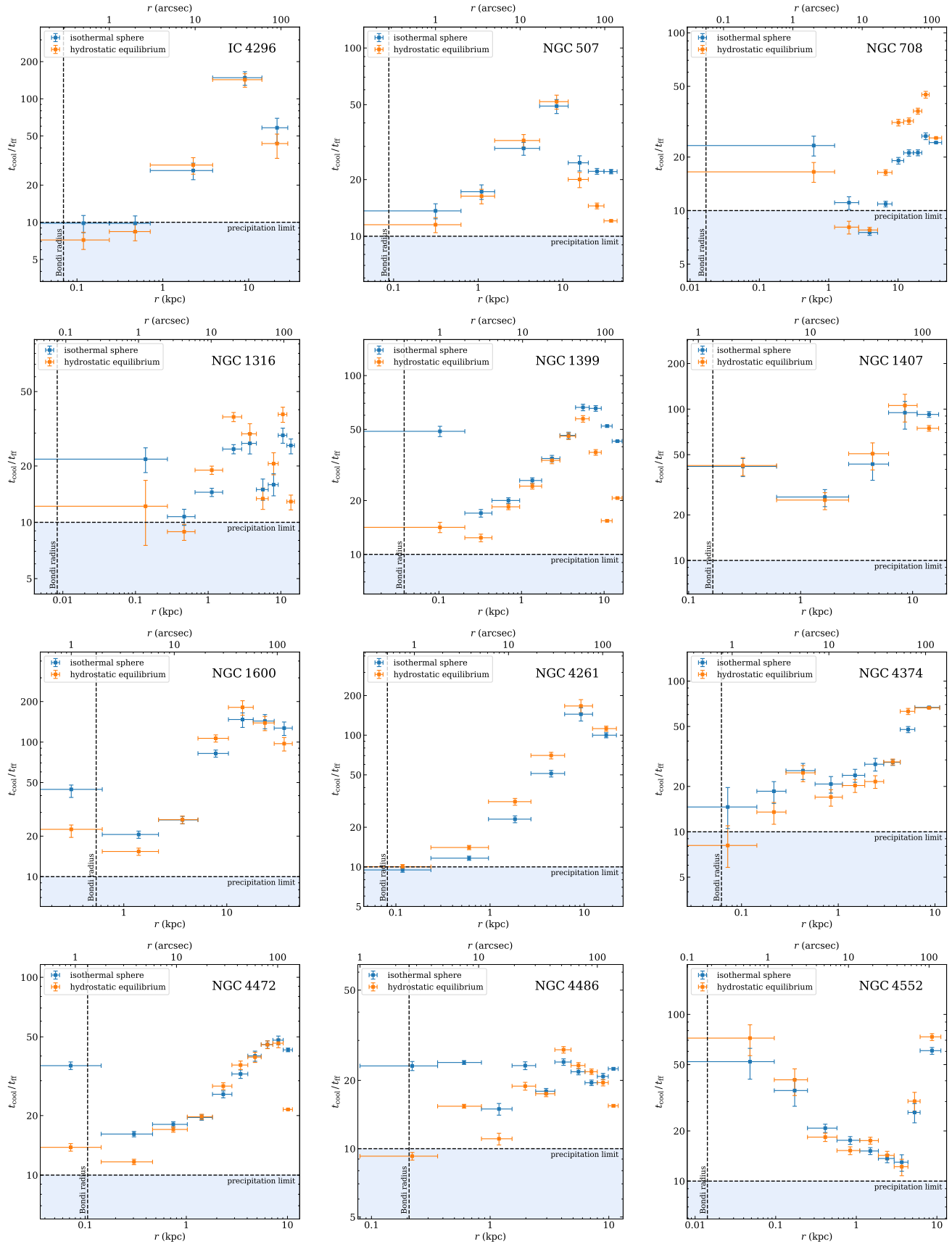


Figure A7: To be continued.

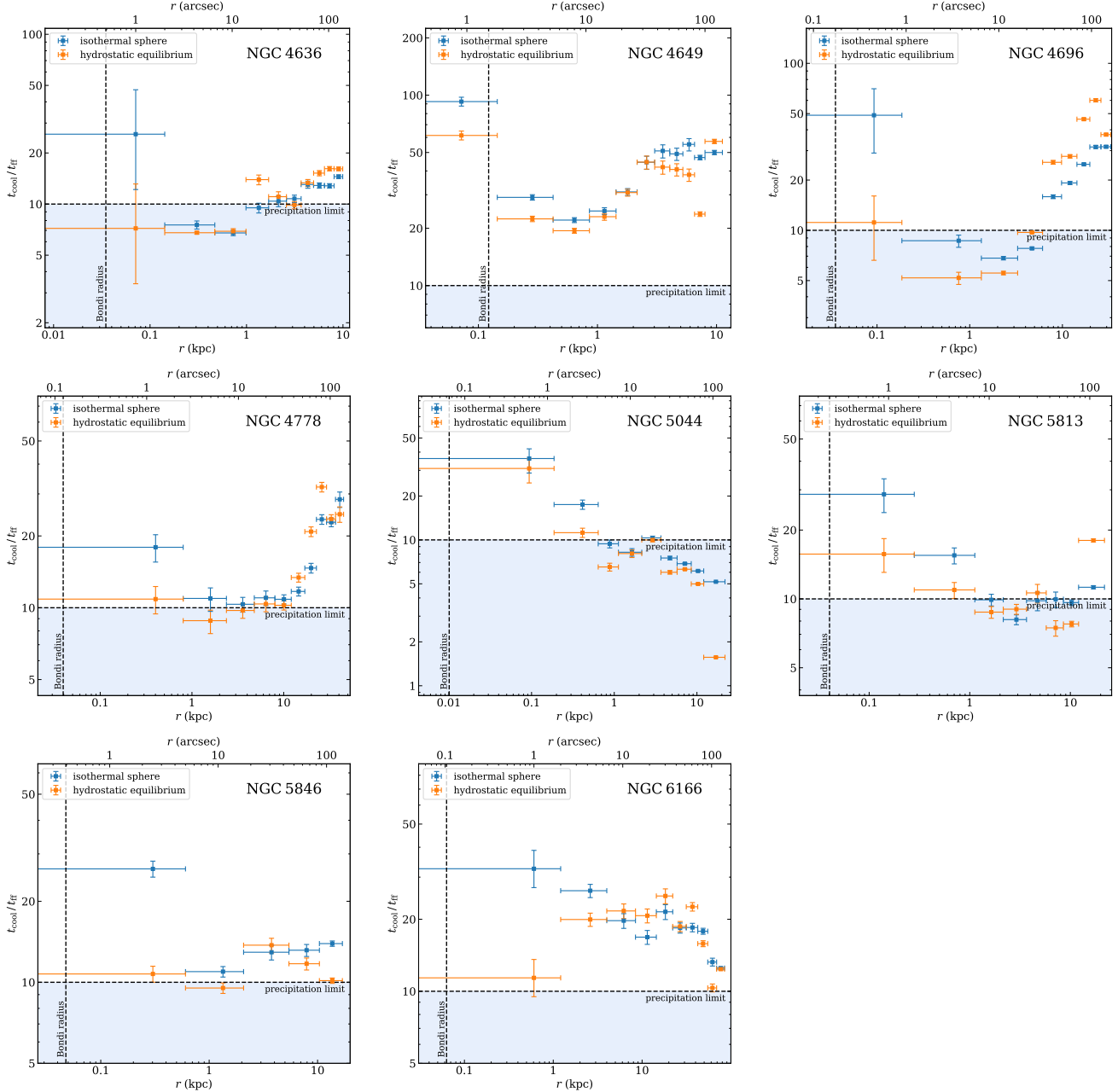


Figure A7: Azimuthally averaged cooling time over free fall time profiles for all the analysed galaxies estimated from local gravitational acceleration calculated both from the assumption of an isothermal sphere and constant velocity dispersion and also from thermodynamical properties and the assumption of hydrostatic equilibrium. The vertical dashed line represents the Bondi radius, while the horizontal dashed line is the precipitation limit $t_{\text{cool}}/t_{\text{ff}} \approx 10$.

Appendix B: Correlated quantities

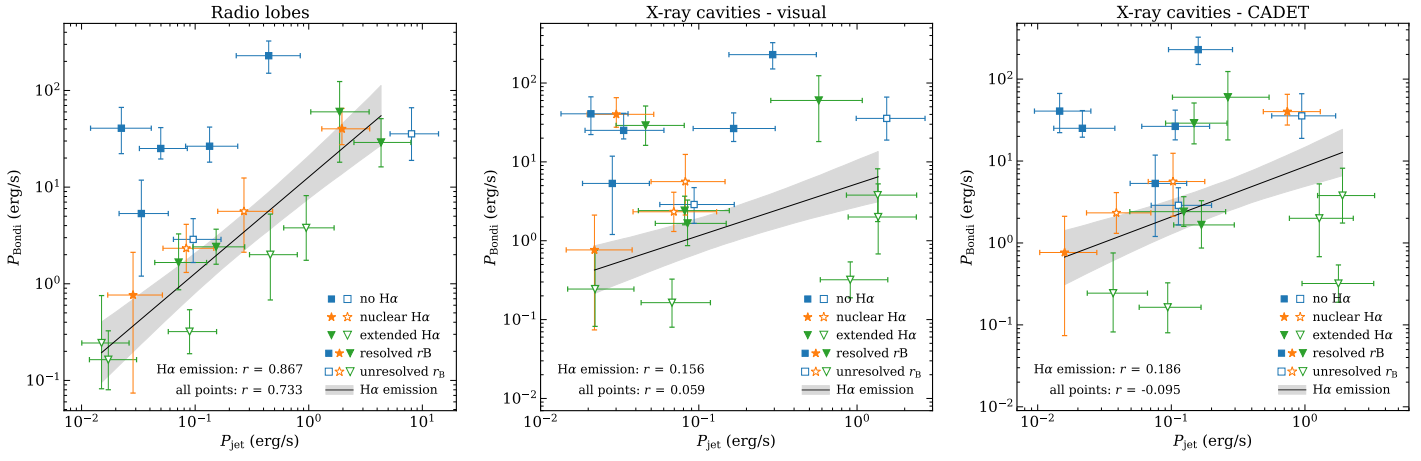


Figure B1: Relation between the Bondi accretion power on mechanical jet power. The jet powers were estimated from visually estimated sizes of radio lobes (left), visually estimated sizes of X-ray cavities (center) and volumes of X-ray cavities predicted by the CADET_size pipeline (right). Correlation coefficients for linear fits of individual linear fits are stated next to the legends.

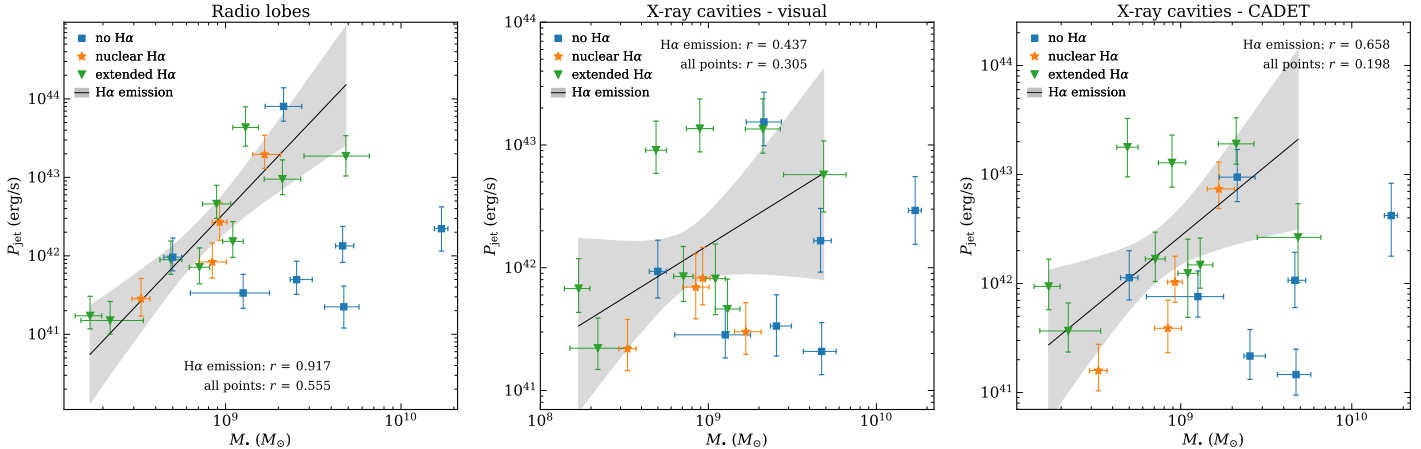


Figure B2: Mechanical jet power versus mass of the supermassive black hole.

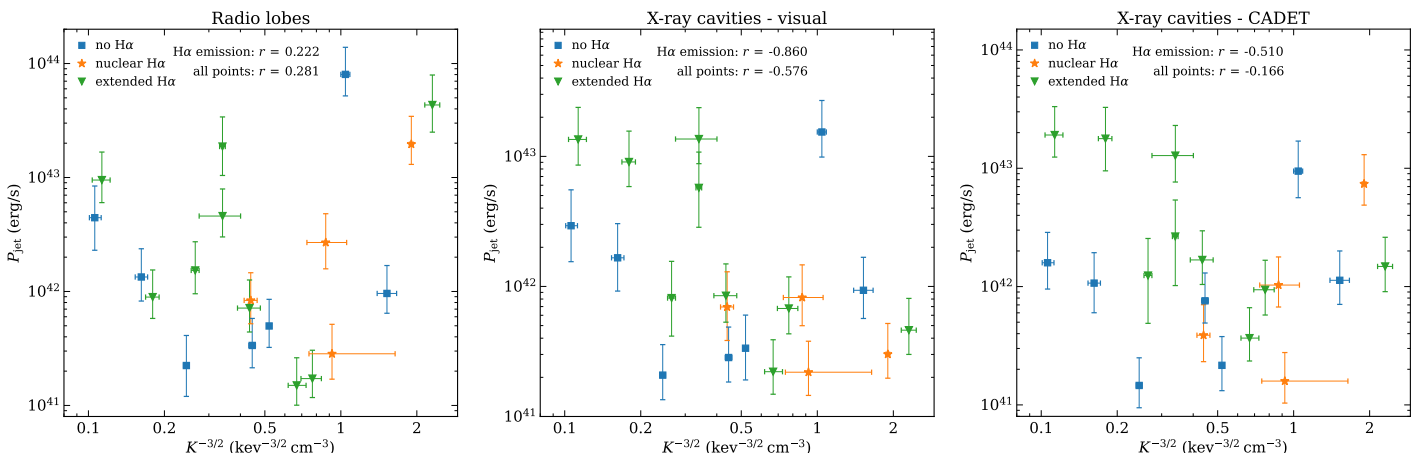


Figure B3: Relation between the mechanical jet power and central (r_B) specific entropy to the power of $-3/2$ (see Equation 1.11).

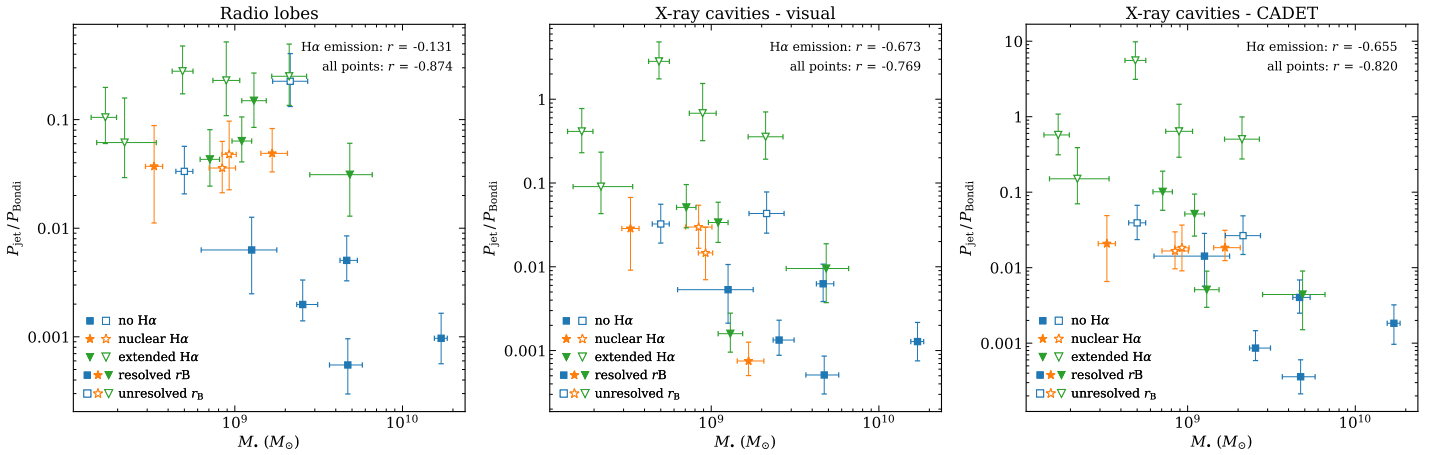


Figure B4: Mechanical jet power to Bondi power efficiency versus the mass of the supermassive black hole.

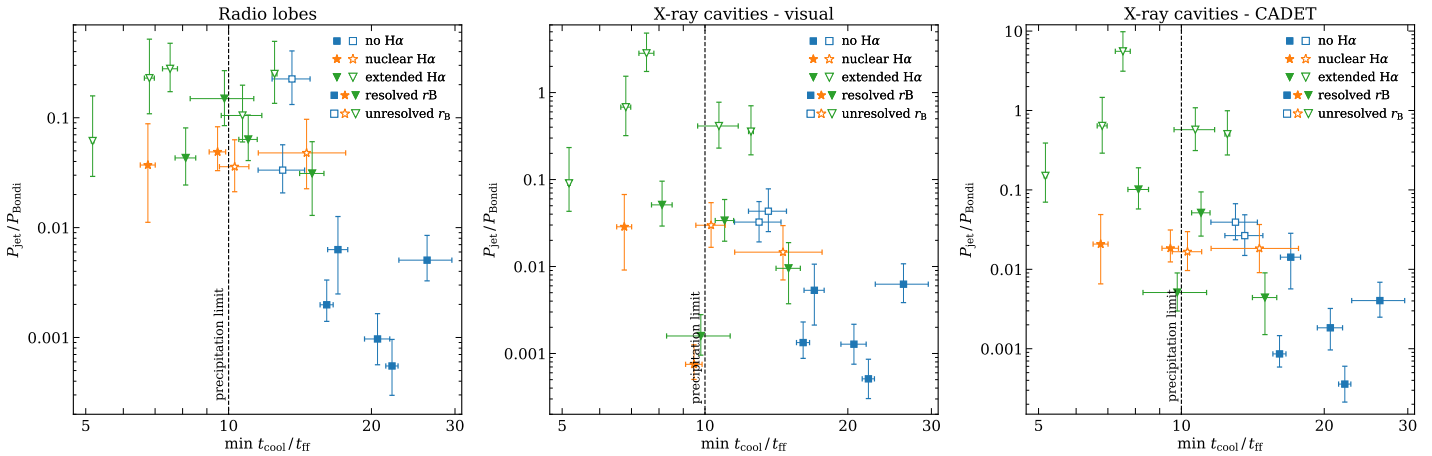


Figure B5: Mechanical jet power to Bondi power efficiency versus the minimal value of the cooling time over free fall time (isothermal sphere) ratio. The dashed line represents the precipitation limit $t_{\text{cool}}/t_{\text{ff}} \approx 10$.

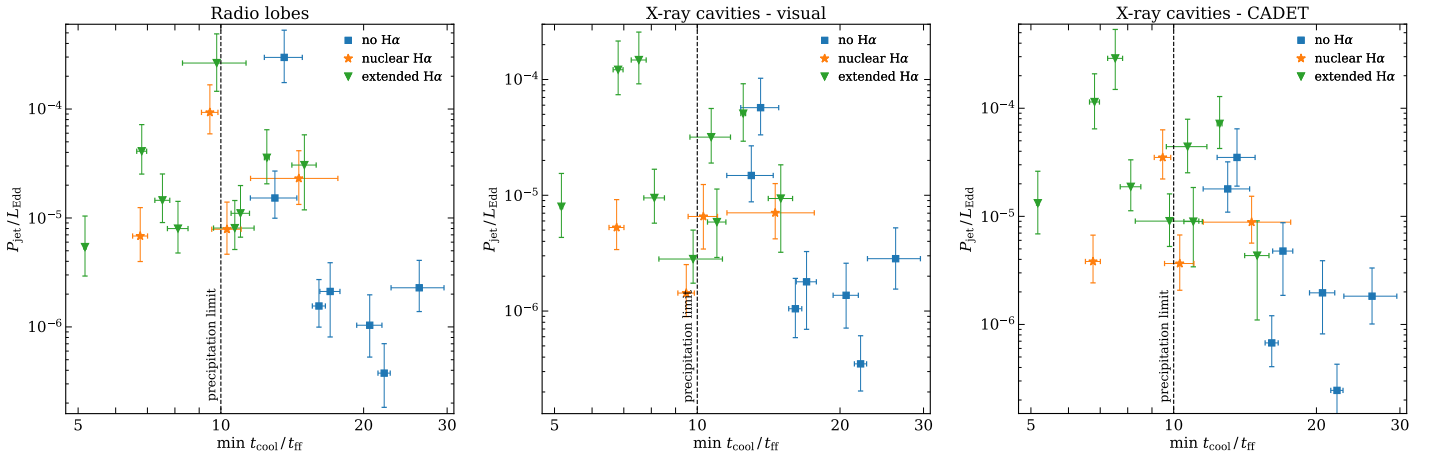


Figure B6: Mechanical jet power to Eddington power efficiency versus the minimal value of the cooling time over free fall time (isothermal sphere) ratio. The dashed line represents the precipitation limit where $t_{\text{cool}}/t_{\text{ff}} \approx 10$.

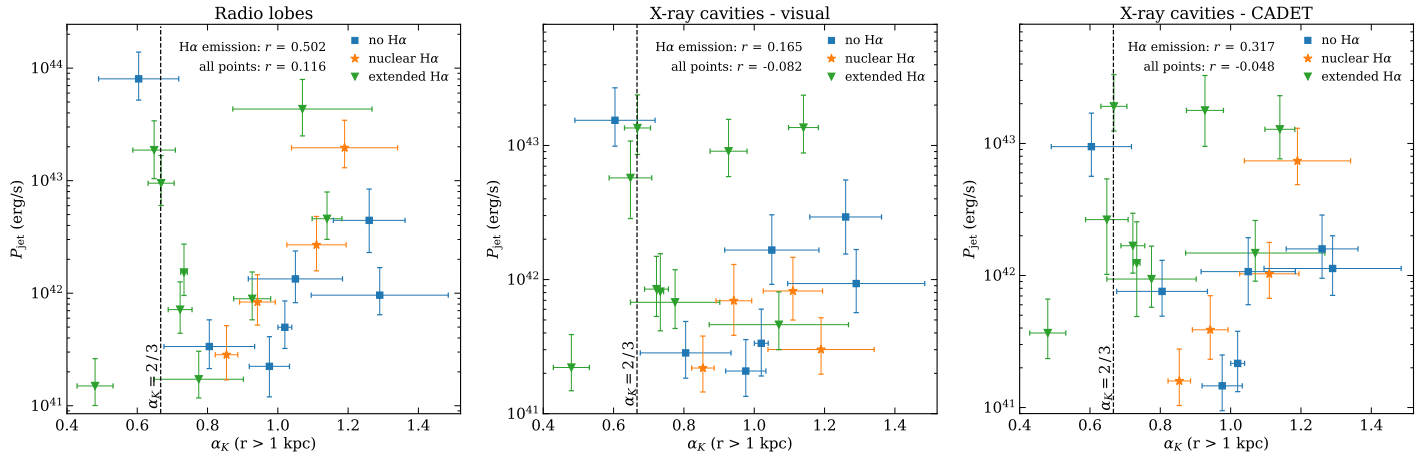


Figure B7: Mechanical jet power versus specific entropy slope at radii higher than 1 kpc.

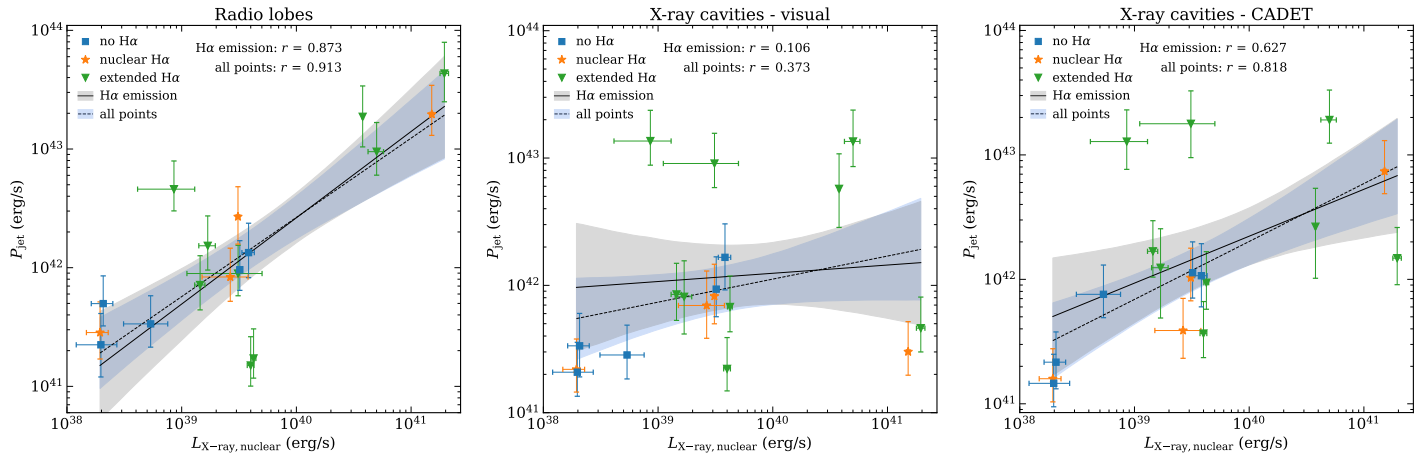


Figure B8: Mechanical jet power versus nuclear (powerlaw) luminosity in the 0.5 – 7.0 keV range.

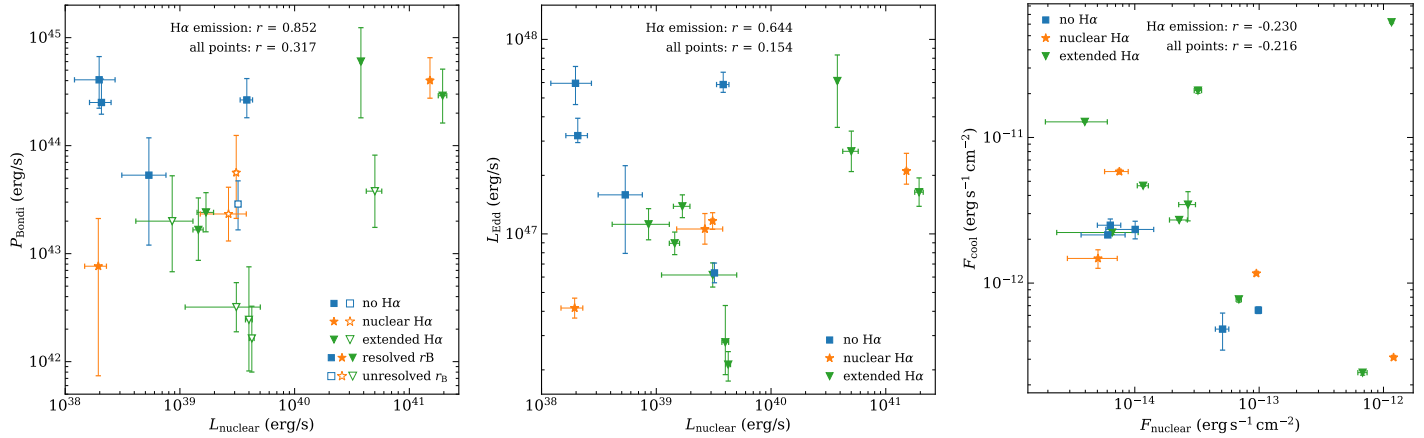


Figure B9: Nuclear (powerlaw) luminosity range versus Bondi accretion rate (left) and Eddington luminosity (center). And relation between nuclear (powerlaw) flux and cooling flux (apec flux from within cooling radius) (right).

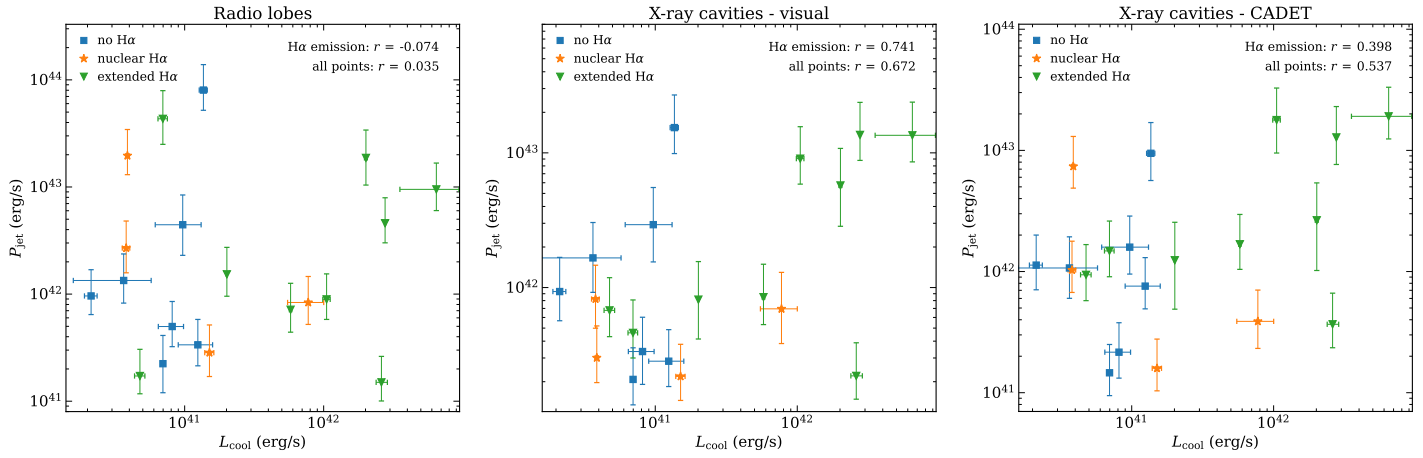


Figure B10: Mechanical jet power versus cooling luminosity.

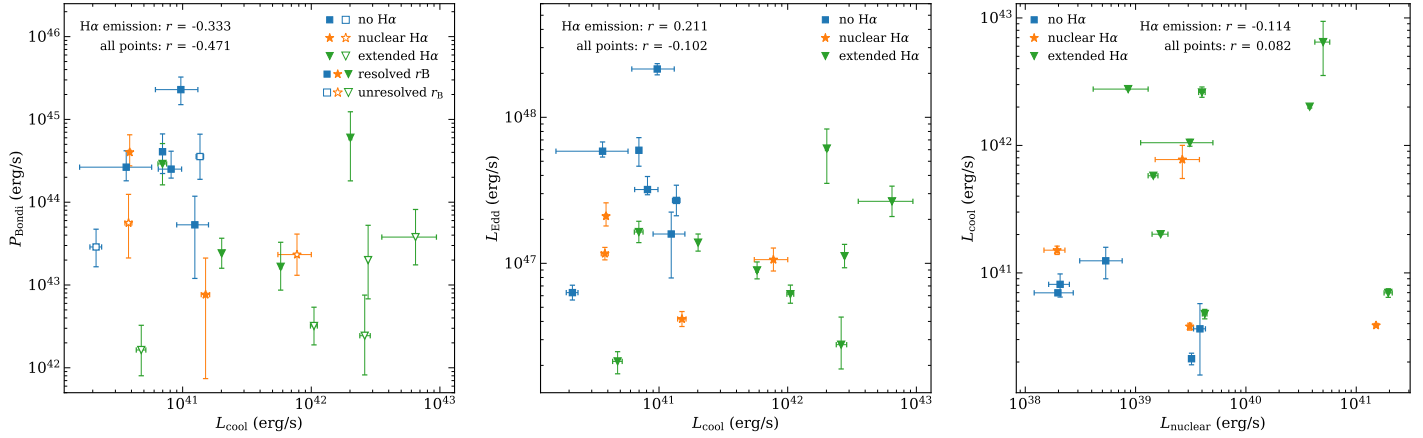


Figure B11: Cooling luminosity versus Bondi accretion rate (left), Eddington luminosity (center) and nuclear (powerlaw) luminosity (right).

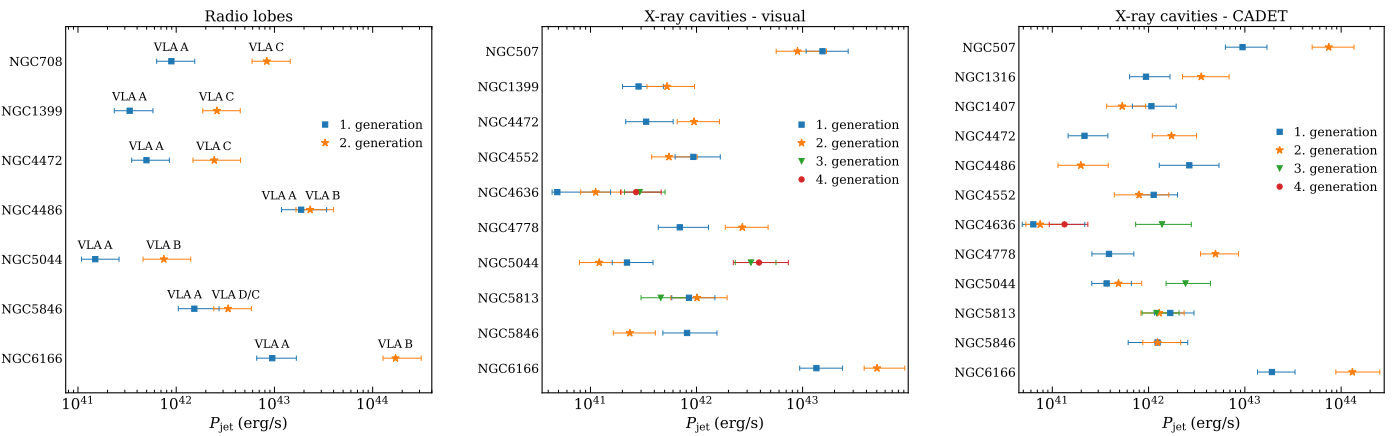


Figure B12: Mechanical jet powers of individual generations of radio lobes determined by visual inspection of radio contours of various VLA array configurations (left), X-ray cavities estimated by visual inspection of residual X-ray images obtained from beta modelling (center) and X-ray cavities calculated from predictions of the CADET network (right).

Appendix C: Application of CADET

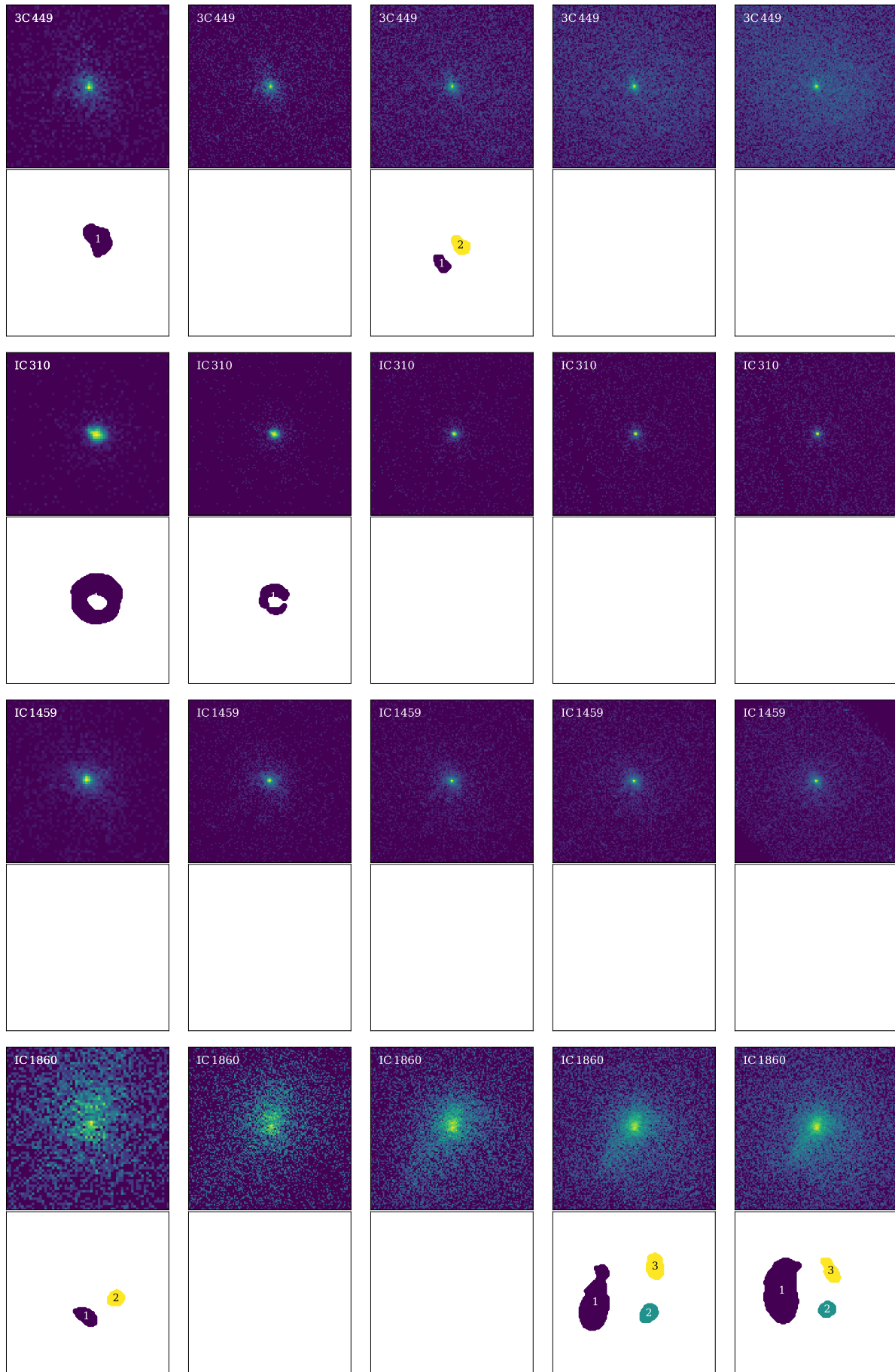


Figure C1: To be continued.

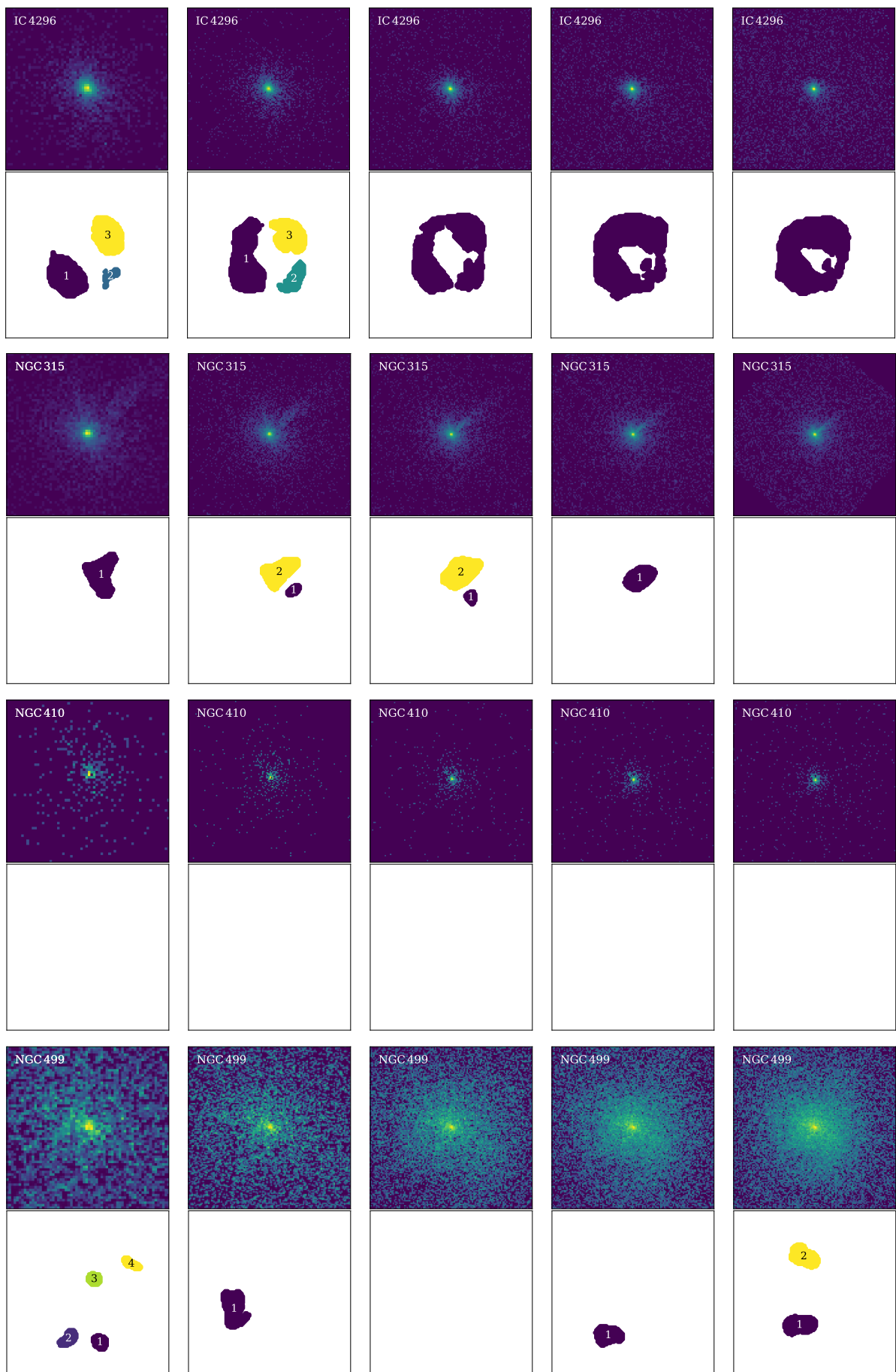


Figure C1: To be continued.

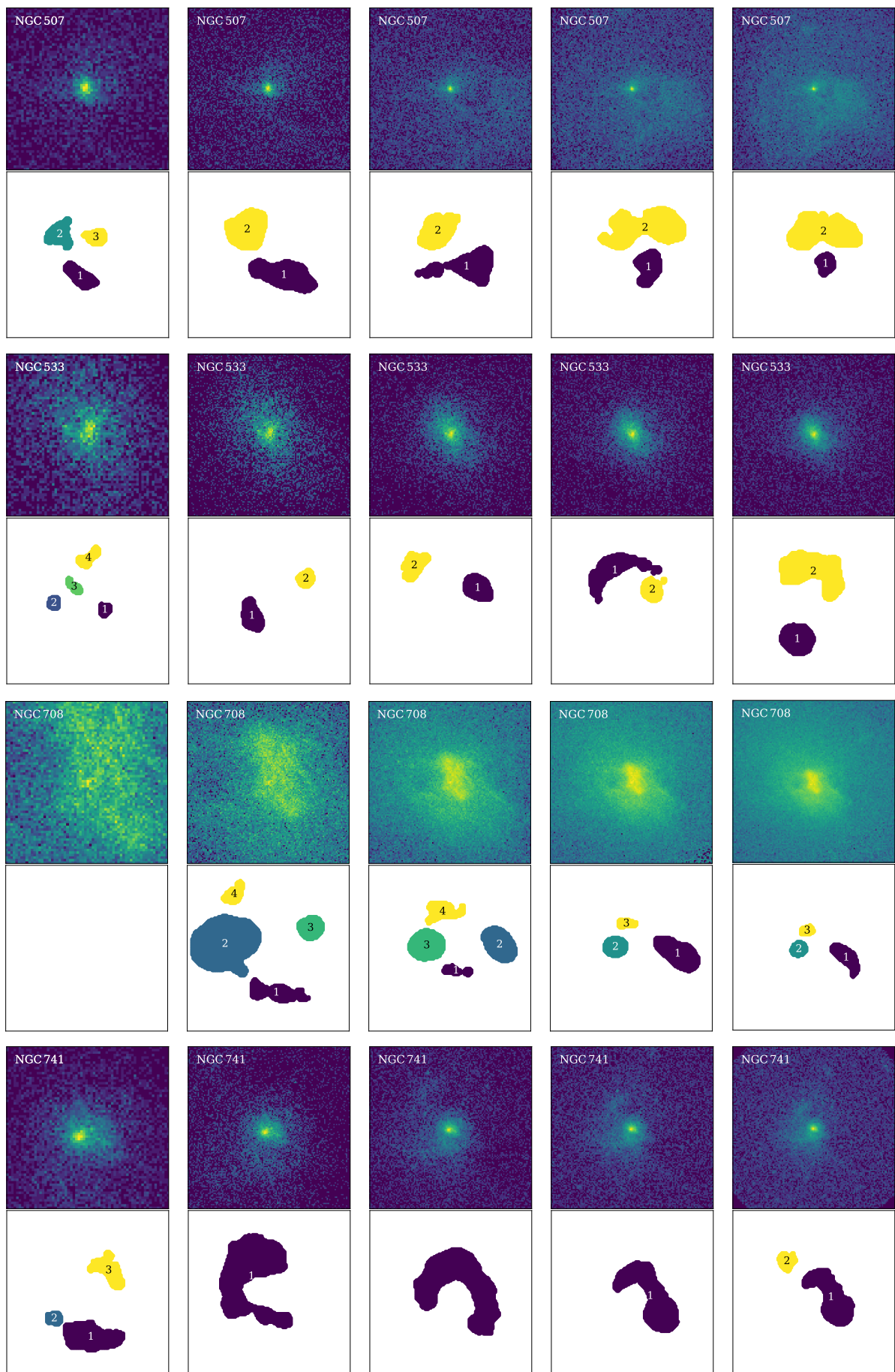


Figure C1: To be continued.

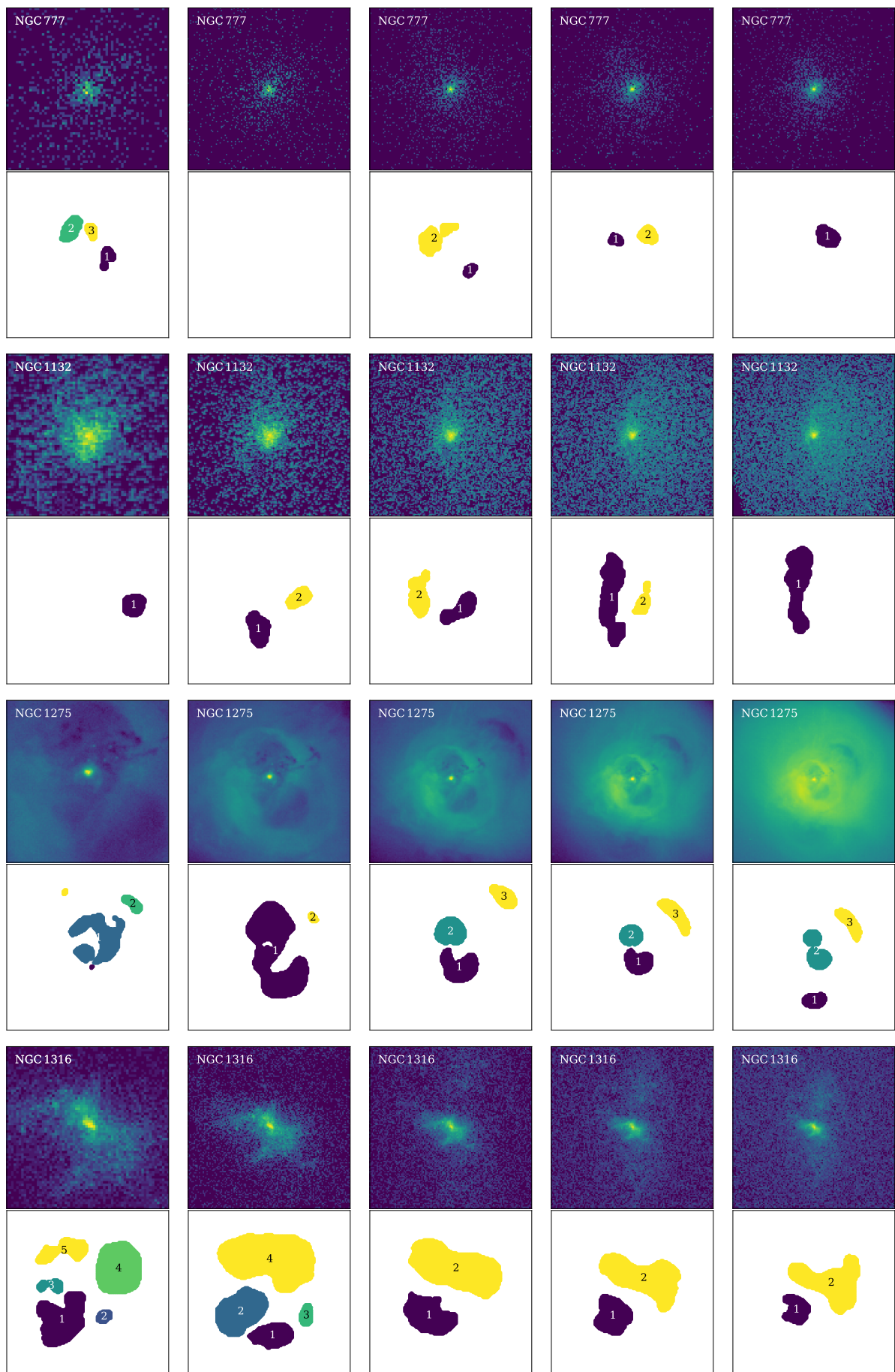


Figure C1: To be continued.

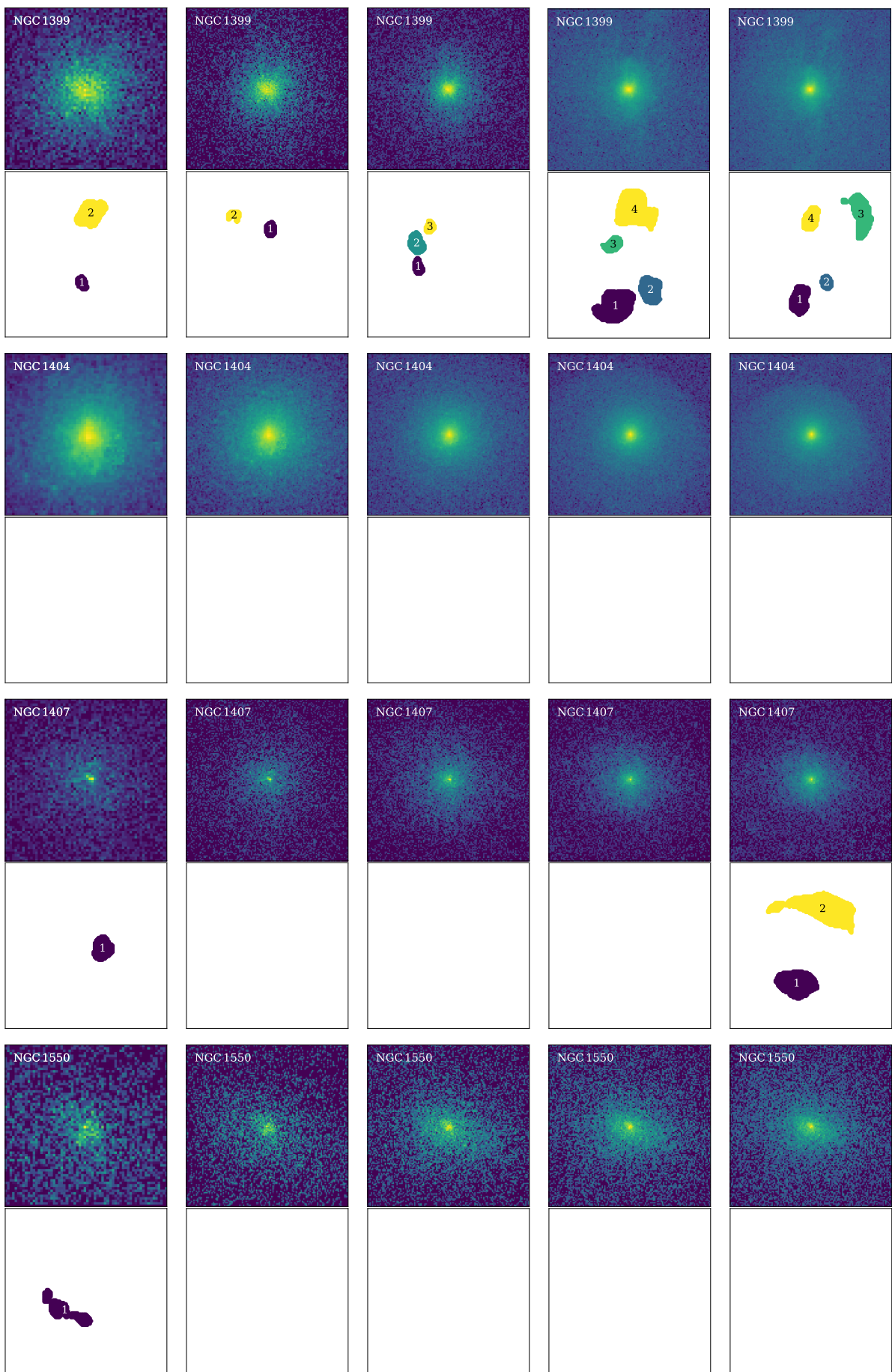


Figure C1: To be continued.

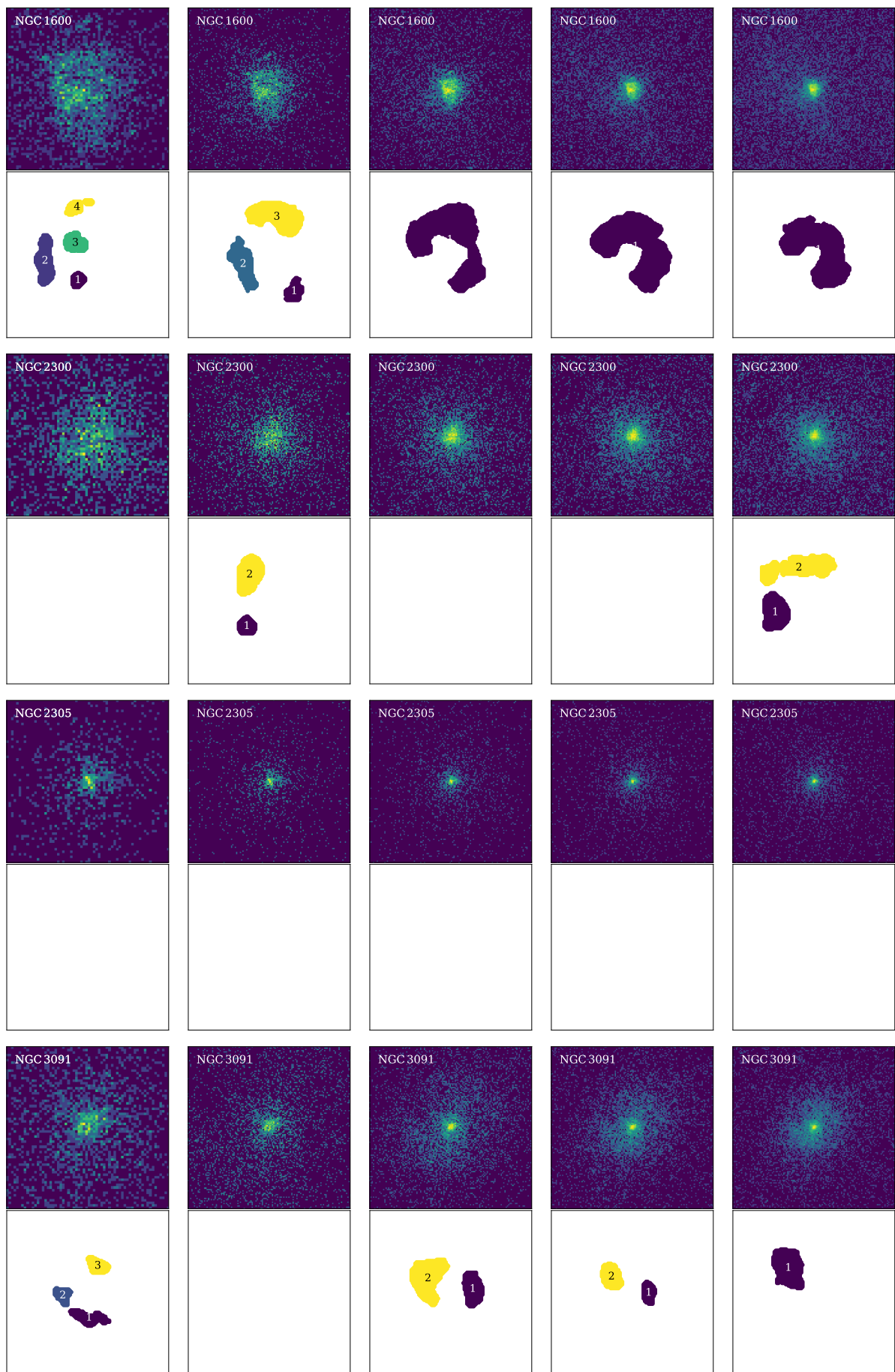


Figure C1: To be continued.

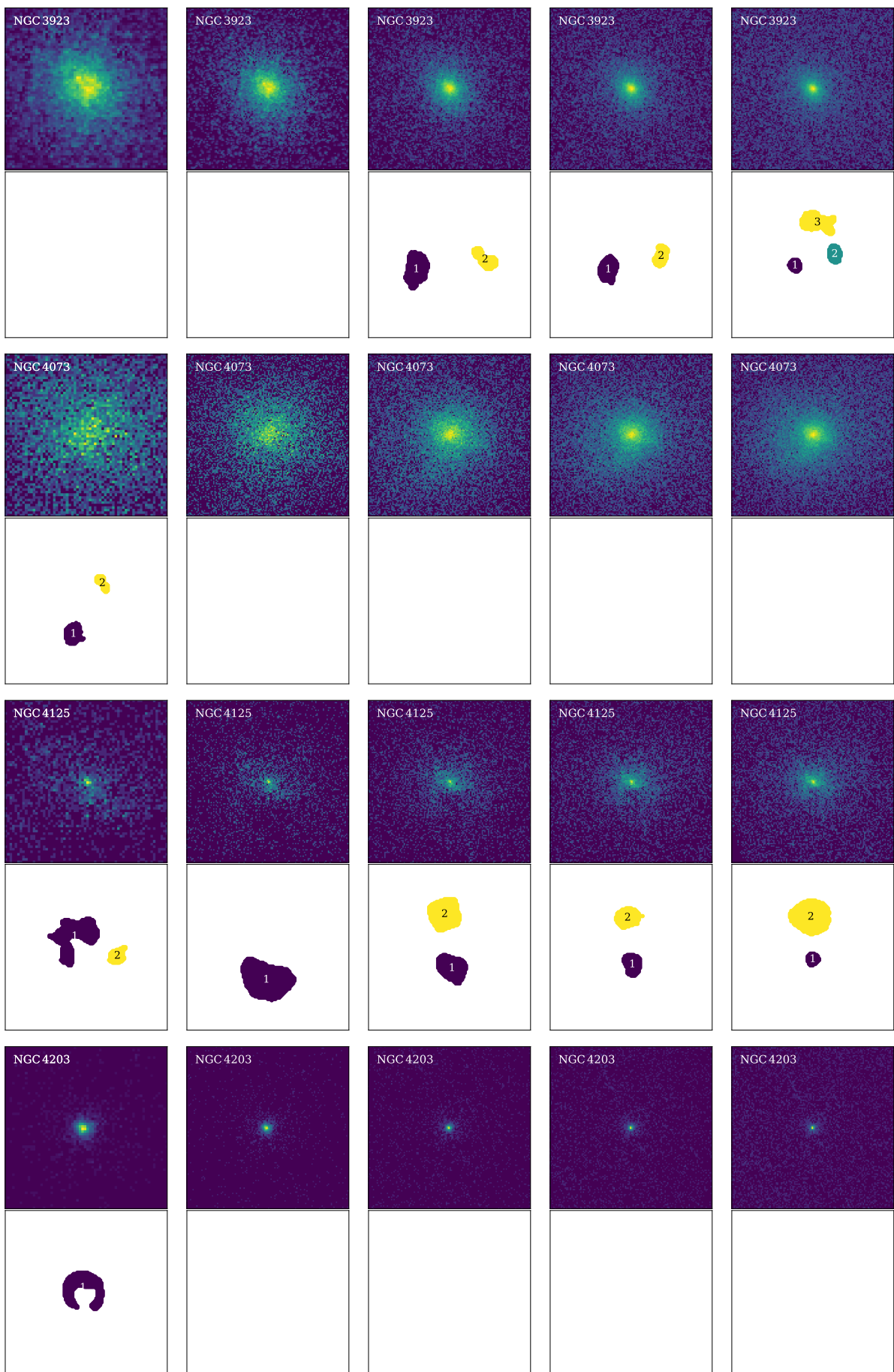


Figure C1: To be continued.

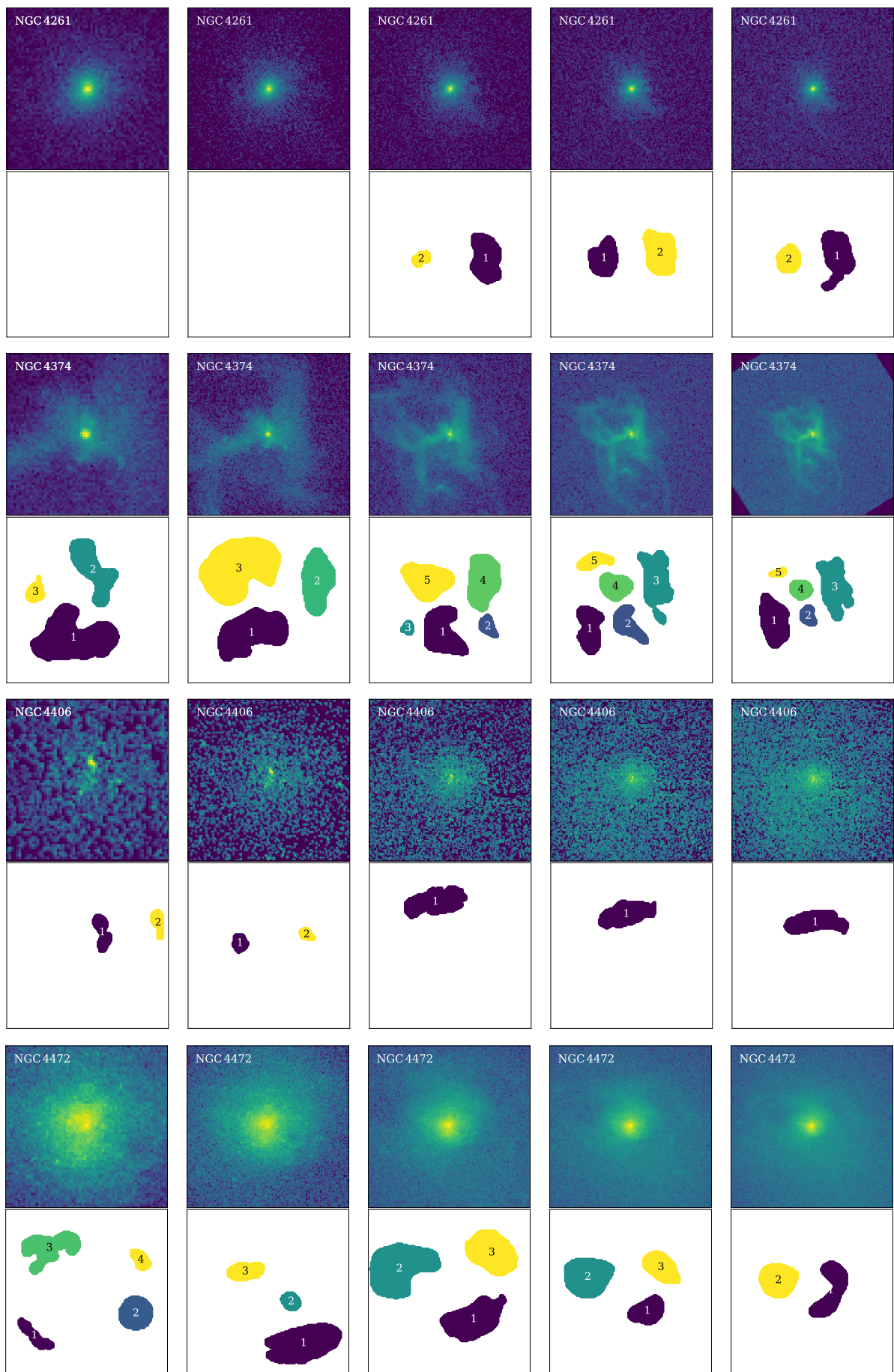


Figure C1: To be continued.

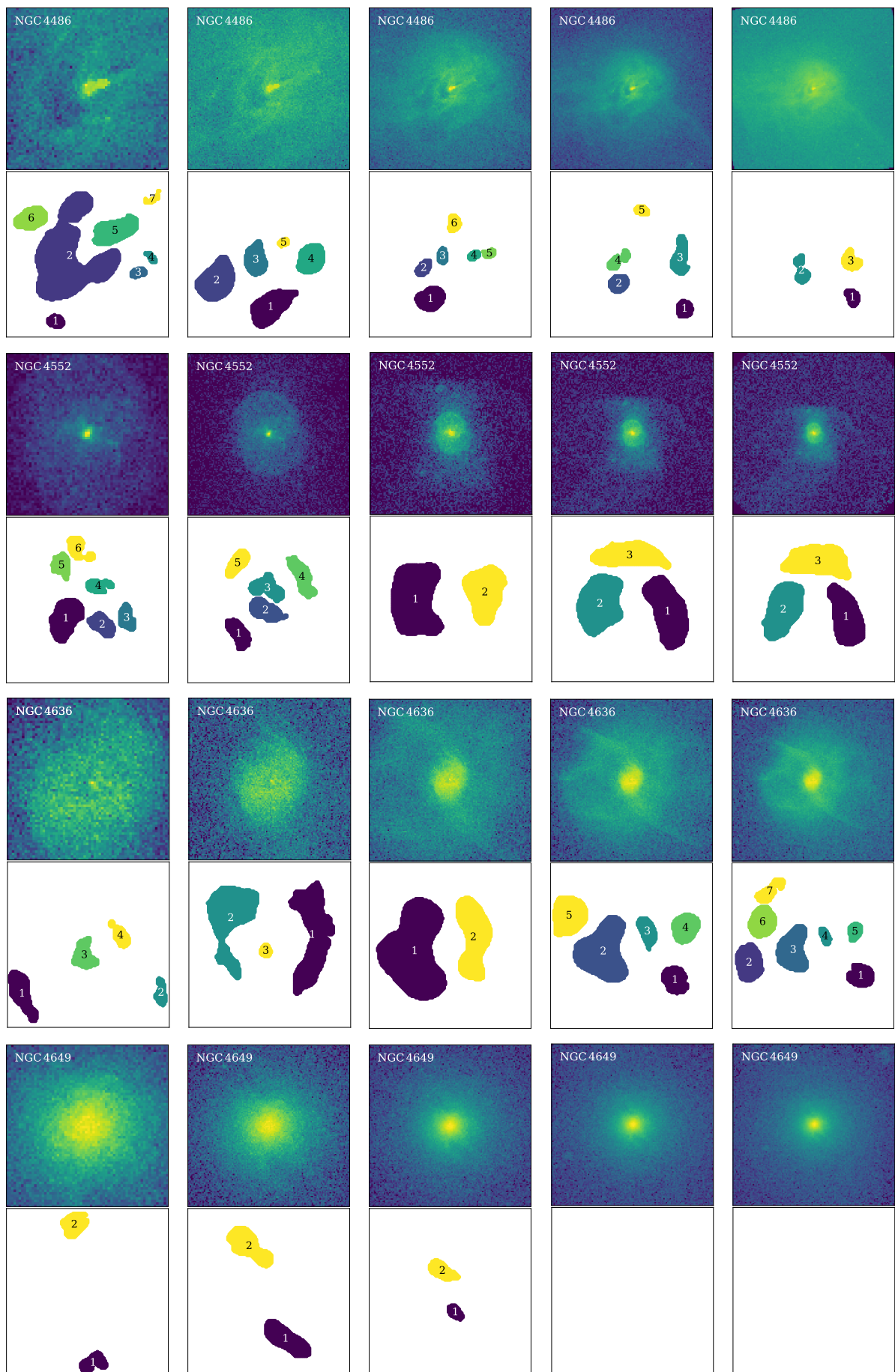


Figure C1: To be continued.

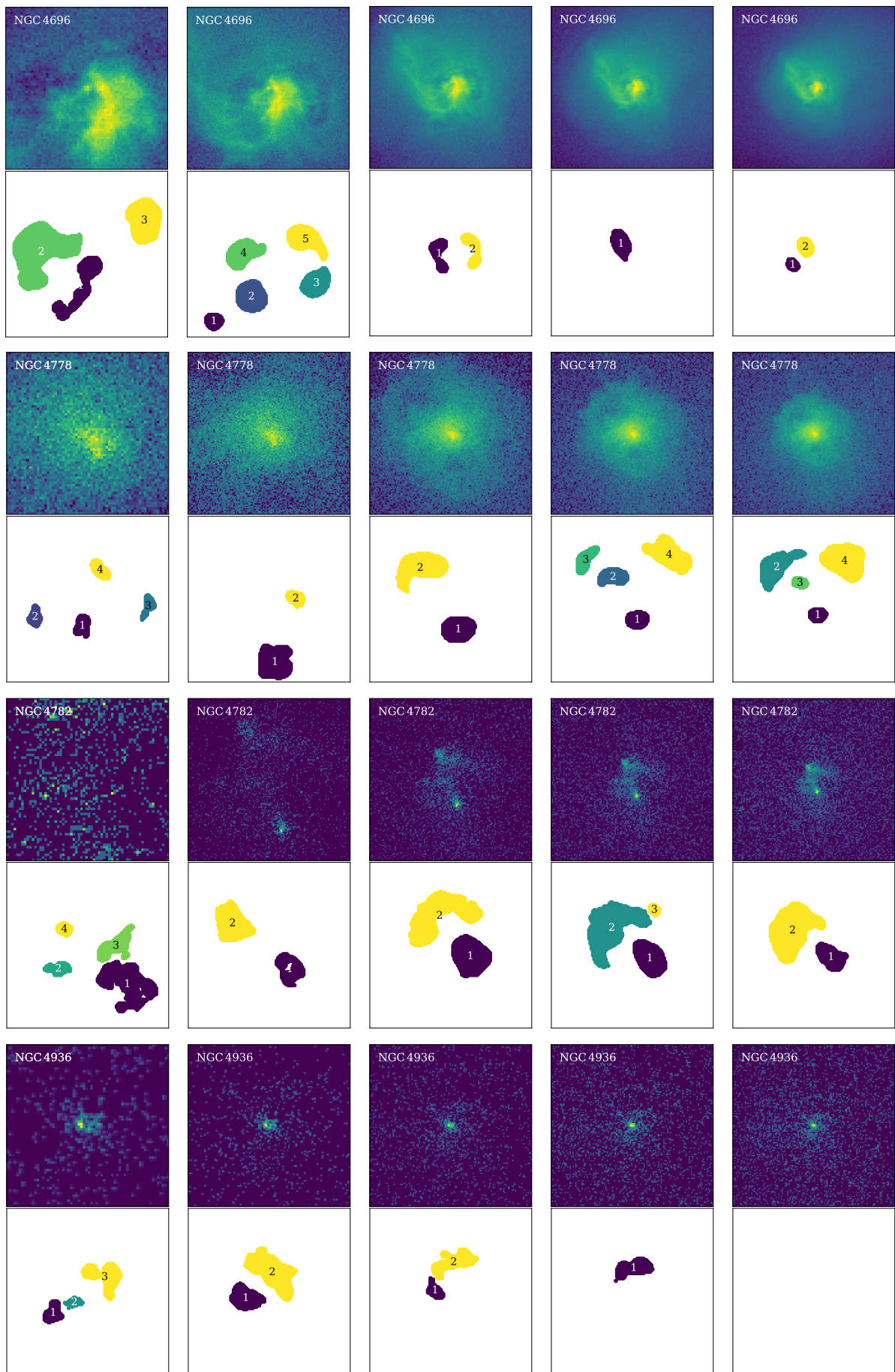


Figure C1: To be continued.

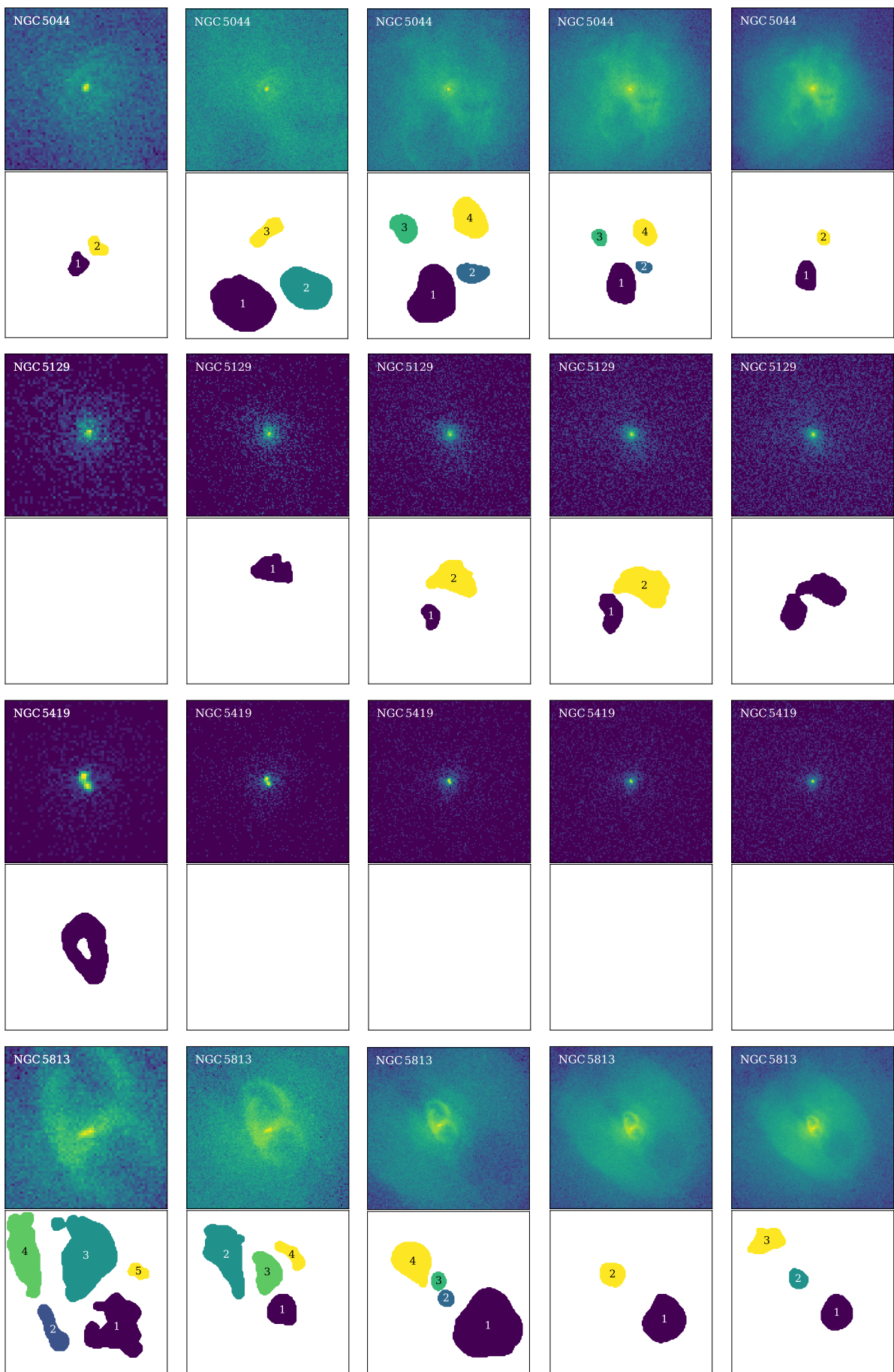


Figure C1: To be continued.

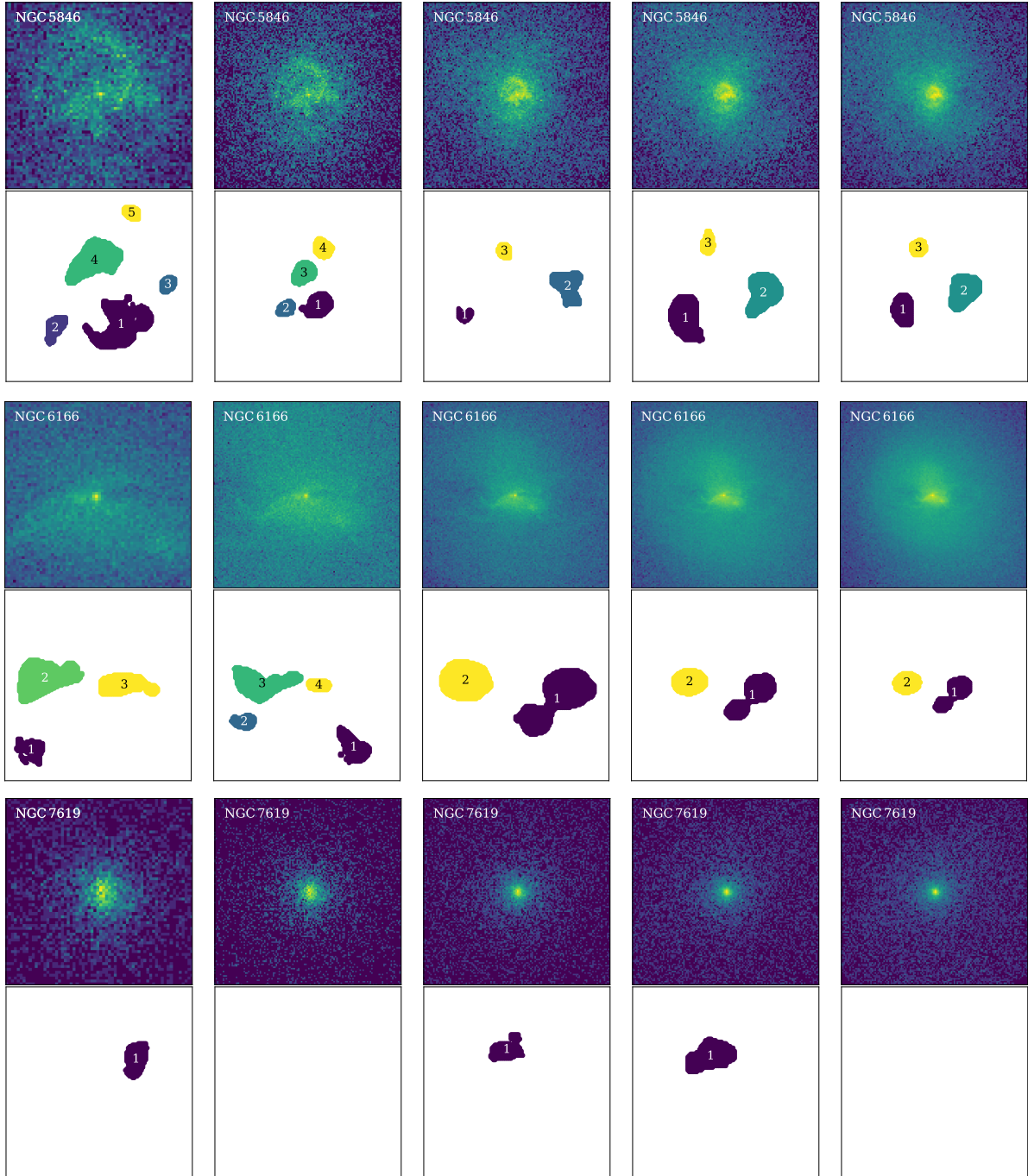


Figure C1: Examples of cavity predictions obtained using the *CADET_search* pipeline when applied on real images of galaxies with and possibly also without cavities. Images of each galaxy were analyzed in five different size realizations (from left to right): 512×512 (binsize 4 pixels), 384×384 (binsize 3 pixels), 256×256 (binsize 2 pixels), 128×128 (binsize 1 pixel) and 64×64 (binsize 0.5 pixels).

Appendix D: Size-estimated X-ray cavities

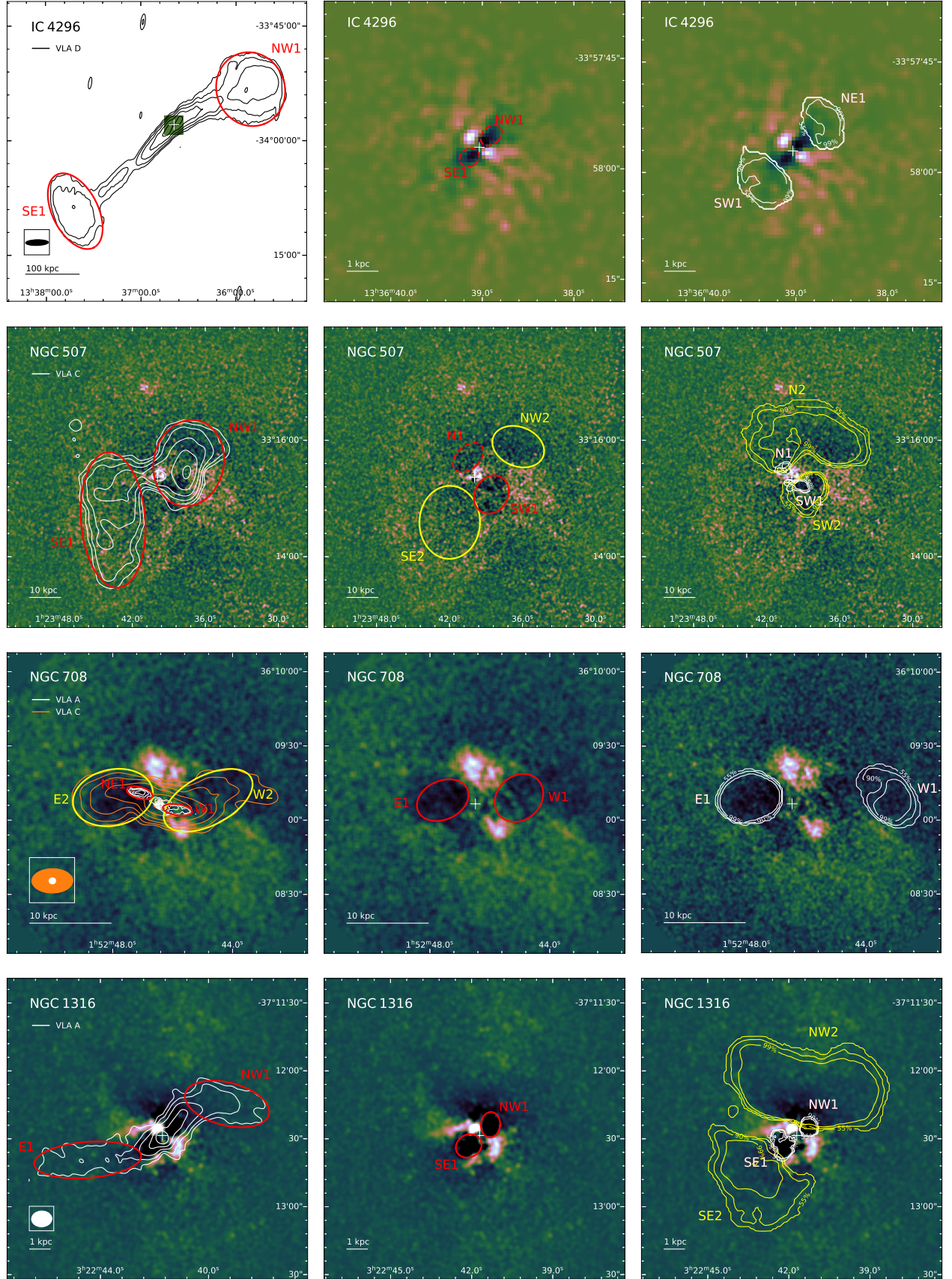


Figure D1: To be continued.

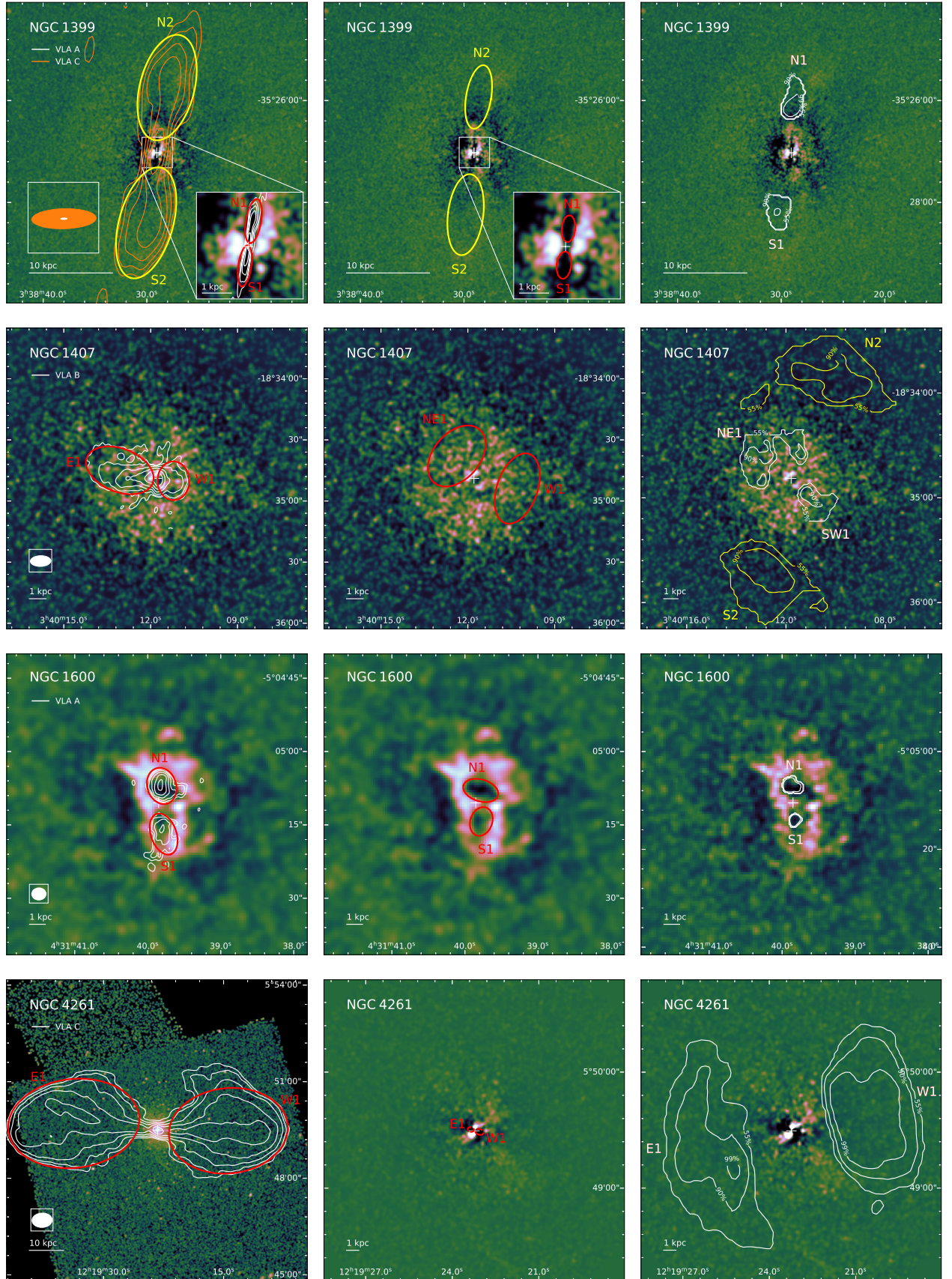


Figure D1: To be continued.

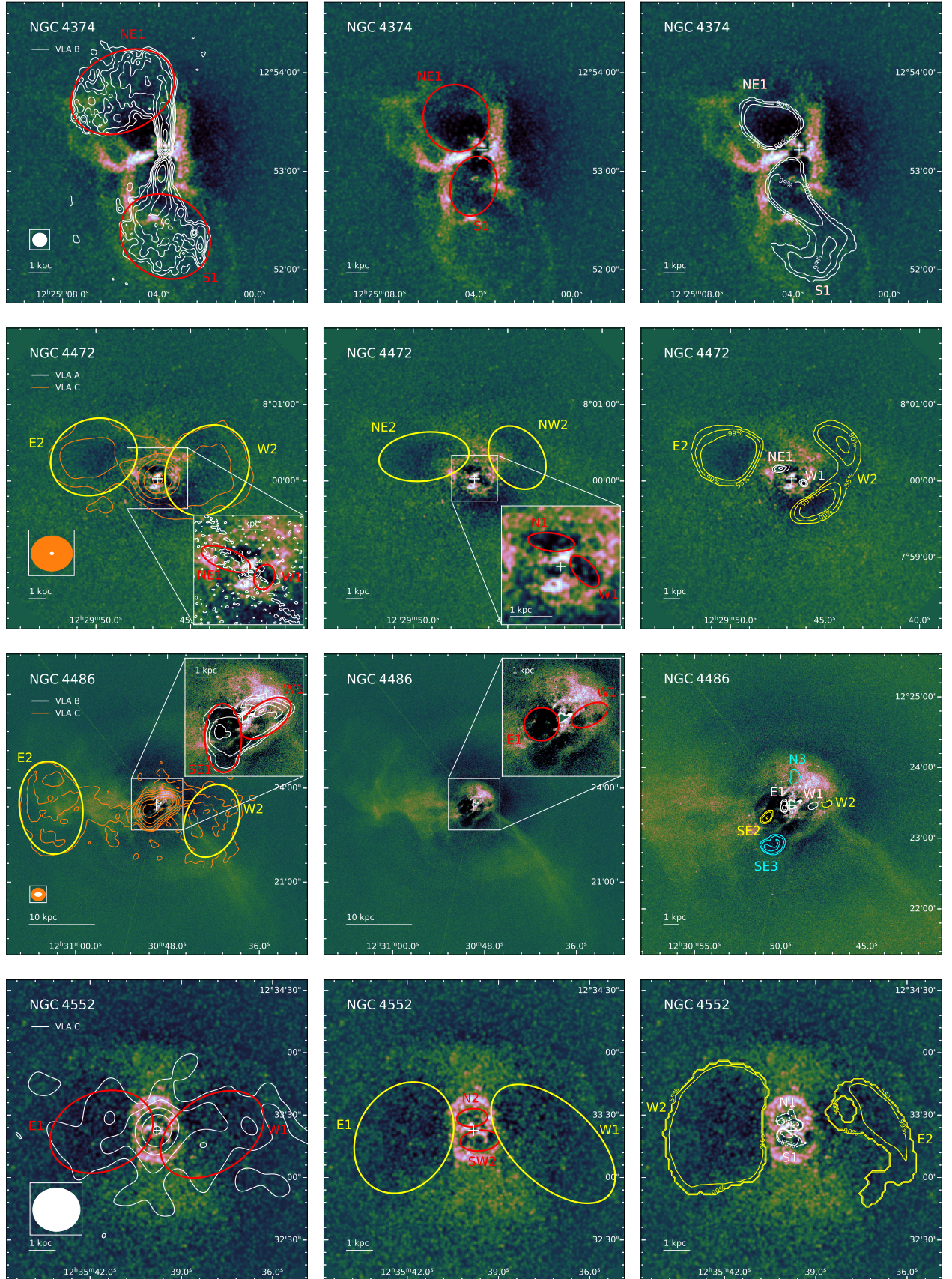


Figure D1: To be continued.

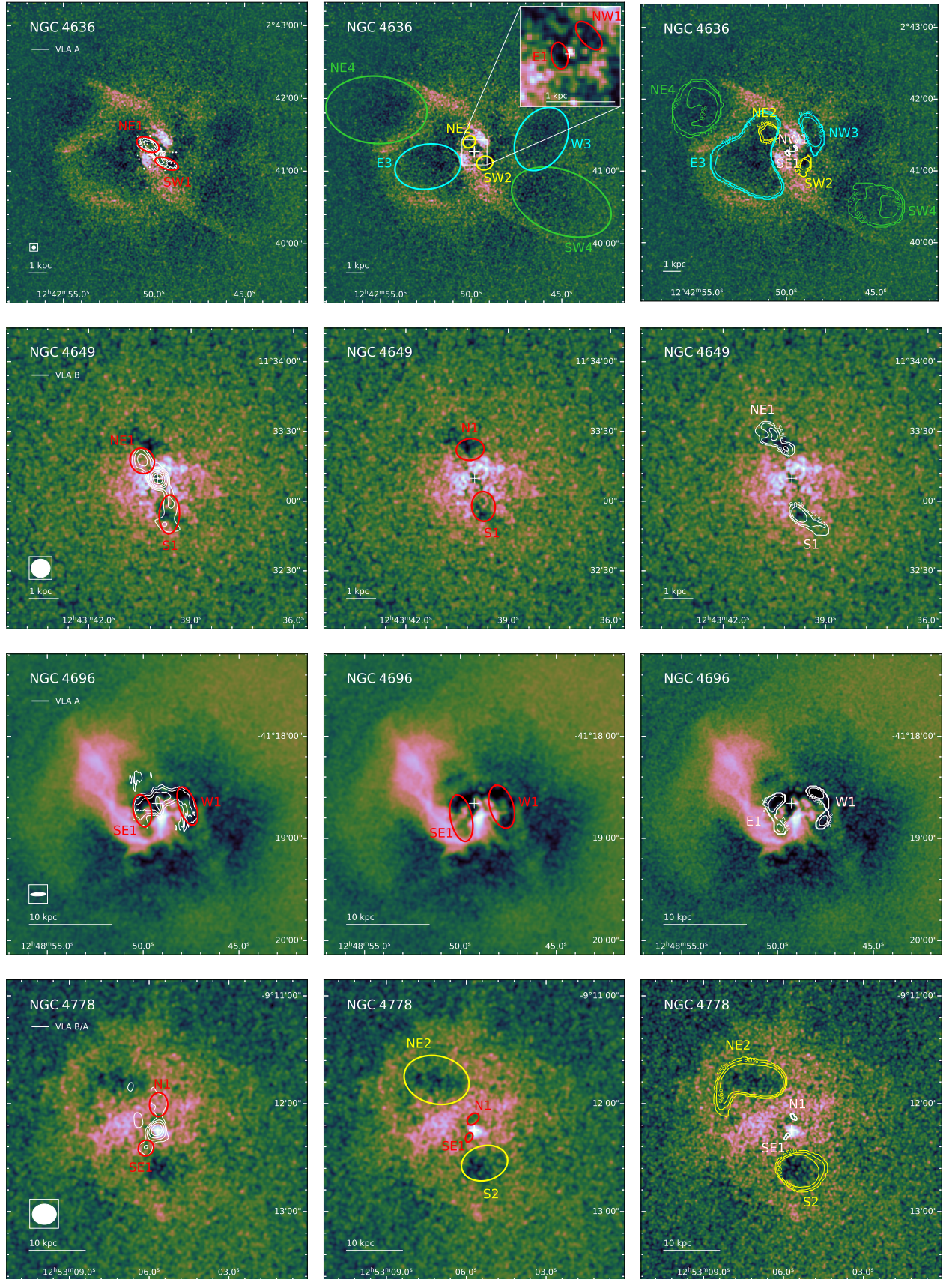


Figure D1: To be continued.

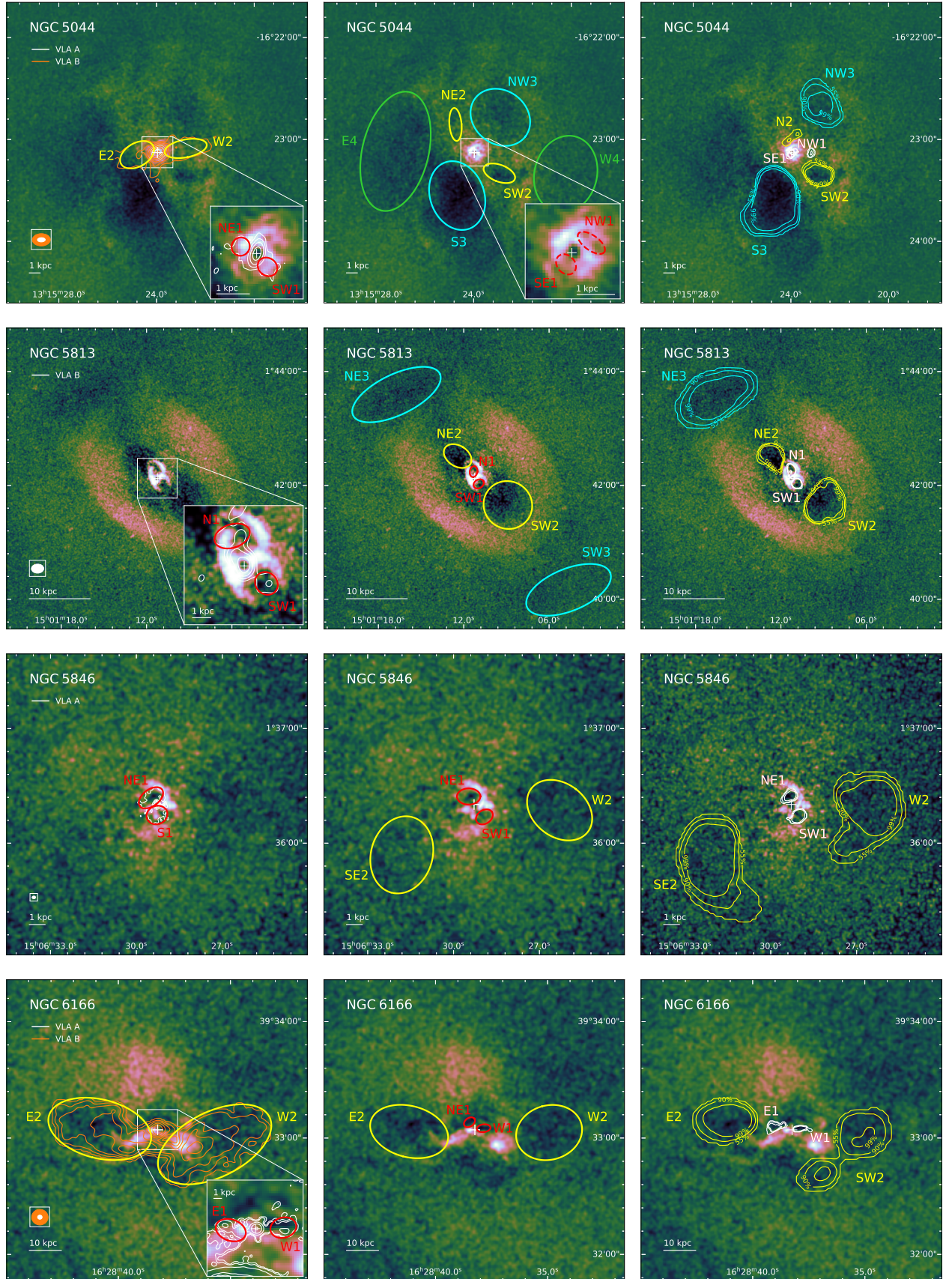


Figure D1: To be continued.

Figure D1: Comparison of individual methods used for X-ray cavity size estimation. The residual images obtained from β -modelling are superimposed by the corresponding cavity estimates: residual image overlaid by radio contours of VLA observations and ellipses marking the estimated sizes of radio lobes (*left*), residual image with ellipses marking the sizes of X-ray cavities (*centre*) and residual image overlaid by the predictions of the *CADET_size* network (*right*). Multiple VLA array configurations as well as cavity generations, were differentiated by different colors. The individual cavities are labeled with their corresponding directions from the centre and their generations (e.g. NW1 represents the youngest cavity of generation 1 located in the North-West from the centre of the galaxy).

Galaxy	Method	Cavity	d (kpc)	V (m^3)	E (erg)	t_{sound} (Myr)	$P_{\text{cav,sound}}$ (erg/s)	t_{bouy} (Myr)	$P_{\text{cav,bouy}}$ (erg/s)
IC 4296	Radio	SE1	243	$3.24 \cdot 10^{64}$	$1.9_{-1.0}^{+1.9} \cdot 10^{59}$	448	$1.3_{-0.7}^{+1.4} \cdot 10^{43}$	998	$6.0_{-2.7}^{+6.7} \cdot 10^{42}$
	Radio	NW1	158	$4.70 \cdot 10^{64}$	$2.8_{-1.5}^{+2.8} \cdot 10^{59}$	291	$3.0_{-1.5}^{+3.2} \cdot 10^{43}$	491	$1.8_{-0.8}^{+2.0} \cdot 10^{43}$
	X-ray visual	SE1	0.461	$3.21 \cdot 10^{57}$	$8.1_{-4.3}^{+8.2} \cdot 10^{54}$	1.02	$2.5_{-1.2}^{+2.7} \cdot 10^{41}$	1.21	$2.1_{-1.0}^{+2.3} \cdot 10^{41}$
	X-ray visual	NW1	0.548	$3.67 \cdot 10^{57}$	$7.9_{-8.0}^{+4.1} \cdot 10^{54}$	1.2	$2.1_{-1.0}^{+2.2} \cdot 10^{41}$	1.54	$1.6_{-0.8}^{+1.8} \cdot 10^{41}$
	X-ray CADET	SE1	1.27	$1.43 \cdot 10^{59}$	$8.0_{-4.2}^{+8.1} \cdot 10^{55}$	2.74	$9.2_{-4.7}^{+9.6} \cdot 10^{41}$	2.94	$8.6_{-4.2}^{+9.0} \cdot 10^{41}$
	X-ray CADET	NW1	1.35	$9.49 \cdot 10^{58}$	$5.1_{-2.7}^{+5.2} \cdot 10^{55}$	2.91	$5.6_{-2.8}^{+5.8} \cdot 10^{41}$	3.46	$4.7_{-2.3}^{+4.9} \cdot 10^{41}$
NGC 507	Radio	NW1	11.1	$2.73 \cdot 10^{62}$	$2.6_{-1.3}^{+2.6} \cdot 10^{58}$	19	$4.4_{-2.1}^{+4.5} \cdot 10^{43}$	24.2	$3.4_{-1.6}^{+3.7} \cdot 10^{43}$
	Radio	SE1	19.9	$6.11 \cdot 10^{62}$	$4.1_{-2.1}^{+4.1} \cdot 10^{58}$	35.9	$3.6_{-1.8}^{+3.7} \cdot 10^{43}$	50.7	$2.6_{-1.2}^{+2.7} \cdot 10^{43}$
	X-ray visual	N1	6.71	$1.47 \cdot 10^{61}$	$2.3_{-1.2}^{+2.3} \cdot 10^{57}$	11.5	$6.4_{-3.1}^{+6.6} \cdot 10^{42}$	18.5	$3.9_{-1.8}^{+4.3} \cdot 10^{42}$
	X-ray visual	SW1	7.77	$2.71 \cdot 10^{61}$	$3.7_{-3.7}^{+1.9} \cdot 10^{57}$	13	$9.0_{-4.4}^{+9.3} \cdot 10^{42}$	20.8	$5.6_{-2.5}^{+6.1} \cdot 10^{42}$
	X-ray CADET	SW1	3.34	$4.09 \cdot 10^{60}$	$1.2_{-0.6}^{+1.2} \cdot 10^{57}$	6.07	$6.4_{-3.1}^{+6.6} \cdot 10^{42}$	8.04	$4.8_{-2.2}^{+5.2} \cdot 10^{42}$
	X-ray CADET	NE1	3.9	$2.53 \cdot 10^{60}$	$6.8_{-3.5}^{+6.8} \cdot 10^{56}$	7.01	$3.1_{-1.5}^{+3.2} \cdot 10^{42}$	11	$2.0_{-0.9}^{+2.1} \cdot 10^{42}$
	X-ray visual	NW2	17.2	$5.82 \cdot 10^{61}$	$4.2_{-2.1}^{+4.2} \cdot 10^{57}$	31.3	$4.3_{-2.1}^{+4.4} \cdot 10^{42}$	60.6	$2.2_{-1.1}^{+2.3} \cdot 10^{42}$
	X-ray visual	SE2	16.6	$1.38 \cdot 10^{62}$	$1.1_{-1.1}^{+0.5} \cdot 10^{58}$	30.2	$1.1_{-0.5}^{+1.1} \cdot 10^{43}$	49.6	$6.7_{-3.1}^{+7.2} \cdot 10^{42}$
	X-ray CADET	SW2	6.96	$7.84 \cdot 10^{61}$	$1.1_{-0.6}^{+1.1} \cdot 10^{58}$	11.8	$2.9_{-1.4}^{+3.0} \cdot 10^{43}$	14.8	$2.3_{-1.0}^{+2.5} \cdot 10^{43}$
	X-ray CADET	N2	14.4	$6.80 \cdot 10^{62}$	$5.0_{-2.5}^{+5.0} \cdot 10^{58}$	25.8	$6.1_{-3.0}^{+6.3} \cdot 10^{43}$	30.7	$5.1_{-2.4}^{+5.5} \cdot 10^{43}$
NGC 708	Radio	NE1	2.73	$1.02 \cdot 10^{59}$	$6.7_{-3.4}^{+6.7} \cdot 10^{55}$	5.29	$4.0_{-1.9}^{+4.1} \cdot 10^{41}$	14.5	$1.5_{-0.7}^{+1.5} \cdot 10^{41}$
	Radio	W1	2.39	$1.04 \cdot 10^{59}$	$7.2_{-3.6}^{+7.2} \cdot 10^{55}$	4.63	$4.9_{-2.4}^{+5.0} \cdot 10^{41}$	11.8	$1.9_{-0.9}^{+2.0} \cdot 10^{41}$
	X-ray visual	E1	4.05	$2.30 \cdot 10^{60}$	$1.2_{-0.6}^{+1.2} \cdot 10^{57}$	7.71	$5.0_{-2.5}^{+5.1} \cdot 10^{42}$	15.6	$2.5_{-1.2}^{+2.6} \cdot 10^{42}$
	X-ray visual	W1	5.4	$2.85 \cdot 10^{60}$	$1.3_{-1.3}^{+0.6} \cdot 10^{57}$	9.86	$4.0_{-2.0}^{+4.1} \cdot 10^{42}$	23.2	$1.7_{-0.8}^{+1.8} \cdot 10^{42}$
	X-ray CADET	W1	12	$1.04 \cdot 10^{61}$	$2.6_{-1.3}^{+2.6} \cdot 10^{57}$	18.5	$4.4_{-2.2}^{+4.4} \cdot 10^{42}$	61.7	$1.3_{-0.6}^{+1.3} \cdot 10^{42}$
	X-ray CADET	E1	5.39	$9.37 \cdot 10^{60}$	$4.2_{-2.1}^{+4.2} \cdot 10^{57}$	9.84	$1.3_{-0.7}^{+1.4} \cdot 10^{43}$	18.9	$7.0_{-3.4}^{+7.1} \cdot 10^{42}$
	Radio	E2	5.63	$7.28 \cdot 10^{60}$	$3.1_{-1.6}^{+3.1} \cdot 10^{57}$	10.2	$9.7_{-4.8}^{+9.8} \cdot 10^{42}$	21.1	$4.7_{-2.3}^{+4.8} \cdot 10^{42}$
	Radio	W2	6.15	$6.79 \cdot 10^{60}$	$2.8_{-1.4}^{+2.8} \cdot 10^{57}$	11	$8.1_{-4.0}^{+8.2} \cdot 10^{42}$	24.3	$3.7_{-1.8}^{+3.7} \cdot 10^{42}$
NGC 1316	Radio	E1	3.82	$2.46 \cdot 10^{59}$	$2.2_{-1.1}^{+2.2} \cdot 10^{55}$	8.84	$7.8_{-3.4}^{+8.5} \cdot 10^{40}$	20.6	$3.4_{-1.4}^{+3.8} \cdot 10^{40}$
	Radio	NW1	3.5	$2.79 \cdot 10^{59}$	$2.4_{-1.2}^{+2.4} \cdot 10^{55}$	7.97	$9.4_{-4.2}^{+10.2} \cdot 10^{40}$	17.7	$4.2_{-1.8}^{+4.8} \cdot 10^{40}$
	X-ray visual	SE1	0.733	$2.39 \cdot 10^{58}$	$2.1_{-1.1}^{+2.1} \cdot 10^{55}$	1.63	$4.0_{-2.0}^{+4.2} \cdot 10^{41}$	2.55	$2.6_{-1.2}^{+2.7} \cdot 10^{41}$
	X-ray visual	NW1	0.745	$1.65 \cdot 10^{58}$	$1.4_{-1.4}^{+0.7} \cdot 10^{55}$	1.66	$2.7_{-1.3}^{+2.8} \cdot 10^{41}$	2.79	$1.6_{-0.8}^{+1.7} \cdot 10^{41}$
	X-ray CADET	SE1	0.849	$5.08 \cdot 10^{58}$	$3.6_{-1.8}^{+3.6} \cdot 10^{55}$	1.87	$6.1_{-3.0}^{+6.3} \cdot 10^{41}$	2.81	$4.1_{-1.9}^{+4.3} \cdot 10^{41}$
	X-ray CADET	NW1	0.746	$1.98 \cdot 10^{58}$	$1.7_{-0.9}^{+1.7} \cdot 10^{55}$	1.66	$3.3_{-1.6}^{+3.4} \cdot 10^{41}$	2.71	$2.0_{-1.0}^{+2.1} \cdot 10^{41}$
	X-ray CADET	SE2	2.87	$2.43 \cdot 10^{60}$	$2.4_{-1.2}^{+2.4} \cdot 10^{56}$	6.35	$1.2_{-0.5}^{+1.3} \cdot 10^{42}$	9.14	$8.4_{-3.6}^{+9.5} \cdot 10^{41}$
	X-ray CADET	N2	2.55	$5.69 \cdot 10^{60}$	$5.6_{-2.9}^{+5.7} \cdot 10^{56}$	5.57	$3.2_{-1.4}^{+3.4} \cdot 10^{42}$	6.65	$2.7_{-1.1}^{+3.0} \cdot 10^{42}$
NGC 1399	Radio	S1	0.683	$4.46 \cdot 10^{57}$	$8.5_{-4.2}^{+8.5} \cdot 10^{54}$	1.38	$1.9_{-1.0}^{+1.9} \cdot 10^{41}$	2.04	$1.3_{-0.6}^{+1.3} \cdot 10^{41}$
	Radio	N1	0.899	$6.60 \cdot 10^{57}$	$8.1_{-4.1}^{+8.2} \cdot 10^{54}$	1.82	$1.4_{-0.7}^{+1.4} \cdot 10^{41}$	2.89	$8.9_{-4.4}^{+9.1} \cdot 10^{40}$
	X-ray visual	N1	0.624	$3.07 \cdot 10^{57}$	$5.5_{-2.8}^{+5.5} \cdot 10^{54}$	1.26	$1.4_{-0.7}^{+1.4} \cdot 10^{41}$	1.9	$9.2_{-4.5}^{+9.3} \cdot 10^{40}$
	X-ray visual	S1	0.649	$3.59 \cdot 10^{57}$	$6.1_{-6.1}^{+3.0} \cdot 10^{54}$	1.31	$1.5_{-0.7}^{+1.5} \cdot 10^{41}$	1.96	$9.8_{-4.8}^{+9.9} \cdot 10^{40}$
	X-ray CADET	S1	7.16	$1.28 \cdot 10^{60}$	$1.4_{-0.7}^{+1.4} \cdot 10^{56}$	12.2	$3.5_{-1.8}^{+3.6} \cdot 10^{41}$	26.9	$1.6_{-0.8}^{+1.7} \cdot 10^{41}$
	X-ray CADET	N1	6.35	$1.24 \cdot 10^{60}$	$1.4_{-0.7}^{+1.4} \cdot 10^{56}$	11	$4.0_{-2.0}^{+4.1} \cdot 10^{41}$	22.7	$2.0_{-0.9}^{+2.0} \cdot 10^{41}$
	Radio	S2	8.6	$9.15 \cdot 10^{60}$	$1.0_{-0.5}^{+1.0} \cdot 10^{57}$	14.5	$2.2_{-1.1}^{+2.2} \cdot 10^{42}$	25.6	$1.2_{-0.6}^{+1.3} \cdot 10^{42}$
	Radio	N2	8.01	$8.84 \cdot 10^{60}$	$9.9_{-5.0}^{+9.9} \cdot 10^{56}$	13.5	$2.3_{-1.1}^{+2.3} \cdot 10^{42}$	23.1	$1.3_{-0.6}^{+1.4} \cdot 10^{42}$
	X-ray visual	N2	6.79	$1.11 \cdot 10^{60}$	$1.2_{-0.6}^{+1.2} \cdot 10^{56}$	11.7	$3.3_{-1.6}^{+3.4} \cdot 10^{41}$	25.5	$1.5_{-0.7}^{+1.6} \cdot 10^{41}$
	X-ray visual	S2	7.58	$2.79 \cdot 10^{60}$	$3.0_{-3.0}^{+1.5} \cdot 10^{56}$	12.8	$7.5_{-3.7}^{+7.6} \cdot 10^{41}$	25.8	$3.7_{-1.8}^{+3.9} \cdot 10^{41}$

Table D1: To be continued.

Galaxy	Method	Cavity	d (kpc)	V (m^3)	E (erg)	t_{sound} (Myr)	$P_{\text{cav,sound}}$ (erg/s)	t_{bouy} (Myr)	$P_{\text{cav,bouy}}$ (erg/s)
NGC 1407	Radio	E1	2.26	$4.35 \cdot 10^{59}$	$7.8_{-4.0}^{+7.9} \cdot 10^{55}$	4.91	$5.0_{-2.5}^{+5.2} \cdot 10^{41}$	7.17	$3.5_{-1.7}^{+3.6} \cdot 10^{41}$
	Radio	W1	1.01	$1.58 \cdot 10^{59}$	$5.6_{-2.9}^{+5.6} \cdot 10^{55}$	2.1	$8.4_{-4.2}^{+8.7} \cdot 10^{41}$	2.52	$7.0_{-3.4}^{+7.4} \cdot 10^{41}$
	X-ray visual	NE1	1.69	$7.52 \cdot 10^{59}$	$1.4_{-0.7}^{+1.4} \cdot 10^{56}$	3.72	$1.2_{-0.6}^{+1.2} \cdot 10^{42}$	4.22	$1.0_{-0.5}^{+1.1} \cdot 10^{42}$
	X-ray visual	W1	2.66	$7.15 \cdot 10^{59}$	$8.4_{-8.5}^{+4.4} \cdot 10^{55}$	5.73	$4.6_{-2.4}^{+4.8} \cdot 10^{41}$	8.43	$3.1_{-1.6}^{+3.3} \cdot 10^{41}$
	X-ray CADET	SW1	2.54	$3.80 \cdot 10^{59}$	$5.7_{-3.0}^{+5.8} \cdot 10^{55}$	5.48	$3.3_{-1.7}^{+3.4} \cdot 10^{41}$	8.74	$2.1_{-1.1}^{+2.1} \cdot 10^{41}$
	X-ray CADET	NE1	2.4	$9.42 \cdot 10^{59}$	$1.2_{-0.6}^{+1.2} \cdot 10^{56}$	5.2	$7.5_{-3.9}^{+7.7} \cdot 10^{41}$	6.89	$5.6_{-2.9}^{+5.8} \cdot 10^{41}$
	X-ray CADET	S2	7.24	$5.40 \cdot 10^{60}$	$2.0_{-1.1}^{+2.1} \cdot 10^{56}$	13.9	$4.6_{-2.5}^{+4.8} \cdot 10^{41}$	27	$2.4_{-1.2}^{+2.5} \cdot 10^{41}$
	X-ray CADET	N2	7.56	$7.36 \cdot 10^{60}$	$2.5_{-1.4}^{+2.6} \cdot 10^{56}$	14.4	$5.6_{-3.0}^{+5.8} \cdot 10^{41}$	27.4	$2.9_{-1.5}^{+3.1} \cdot 10^{41}$
NGC 1600	Radio	N1	1.08	$2.39 \cdot 10^{59}$	$2.3_{-1.2}^{+2.3} \cdot 10^{56}$	2.06	$3.5_{-1.7}^{+3.6} \cdot 10^{42}$	2.1	$3.4_{-1.5}^{+3.8} \cdot 10^{42}$
	Radio	S1	2	$2.15 \cdot 10^{59}$	$1.2_{-0.6}^{+1.2} \cdot 10^{56}$	3.84	$9.5_{-4.5}^{+10.0} \cdot 10^{41}$	5.39	$6.8_{-3.0}^{+7.5} \cdot 10^{41}$
	X-ray visual	N1	0.839	$1.09 \cdot 10^{59}$	$1.1_{-0.6}^{+1.1} \cdot 10^{56}$	1.59	$2.3_{-1.1}^{+2.4} \cdot 10^{42}$	1.63	$2.2_{-1.0}^{+2.4} \cdot 10^{42}$
	X-ray visual	S1	1.23	$5.45 \cdot 10^{58}$	$4.9_{-4.9}^{+2.5} \cdot 10^{55}$	2.35	$6.6_{-3.2}^{+6.9} \cdot 10^{41}$	3.26	$4.8_{-2.1}^{+5.2} \cdot 10^{41}$
	X-ray CADET	S1	1.34	$4.77 \cdot 10^{58}$	$4.2_{-2.1}^{+4.2} \cdot 10^{55}$	2.57	$5.1_{-2.4}^{+5.4} \cdot 10^{41}$	3.8	$3.5_{-1.5}^{+3.8} \cdot 10^{41}$
	X-ray CADET	N1	1.07	$6.98 \cdot 10^{58}$	$6.9_{-3.5}^{+6.9} \cdot 10^{55}$	2.03	$1.1_{-0.5}^{+1.1} \cdot 10^{42}$	2.52	$8.7_{-3.9}^{+9.6} \cdot 10^{41}$
NGC 4261	Radio	E1	24.7	$4.01 \cdot 10^{62}$	$1.3_{-0.7}^{+1.3} \cdot 10^{58}$	41.1	$9.9_{-4.7}^{+10.5} \cdot 10^{42}$	74.1	$5.5_{-2.2}^{+6.3} \cdot 10^{42}$
	Radio	W1	20.7	$3.34 \cdot 10^{62}$	$1.1_{-0.5}^{+1.1} \cdot 10^{58}$	34.4	$9.7_{-4.6}^{+10.3} \cdot 10^{42}$	58.6	$5.7_{-2.3}^{+6.5} \cdot 10^{42}$
	X-ray visual	E1	0.302	$1.04 \cdot 10^{57}$	$3.2_{-1.6}^{+3.2} \cdot 10^{54}$	0.696	$1.4_{-0.7}^{+1.5} \cdot 10^{41}$	0.856	$1.2_{-0.6}^{+1.2} \cdot 10^{41}$
	X-ray visual	W1	0.43	$2.34 \cdot 10^{57}$	$4.9_{-4.9}^{+2.4} \cdot 10^{54}$	0.986	$1.6_{-0.8}^{+1.6} \cdot 10^{41}$	1.27	$1.2_{-0.6}^{+1.2} \cdot 10^{41}$
	X-ray CADET	E1	6.26	$4.56 \cdot 10^{61}$	$1.6_{-0.8}^{+1.6} \cdot 10^{57}$	11.9	$4.1_{-1.9}^{+4.4} \cdot 10^{42}$	13.6	$3.6_{-1.5}^{+4.1} \cdot 10^{42}$
	X-ray CADET	W1	6.9	$3.69 \cdot 10^{61}$	$1.3_{-0.7}^{+1.3} \cdot 10^{57}$	12.9	$3.3_{-1.5}^{+3.5} \cdot 10^{42}$	16.3	$2.6_{-1.1}^{+2.9} \cdot 10^{42}$
NGC 4374	Radio	NE1	3.31	$4.37 \cdot 10^{60}$	$4.1_{-2.1}^{+4.2} \cdot 10^{56}$	7.17	$1.8_{-0.9}^{+1.9} \cdot 10^{42}$	8.28	$1.6_{-0.8}^{+1.6} \cdot 10^{42}$
	Radio	S1	4.06	$2.81 \cdot 10^{60}$	$2.3_{-1.2}^{+2.3} \cdot 10^{56}$	8.53	$8.6_{-4.2}^{+8.8} \cdot 10^{41}$	12.1	$6.1_{-2.9}^{+6.3} \cdot 10^{41}$
	X-ray visual	NE1	1.99	$5.11 \cdot 10^{59}$	$8.0_{-4.1}^{+8.0} \cdot 10^{55}$	4.7	$5.4_{-2.6}^{+5.6} \cdot 10^{41}$	5.51	$4.6_{-2.2}^{+4.8} \cdot 10^{41}$
	X-ray visual	S1	1.82	$2.23 \cdot 10^{59}$	$3.9_{-3.9}^{+2.0} \cdot 10^{55}$	4.33	$2.8_{-1.4}^{+2.9} \cdot 10^{41}$	5.53	$2.2_{-1.1}^{+2.3} \cdot 10^{41}$
	X-ray CADET	S1	3.94	$1.21 \cdot 10^{60}$	$1.2_{-0.6}^{+1.2} \cdot 10^{56}$	8.29	$4.7_{-2.3}^{+4.7} \cdot 10^{41}$	13.3	$2.9_{-1.4}^{+3.0} \cdot 10^{41}$
	X-ray CADET	NE1	1.88	$4.72 \cdot 10^{59}$	$7.9_{-4.0}^{+7.9} \cdot 10^{55}$	4.47	$5.6_{-2.7}^{+5.8} \cdot 10^{41}$	5.14	$4.9_{-2.3}^{+5.1} \cdot 10^{41}$
NGC 4472	Radio	W1	0.594	$8.60 \cdot 10^{57}$	$1.0_{-0.5}^{+1.0} \cdot 10^{55}$	1.26	$2.6_{-1.3}^{+2.6} \cdot 10^{41}$	1.75	$1.8_{-0.9}^{+1.9} \cdot 10^{41}$
	Radio	NE1	0.889	$1.42 \cdot 10^{58}$	$1.4_{-0.7}^{+1.4} \cdot 10^{55}$	1.87	$2.4_{-1.2}^{+2.4} \cdot 10^{41}$	2.94	$1.5_{-0.8}^{+1.5} \cdot 10^{41}$
	X-ray visual	N1	0.638	$8.67 \cdot 10^{57}$	$1.0_{-0.5}^{+1.0} \cdot 10^{55}$	1.35	$2.4_{-1.2}^{+2.4} \cdot 10^{41}$	1.94	$1.6_{-0.8}^{+1.6} \cdot 10^{41}$
	X-ray visual	W1	0.591	$3.03 \cdot 10^{57}$	$3.9_{-3.9}^{+2.0} \cdot 10^{54}$	1.25	$10.0_{-4.9}^{+10.0} \cdot 10^{40}$	2.07	$6.0_{-3.0}^{+6.1} \cdot 10^{40}$
	X-ray CADET	W1	0.785	$4.27 \cdot 10^{57}$	$4.1_{-2.0}^{+4.1} \cdot 10^{54}$	1.65	$7.9_{-3.9}^{+7.9} \cdot 10^{40}$	2.99	$4.3_{-2.1}^{+4.4} \cdot 10^{40}$
	X-ray CADET	NE1	0.94	$1.11 \cdot 10^{58}$	$8.6_{-4.3}^{+8.6} \cdot 10^{54}$	1.97	$1.4_{-0.7}^{+1.4} \cdot 10^{41}$	3.33	$8.2_{-4.0}^{+8.2} \cdot 10^{40}$
	Radio	E2	4.22	$1.90 \cdot 10^{60}$	$2.5_{-1.2}^{+2.5} \cdot 10^{56}$	8.26	$9.5_{-4.7}^{+9.6} \cdot 10^{41}$	13.4	$5.9_{-2.9}^{+6.0} \cdot 10^{41}$
	Radio	W2	3.17	$2.77 \cdot 10^{60}$	$4.8_{-2.4}^{+4.9} \cdot 10^{56}$	6.37	$2.4_{-1.2}^{+2.4} \cdot 10^{42}$	8.25	$1.9_{-0.9}^{+1.9} \cdot 10^{42}$
	X-ray visual	NW2	3	$9.18 \cdot 10^{59}$	$1.6_{-0.8}^{+1.6} \cdot 10^{56}$	6.04	$8.5_{-4.2}^{+8.6} \cdot 10^{41}$	9.09	$5.6_{-2.8}^{+5.7} \cdot 10^{41}$
	X-ray visual	NE2	3.46	$8.18 \cdot 10^{59}$	$1.4_{-1.4}^{+0.7} \cdot 10^{56}$	6.9	$6.4_{-3.2}^{+6.4} \cdot 10^{41}$	11.5	$3.8_{-1.9}^{+3.9} \cdot 10^{41}$
NGC 4486	X-ray CADET	W2	2.77	$1.67 \cdot 10^{60}$	$2.9_{-1.5}^{+2.9} \cdot 10^{56}$	5.62	$1.6_{-0.8}^{+1.6} \cdot 10^{42}$	7.32	$1.2_{-0.6}^{+1.3} \cdot 10^{42}$
	X-ray CADET	E2	4.34	$1.66 \cdot 10^{60}$	$2.2_{-1.1}^{+2.2} \cdot 10^{56}$	8.47	$8.2_{-4.0}^{+8.2} \cdot 10^{41}$	14.4	$4.8_{-2.4}^{+4.9} \cdot 10^{41}$
	Radio	SE1	1.8	$7.89 \cdot 10^{59}$	$1.2_{-0.6}^{+1.2} \cdot 10^{57}$	2.89	$1.4_{-0.7}^{+1.4} \cdot 10^{43}$	3.79	$1.0_{-0.5}^{+1.1} \cdot 10^{43}$
	Radio	W1	1.56	$2.48 \cdot 10^{59}$	$4.3_{-2.1}^{+4.3} \cdot 10^{56}$	2.64	$5.1_{-2.5}^{+5.2} \cdot 10^{42}$	3.7	$3.7_{-1.7}^{+3.8} \cdot 10^{42}$
NGC 4486	X-ray visual	E1	1.25	$1.74 \cdot 10^{59}$	$3.3_{-1.7}^{+3.3} \cdot 10^{56}$	2.28	$4.6_{-2.3}^{+4.6} \cdot 10^{42}$	2.82	$3.7_{-1.8}^{+3.8} \cdot 10^{42}$
	X-ray visual	W1	2.03	$7.23 \cdot 10^{58}$	$1.2_{-1.2}^{+0.6} \cdot 10^{56}$	3.15	$1.2_{-0.6}^{+1.2} \cdot 10^{42}$	6.74	$5.5_{-2.6}^{+5.7} \cdot 10^{41}$
	X-ray CADET	E1	0.43	$2.12 \cdot 10^{58}$	$6.2_{-3.1}^{+6.2} \cdot 10^{55}$	0.807	$2.4_{-1.2}^{+2.5} \cdot 10^{42}$	0.808	$2.4_{-1.1}^{+2.6} \cdot 10^{42}$
	X-ray CADET	W1	1.53	$9.83 \cdot 10^{57}$	$1.7_{-0.9}^{+1.7} \cdot 10^{55}$	2.61	$2.1_{-1.0}^{+2.1} \cdot 10^{41}$	6.17	$8.7_{-4.1}^{+9.1} \cdot 10^{40}$

Table D1: To be continued.

Galaxy	Method	Cavity	d (kpc)	V (m^3)	E (erg)	t_{sound} (Myr)	$P_{\text{cav,sound}}$ (erg/s)	t_{bouy} (Myr)	$P_{\text{cav,bouy}}$ (erg/s)
NGC 4486*	Radio	E2	15.9	$3.10 \cdot 10^{61}$	$2.1^{+2.1}_{-1.0} \cdot 10^{58}$	22.7	$2.9^{+2.9}_{-1.4} \cdot 10^{43}$	54.1	$1.2^{+1.2}_{-0.6} \cdot 10^{43}$
	Radio	W2	8.82	$1.65 \cdot 10^{61}$	$8.7^{+8.7}_{-4.4} \cdot 10^{57}$	13.6	$2.0^{+2.0}_{-1.0} \cdot 10^{43}$	24.8	$1.1^{+1.2}_{-0.5} \cdot 10^{43}$
	X-ray CADET	SE2	1.8	$2.05 \cdot 10^{58}$	$3.5^{+3.5}_{-1.8} \cdot 10^{55}$	2.89	$3.9^{+3.9}_{-1.9} \cdot 10^{41}$	6.94	$1.6^{+1.7}_{-0.8} \cdot 10^{41}$
	X-ray CADET	W2	2.48	$9.57 \cdot 10^{57}$	$1.5^{+1.5}_{-0.7} \cdot 10^{55}$	3.9	$1.2^{+1.2}_{-0.6} \cdot 10^{41}$	12.8	$3.6^{+3.7}_{-1.7} \cdot 10^{40}$
NGC 4552	Radio	E1	2.12	$5.73 \cdot 10^{59}$	$9.5^{+9.5}_{-4.8} \cdot 10^{55}$	5.65	$5.3^{+5.6}_{-2.4} \cdot 10^{41}$	6.6	$4.5^{+4.8}_{-2.1} \cdot 10^{41}$
	Radio	W1	2.15	$5.48 \cdot 10^{59}$	$7.8^{+7.8}_{-3.9} \cdot 10^{55}$	5.75	$4.3^{+4.6}_{-2.0} \cdot 10^{41}$	6.76	$3.7^{+3.9}_{-1.7} \cdot 10^{41}$
	X-ray visual	N1	0.487	$1.49 \cdot 10^{58}$	$1.1^{+1.1}_{-0.6} \cdot 10^{55}$	1.12	$3.2^{+3.3}_{-1.5} \cdot 10^{41}$	1.34	$2.7^{+2.8}_{-1.3} \cdot 10^{41}$
	X-ray visual	SW1	0.463	$2.79 \cdot 10^{58}$	$2.1^{+1.1}_{-2.1} \cdot 10^{55}$	1.06	$6.2^{+6.5}_{-3.0} \cdot 10^{41}$	1.11	$5.9^{+6.3}_{-2.8} \cdot 10^{41}$
	X-ray CADET	S1	0.322	$1.68 \cdot 10^{58}$	$1.6^{+1.6}_{-0.8} \cdot 10^{55}$	0.704	$7.0^{+7.3}_{-3.4} \cdot 10^{41}$	0.702	$7.1^{+7.5}_{-3.3} \cdot 10^{41}$
	X-ray CADET	N1	0.383	$1.35 \cdot 10^{58}$	$1.2^{+1.2}_{-0.6} \cdot 10^{55}$	0.87	$4.3^{+4.5}_{-2.1} \cdot 10^{41}$	0.947	$3.9^{+4.2}_{-1.9} \cdot 10^{41}$
	X-ray visual	E2	2.7	$1.11 \cdot 10^{60}$	$1.0^{+1.0}_{-0.5} \cdot 10^{56}$	7.82	$4.1^{+4.5}_{-1.8} \cdot 10^{41}$	8.5	$3.8^{+4.1}_{-1.6} \cdot 10^{41}$
	X-ray visual	W2	3.1	$8.70 \cdot 10^{59}$	$6.0^{+3.0}_{-6.0} \cdot 10^{55}$	9.18	$2.1^{+2.3}_{-0.9} \cdot 10^{41}$	10.9	$1.7^{+1.9}_{-0.8} \cdot 10^{41}$
	X-ray CADET	W2	3.4	$6.77 \cdot 10^{59}$	$4.2^{+4.2}_{-2.1} \cdot 10^{55}$	10.3	$1.3^{+1.5}_{-0.6} \cdot 10^{41}$	13	$1.0^{+1.1}_{-0.4} \cdot 10^{41}$
	X-ray CADET	E2	2.82	$2.22 \cdot 10^{60}$	$1.8^{+1.8}_{-0.9} \cdot 10^{56}$	8.2	$6.8^{+7.6}_{-3.0} \cdot 10^{41}$	8.06	$6.9^{+7.6}_{-3.0} \cdot 10^{41}$
NGC 4636	X-ray visual	E1	0.15	$5.73 \cdot 10^{56}$	$4.1^{+5.3}_{-2.4} \cdot 10^{53}$	0.502	$2.6^{+8.3}_{-0.3} \cdot 10^{40}$	0.491	$2.6^{+4.6}_{-0.3} \cdot 10^{40}$
	X-ray visual	NW1	0.39	$1.00 \cdot 10^{57}$	$8.4^{+5.0}_{-10.8} \cdot 10^{53}$	1.17	$2.3^{+6.6}_{-0.5} \cdot 10^{40}$	1.88	$1.4^{+2.5}_{-0.2} \cdot 10^{40}$
	X-ray CADET	SE1	0.122	$8.55 \cdot 10^{56}$	$6.1^{+7.9}_{-3.6} \cdot 10^{53}$	0.41	$4.7^{+15.3}_{-0.5} \cdot 10^{40}$	0.336	$5.7^{+10.1}_{-0.6} \cdot 10^{40}$
	X-ray CADET	NW1	0.451	$7.68 \cdot 10^{56}$	$6.7^{+6.7}_{-3.4} \cdot 10^{53}$	1.28	$1.7^{+1.8}_{-0.8} \cdot 10^{40}$	2.45	$8.7^{+9.2}_{-4.0} \cdot 10^{39}$
	Radio	NE2	0.685	$1.32 \cdot 10^{58}$	$1.0^{+1.0}_{-0.5} \cdot 10^{55}$	1.67	$1.9^{+2.0}_{-0.9} \cdot 10^{41}$	2.85	$1.1^{+1.2}_{-0.5} \cdot 10^{41}$
	Radio	SW2	0.891	$8.72 \cdot 10^{57}$	$6.0^{+6.0}_{-3.0} \cdot 10^{54}$	2.14	$8.9^{+9.1}_{-4.3} \cdot 10^{40}$	4.53	$4.2^{+4.3}_{-2.0} \cdot 10^{40}$
	X-ray visual	NE2	0.654	$5.97 \cdot 10^{57}$	$5.4^{+5.4}_{-2.7} \cdot 10^{54}$	1.63	$1.1^{+1.1}_{-0.5} \cdot 10^{41}$	3.04	$5.7^{+6.0}_{-2.6} \cdot 10^{40}$
	X-ray visual	SW2	0.897	$1.13 \cdot 10^{58}$	$7.7^{+3.9}_{-7.7} \cdot 10^{54}$	2.16	$1.1^{+1.2}_{-0.5} \cdot 10^{41}$	4.38	$5.6^{+5.7}_{-2.7} \cdot 10^{40}$
	X-ray CADET	SW2	1.25	$2.16 \cdot 10^{58}$	$8.7^{+8.7}_{-4.4} \cdot 10^{54}$	3.06	$9.0^{+9.2}_{-4.4} \cdot 10^{40}$	6.46	$4.3^{+4.4}_{-2.0} \cdot 10^{40}$
	X-ray CADET	NE2	1.65	$3.61 \cdot 10^{58}$	$9.2^{+9.2}_{-4.6} \cdot 10^{54}$	4.19	$6.9^{+7.3}_{-3.2} \cdot 10^{40}$	9.01	$3.2^{+3.4}_{-1.5} \cdot 10^{40}$
	X-ray visual	E3	2.86	$4.11 \cdot 10^{59}$	$6.5^{+6.5}_{-3.3} \cdot 10^{55}$	7.15	$2.9^{+3.0}_{-1.4} \cdot 10^{41}$	13.7	$1.5^{+1.6}_{-0.7} \cdot 10^{41}$
	X-ray visual	W3	4.01	$6.89 \cdot 10^{59}$	$9.3^{+4.7}_{-9.4} \cdot 10^{55}$	9.02	$3.3^{+3.3}_{-1.6} \cdot 10^{41}$	20.9	$1.4^{+1.4}_{-0.7} \cdot 10^{41}$
	X-ray CADET	E3	2.18	$1.71 \cdot 10^{60}$	$2.8^{+2.8}_{-1.4} \cdot 10^{56}$	5.82	$1.5^{+1.6}_{-0.7} \cdot 10^{42}$	7.21	$1.2^{+1.3}_{-0.6} \cdot 10^{42}$
	X-ray CADET	NW3	1.78	$1.92 \cdot 10^{59}$	$3.9^{+3.9}_{-2.0} \cdot 10^{55}$	4.58	$2.7^{+2.9}_{-1.3} \cdot 10^{41}$	7.65	$1.6^{+1.7}_{-0.8} \cdot 10^{41}$
	X-ray visual	NE4	6.24	$1.43 \cdot 10^{60}$	$1.5^{+1.5}_{-0.8} \cdot 10^{56}$	13.3	$3.6^{+3.7}_{-1.8} \cdot 10^{41}$	35.9	$1.4^{+1.4}_{-0.7} \cdot 10^{41}$
	X-ray visual	SW4	5.9	$1.28 \cdot 10^{60}$	$1.4^{+0.7}_{-1.4} \cdot 10^{56}$	12.6	$3.6^{+3.7}_{-1.8} \cdot 10^{41}$	33.6	$1.4^{+1.4}_{-0.7} \cdot 10^{41}$
	X-ray CADET	SW4	6.05	$5.86 \cdot 10^{59}$	$6.6^{+6.6}_{-3.3} \cdot 10^{55}$	12.9	$1.6^{+1.6}_{-0.8} \cdot 10^{41}$	39.8	$5.2^{+5.4}_{-2.5} \cdot 10^{40}$
	X-ray CADET	NE4	6.11	$8.75 \cdot 10^{59}$	$9.7^{+9.7}_{-4.9} \cdot 10^{55}$	13	$2.4^{+2.4}_{-1.2} \cdot 10^{41}$	37.7	$8.1^{+8.3}_{-3.9} \cdot 10^{40}$
NGC 4649	Radio	NE1	0.798	$9.24 \cdot 10^{57}$	$8.7^{+8.7}_{-4.4} \cdot 10^{54}$	1.64	$1.7^{+1.7}_{-0.8} \cdot 10^{41}$	2.3	$1.2^{+1.2}_{-0.6} \cdot 10^{41}$
	Radio	S1	1.31	$1.01 \cdot 10^{58}$	$4.8^{+4.8}_{-2.4} \cdot 10^{54}$	2.74	$5.6^{+5.6}_{-2.8} \cdot 10^{40}$	4.76	$3.2^{+3.3}_{-1.6} \cdot 10^{40}$
	X-ray visual	N1	1	$1.06 \cdot 10^{58}$	$7.1^{+7.1}_{-3.6} \cdot 10^{54}$	2.08	$1.1^{+1.1}_{-0.5} \cdot 10^{41}$	3.16	$7.1^{+7.2}_{-3.5} \cdot 10^{40}$
	X-ray visual	S1	1.02	$1.03 \cdot 10^{58}$	$6.7^{+3.4}_{-6.7} \cdot 10^{54}$	2.12	$1.0^{+1.0}_{-0.5} \cdot 10^{41}$	3.25	$6.5^{+6.6}_{-3.2} \cdot 10^{40}$
	X-ray CADET	S1	1.56	$1.86 \cdot 10^{58}$	$7.1^{+7.1}_{-3.6} \cdot 10^{54}$	3.27	$6.9^{+7.0}_{-3.4} \cdot 10^{40}$	5.59	$4.0^{+4.1}_{-2.0} \cdot 10^{40}$
	X-ray CADET	NE1	1.55	$1.98 \cdot 10^{58}$	$7.8^{+7.8}_{-3.9} \cdot 10^{54}$	3.24	$7.7^{+7.7}_{-3.8} \cdot 10^{40}$	5.47	$4.5^{+4.6}_{-2.2} \cdot 10^{40}$
NGC 4696	Radio	E1	2.22	$3.91 \cdot 10^{59}$	$3.6^{+3.6}_{-1.8} \cdot 10^{56}$	4.52	$2.5^{+2.6}_{-1.2} \cdot 10^{42}$	7.77	$1.5^{+1.6}_{-0.7} \cdot 10^{42}$
	Radio	W1	3.75	$5.00 \cdot 10^{59}$	$4.5^{+4.5}_{-2.3} \cdot 10^{56}$	6.87	$2.1^{+2.1}_{-1.0} \cdot 10^{42}$	16.4	$8.8^{+8.9}_{-4.3} \cdot 10^{41}$
	X-ray visual	SE1	2.38	$1.30 \cdot 10^{60}$	$1.2^{+1.2}_{-0.6} \cdot 10^{57}$	4.8	$7.9^{+8.3}_{-3.7} \cdot 10^{42}$	7.05	$5.4^{+5.9}_{-2.4} \cdot 10^{42}$
	X-ray visual	W1	3.34	$1.25 \cdot 10^{60}$	$1.1^{+0.6}_{-1.1} \cdot 10^{57}$	6.28	$5.7^{+5.7}_{-2.8} \cdot 10^{42}$	11.8	$3.0^{+3.1}_{-1.5} \cdot 10^{42}$
	X-ray CADET	E1	1.84	$1.12 \cdot 10^{60}$	$1.0^{+1.0}_{-0.5} \cdot 10^{57}$	3.77	$8.8^{+9.2}_{-4.1} \cdot 10^{42}$	4.9	$6.8^{+7.3}_{-3.0} \cdot 10^{42}$
	X-ray CADET	W1	3.88	$9.99 \cdot 10^{59}$	$9.0^{+9.0}_{-4.5} \cdot 10^{56}$	7.04	$4.0^{+4.1}_{-2.0} \cdot 10^{42}$	15.3	$1.9^{+1.9}_{-0.9} \cdot 10^{42}$

Table D1: To be continued.

Galaxy	Method	Cavity	d (kpc)	V (m^3)	E (erg)	t_{sound} (Myr)	$P_{\text{cav,sound}}$ (erg/s)	t_{bouy} (Myr)	$P_{\text{cav,bouy}}$ (erg/s)
NGC 4778	Radio	SE1	3.79	$3.20 \cdot 10^{59}$	$8.4^{+8.4}_{-4.3} \cdot 10^{55}$	8.21	$3.2^{+3.3}_{-1.6} \cdot 10^{41}$	17.3	$1.5^{+1.6}_{-0.7} \cdot 10^{41}$
	Radio	N1	4.54	$6.96 \cdot 10^{59}$	$1.6^{+1.6}_{-0.8} \cdot 10^{56}$	9.74	$5.1^{+5.2}_{-2.5} \cdot 10^{41}$	19.9	$2.5^{+2.6}_{-1.2} \cdot 10^{41}$
	X-ray visual	N1	1.96	$1.54 \cdot 10^{59}$	$7.0^{+7.0}_{-3.6} \cdot 10^{55}$	4.28	$5.2^{+5.5}_{-2.5} \cdot 10^{41}$	7.26	$3.0^{+3.3}_{-1.4} \cdot 10^{41}$
	X-ray visual	SE1	1.6	$3.65 \cdot 10^{58}$	$2.0^{+1.0}_{-2.0} \cdot 10^{55}$	3.49	$1.8^{+1.9}_{-0.9} \cdot 10^{41}$	6.8	$9.2^{+10.0}_{-4.2} \cdot 10^{40}$
	X-ray CADET	SE1	1.23	$3.46 \cdot 10^{58}$	$2.3^{+2.3}_{-1.2} \cdot 10^{55}$	2.71	$2.6^{+2.8}_{-1.3} \cdot 10^{41}$	4.61	$1.6^{+1.7}_{-0.7} \cdot 10^{41}$
	X-ray CADET	N1	2.47	$5.44 \cdot 10^{58}$	$2.1^{+2.1}_{-1.1} \cdot 10^{55}$	5.37	$1.2^{+1.3}_{-0.6} \cdot 10^{41}$	12.2	$5.5^{+5.7}_{-2.6} \cdot 10^{40}$
	X-ray visual	S2	6.19	$6.67 \cdot 10^{60}$	$1.1^{+1.1}_{-0.6} \cdot 10^{57}$	13	$2.8^{+2.8}_{-1.4} \cdot 10^{42}$	21.8	$1.6^{+1.7}_{-0.8} \cdot 10^{42}$
	X-ray visual	NE2	11.2	$1.32 \cdot 10^{61}$	$1.6^{+0.8}_{-1.6} \cdot 10^{57}$	22.6	$2.2^{+2.2}_{-1.1} \cdot 10^{42}$	47.1	$1.0^{+1.1}_{-0.5} \cdot 10^{42}$
	X-ray CADET	S2	7.3	$1.44 \cdot 10^{61}$	$2.2^{+2.2}_{-1.1} \cdot 10^{57}$	15.2	$4.7^{+4.7}_{-2.3} \cdot 10^{42}$	24.5	$2.9^{+3.0}_{-1.4} \cdot 10^{42}$
	X-ray CADET	NE2	11.8	$2.63 \cdot 10^{61}$	$3.0^{+3.0}_{-1.5} \cdot 10^{57}$	23.7	$4.0^{+4.0}_{-2.0} \cdot 10^{42}$	45.6	$2.1^{+2.1}_{-1.0} \cdot 10^{42}$
NGC 5044	Radio	NE1	0.521	$2.72 \cdot 10^{57}$	$2.8^{+2.8}_{-1.4} \cdot 10^{54}$	1.17	$7.5^{+7.9}_{-3.5} \cdot 10^{40}$	2.18	$4.0^{+4.4}_{-1.8} \cdot 10^{40}$
	Radio	SW1	0.532	$2.78 \cdot 10^{57}$	$2.8^{+2.8}_{-1.4} \cdot 10^{54}$	1.2	$7.5^{+7.9}_{-3.5} \cdot 10^{40}$	2.24	$4.0^{+4.3}_{-1.8} \cdot 10^{40}$
	X-ray visual	SE1	0.347	$2.52 \cdot 10^{57}$	$2.9^{+2.9}_{-1.5} \cdot 10^{54}$	0.783	$1.2^{+1.3}_{-0.5} \cdot 10^{41}$	1.2	$7.7^{+8.7}_{-3.4} \cdot 10^{40}$
	X-ray visual	NW1	0.582	$4.36 \cdot 10^{57}$	$4.3^{+2.2}_{-4.3} \cdot 10^{54}$	1.31	$1.0^{+1.1}_{-0.5} \cdot 10^{41}$	2.38	$5.7^{+6.2}_{-2.6} \cdot 10^{40}$
	X-ray CADET	SE1	0.329	$4.60 \cdot 10^{57}$	$5.4^{+5.5}_{-2.8} \cdot 10^{54}$	0.742	$2.3^{+2.5}_{-1.1} \cdot 10^{41}$	1	$1.7^{+1.9}_{-0.8} \cdot 10^{41}$
	X-ray CADET	NW1	0.447	$4.07 \cdot 10^{57}$	$4.3^{+4.3}_{-2.2} \cdot 10^{54}$	1.01	$1.4^{+1.5}_{-0.6} \cdot 10^{41}$	1.62	$8.4^{+9.6}_{-3.7} \cdot 10^{40}$
	Radio	E2	1.86	$2.40 \cdot 10^{59}$	$1.3^{+1.3}_{-0.6} \cdot 10^{56}$	4.15	$9.6^{+9.9}_{-4.6} \cdot 10^{41}$	6.96	$5.7^{+6.0}_{-2.7} \cdot 10^{41}$
	Radio	W2	2.65	$1.62 \cdot 10^{59}$	$7.0^{+7.0}_{-3.5} \cdot 10^{55}$	5.58	$4.0^{+4.0}_{-1.9} \cdot 10^{41}$	12.6	$1.8^{+1.8}_{-0.8} \cdot 10^{41}$
	X-ray visual	NE2	3.12	$5.81 \cdot 10^{58}$	$2.2^{+2.2}_{-1.1} \cdot 10^{55}$	6.47	$1.1^{+1.1}_{-0.5} \cdot 10^{41}$	19.2	$3.6^{+3.7}_{-1.7} \cdot 10^{40}$
	X-ray visual	SW2	2.98	$1.11 \cdot 10^{59}$	$4.3^{+2.2}_{-4.3} \cdot 10^{55}$	6.17	$2.2^{+2.2}_{-1.1} \cdot 10^{41}$	16.1	$8.5^{+8.7}_{-4.1} \cdot 10^{40}$
	X-ray CADET	SW2	3.11	$3.25 \cdot 10^{59}$	$1.2^{+1.2}_{-0.6} \cdot 10^{56}$	6.45	$6.1^{+6.2}_{-3.0} \cdot 10^{41}$	14.3	$2.8^{+2.8}_{-1.3} \cdot 10^{41}$
	X-ray CADET	N2	1.44	$6.50 \cdot 10^{58}$	$4.0^{+4.0}_{-2.0} \cdot 10^{55}$	3.26	$3.8^{+3.9}_{-1.8} \cdot 10^{41}$	5.91	$2.1^{+2.2}_{-1.0} \cdot 10^{41}$
	X-ray visual	S3	4.24	$2.46 \cdot 10^{60}$	$7.9^{+7.9}_{-3.9} \cdot 10^{56}$	8.85	$2.8^{+2.9}_{-1.4} \cdot 10^{42}$	16.3	$1.5^{+1.6}_{-0.7} \cdot 10^{42}$
	X-ray visual	NW3	4.04	$2.54 \cdot 10^{60}$	$8.2^{+4.1}_{-8.2} \cdot 10^{56}$	8.4	$3.1^{+3.1}_{-1.5} \cdot 10^{42}$	15	$1.7^{+1.8}_{-0.8} \cdot 10^{42}$
	X-ray CADET	S3	5.07	$3.66 \cdot 10^{60}$	$1.1^{+1.1}_{-0.6} \cdot 10^{57}$	10.6	$3.3^{+3.3}_{-1.6} \cdot 10^{42}$	20	$1.8^{+1.8}_{-0.9} \cdot 10^{42}$
	X-ray CADET	NW3	5.21	$1.69 \cdot 10^{60}$	$5.0^{+5.0}_{-2.5} \cdot 10^{56}$	10.8	$1.4^{+1.4}_{-0.7} \cdot 10^{42}$	23.6	$6.6^{+6.7}_{-3.3} \cdot 10^{41}$
	X-ray visual	E4	7.25	$1.18 \cdot 10^{61}$	$2.8^{+2.8}_{-1.4} \cdot 10^{57}$	14.8	$5.9^{+6.0}_{-2.9} \cdot 10^{42}$	28	$3.1^{+3.2}_{-1.5} \cdot 10^{42}$
	X-ray visual	W4	8.63	$4.53 \cdot 10^{60}$	$1.0^{+0.5}_{-1.0} \cdot 10^{57}$	17.6	$1.8^{+1.8}_{-0.9} \cdot 10^{42}$	42.7	$7.5^{+7.5}_{-3.7} \cdot 10^{41}$
NGC 5813	Radio	SW1	1.52	$5.64 \cdot 10^{58}$	$2.8^{+2.8}_{-1.4} \cdot 10^{55}$	3.41	$2.6^{+2.7}_{-1.3} \cdot 10^{41}$	6.24	$1.4^{+1.5}_{-0.7} \cdot 10^{41}$
	Radio	N1	1.77	$1.36 \cdot 10^{59}$	$5.8^{+5.8}_{-2.9} \cdot 10^{55}$	4	$4.5^{+4.7}_{-2.2} \cdot 10^{41}$	6.76	$2.7^{+2.8}_{-1.3} \cdot 10^{41}$
	X-ray visual	N1	1.15	$4.30 \cdot 10^{58}$	$2.6^{+2.6}_{-1.3} \cdot 10^{55}$	2.56	$3.2^{+3.3}_{-1.6} \cdot 10^{41}$	4.31	$1.9^{+2.0}_{-0.9} \cdot 10^{41}$
	X-ray visual	SW1	1.11	$6.89 \cdot 10^{58}$	$4.1^{+2.1}_{-4.1} \cdot 10^{55}$	2.46	$5.3^{+5.4}_{-2.6} \cdot 10^{41}$	3.76	$3.4^{+3.6}_{-1.6} \cdot 10^{41}$
	X-ray CADET	SW1	1.12	$1.41 \cdot 10^{59}$	$8.3^{+8.4}_{-4.2} \cdot 10^{55}$	2.5	$1.1^{+1.1}_{-0.5} \cdot 10^{42}$	3.41	$7.8^{+8.0}_{-3.7} \cdot 10^{41}$
	X-ray CADET	N1	1.51	$1.27 \cdot 10^{59}$	$6.6^{+6.6}_{-3.4} \cdot 10^{55}$	3.39	$6.2^{+6.3}_{-3.0} \cdot 10^{41}$	5.39	$3.9^{+4.0}_{-1.9} \cdot 10^{41}$
	X-ray visual	NE2	4.63	$8.82 \cdot 10^{59}$	$1.2^{+1.2}_{-0.6} \cdot 10^{56}$	11.4	$3.3^{+3.4}_{-1.6} \cdot 10^{41}$	21	$1.8^{+1.9}_{-0.9} \cdot 10^{41}$
	X-ray visual	SW2	6.99	$7.54 \cdot 10^{60}$	$7.1^{+3.6}_{-7.1} \cdot 10^{56}$	16.9	$1.3^{+1.4}_{-0.7} \cdot 10^{42}$	27.2	$8.3^{+8.5}_{-4.0} \cdot 10^{41}$
	X-ray CADET	SW2	6.53	$7.50 \cdot 10^{60}$	$7.1^{+7.1}_{-3.6} \cdot 10^{56}$	15.8	$1.4^{+1.4}_{-0.7} \cdot 10^{42}$	24.6	$9.1^{+9.4}_{-4.4} \cdot 10^{41}$
	X-ray CADET	NE2	5.03	$1.94 \cdot 10^{60}$	$2.5^{+2.5}_{-1.3} \cdot 10^{56}$	12.3	$6.4^{+6.6}_{-3.1} \cdot 10^{41}$	20.8	$3.8^{+3.9}_{-1.8} \cdot 10^{41}$
	X-ray visual	NE3	18.9	$2.57 \cdot 10^{61}$	$9.8^{+9.8}_{-4.9} \cdot 10^{56}$	41.6	$7.5^{+7.5}_{-3.7} \cdot 10^{41}$	98.5	$3.1^{+3.2}_{-1.6} \cdot 10^{41}$
	X-ray visual	SW3	23.9	$2.33 \cdot 10^{61}$	$6.5^{+3.3}_{-6.5} \cdot 10^{56}$	52.9	$3.9^{+3.9}_{-1.9} \cdot 10^{41}$	143	$1.4^{+1.4}_{-0.7} \cdot 10^{41}$
	X-ray CADET	NE3	18.4	$4.06 \cdot 10^{61}$	$1.7^{+1.7}_{-0.8} \cdot 10^{57}$	40.6	$1.3^{+1.3}_{-0.7} \cdot 10^{42}$	87.7	$6.1^{+6.1}_{-3.0} \cdot 10^{41}$
	X-ray CADET	NE3	18.4	$4.06 \cdot 10^{61}$	$1.7^{+1.7}_{-0.8} \cdot 10^{57}$	40.6	$1.3^{+1.3}_{-0.7} \cdot 10^{42}$	87.7	$6.1^{+6.1}_{-3.0} \cdot 10^{41}$

Table D1: T be continued.

Galaxy	Method	Cavity	d (kpc)	V (m^3)	E (erg)	t_{sound} (Myr)	$P_{\text{cav,sound}}$ (erg/s)	t_{bouy} (Myr)	$P_{\text{cav,bouy}}$ (erg/s)
NGC 5846	Radio	NE1	0.567	$5.00 \cdot 10^{58}$	$3.9_{-2.0}^{+3.9} \cdot 10^{55}$	1.25	$9.9_{-4.6}^{+10.4} \cdot 10^{41}$	1.45	$8.5_{-3.9}^{+9.2} \cdot 10^{41}$
	Radio	S1	0.666	$3.19 \cdot 10^{58}$	$2.5_{-1.3}^{+2.5} \cdot 10^{55}$	1.46	$5.4_{-2.5}^{+5.7} \cdot 10^{41}$	1.98	$4.0_{-1.8}^{+4.3} \cdot 10^{41}$
	X-ray visual	NE1	0.612	$3.48 \cdot 10^{58}$	$2.8_{-1.4}^{+2.8} \cdot 10^{55}$	1.34	$6.5_{-3.1}^{+6.8} \cdot 10^{41}$	1.72	$5.1_{-2.3}^{+5.5} \cdot 10^{41}$
	X-ray visual	SW1	1.02	$1.73 \cdot 10^{58}$	$1.1_{-1.1}^{+0.6} \cdot 10^{55}$	2.25	$1.6_{-0.8}^{+1.7} \cdot 10^{41}$	4.18	$8.7_{-4.0}^{+9.4} \cdot 10^{40}$
	X-ray CADET	S1	0.843	$1.08 \cdot 10^{59}$	$6.7_{-3.4}^{+6.7} \cdot 10^{55}$	1.85	$1.1_{-0.5}^{+1.2} \cdot 10^{42}$	2.3	$9.2_{-4.2}^{+9.9} \cdot 10^{41}$
	X-ray CADET	NW1	1.73	$2.79 \cdot 10^{58}$	$1.2_{-0.6}^{+1.2} \cdot 10^{55}$	3.85	$9.8_{-4.6}^{+10.3} \cdot 10^{40}$	8.5	$4.4_{-2.0}^{+4.8} \cdot 10^{40}$
	Radio	SE2	3.53	$3.40 \cdot 10^{60}$	$6.1_{-3.1}^{+6.1} \cdot 10^{56}$	8.18	$2.3_{-1.1}^{+2.4} \cdot 10^{42}$	11.1	$1.7_{-0.8}^{+1.8} \cdot 10^{42}$
	Radio	NW2	3.32	$2.70 \cdot 10^{60}$	$5.5_{-2.8}^{+5.5} \cdot 10^{56}$	7.65	$2.3_{-1.1}^{+2.3} \cdot 10^{42}$	10.5	$1.6_{-0.8}^{+1.7} \cdot 10^{42}$
	X-ray visual	SE2	5.58	$1.16 \cdot 10^{60}$	$1.2_{-0.6}^{+1.2} \cdot 10^{56}$	12.9	$2.9_{-1.4}^{+2.9} \cdot 10^{41}$	26.4	$1.4_{-0.7}^{+1.4} \cdot 10^{41}$
	X-ray visual	W2	5.43	$7.91 \cdot 10^{59}$	$8.2_{-8.2}^{+4.1} \cdot 10^{55}$	12.5	$2.1_{-1.0}^{+2.1} \cdot 10^{41}$	27.1	$9.5_{-4.6}^{+9.8} \cdot 10^{40}$
	X-ray CADET	SE2	6.3	$4.66 \cdot 10^{60}$	$4.1_{-2.1}^{+4.2} \cdot 10^{56}$	14.4	$9.1_{-4.5}^{+9.3} \cdot 10^{41}$	25.2	$5.2_{-2.5}^{+5.4} \cdot 10^{41}$
	X-ray CADET	W2	4.73	$3.42 \cdot 10^{60}$	$3.9_{-2.0}^{+3.9} \cdot 10^{56}$	11	$1.1_{-0.6}^{+1.1} \cdot 10^{42}$	17.2	$7.2_{-3.5}^{+7.3} \cdot 10^{41}$
NGC 6166	Radio	W1	3.62	$3.64 \cdot 10^{59}$	$5.9_{-3.0}^{+6.0} \cdot 10^{56}$	4.96	$3.8_{-1.8}^{+3.9} \cdot 10^{42}$	13.2	$1.4_{-0.6}^{+1.6} \cdot 10^{42}$
	Radio	E1	3.23	$4.75 \cdot 10^{59}$	$8.0_{-4.1}^{+8.1} \cdot 10^{56}$	4.45	$5.7_{-2.8}^{+6.0} \cdot 10^{42}$	10.6	$2.4_{-1.0}^{+2.8} \cdot 10^{42}$
	X-ray visual	W1	2.79	$3.89 \cdot 10^{59}$	$6.8_{-3.5}^{+6.8} \cdot 10^{56}$	3.86	$5.5_{-2.7}^{+5.8} \cdot 10^{42}$	8.81	$2.4_{-1.0}^{+2.8} \cdot 10^{42}$
	X-ray visual	NE1	2.91	$5.87 \cdot 10^{59}$	$1.0_{-1.0}^{+0.5} \cdot 10^{57}$	4.03	$8.0_{-3.9}^{+8.4} \cdot 10^{42}$	8.81	$3.7_{-1.5}^{+4.2} \cdot 10^{42}$
	X-ray CADET	E1	5.76	$1.91 \cdot 10^{60}$	$2.5_{-1.3}^{+2.5} \cdot 10^{57}$	7.69	$1.0_{-0.5}^{+1.1} \cdot 10^{43}$	20.1	$4.0_{-1.6}^{+4.5} \cdot 10^{42}$
	X-ray CADET	W1	2.82	$6.39 \cdot 10^{59}$	$1.1_{-0.6}^{+1.1} \cdot 10^{57}$	3.91	$8.7_{-4.3}^{+9.1} \cdot 10^{42}$	8.27	$4.1_{-1.7}^{+4.7} \cdot 10^{42}$
	Radio	E2	18.1	$1.70 \cdot 10^{62}$	$1.2_{-0.6}^{+1.2} \cdot 10^{59}$	21.9	$1.7_{-0.8}^{+1.8} \cdot 10^{44}$	53	$7.0_{-2.9}^{+8.0} \cdot 10^{43}$
	Radio	W2	18.4	$2.44 \cdot 10^{62}$	$1.6_{-0.8}^{+1.6} \cdot 10^{59}$	22.1	$2.3_{-1.1}^{+2.4} \cdot 10^{44}$	51	$1.0_{-0.4}^{+1.1} \cdot 10^{44}$
	X-ray visual	E2	20.5	$9.76 \cdot 10^{61}$	$6.3_{-3.2}^{+6.3} \cdot 10^{58}$	24.1	$8.2_{-4.0}^{+8.5} \cdot 10^{43}$	70.3	$2.8_{-1.1}^{+3.3} \cdot 10^{43}$
	X-ray visual	W2	23.2	$9.22 \cdot 10^{61}$	$5.9_{-5.9}^{+3.0} \cdot 10^{58}$	26.5	$7.1_{-3.4}^{+7.3} \cdot 10^{43}$	85.2	$2.2_{-0.9}^{+2.5} \cdot 10^{43}$
	X-ray CADET	W2	18.5	$2.46 \cdot 10^{62}$	$1.6_{-0.8}^{+1.6} \cdot 10^{59}$	22.2	$2.2_{-1.1}^{+2.3} \cdot 10^{44}$	51.6	$9.6_{-3.9}^{+11.0} \cdot 10^{43}$
	X-ray CADET	E2	21.3	$1.23 \cdot 10^{62}$	$7.9_{-4.0}^{+7.9} \cdot 10^{58}$	24.8	$1.0_{-0.5}^{+1.0} \cdot 10^{44}$	71.6	$3.5_{-1.4}^{+4.0} \cdot 10^{43}$

Table D1: Properties of individual cavities: method used for size estimation - either β -modelling (X-ray) or radio contours (Radio), cavity direction with respect to galactic centre and corresponding generation (e.g. NW1), semi-axis along the jet direction (length) r_l , semi-axis perpendicular to the jet direction (width) r_w , distance from galactic centre d , total internal energy E , cavity age assuming inflation at speed of sound t_{sound} , corresponding power required to inflate the cavity P_{sound} , cavity age assuming inflation at bouyant speed t_{bouy} and corresponding jet power P_{bouy} .

Appendix E: List of OBSIDs

Galaxy	OBSID	Instrument	Date (yyyy-mm-dd)	Cleaned exptime (ks)
IC 4926	3394	ACIS-S	2001-12-15	18.6
NGC 507	317	ACIS-S	2000-10-11	26.9
	2882	ACIS-I	2002-01-08	43.6
NGC 708	2215	ACIS-S	2001-08-03	28.7
	7921	ACIS-S	2006-11-20	110.7
NGC 1316	2022	ACIS-S	2001-04-17	28.4
	20340	ACIS-S	2019-04-16	45.0
	20341	ACIS-S	2019-04-22	51.4
	22179	ACIS-S	2019-04-17	39.0
	22180	ACIS-S	2019-04-20	13.6
	22187	ACIS-S	2019-04-25	53.2
NGC 1399	319	ACIS-S	2000-01-18	56.0
	9530	ACIS-S	2008-06-08	59.4
	14527	ACIS-S	2013-07-01	27.8
	14529	ACIS-S	2015-11-06	31.6
	16639	ACIS-S	2014-10-12	29.7
NGC 1407	791	ACIS-S	2000-08-16	44.5
NGC 1600	4283	ACIS-S	2002-09-18	22.7
	4371	ACIS-S	2002-09-20	26.8
	21374	ACIS-S	2018-12-03	25.7
	21375	ACIS-S	2019-11-28	42.2
	21998	ACIS-S	2018-12-03	13.9
	22878	ACIS-S	2019-11-25	45.0
	22911	ACIS-S	2019-11-01	31.0
	22912	ACIS-S	2019-11-02	35.6
NGC 4261	834	ACIS-S	2000-05-06	30.92
	9569	ACIS-S	2008-02-12	100.9
NGC 4374	20539	ACIS-S	2019-04-05	39.5
	20540	ACIS-S	2019-02-26	30.2
	20541	ACIS-S	2019-04-10	11.3
	20542	ACIS-S	2019-03-18	34.6
	20543	ACIS-S	2019-04-27	54.3
	21845	ACIS-S	2019-03-28	27.7
	21852	ACIS-S	2019-02-18	15.6
	21867	ACIS-S	2019-03-13	23.6
	22113	ACIS-S	2019-02-20	21.8
	22126	ACIS-S	2019-02-28	35.1
	22127	ACIS-S	2019-03-02	22.8
	22128	ACIS-S	2019-03-03	23.8
	22142	ACIS-S	2019-03-14	20.8
	22143	ACIS-S	2019-03-16	22.8
	22144	ACIS-S	2019-03-15	31.8
	22153	ACIS-S	2019-03-23	21.1
	22163	ACIS-S	2019-03-29	35.6
	22164	ACIS-S	2019-03-31	32.6
	22166	ACIS-S	2019-04-06	38.6
	22174	ACIS-S	2019-04-11	49.4
	22175	ACIS-S	2019-04-12	27.2
	22176	ACIS-S	2019-04-13	51.4
	22177	ACIS-S	2019-04-14	36.6
	22195	ACIS-S	2019-04-28	38.1
	22196	ACIS-S	2019-05-07	20.6

Table E1: To be continued.

Galaxy	OBSID	Instrument	Date (yyyy-mm-dd)	Cleaned exptime (ks)
NGC 4472	321	ACIS-S	2000-06-12	34.5
	11274	ACIS-S	2010-02-27	39.7
	12888	ACIS-S	2011-02-21	159.3
	12889	ACIS-S	2011-02-14	133.5
NGC 4486	352	ACIS-S	2000-07-29	37.7
	2707	ACIS-S	2002-07-06	98.7
	18232	ACIS-S	2016-04-27	18.2
	18233	ACIS-S	2016-02-23	37.2
	18781	ACIS-S	2016-02-24	39.5
	18782	ACIS-S	2016-02-26	34.1
	18783	ACIS-S	2016-04-20	36.1
	18836	ACIS-S	2016-04-28	38.9
	18837	ACIS-S	2016-04-30	13.7
	18838	ACIS-S	2016-05-28	56.3
	18856	ACIS-S	2016-06-12	25.5
	20034	ACIS-S	2017-04-11	13.1
	20035	ACIS-S	2017-04-14	13.1
	21075	ACIS-S	2018-04-22	9.1
	21076	ACIS-S	2018-04-24	9.0
NGC 4552	21457	ACIS-S	2019-03-27	14.1
	21458	ACIS-S	2019-03-28	12.8
NGC 4636	2072	ACIS-S	2001-04-22	54.4
	13985	ACIS-S	2012-04-22	49.4
	14358	ACIS-S	2012-08-10	49.4
	14359	ACIS-S	2012-04-23	48.1
NGC 4649	323	ACIS-S	2000-01-26	45.1
	3926	ACIS-I	2003-02-14	74.7
	4415	ACIS-I	2003-02-15	74.4
	785	ACIS-S	2000-04-20	26.9
	8182	ACIS-S	2007-01-30	49.5
NGC 4696	8507	ACIS-S	2007-02-01	17.5
	12975	ACIS-S	2011-08-08	84.9
	12976	ACIS-S	2011-02-24	101.0
	14328	ACIS-S	2011-08-12	14.0
	504	ACIS-S	2000-05-22	31.8
	505	ACIS-S	2000-06-08	10.0
	4954	ACIS-S	2004-04-01	89.0
	4955	ACIS-S	2004-04-02	44.7
	5310	ACIS-S	2004-04-04	49.3
	16223	ACIS-S	2014-05-26	179.0
NGC 4778	16224	ACIS-S	2014-04-09	42.3
	16225	ACIS-S	2014-04-26	30.1
	16534	ACIS-S	2014-06-05	55.4
	16607	ACIS-S	2014-04-12	45.7
	16608	ACIS-S	2014-04-07	34.1
	16609	ACIS-S	2014-05-04	82.3
	16610	ACIS-S	2014-04-27	17.3
	921	ACIS-S	2000-01-25	48.5
	10462	ACIS-S	2009-03-02	67.2
	10874	ACIS-S	2009-03-03	51.4

Table E1: To be continued.

Galaxy	OBSID	Instrument	Date (yyyy-mm-dd)	Cleaned exptime (ks)
NGC 5044	798	ACIS-S	2000-03-19	20.5
	9399	ACIS-S	2008-03-07	82.7
	17195	ACIS-S	2015-06-06	78.0
	17196	ACIS-S	2015-05-11	88.9
	17653	ACIS-S	2015-05-07	35.5
	17654	ACIS-S	2015-05-10	25.0
	17666	ACIS-S	2015-08-23	88.5
NGC 5813	5907	ACIS-S	2005-04-02	48.4
	9517	ACIS-S	2008-06-05	98.8
	12951	ACIS-S	2011-03-28	74.0
	12952	ACIS-S	2011-04-05	143.1
	12953	ACIS-S	2011-04-07	31.8
	13246	ACIS-S	2011-03-30	45.0
	13247	ACIS-S	2011-03-31	35.8
	13253	ACIS-S	2011-04-08	118.0
	13255	ACIS-S	2011-04-10	43.4
NGC 5846	788	ACIS-S	2000-05-24	23.4
	7923	ACIS-I	2007-06-12	90.0
NGC 6166	497	ACIS-S	2000-05-13	19.5
	498	ACIS-S	1999-12-11	17.9
	10748	ACIS-I	2009-11-19	40.6
	10803	ACIS-I	2009-11-17	30.2
	10804	ACIS-I	2009-06-23	18.8
	10805	ACIS-I	2009-11-23	30.3

Table E1: Parameters of individual *Chandra* ACIS observations of all the analysed galaxies.

Bibliography

- Abadi M., et al., 2015, TensorFlow: Large-Scale Machine Learning on Heterogeneous Systems, <https://www.tensorflow.org/>
- Abdulla Z., et al., 2019, *ApJ*, 871, 195
- Alhassan W., Taylor A. R., Vaccari M., 2018, *MNRAS*, 480, 2085
- Allen S. W., Dunn R. J. H., Fabian A. C., Taylor G. B., Reynolds C. S., 2006, *MNRAS*, 372, 21
- Arnaud K. A., 1996, in Jacoby G. H., Barnes J., eds, Astronomical Society of the Pacific Conference Series Vol. 101, Astronomical Data Analysis Software and Systems V. p. 17
- Balucinska-Church M., McCammon D., 1992, *ApJ*, 400, 699
- Binney J., 1978, *Comments on Astrophysics*, 8, 27
- Binney J., Tremaine S., 1987, *Galactic dynamics*. Princeton: Princeton Univ. Press
- Bîrzan L., Rafferty D. A., McNamara B. R., Wise M. W., Nulsen P. E. J., 2004, *ApJ*, 607, 800
- Blandford R. D., Payne D. G., 1982, *MNRAS*, 199, 883
- Blandford R. D., Znajek R. L., 1977, *MNRAS*, 179, 433
- Blanton E. L., Sarazin C. L., McNamara B. R., Wise M. W., 2001, *ApJL*, 558, L15
- Boehringer H., Voges W., Fabian A. C., Edge A. C., Neumann D. M., 1993, *MNRAS*, 264, L25
- Boggs P. T., Rogers J. E., 1990, in Statistical analysis of measurement error models and applications: proceedings of the AMS-IMS-SIAM joint summer research conference held June 10-16, 1989.
- Boizelle B. D., et al., 2021, *ApJ*, 908, 19
- Bondi H., 1952, *MNRAS*, 112, 195
- Brüggen M., Scannapieco E., Heinz S., 2009, *MNRAS*, 395, 2210
- Burkert A., Tremaine S., 2010, *ApJ*, 720, 516
- Cash W., 1979, *ApJ*, 228, 939
- Cavagnolo K. W., McNamara B. R., Nulsen P. E. J., Carilli C. L., Jones C., Bîrzan L., 2010, *ApJ*, 720, 1066

- Cavaliere A., Fusco-Femiano R., 1976, *A&A*, **500**, 95
- Chollet F., et al., 2015, Keras, <https://keras.io>
- Churazov E., Brüggen M., Kaiser C. R., Böhringer H., Forman W., 2001, *ApJ*, **554**, 261
- Churazov E., Sunyaev R., Forman W., Böhringer H., 2002, *MNRAS*, **332**, 729
- Churazov E., et al., 2010, *MNRAS*, **404**, 1165
- Clarke D. A., Harris D. E., Carilli C. L., 1997, *MNRAS*, **284**, 981
- Condon J., Darling J., Kovalev Y. Y., Petrov L., 2013, arXiv e-prints, p. [arXiv:1110.6252](https://arxiv.org/abs/1110.6252)
- D'Isanto A., Polsterer K. L., 2018, *A&A*, **609**, A111
- Dai B., Seljak U., 2021, *Proceedings of the National Academy of Science*, **118**, 2020324118
- Diehl S., Li H., Fryer C. L., Rafferty D., 2008, *ApJ*, **687**, 173
- Dieleman S., Willett K. W., Dambre J., 2015, *MNRAS*, **450**, 1441
- Dong R., Rasmussen J., Mulchaey J. S., 2010, *ApJ*, **712**, 883
- Dunn R. J. H., Allen S. W., Taylor G. B., Shurkin K. F., Gentile G., Fabian A. C., Reynolds C. S., 2010, *MNRAS*, **404**, 180
- Emonts B. H. C., Morganti R., Oosterloo T. A., van der Hulst J. M., van Moorsel G., Tadhunter C. N., 2007, *A&A*, **464**, L1
- Enßlin T. A., Heinz S., 2002, *A&A*, **384**, L27
- Ester M., Kriegel H.-P., Sander J., Xu X., 1996, in Proceedings of the Second International Conference on Knowledge Discovery and Data Mining. KDD'96. AAAI Press, p. 226–231
- Ettori S., 2000, *MNRAS*, **311**, 313
- Fabian A. C., et al., 2000, *MNRAS*, **318**, L65
- Fabian A. C., Celotti A., Blundell K. M., Kassim N. E., Perley R. A., 2002, *MNRAS*, **331**, 369
- Fabian A. C., Reynolds C. S., Taylor G. B., Dunn R. J. H., 2005, *MNRAS*, **363**, 891
- Fabian A. C., Sanders J. S., Taylor G. B., Allen S. W., Crawford C. S., Johnstone R. M., Iwasawa K., 2006, *MNRAS*, **366**, 417
- Finoguenov A., Ruszkowski M., Jones C., Brüggen M., Vikhlinin A., Mandel E., 2008, *ApJ*, **686**, 911
- Fort S., 2017, arXiv e-prints, p. [arXiv:1712.00523](https://arxiv.org/abs/1712.00523)
- Freeman P., Doe S., Siemiginowska A., 2001, in Starck J.-L., Murtagh F. D., eds, Society of Photo-Optical Instrumentation Engineers (SPIE) Conference Series Vol. 4477, Astronomical Data Analysis. pp 76–87 ([arXiv:astro-ph/0108426](https://arxiv.org/abs/astro-ph/0108426)), doi:10.1117/12.447161

- Fruscione A., et al., 2006, in Silva D. R., Doxsey R. E., eds, Society of Photo-Optical Instrumentation Engineers (SPIE) Conference Series Vol. 6270, Society of Photo-Optical Instrumentation Engineers (SPIE) Conference Series. p. 62701V, [doi:10.1117/12.671760](https://doi.org/10.1117/12.671760)
- Gaspari M., Ruszkowski M., Oh S. P., 2013, *MNRAS*, **432**, 3401
- Gaspari M., et al., 2019, *ApJ*, **884**, 169
- Giacintucci S., et al., 2011, *ApJ*, **732**, 95
- Gilli R., Comastri A., Hasinger G., 2007, *A&A*, **463**, 79
- Gitti M., Feretti L., Schindler S., 2006, *A&A*, **448**, 853
- Grossová R., et al., 2019, *MNRAS*, **488**, 1917
- Gültekin K., et al., 2009, *ApJ*, **698**, 198
- Guo F., 2015, *ApJ*, **803**, 48
- HI4PI Collaboration et al., 2016, *A&A*, **594**, A116
- Harris C. R., et al., 2020, *Nature*, 585, 357
- Hausen R., Robertson B. E., 2020, *AJS*, **248**, 20
- He S., Li Y., Feng Y., Ho S., Ravanbakhsh S., Chen W., Póczos B., 2019, *Proceedings of the National Academy of Sciences*, **116**, 13825
- Heinz S., Reynolds C. S., Begelman M. C., 1998, *ApJ*, **501**, 126
- Hlavacek-Larrondo J., Fabian A. C., Edge A. C., Ebeling H., Sanders J. S., Hogan M. T., Taylor G. B., 2012, *MNRAS*, **421**, 1360
- Hlavacek-Larrondo J., et al., 2015, *ApJ*, **805**, 35
- Huang Z., Sarazin C. L., 1998, *ApJ*, **496**, 728
- Ichinohe Y., Yamada S., 2019, *MNRAS*, **487**, 2874
- Ichinohe Y., Yamada S., Miyazaki N., Saito S., 2018, *MNRAS*, **475**, 4739
- Irwin J. A., Athey A. E., Bregman J. N., 2003, *ApJ*, **587**, 356
- Jensen J. B., Tonry J. L., Barris B. J., Thompson R. I., Liu M. C., Rieke M. J., Ajhar E. A., Blakeslee J. P., 2003, *ApJ*, **583**, 712
- Jones C., Forman W., Vikhlinin A., Markevitch M., David L., Warmflash A., Murray S., Nulsen P. E. J., 2002, *ApJL*, **567**, L115
- Joye W. A., Mandel E., 2003, in Payne H. E., Jedrzejewski R. I., Hook R. N., eds, Astronomical Society of the Pacific Conference Series Vol. 295, Astronomical Data Analysis Software and Systems XII. p. 489
- Karzas W. J., Latter R., 1961, *AJS*, **6**, 167
- Kellogg E., Baldwin J. R., Koch D., 1975, *ApJ*, **199**, 299
- Kelly B. C., 2007, *ApJ*, **665**, 1489

- Kingma D. P., Ba J., 2014, arXiv e-prints, p. [arXiv:1412.6980](https://arxiv.org/abs/1412.6980)
- Kormendy J., Ho L. C., 2013, *Annual Review of A&A*, **51**, 511
- Kosiba M., et al., 2020, *MNRAS*, **496**, 4141
- Kraft R. P., et al., 2017, *ApJ*, **848**, 27
- Lakhchaura K., et al., 2018, *MNRAS*, **481**, 4472
- Lakhchaura K., Truong N., Werner N., 2019, *MNRAS*, **488**, L134
- Lauer T. R., et al., 2007, *ApJ*, **662**, 808
- Levenberg K., 1944, Quarterly of applied mathematics, **2**, 164
- Lodders K., 2003, *ApJ*, **591**, 1220
- Makarov D., Prugniel P., Terekhova N., Courtois H., Vauglin I., 2014, *A&A*, **570**, A13
- Malin D. F., 1977, AAS Photo Bulletin, **16**, 10
- Mancini L., Feoli A., 2012, *A&A*, **537**, A48
- Marquardt D. W., 1963, Journal of the society for Industrial and Applied Mathematics, **11**, 431
- Martín-Navarro I., Burchett J. N., Mezcua M., 2020, *MNRAS*, **491**, 1311
- McCourt M., Sharma P., Quataert E., Parrish I. J., 2012, *MNRAS*, **419**, 3319
- McMullin J. P., Waters B., Schiebel D., et al., 2007, CASA Architecture and Applications. p. 127
- McNamara B. R., Nulsen P. E. J., 2007, *Annual Review of A&A*, **45**, 117
- McNamara B. R., Nulsen P. E. J., 2012, *New Journal of Physics*, **14**, 055023
- McNamara B. R., Wise M. W., David L. P., Nulsen P. E. J., Sarazin C. L., 2000a, in Durret F., Gerbal D., eds, Constructing the Universe with Clusters of Galaxies. p. 6.6 ([arXiv:astro-ph/0012331](https://arxiv.org/abs/astro-ph/0012331))
- McNamara B. R., et al., 2000b, *ApJL*, **534**, L135
- McNamara B. R., et al., 2001, *ApJL*, **562**, L149
- McNamara B. R., Rohanizadegan M., Nulsen P. E. J., 2011, *ApJ*, **727**, 39
- Mehrgan K., Thomas J., Saglia R., Mazzalay X., Erwin P., Bender R., Kluge M., Fabricius M., 2019, *ApJ*, **887**, 195
- Mendygral P. J., O'Neill S. M., Jones T. W., 2011, *ApJ*, **730**, 100
- Merritt D., Ferrarese L., 2001, *ApJ*, **547**, 140
- Mitchell R. J., Culhane J. L., Davison P. J. N., Ives J. C., 1976, *MNRAS*, **175**, 29P
- Nagar N. M., Falcke H., Wilson A. S., Ulvestad J. S., 2002, *A&A*, **392**, 53

- Narayan R., Yi I., 1994, *ApJL*, **428**, L13
- Navarro J. F., Frenk C. S., White S. D. M., 1996, *ApJ*, **462**, 563
- Nulsen P. E. J., 1986, *MNRAS*, **221**, 377
- Nulsen P. E. J., Hambrick D. C., McNamara B. R., Rafferty D., Birzan L., Wise M. W., David L. P., 2005, *ApJL*, **625**, L9
- Omma H., Binney J., 2004, *MNRAS*, **350**, L13
- Omma H., Binney J., Bryan G., Slyz A., 2004, *MNRAS*, **348**, 1105
- Panagoulia E. K., Fabian A. C., Sanders J. S., Hlavacek-Larrondo J., 2014, *MNRAS*, **444**, 1236
- Pedregosa F., et al., 2011, *Journal of Machine Learning Research*, **12**, 2825
- Perley R. A., Butler B. J., 2013, *AJS*, **204**, 19
- Petrov L., 2021, *AJ*, **161**, 14
- Pringle J. E., 1981, *Annual Review of A&A*, **19**, 137
- Rafferty D. A., McNamara B. R., Nulsen P. E. J., Wise M. W., 2006, *ApJ*, **652**, 216
- Randall S. W., et al., 2011, *ApJ*, **726**, 86
- Randall S. W., et al., 2015, *ApJ*, **805**, 112
- Russell H. R., Sanders J. S., Fabian A. C., 2008, *MNRAS*, **390**, 1207
- Russell H. R., McNamara B. R., Edge A. C., Hogan M. T., Main R. A., Vantyghem A. N., 2013, *MNRAS*, **432**, 530
- Russell H. R., Fabian A. C., McNamara B. R., Broderick A. E., 2015, *MNRAS*, **451**, 588
- Russell H. R., Fabian A. C., McNamara B. R., Miller J. M., Nulsen P. E. J., Piotrowska J. M., Reynolds C. S., 2018, *MNRAS*, **477**, 3583
- Saglia R. P., et al., 2016, *ApJ*, **818**, 47
- Sanders J. S., Fabian A. C., 2007, *MNRAS*, **381**, 1381
- Sanders J. S., et al., 2016a, *MNRAS*, **457**, 82
- Sanders J. S., Fabian A. C., Russell H. R., Walker S. A., Blundell K. M., 2016b, *MNRAS*, **460**, 1898
- Schellenberger G., David L. P., Vrtilek J., O'Sullivan E., Giacintucci S., Forman W., Jones C., Venturi T., 2021, *ApJ*, **906**, 16
- Schneider P., 2006, *Extragalactic Astronomy and Cosmology*
- Schure K. M., Kosenko D., Kaastra J. S., Keppens R., Vink J., 2009, *A&A*, **508**, 751
- Secká J., 2018, Určování výkonů jetů v obřích eliptických galaxiích [online], <https://is.muni.cz/th/rnxoz/>

- Serlemitsos P. J., Smith B. W., Boldt E. A., Holt S. S., Swank J. H., 1977, *ApJL*, **211**, L63
- Sérsic J. L., 1963, Boletin de la Asociacion Argentina de Astronomia La Plata Argentina, **6**, 41
- Shilon I., et al., 2019, *Astroparticle Physics*, **105**, 44
- Shin J., Woo J.-H., Mulchaey J. S., 2016, *AJS*, **227**, 31
- Storn R., 1995, Technical report, International Computer Science Institute, 11
- Student 1908, *Biometrika*, **6**, 302
- Szegedy C., et al., 2015, in 2015 IEEE Conference on Computer Vision and Pattern Recognition (CVPR). pp 1–9, doi:10.1109/CVPR.2015.7298594
- Temi P., Amblard A., Gitti M., Brighenti F., Gaspari M., Mathews W. G., David L., 2018, *ApJ*, **858**, 17
- Thomas J., Ma C.-P., McConnell N. J., Greene J. E., Blakeslee J. P., Janish R., 2016, *Nature*, **532**, 340
- Tonry J. L., Blakeslee J. P., Ajhar E. A., Dressler A., 2000, *ApJ*, **530**, 625
- Tremaine S., et al., 2002, *ApJ*, **574**, 740
- Truong N., Pillepich A., Werner N., 2021, *MNRAS*, **501**, 2210
- Tully R. B., et al., 2013, *AJ*, **146**, 86
- Voit G. M., Donahue M., 2015, *ApJL*, **799**, L1
- Werner N., Mernier F., 2020, Hot Atmospheres of Galaxies, Groups, and Clusters of Galaxies. pp 279–310, doi:10.1007/978-3-030-38509-5_10
- Wu C., et al., 2019, *MNRAS*, **482**, 1211

